University of Stellenbosch
Department of Process Engineering

# *Selective Oxidation of Propene to Acrolein on α-$Bi_2Mo_3O_{12}$ Nano-particles*

Peter van Vuuren

Thesis submitted in partial fulfilment of the requirements for the degree Master of Science in Engineering (Chemical Engenering) in the departmint of Process Engenering at the University of Stellenbosch.

**Study leader: Dr L. Callanan**

April 2005

# Declaration

I, the undersigned, hereby declare that the work contained in this thesis is my own original work and has not previously in its entirety or in part been submitted at any university for a degree.


…… ……

**Signature** Date:

# Synopsis

Although selective oxidation catalysts are widely used and extensively studied for their industrial and academic value, their complex mechanisms are, to a large extent, still unclear. The field of so-called allylic (amm)oxidations reactions was chosen for further investigation, in particular the simplistic selective oxidation of propene to acrolein over an $\alpha$-$Bi_2Mo_3O_{12}$ catalyst.

One of the most important approaches in selective oxidation is to try to correlate the physicochemical properties of catalysts with their catalytic performance (activity and selectivity). The most interesting, and seemingly most widely invoked parameter, is lattice oxygen mobility. The problem, however, is the difficulty encountered in measuring oxygen mobility.

It is hypothesised that the depth of oxygen utilisation and lattice oxygen mobility of bismuth molybdate during the partial oxidation of propene to acrolein may be determined by measuring the rate of acrolein formation and lattice oxygen usage over a range of discrete particle sizes that could be synthesised using reverse micelle technology.

**Catalyst Preparation**

A preliminary investigation into the reverse micelle technique showed that discrete nano-sized particles could be synthesised, but that there was no size control over the outcome and that, in most cases there were some degree of particle agglomeration. It was also found that nanorod formation occurred due to adsorbtion of surfactant. More in-depth investigation had to be done in order to achieve particle size control and the liberation of the calcined $\alpha$-$Bi_2Mo_3O_{12}$ catalyst particles required for kinetic experiments. Simple precipitation methods, the catalyst calcination step, and the formation and stability of reverse micelles were investigated.

A simple precipitation method to prepare $\alpha$-$Bi_2Mo_3O_{12}$, suitable to be integrated into the reverse micelle technique was found by buffering the mixture of bismuth nitrate and ammonium molybdate solutions with an excess of molybdate. This prevented the pH from decreasing below a critical value of 1.3 (at which $\beta$-$Bi_2Mo_2O_9$ forms as an impurity).

The excess molybdenum caused the formation of $MoO_3$ in the calcined product, which was selectively and successfully removed using a warm ammonium wash followed by a water rinse and a recalcination step.

XRD of a temperature range calcination shows that the calcination starts at temperatures as low as 200°C and almost complete calcination of the catalyst at 280°C. DSC analyses show a 47.15 J/g crystal formation peak only at 351°C. The $Mo_{18}O_{56}(H2O)_8^{4-}$ anion or its double, $Mo_{36}O_{112}(H_2O)_{16}^{8-}$, is responsible for the formation of $\alpha$-$Bi_2Mo_3O_{12}$ in the precipitation calcination reaction.

Reverse micelles were investigated using a Malvern Zetasizer and showed a complex dynamic system in which the reverse micelle sizes and size distributions change over time as a function of surfactant and aqueous concentrations, the salt used and aqueous phase salinity. Although much was accomplished in this study, more investigations into the constituent steps of the reverse micelle technique are needed to develop a method to synthesise the range of discrete catalyst particle sizes required for kinetic studies.

**Kinetic Studies**

For the purpose of kinetic experiments a metal reactor was found to be superior to that of a glass reactor. The reactor rig was adequate for these kinetic studies but do not meet the requirements for detailed reaction order experiments. The analysing apparatus could not measure $CO_2$ formation accurately and it had to be calculated using a carbon balance.

Only the model proposed by Keulks and Krenzke [1980[a]] was able to describe the kinetic result, but the model parameter describing the oxidative state of the catalyst surface could not be calculated due to the lack compatibility between published data. Values were awarded to this parameter so to give an Arrhenius plot which corresponded to published data. The parameter describing the oxidative state vs. temperature took on a function that was consistant with the reasoning of Keulks and Krenzke [1980[a]].

Comprehensive preliminary kinetic studies are needed, both in catalyst reduction and re-oxidation, in order to determine the reaction conditions, explore more advanced kinetic models and investigate model parameters that are theoretically and/or empirically obtainable and quantifiable.

# Opsomming

Hoewel selektief oksidasie katalis deeglik bestudeer word vir hul grootskaalse industriële gebruik sowel as akademiese waarde, is die komplekse meganistiese aspekte daarvan, tot ‘n groot mate, steeds onbekend. Die snel ontwikkelende groep van *allylic* (amm)oksidasie reaksies, spesifiek die selektiewe oksidasie van propeen na akrolien met die gebruik van $\alpha$-$Bi_2Mo_3O_{12}$ as ‘n katalis, is gekies vir verdere studies.

In die selektiewe oksidasie, soos in ander gebiede van kataliese, is dit van kardinale belang om korrelasies te vind tussen die fisies-chemiese eienskappe en die katalis se verrigting (aktiwiteit en selektiwiteit). Die mobiliteit van die kristalsuurstof is só ‘n opspraakwekkende eienskap wat gebruik kan word vir hierdie korrelasies. Die uitdaging is in die meting en kwantifisering van hierdie suurstof-mobiliteit parameter.

Die hipotese lui dat die reaksie-diepte en suurstof-mobiliteit tydens die reaksie van propeen na akrolien bepaal kan word deur die reaksie tempo’s oor diskrete partikel-groottes te bestudeer. Hierdie reeks van diskrete partikel-groottes is moontlik verkrygbaar deur die gebruik van miselle-tegnologie.

**Katalis Voorbereiding**

‘n Voorlopige studie van die omgekeerde miselle-tegniek bevestig die moontlikheid om partikels met diskrete groottes deur middel van hierdie tegniek voor te berei, hoewel beheer oor die partikel-groottes en herhaalbaarheid nie bewerkstellig kon word nie. Nano-staaf formasie uit katalis-partikels is ‘n resultaat van surfaktant adsorbasie. ‘n Eenvoudige presipitasie metode, katalis-kalsinasie en die formasie en stabilieit van omgekeerde miselle is verder bestudeer.

‘n Geskikte presipitasie metode vir die voorbereiding van $\alpha$-$Bi_2Mo_3O_{12}$ is ontwikkel sodat dit geïntegreer kan word met the omgekeerde miselle tegniek. Die mengsel van bismut en molubdeen is gebuffer teen die verlaging in pH benede 1.3 deur die gebruik van oormaat molubdeen. Hierdie oormaat molubdeen veroorsaak die vorming van $MoO_3$ as ‘n onsuiwerheid in die gekalsineerde produk wat verwyder kan word deur ‘n behandeling met warm ammonium gevolg deur ‘n waterspoel en ‘n kalsinas.

Die XRD-analiese vir ‘n temperatuur reeks kalsineer dui dat die kalsineringsreaksie by temperature so laag as 200°C begin en teen 280°C volledig verloop het vir ‘n kalsineringstydperk van 24 uur. ‘n DSC-analiese van die selfde presipitaat dui ‘n 47.15 J/g kristal-formasie piek aan by 351°C. Die $Mo_{18}O_{56}(H_2O)_8^{4-}$ anion of sy dubbel, $Mo_{36}O_{112}(H_2O)_{16}^{8-}$, is vermoedelik vir antwordelik vir $\alpha$-$Bi_2Mo_3O_{12}$ formasie.

Omgekeerde miselle is ondersoek met die gebruik van ‘n Malvern Zetasizer. Die resultate wys op ‘n dinamiese sisteem wat sterk beïnvloed word deur die mengsel-samestelling, die tipe sout in oplossing en die konsentrasie van die sout in oplossing.

Hoewel veel bereik is in hierdie ondersoek is verdere studies in die agtereenvolgende stappe van die omgekeerde miselle tegniek nodig, voordat die vereiste reeks van partikel-groottes berei kan word vir die doel van kinetiese eksperimente.

**Kinetiese Eksperimente**

‘n Metaalreaktor het oor die algemeen beter gevaar as ‘n glasreaktor in die kinetiese eksperimente. Die eksperimentele opstelling was doeltreffend vir die inleidende kinetiese eksperimente, maar voldoen nie aan die vereistes om akkurate reaksie orde eksperimente te doen nie. Die analitiese apparaat kon ook nie die $CO_2$ akkuraat meet nie, dus moes dit bereken word met behulp van ‘n koolstof balans oor die sisteem.



Die kinetiese modelle is getoets om te sien of dit die kinetiese resultate kon verklaar. Slegs die model van Keulks and Krenzke [1980[a]] kon die resultate verklaar, maar die model-parameter wat die oksidasie-toestand van die katalis-oppervlak beskryf kon nie bereken word nie weens onvoorsoenbaarheid tussen gepubliseerde data en modelparameters. Aan hierdie oksidasie-toestand parameter is waardes toegeken sodat die gevolglike Arrhenius plot en die aktiverings energie daaruit verkry, ooreengestem het met dié van gepubliseerde waardes. Die oksidasie-toestand as ‘n funksie van temperatuur het ooreengestem met redenasies uit die literatuur.

Uitgebreide kinetiese studies is nodig in beide die reduksie en oksidasie van die katalis, sodat reaksie toestande, meer komplekse kinetiese modelle en bepaalbare model-parameters ontwikkel en getoets kan word.

# Acknowledgements

The author greatly acknowledges Dr L. Callanan, who assisted in writing up of this thesis, and Mr A. Miller and Mr J. Tee, for carrying out part of the kinetic experiments and titration experiments respectively. Great thanks to Dr R. Buchner, who obtained the XRD, and Mr F. Greef, who obtained the TGA and DSC data. Acknowledgments are also made to the NRF (National Research Foundation) and the University of Stellenbosch for financial support and to both iThemba and Plascon Labs, for the use of their facilities. Also thanks to the catalyst group at the Department of Chemical Engineering at the University of Cape Town for their support.

# Table of Contents

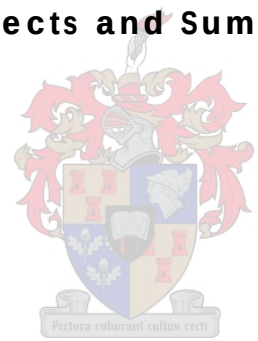

# Glossary

| | | |
|---|---|---|
| *a* | Activity (concentration) | [mol/l] |
| $A_i$ | Peak area of component i | [$m^2$] |
| $A_{st}$ | Peak area of the internal standard | [$m^2$] |
| $A_{sp}$ | Specific area of catalyst | [$m^2/g$] |
| $c_i$ | Intensity weight of particles | |
| $C_{noi}$ | Carbon number of component i | |
| $C_\infty$ | Bulk phase solubility (solubility of an infinitely large droplet) | |
| D | Diffusion in the continuous phase | [m/s] |
| d(H) | Hydrodynamic diameter | [m] |
| E | Activation energy | [J/mole] |
| E(t) | Exit age | |
| F(t) | Cumulative residence-time distribution | [sec] |
| $g_1$ | Correlation function | |
| *k* | Boltzmann constant | |
| k | Thermal conductivity | |
| k, $k_R$, $k_{ox}$ | Rate constant, reduction rate, oxidation rate | |
| $k_0$ | Pre-exponential factor | |
| $m_1$ | Refractive index | |
| Mr | Molecular Weight | [g/mole] |
| $P^x_i$ | Partial pressures of component i to the power of its reaction order x | [Pa] |
| $r_{sp\,i}$ | Specific rate formation of product i | [$mol/m^2/s$] |
| R | Universal gas constant | [8.314] |
| $RF_i$ | Response factor of component i | |
| Ri, r | Radius | [m] |
| *t* | Time | [sec] |
| $t_m$ | Mean residence time | [sec] |
| T | Absolute temperature | [K] |
| T(r) | Reactor radial temperature | [°C] |
| V | Reactor volume | [$m^3$] |
| $V_m$ | Molar volume of oil | [$m^3$/mole] |
| WHSV | Weight hourly space velocity | [$g_{propene}/g_{catal}.hr^-$] |
| $\dot{q}$ | Rate at which heat is generated | [W] |
| q | $(4\pi m_1/\lambda_o)\ \sin\theta/2$ | |
| Å | Amstrong | [10 Å = 1nm] |
| $\Theta_{ox}$ | Fraction of active sites that are fully oxidised | |
| $\Gamma$ | Surface excess | [$mole/m^2$] |
| $\gamma$ | Interfacial tension | |
| $\eta$ | Viscosity | [cP] |
| $\tau$ | Correlation time delay | [sec] |
| $\lambda_o$ | Wavelength of laser | [m] |
| $\theta$ | Scattering angle | [°] |
| $\rho$ | Density | [$kg/m^3$] |

# 1. Introduction and Project Relevance

## *1.1 Introduction*

The selective oxidation of hydrocarbons is one of the most applied reactions in the chemical industry for the preparation of aldehydes, ketones and organic acids. Catalytic systems work by suppressing the thermodynamically favourable product by providing an alternative reaction pathway to yield the preferred product. Although partial oxidation is widely used and investigated, its complex mechanism is still largely unclear, to the extent that it cannot be modelled effectively. If the mechanisms over the catalyst were understood, to the extent that an accurate model could be obtained, a powerful tool could be developed.

An important family of selective oxidation reactions is that of the so-called allylic (amm)oxidations. This is namely the selective oxidation of alkenes, e.g. propene. Thanks to the rapid development of physicochemical techniques, the understanding of the performance of the catalyst and the reaction mechanism in selective oxidation has been improved considerably [Weng, 1992]. This field has been chosen for further investigation, especially the selective oxidation of propene to acrolein over a bismuth molybdate catalyst. The system has been chosen for its simplicity. Firstly, propane has no extra functional group, but has the main features required, namely, oxidation of the saturated end of the molecule while leaving the double bond intact. Secondly bismuth molybdate is a well studied [Weng, 1992; Bettahar, 1996; Grasselli, 1999 & Hanna, 2004] and simplistic catalyst with universal oxide characteristics. Nowadays, it is generally agreed that the selective oxidation of alkenes occurs according to the three-step Mars-Van Krevelen mechanism (this will be discussed further in section 2.1.4) [Keulks & Krenzke, 1980[b]; Haber, 1988 & Wragg *et al.,* 1973]. Detailed kinetic mechanisms over bismuth molybdate have already been proposed [Grasselli, 1983 & 1984]. These mechanisms are generally accepted and indicate that the transfer of both protons and electrons between alkenes and catalysts is needed. This necessitates that the catalyst not only has adequate redox properties, but also correct acid-base properties.

One of the most important approaches in selective oxidation, as in many fields relating to catalysts, is to try to correlate the physicochemical properties of catalysts with their catalytic performance (activity and selectivity). Many parameters have been proposed, and these can be conveniently classified into five groups, namely those related to lattice oxygen ions, cations, electron mobility, cation-oxygen bonds and crystallographic structures [Weng, 1992]. The most interesting, and seemingly most widely invoked parameter, is oxygen mobility, which has shown to be relevant to many simple and some compound oxides. The problem, however, is the difficulty encountered in measuring oxygen mobility, as it is dependent on pre-treatment of the catalyst during the measurements.

Correlations between the specific activity and the oxygen mobility of lattice oxygen have been suggested, but no correlation is universally accepted due to the fact that the selective oxidation is a multi-step process and each step needs different catalytic properties.

It is accepted that the reduction-re-oxidation properties are the most important ones for the selective oxidation catalyst. Very few investigations, in comparison with those focusing on mechanistic aspects, have been devoted to the kinetic study of reduction, even fewer to the re-oxidation process.

The purpose of this work is to investigate the reduction of the bismuth molybdate catalyst in the presence of propene. The reduction depth of the catalyst is of particular interest. Keulks [1970] and Ueda *et al.* [1981 & 1984] used a Keulks-developed $^{18}O_2$ technique to calculate the equivalent molecular layers that are related to the amount of lattice oxygen used in the reactions to form products. The actual reaction depth will be dependent on the reducibility of the catalyst and lattice oxygen mobility in the bulk of the catalyst. Using micro-emulsion technology, nano-sized catalyst particles with a narrow size distribution were synthesised. A range of discreet particle sizes was needed in an attempt to determine the reaction depth by determining the amount of catalyst volume utilised in the reaction.

The first step in the project was to build an experimental setup that is reliable and adequate for the research. The testing of the experimental setup was done by trying to

reproduce and verify previous experimental results on similar systems [Keulks *et al.,* 1980[b]]. Thereafter, a technique had to be developed to synthesise the range of discreet particle sizes required for the kinetic experiments. The focus of the work is on the synthesis and characterisation of the catalyst.

## *1.2 Project Relevance*

The selective oxidation of hydrocarbons is one of the most applied reactions in the chemical industry for the preparation of aldehydes, ketones and organic acids (approximately 25% of all chemicals produced by catalyst and 18% of sales) [Greek, 1989]. Thus, partial oxidation products make up a considerable amount of chemical products. The process invented by the Standard Oil of Ohio Company (SOHIO, now BP America), which is used in the industry on a large scale, is the oxidation/ammoxidation of propene over bismuth-molybdate catalyst to produce acrolein and acrylonitrile [Grasselli and Burrington, 1981]. In 2000, the worldwide demand for acrylonitrile alone was estimated at 5,000,000 tons per year [AsahiKasei Press Release, 2000]. More locally, a large part of the revenue generated by Sasol comes from alpha-olefins produced by the Fisher Tropsch process. In this process, 500,000 tons of propene are produced per year as a by-product (22% of olefins). Since the discovery of the SOHIO process to obtain acrolein and acrylonitraile from propene [Grasselli *et al.,* 1981], commercial catalysts based on $Bi_2O_3{\cdot}MoO_3$, U-Sb, Fe-Sb, Sn-Sb and multi component bismuth molybdates have been developed [Idol, 1959, Callanhan *et al.,* 1962 and Moro-oka, 1994]. This has become one of the most active fields. These catalytic systems usually improve activity and/or selectivity when added to other constituents, such as oxides of Bi, Ni, Co, Sb, Fe, etc. [Ueda and Moro-oka, 1981]. The further study of this field not only has great industrial importance, but is also of academic interest.

A research project on the selective oxidation of propene to acrolein over a bismuth-molybdate catalyst opens up a variety of research opportunities. The following are typical topics relevant to such a research project:

- To investigate the time dependence of the reaction and the subsequent re-oxidation of the mixed metal oxide catalyst during a selective oxidation reaction.
- To study the reversibility of the reduction.

- To measure the kinetics of the catalyst re-oxidation.
- To determine the percentage of framework oxygen that is involved in the selective oxidation reaction.
- To study the influences of and the catalytic enhancements that are and may be achieved with the incorporation of other metals in a mixed metal oxide system.
- The reaction kinetic studies promote further study into catalyst preparation techniques. Physical dimensions (nano-size particles and crystals) are known to govern the properties of the catalyst, although little attention has been focused on binary oxides, despite of their wide applicability.

These were the initial focus areas using the proposed system as the test reaction. At a later date, projects could be extended to include other light alkenes, alkanes and aldehydes.

# 2. Literature Review

## *2.1 Selective Oxidation Catalysis*

This section will discuss and summarise the mechanistic aspects of bismuth-molybdate catalysts. The catalysts are evaluated structurally, thermodynamically and kinetically.

### 2.1.1 Selective Oxidation Catalysts

Selective oxidation catalysts work by providing an alternative reaction pathway that has lower activation energy than the total combustion product pathway to form selective oxidation products in high yields. Thus, the catalyst must be able to activate the hydrocarbon at relatively low temperatures so as not to promote total combustion products. This may pose a problem, as the C-H bonds of the reactant are much stronger than those of the intermediate product, and therefore is a tendency for the oxide catalyst to oxidise the intermediate further into the total combustion products. This is the typical problem if the reactant is an alkane. Due to its low activity, the activation of the reactant needs operating conditions (temperatures as high as 500°C, for example) that are detrimental to the stability of the product [Bettahar *et al.,* 1996]. The metal-oxygen bond in the oxide catalyst should be of intermediate strength, as lattice oxygen participates exclusively in the oxidation reaction [Keulks, 1970 & Ueda and Moro-oka, 1986]. The metal-oxygen bond strength must be such that the removal of the product and regeneration of the catalyst by gaseous oxygen can occur rapidly. Weak interaction between the desired selective oxidation products and the catalyst surface is desirable so that fast desorption of the product occurs and no further oxidation of the total combustion products takes place. It seems essential, therefore, that the selective oxidation products desorb as soon as possible after being formed. Total oxidation products can also be formed on active sites other than those responsible for the selective partial oxidation products and are thus formed in a parallel reaction. These different sites in the catalyst of interest will be discussed further in section 2.1.10

### 2.1.2 Bismuth Molybdates

The mixed oxide catalyst used in the selective oxidation of hydrocarbons commonly consists of at least two metal oxides. Metal oxide catalysts frequently have different crystal structures with a consequent variation in catalytic properties. The most widely used metal oxide catalyst currently is the multicomponent bismuth molybdate (MCM) catalysts $M_x^{2+}M_y^{3+}Bi_zMo_wO_n$ (where $M^{2+}$ refers to $Co^{2+}$, $Ni^{2+}$ or $Mg^{2+}$ and $M^{3+}$ to $Fe^{3+}$, $Al^{3+}$ etc.), which contain, in addition to the elements mentioned, small amounts of phosphorus and potassium. It is usually accepted that the main phases present in the system are $M^{2+}MoO_4$, $M_2^{3+}(MoO_4)_3$, $Bi_2MoO_6$ and $Bi_2Mo_3O_{12}$ [Bettahar *et al.,* 1996]. Table 1 sums up the main industrial catalyst and their performance. The addition of divalent molybdates improves both the activity and the selectivity of the catalyst by interacting with the basic molybdates in so-called synergy effects [Legendre and Jaeger, 1992]. $^{18}O$ studies [Keulks, 1970] have also shown that lattice oxygen anions are involved in the oxidation process and that the degree of mobility of these anions, which is in turn influenced by constituents and temperature, influences the catalytic performance [Keulks *et al.,* 1980[a]].

**Table 1: Active phases used in industry for the oxidation and ammoxidation of propene to acrolein [Bettahar *et al.,* 1996]**

| Oxides | Reaction Temperature °C | Propene Conversion % | Acrolein (Acrylonitrile) % |
|---|---|---|---|
| Mo, Bi, Fe, Co, Ni, P, Mg | 350 | 98 | 95 |
| Mo(W)Bi Fe, Co, Ni, Si | 250-450 | 96 | 90-93 |
| Mo, Bi, Fe, Co, Ni, Sn, K | 300 | 87 | 97 |
| Bi-Mo (multicomponent) | 290-350 | 95-99 | 92-96 |
| | 430-480 | 97-99 | (80-84) |

Thus, to simplify the system, a pure mixed oxide $Bi_2O_3$-$MoO_3$ phase is chosen to avoid unnecessary complications within the system. Three crystal structures are observed for the simple mixed oxide $Bi_2O_3$-$MoO_3$ catalyst, namely: $\alpha$-$Bi_2Mo_3O_{12}$ [Marinova and Veleva, 2002], $\beta$-$Bi_2Mo_2O_9$ and $\gamma$-$Bi_2MoO_6$ [Bleijenberg *et al.,* 1965]. The focus of this study is on the properties and characteristics of $\alpha$-$Bi_2Mo_3O_{12}$.

### 2.1.3 α-Bismuth Molybdate Crystal Structure

Precision photographs taken with Cu-$K_\alpha$ radiation show that the $Bi_2Mo_3O_{12}$ crystal belongs to the monoclinic system, with unit cell parameters of a = 7.67Å, b = 11.54Å, c = 12.00Å and β = 115°24' [Miyazawa, 1974], and a = 7.719Å, b = 11.516Å, c = 11.985Å, and β = 115°25' [Aykan, 1968].

The crystal structure of $Bi_2Mo_3O_{12}$ can be viewed as a distorted Scheelite with ordered Bi vacancies. The structure contains three distinct Mo sites, $\alpha_1$, $\alpha_2$ and $\alpha_3$, each of which is normally coordinated by five O. As a result, the Mo co-ordination is usually regarded as tetrahedral. In each case, four of the Mo-O bonds are short (1.68 to 1.91 Å), while the fifth is considerably longer (> 2.13 Å). As seen in Figure 1a, $\alpha_1$ and $\alpha_2$ have Bi ions adjacent to the tetrahedra, while there is a Bi ion vacancy near the $\alpha_3$ tetrahedron. There are two Bi sites. Each has four close O neighbours (at distances of 2.12 to 2.34 Å) and four that are much further away (2.61 to 2.94 Å). The Bi and Mo are concentrated in layers parallel to the (010) that intersect *b* at approximately 1/8, 3/8, 5/8 and 7/8 (see Figure 2b). Adjacent layers are bridged and held together by metal-oxygen, primarily Bi-O, bonds.

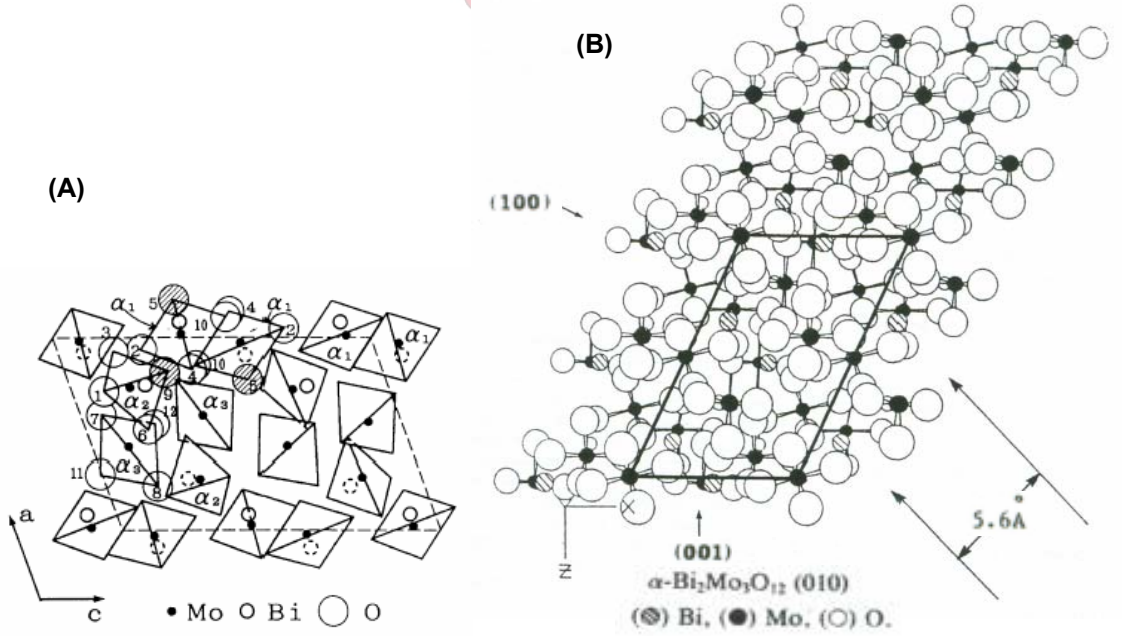


**Figure 1: (a) Projection along the b axis of the structure of α-$Bi_2Mo_3O_{12}$. $\alpha_1$, $\alpha_2$ and $\alpha_3$ denote Mo tetrahedral [Ono, 1988], and (b) : α-$Bi_2Mo_3O_{12}$ Solid-state structure [Grasselli *et al.*, 1984]**

As can be seen in Figure 2c, each cation layer contains the expected Bi/Mo ratio of 2/3. Due to the 21 screw axes along the <010>, the plates at 1/4 and 3/4 (Figure 2b) are equivalent, although rotated 180° with respect to one another. The planes in 1/2 and 1 are related in the same manner, but they are not equivalent to those at 1/4 and 1/3 [Yanina, 2003].

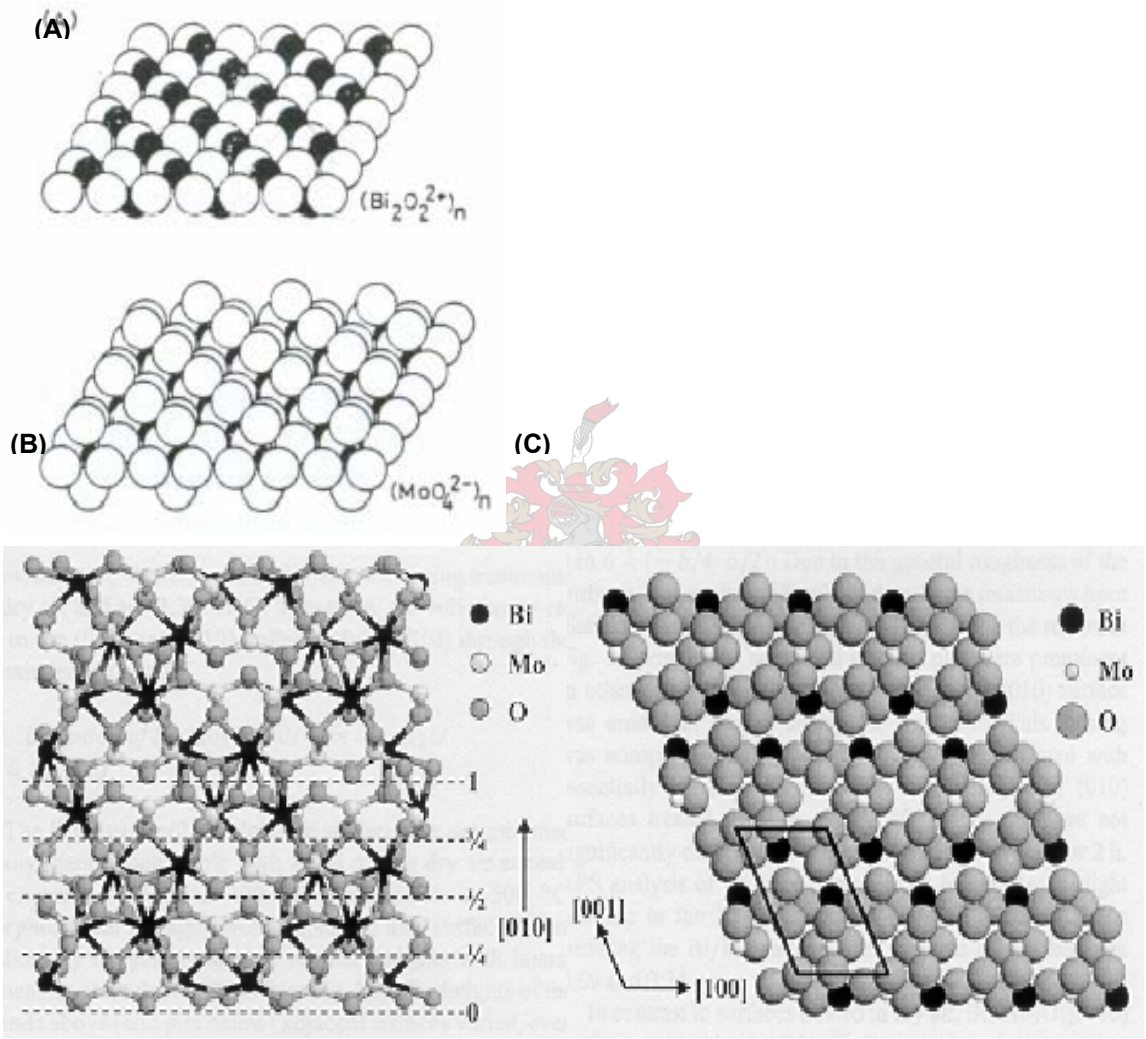


**Figure 2: (A&B) Bi and Mo layers of γ-$Bi_2MoO_6$ [Miura *et al.*, 1981] and (C) α-$Bi_2Mo_3O_{12}$ [Yanina and Smit, 2003]**

The binding energies for $Bi_2Mo_3O_{12}$, in its oxidised and reduced surface states were determined by Devillers *et al.* [1996] and Ayame and Uchida [1996], respectively using XPS and XPS equipped with an $Ar^+$ ion gun. The results are summed in the Tabel 2.

**Table 2: Binding energies determined by Devillers *et al.* [1996] and Ayame *et al.* [1996].**

| Catal. | $T_{cals}$ K | Binding Energy (eV) | | | | |
|---|---|---|---|---|---|---|
| | | O1s | $Bi4f_{7/2}$ | | $Mo3d_{5/2}$ | |
| | | | $Bi^{3+}$ | $Bo^{0}$ | $Mo^{6+}$ | $Mo^{5+}$ |
| $Bi_2Mo_3O_{12}$ | 773 | 532.7 (II)<br>530.5(II) | 159.5 | 157.3 | 232.7 | 231.4 |

## 2.1.4 Mars-van-Krevelen Mechanism

According to Keulks [1970] and Keulks and Krenzke [1980[c]], the oxidation of hydrocarbons over a bismuth molybdate catalyst obeys the three-step Mars-van-Krevelen mechanism:

1. Adsorption of the alkene and abstraction of the $\alpha$-hydrogen from the alkene to form an allylic species;
2. Insertion of oxygen into the activated allylic species with corresponding loss of oxygen by the catalyst;
3. Re-oxidation of the thus-reduced catalyst by gaseous oxygen.

The mechanism indicates that the transfer of both protons and electrons between the alkene and the catalyst is needed. This requires that the catalyst not only has adequate redox properties, but also the correct acid-base properties.

The inner workings of the Mars-van-Krevelen mechanism will be explained in more detail in sections 2.1.6-2.1.10 by looking at reaction mechanisms, lattice oxygen mobility, active sites for the various steps proposed and re-oxidation of the catalyst.

## 2.1.5 Product Formation

Although acrolein is the main product in the highly exothermic ($\Delta H° = -300kJ/mol$) selective oxidation of propene over a $Bi_2Mo_3O_{12}$ catalyst, it gives rise to the concomitant formation of acetaldehyde, methanol and formaldehyde. Acrolein is formed via a symmetric $\pi$-allylic species, which will be discussed in the following section, while the main source of acetaldehyde and formaldehyde formation is the oxidative breaking of its

C=C bond [Bettahar *et al.,* 1996]. 1,5-Hexadiene can also be formed by dimerisation of the severely reduced catalyst [Grasselli *et al.,* 1981]. CO and $CO_2$ are formed as total combustion products.

Acrolein (primary reaction):

$$CH_3 - CH = CH_2 + O_2 \xrightarrow{Catal} COH - CH = CH_2 + H_2O \quad ....1$$

Acrylic acid:

$$CH_2 = CH - CH + 3/2\,O_2 \rightarrow CH_2 = CHCOOH \quad ....2$$

Acetaldehyde:

$$CH_3 - CH = CH_2 + O_2 \rightarrow CH_3 - CHO + CH_2O \quad ....3$$

Formaldehyde:

$$2CH_2O + 1/2O_2 \xrightarrow{H_2O} CH_3OH + CO_2 \quad ....4$$

1,5-Hexadiene:

$$2CH_3 - CH = CH_2 \xrightarrow{\text{Reduced}-Catal.} CH_2 = CH - (CH_2)_2 - CH = CH_2 \quad ....5$$

In a study done by Keulks and Daniel [1972] on the pre- and postcatalytic volumes (void space before and after the catalyst bed at reaction conditions) of his reactor, he noted that an increase in postcatalytic volume caused an increase in propene conversion, a decrease in acrolein formation and an increase in the formation of CO, $CO_2$, propylene oxide and $CH_4$ in some cases. Keulks suggested a surface-initiated homogeneous reaction in which propene, acrolein and acetaldehyde take part. The formation of $CH_4$ suggests a radical reaction in the gas phase. Propene oxide formation under conditions that favour homogeneous reactions is a result of a gas phase reaction between propene and an intermediate which is generated on the surface.

### 2.1.6 Reaction Mechanism for Propene Oxidation

A few multi-step reaction mechanisms have been proposed for the selective oxidation of propene, namely the hydro-peroxide and the redox mechanisms. These two mechanisms can be differentiated on the basis of the type of oxygen involved. The peroxide pathway utilises adsorbed molecular oxygen and only a monolayer, or less, of oxygen can therefore participate. In the redox pathway, lattice oxide ions are incorporated into the product and, consequently, a large fraction of lattice oxygen can be involved. Deuterium-marked propene selective oxidation studies have concluded that the peroxide mechanism is the most probable reaction pathway for temperatures below 350°C and that acrolein forms exclusively via the redox pathway over α- and γ-bismuth molybdate in the temperature range of 350 to 450°C [Keulks Krenzke, 1980[a]].

Mechanistic studies show that the first step in the partial oxidation of propene is the formation of symmetric π-allylic species [Keulks and Krenzke, 1980[b]]. This has been confirmed by various labelling and radical *in situ* methods, which are summarised by Bettahar *et al.* [1996].

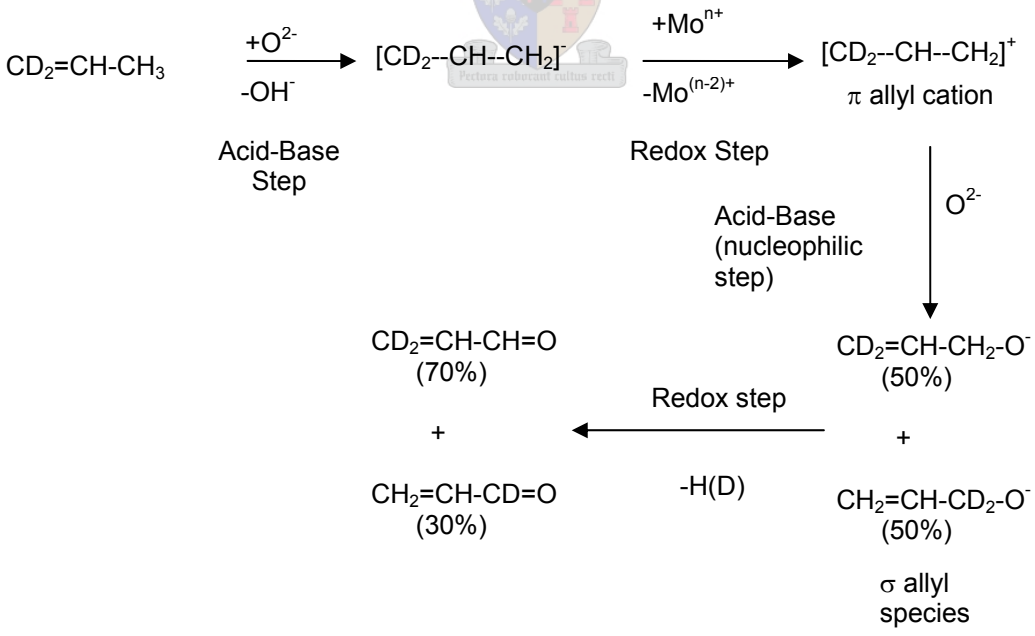


**Figure 3: Mechanism of the catalytic oxidation of propene to acrolein on Bi-Mo-O through allylic surface species [Bettahar *et al.*, 1996].**

The subsequent step from the allylic radical to acrolein [Grasselli & Brazdil, 1980, Grasselli *et al.,* 1984] can be summarised as a succession of redox and acid-base steps [Grasselli *et al.,* 1984]. The π-allylic atom is first formed by proton abstraction on a basic active site and then oxidised to the π-allylic cation on a redox active site. Through a nucleophilic attack by a lattice $O^{2-}$ anion, the later species forms the σ-allylic species which, in turn, gives rise to acrolein by a hydride abstraction in a redox step. The investigation of π-allylic species is invoked to explain the attainment of 1-d1 and 3,3-d2 acrolein molecules from 1,1-d2 propene (cf. Figure 3) in the same proportions (30% and 70%, respectively) as from a 1:1 mixture of 1,1-d2 and 3,3-d2 allyl alcohol molecules. The obtained, labelled acrolein molecules should reflect the nucleophilic attack of $O^{2-}$ anion on either the C1 or the C3 of the π-allylic species to form isomeric σ-allylic species, whereas their proportions reflect the $k_H/k_D$ ratio during the abstraction step of a hydrogen atom from the σ-allylic species. These results show that the intervention between π and σ species is reversible and that it is most probably a redox mechanism [Grasselli *et al.,* 1984]. Figure 4 shows the mechanism for the SOHIO process proposed by Grasselli *et al.* [1984].

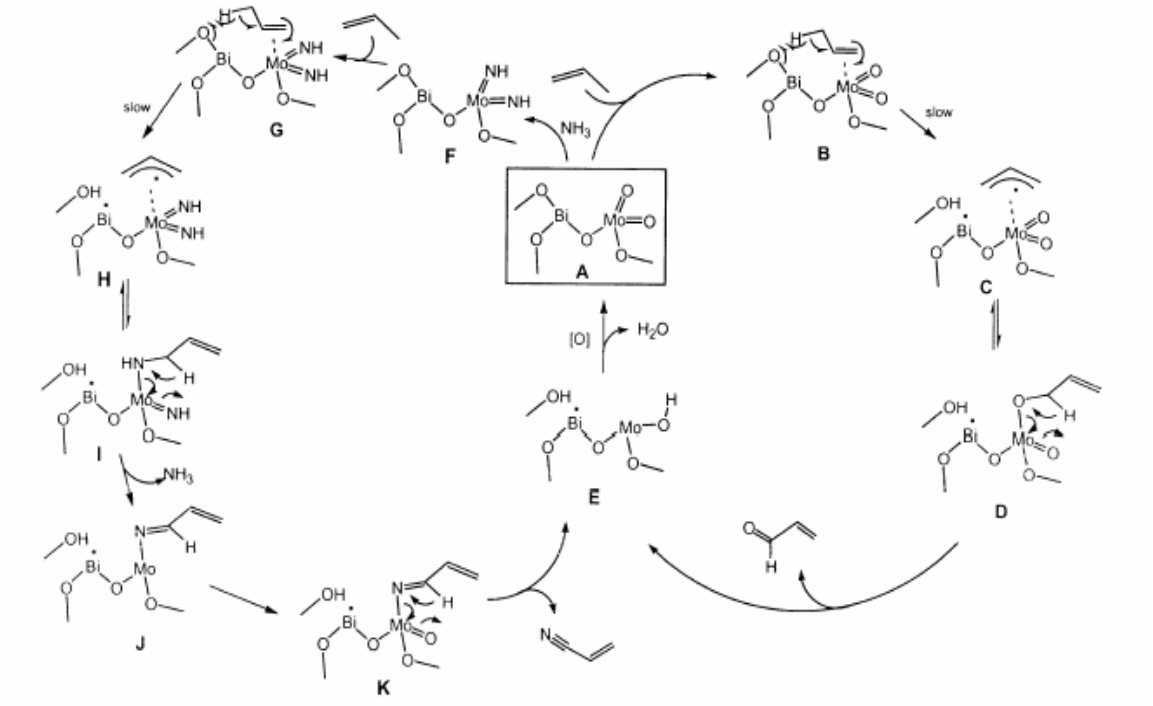


**Figure 4: Grasselli's proposed mechanism for the SOHIO** process [Grasselli *et al.,* 1984].

### 2.1.7 Kinetics

For a surface catalytic reaction, the rate of the reaction, $-r_A$, is defined as the number of moles chloral reacting (disappearing, combining or isomerisation) per unit time per unit catalytic surface area ($mol.m^{-2}.sec^{-1}$). This may be calculated as follows:

$$-r = kP^{x}{}_{A} \qquad ....6$$

$$k = k_0 . e^{\frac{-E}{RT}} \qquad ....7$$

With $P_A$ being the partial pressures of reactant A to the power of its reaction order x. The rate constant, k, is a product of the pre-exponential factor $k_0$, and an exponential function of the activation energy, E, absolute temperature, T, and the universal gas constant, R.

A plot of ln(rate) vs. ln(partial pressure of the reactant being varied) will yield a straight line with a slope equal to the reaction order of the reactant being varied and a y intercept equal to ln(k'), where k' is the proportionality constant equal to k(reactant held constant).

The formation of a product in a catalytic reaction is usually a consecutive multi-step reaction (for instance: adsorption, dissociation, activation, reaction and desorption). The activation energy for the multi-step reaction is the same as the activation energy of the limiting step. Using the reaction order for individual components derived above the specific rate constant can be calculated from equation 1. The slope in the plot of $ln(k_{sp})$ vs. $1/T$ ($K^{-1}$), the Arrhenius plot, will give -E/R, from which the activation energy is calculated. The change in slope indicates a change in activation energy, indicating a change in the limiting step [Perry and Green, 1998].

Keulks and Krenzke [1980[c]] investigated the propene oxidation kinetics over BiMoO across the temperature range of 325 to 475°C. The reaction was found to obey the Mars-van-Krevelen mechanism and was controlled by the catalyst re-oxidation step (diffusion-controlling) at low temperatures and by the catalyst reduction step ($\alpha$-hydrogen abstraction) at high temperatures. The apparent activation energy and reaction order for both propene and oxygen changed with temperature and are summarised in Table 3.

Keulks and Krenzke [1980[a&c]] also suggest that $CO_2$ formation is by the consecutive oxidation of acrolein on the basis of the same fraction of $^{18}O$ incorporated in $CO_2$ as in the acrolein. They suggest that only lattice oxygen is involved in the formation of total combustion products over $Bi_2Mo_3O_{12}$ and that it is initiated by a charge transfer process that results in the activation of an oxide to an $O^-$ ion.

**Table 3: Reaction orders and activation energy for $Bi_2Mo_3O_{12}$ at different temperatures [Keulks and Krenzke, 1980[c]].**

| Temp. | Acrolein. formation | | $CO_2$ formation | | Temp. | E (kJ/mol) | |
|---|---|---|---|---|---|---|---|
| °C | $C_3H_6$ | $O_2$ | $C_3H_6$ | $O_2$ | °C | Acrolein | $CO_2$ |
| 475 | 1 | 0 | 1 | 0.4 | <410 | 222 | 205 |
| 450 | 1 | 0 | 1 | 0.4 | >410 | 75 | 55 |
| 425 | 1 | 0 | 1 | 0.4 | | | |
| 400 | 1 | 0 | 1 | 0.4 | | | |
| 375 | 0.7 | 0 | 0.7 | 0.4 | | | |
| 350 | 0 | 0 | 0 | 0.4 | | | |
| 325 | 0 | 0 | 0 | 0.4 | $Bi_2Mo_3O_{12}$ | | |

Keulks and Krenzke argue that product formation and catalyst reduction are quantifiably similar (propene is oxidised at the expense of the catalyst) and that the reaction rate decreases rapidly with an increase in catalyst reduction. Consequently, in order to maintain a continuous catalytic reaction, the catalyst lattice oxygen must be continuously replenished by re-oxidation with gaseous oxygen.

$$\frac{-d[C_3H_6]}{dt} = k_R P^x{}_{C_3} \Theta_{ox} \qquad ....8$$

$$\frac{-d[O_2]}{dt} = k_{ox} P^y{}_{O_2} \left(1 - \Theta_{ox}\right) \qquad ....9$$

At steady state, the rate of catalyst reduction (or propene oxidation) is equal to the rate at which catalytic oxygen is replenished, and the equations may thus be equated to solve for $\Theta_{ox}$.

$$\Theta_{ox} = \frac{k_{ox} P^{y}{}_{O_2} / k_R P^{x}{}_{C_3}}{1 + \left( k_{ox} P^{y}{}_{O_2} / k_R P^{x}{}_{C_3} \right)} \qquad \text{....10}$$

$k_R$ & $k_{ox}$ : Rate constants for catalyst reduction and re-oxidation

$P_{C_3}$ & $P_{O_2}$ : Partial pressure of propene and oxygen

$x$ & $y$ : Reaction order of propene for catalyst reduction and of oxygen for catalyst re-oxidation

$\Theta_{ox}$ : Fraction of sites that are fully oxidised.

If the fraction of fully-oxidised sites is plotted as a function of the ratio of the rate of re-oxidation to the rate of reduction, Figure 5 is obtained. The reduction-limited and re-oxidation-limited regions are indicated on the graph.

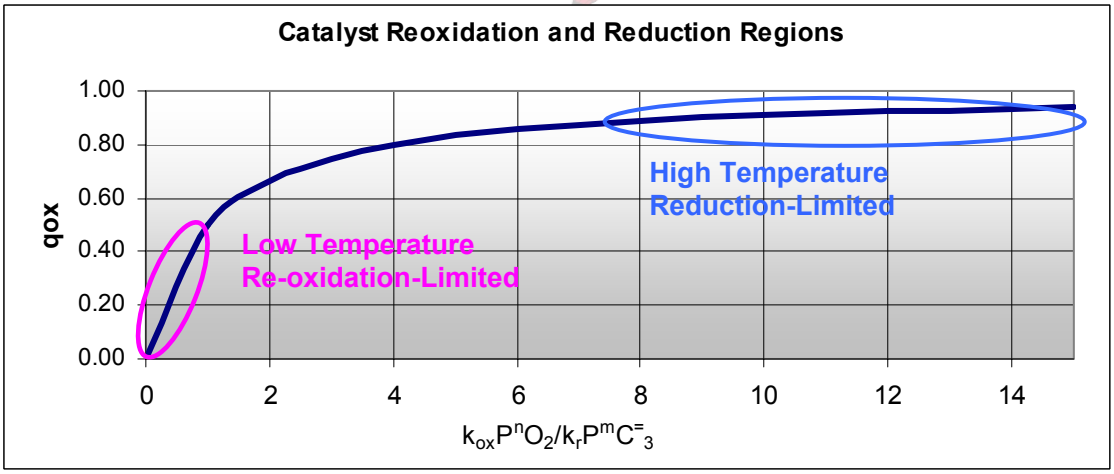


**Figure 5: Fraction of fully oxidised sites vs. the ratio of the rate of re-oxidation to the rate of reduction [Keulks and Krenzke, 1980[b]].**

Thus, if $k_{ox}P^{y}{}_{O2}/k_RP^{x}{}_{C3}$ >>1, Eq. (8) can be reduced to:

$$\frac{-d[C_3H_6]}{dt} = k_{ox} P^{x}{}_{C_3} \qquad \text{....11}$$

This shows that the kinetics of propene oxidation is the same as the kinetics of catalyst reduction. And, if $k_{ox}P^{y}{}_{O2}/k_RP^{x}{}_{C3}$ <<1, Eq. (8) can be reduced to:

$$\frac{-d[C_3H_6]}{dt} = k_R P^{y}{}_{O_2} \qquad \text{....12}$$

Now the kinetics of propene oxidation is controlled by the kinetics of catalyst re-oxidation. By changing the reaction conditions, the kinetics of propene oxidation is expected to change drastically when the process is shifted from a reduction-limited regime to a re-oxidation-limited regime. This transition would involve not only a change in activation energy, but also a change in the reaction order of oxygen and propene.

The kinetic studies of Haber and Brückman, [1988] also observed a high and low temperature regime, like that observed by Keulks and Krenzke, but they awarded the temperature regime below 377°C (characterised by the higher activation energy) to a kinetic-controlled range and the high temperature regime above 417°C to a diffusion-controlled range. Haber *et al.* [1987[b]] indicate that $Bi^{3+}$ is involved in the rate-limiting activation of propene by $\alpha$-hydrogen abstraction to form an allylic species. The activation energy may thus be taken as a value characterising the activation of propene molecules on $Bi^{3+}$ ions. Haber and Brückman [1988] suggested a parallel total oxidation reaction pathway with zero order with respect to propene and first order with respect to oxygen. They used the following rate equation:

$$r = kP^{x}{}_{C_3} P^{y}{}_{O_2} \qquad \text{....13}$$

| | |
|---|---|
| $r$ : | Reaction rate |
| $k$ : | Reaction rate constant |
| $P_{C_3}$ & $P_{O_2}$ : | Partial pressure of propene and oxygen |

Grasselli *et al.* [1980[a]], using a pulse micro-reactor method, did kinetic studies on the re-oxidation of the BiMoO catalyst and also observed two activation energy regimes. One regime is characterised by a low activation energy at low degrees of initial reduction and involves the re-oxidation of surface vacancies. The second regime is observed for deeper degrees of reduction, which are characterised by high activation energy and

involve the re-oxidation of anion vacancies in the bulk of the catalyst (Table 4). The activation energies for the re-oxidation of the catalyst bulk are strongly dependent upon the structure and composition of the catalyst.

The difference in activation energies due to differences in structure and composition can be seen clearly in Figure 6, in which the rate of acrolein formation is listed for a few pure and multicomponent bismuth molybdate catalysts.

**Table 4: Activation energies for catalyst re-oxidation [Grasselli *et al.*, 1980[a]].**

| Catalyst | Initial reduction ([O] x $10^{19}$/$m^2$ | Activation energy (kJ/mole) | Temp. °C |
|---|---|---|---|
| $Bi_2Mo_3O_{12}$ | 0.2 | 5.4 | |
| | 0.5 | 5.9 | 430-460 |
| | | 102.6 | 320-400 |
| | 1.4 | 108.4 | |
| $Bi_2Mo_2O_9$ | 0.1 | 33.9 | |
| | 0.3 | 40.2 | |
| | 0.8 | 111.4 | |
| | 1.5 | 108.0 | |
| $Bi_2MoO_6$ | 0.2 | 5.0 | |
| | 0.5 | 2.9 | 430-460 |
| | | 33.9 | 320-380 |
| | 1.3 | 33.1 | |

Temperature range = 320-460°C

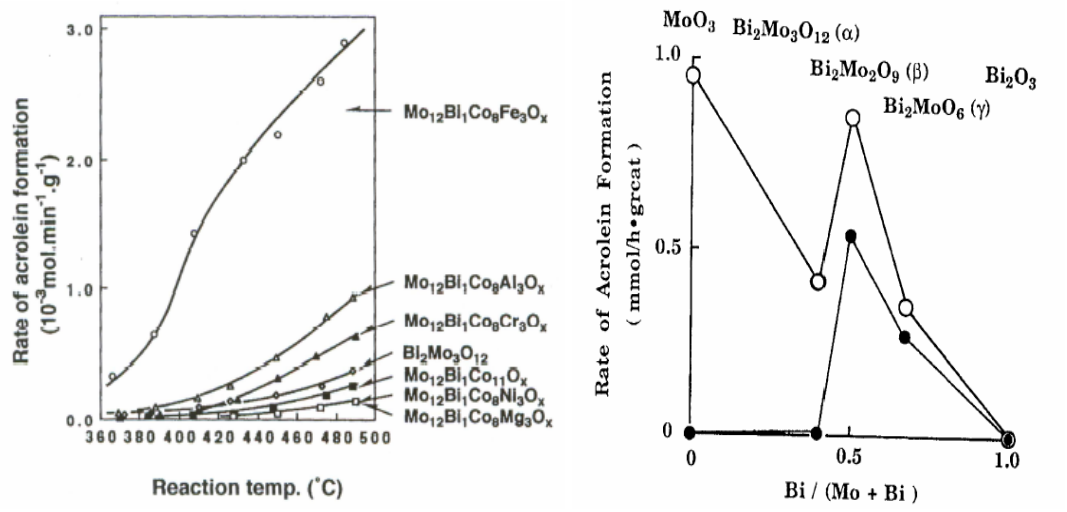


**Figure 6: Rate of acrolein formation for bismuth molybdates and multiphase catalysts [Moro-Oka, 1994].**

### 2.1.8 Diffusion and Mobility of Oxygen Ions/Redox Property

Mobility of the lattice oxide ions is observed in the oxides of group V and VI metals, which are used as active components in the catalysts for the selective oxidation of olefins. Lattice oxide anions diffuse in these substoichiometric oxides when oxygen anion vacancies are produced in the lattice under reductive conditions at high temperatures. Although the mobility of the lattice oxide ions in scheelite oxide catalysts increases by introducing cation vacancies, the enhancement is not ascribed directly to the formation of cation vacancies [Keulks, 1970]. Lattice oxygen mobility is a function of crystal structure, thus composition, and of the concentration of cation vacant sites [Grasselli *et al.,* 1980[a] & Gazzoli, 1989]. Ueda Moro-oka[1986] concluded that the tetrahedral sharing that arose from the formation of cation vacancies accelerates the migration of lattice oxide in the scheelite oxides. If these tetrahedra are undistorted and unshared with each other, the structure seems to be unfavourable for lattice oxide ion movement. The low mobility of lattice oxide ions in $Bi_2Mo_3O_{12}$, in spite of it having the highest concentration of cation vacancies in a scheelite oxide system, may be due to the formation of ordered cation vacancies that are not true defects.

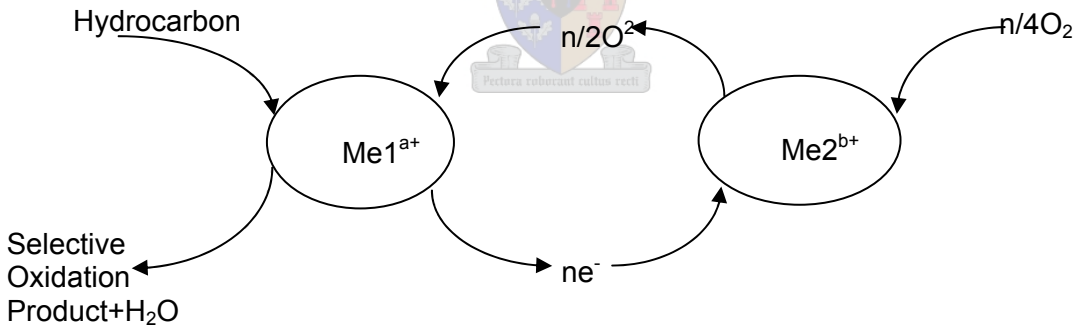


**Figure 7: Oxidation and reduction cycle in the selective oxidation of hydrocarbons [redrawn from Grasselli and Bürrington, 1972]**

Lattice oxygen, $O^{2-}$ ,has to move from the neighbouring site, $Me2^{b+}$ ,to the $Me1^{a+}$ site with a *vice versa* transfer of electrons (See Fig. 7), which are released on hydrocarbon adsorption. It has been shown that bismuth-molybdate behaves as a donor for spillover oxygen with respect to $MoO_3$ [Godard *et al.,* 2000]. To avoid over-oxidation of the products, the Me1 must maintain a high degree of oxidation. The Me2 site becomes an electron donor on which gaseous oxygen can adsorb and convert to lattice oxygen ions.

By studying the extent of participation of lattice oxygen with the aid of $^{18}O_2$ tracer on a number of molybdenum catalysts, Ueda and Moro-oka [1981 & 1984] obtained a correlation between the specific activity and the mobility of lattice oxide ions, relating the catalytic activity exclusively to the mobility of lattice oxide ion. This demonstrates the importance of the rapid bulk diffusion of oxygen ions in the catalyst in order to restore the adsorption site, to maintain the overall catalytic process and to stabilise the catalyst under catalytic conditions [Gozzoli *et al.,* 1989]. Structural changes during catalysis (due to the reduction of the catalyst) result in changes in the catalytic properties. Thus, catalysts are deactivated as a result of the decomposition of the active composite oxides. Structural deformation would be minimised by the rapid diffusion of the lattice oxide ions preventing over-oxidation and thereby improving the stability of the catalyst, thus increasing the catalyst life [Ueda and Moro-oka,1986].

Allylic species activated by $\alpha$-hydrogen abstraction are oxidised at the expense of the catalyst. Lattice oxygen is used for oxidation purposes, leaving vacancies on the surface. This implies that the catalyst also takes part in the reaction as a reactant to some extent. In order to explain these results, the concept of a *pseudo homogenous phase of active oxygen* was introduced. According to this concept, several kinds of active sites will be present on the surface, some of them for activating propene and some to activate gaseous oxygen. The transport of lattice oxygen-activating sites to propene-activating sites is carried out via the bulk, which can be considered as constituting a sort of storage tank (this is also called the water tank model) [Ueda and Moro-oka, 1981].

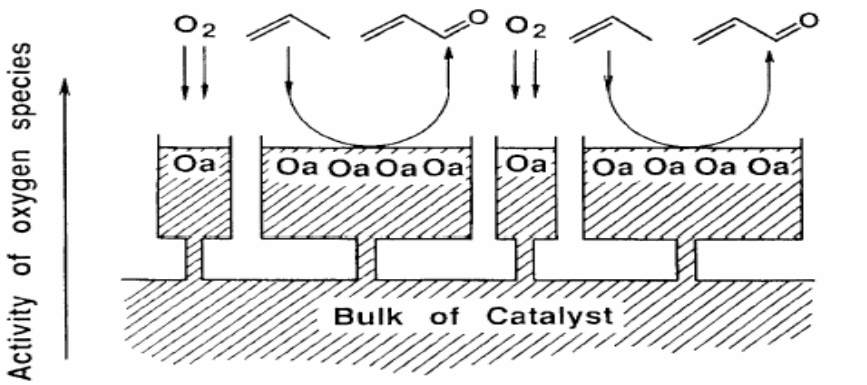


**Figure 8: Water tank model for the concept of multicomponent bismuth molybdate catalyst [Ueda and Moro-oka,1994].**

According to Keulks *et al.* [1979], the percentage of the total amount of lattice oxygen available for catalysis depends on the phase type: 16 and 100% respectively for the α- and γ-phase at 430°C when the percentage of lattice participation in the product formation of $CO_2$ and acrolein is the same. Keulks also suggests that the dioxide bridge between two molybdates is responsible for lattice ion diffusion within the α-phase. Therefore, the activity would depend on the diffusion rate of oxygen species from the bulk. A second, more complex model was proposed which takes into account not only the bulk diffusion of lattice oxygen, but also that of the nearby surface [Grasselli *et al.,* 1980[b] & 1981].

**Table 5: Lattice $O^{2-}$ participation [Keulks *et al.,* 1979].**

| Catalyst | Temp. °C | Percentage of lattice $O^{2-}$ participating in product formation | |
|---|---|---|---|
| | | Acrolein | $CO_2$ |
| $Bi_2Mo_3O_{12}$ | 450 | 9 | 9 |
| | 400 | 4 | 4 |
| $Bi_2Mo_2O_9$ | 450 | 98 | 98 |
| | 400 | 56 | 60 |
| $Bi_2MoO_6$ | 450 | 100 | 100 |
| | 400 | 45 | 45 |



When diffusion is very efficient, collaboration between the different phases would be possible, i.e. one site would exclusively activate molecular oxygen and the other would oxidise propene. In mixed metal oxide catalysts, one of the metal ions must promote the rapid exchange of oxygen between the surface and the bulk of the catalyst; that is, the ion must facilitate the migration of lattice oxygen ions from the bulk to the surface [Weng, 1992].

Batist *et al.* [1968] suggested that all bismuth-molybdate structures can be derived from $(Bi_2O_2)_n^{2-}$ and $(MoO_2)_n^{2+}$, connected by layers of $O^{2-}$. For catalysts having Bi/Mo ratios of two or less, the oxygen boundary layer occurs on $(MoO2)_n^{2+}$ layers, which create anion vacancies on molybdenum atoms. Keulks [1970] suggested that these oxygen boundary layers serve as the source of oxygen that is incorporated into the product. Assuming that 1 $m^2$ of surface contains $6x10^{18}$ oxygen atoms, approximately 500 sub-layers take part in

the diffusion process. The re-oxidation of these layers, after being reduced in the product formation, happens by diffusion of $O^{2-}$ from the bulk rather that the gas phase oxygen. In an oxidation of carbon monoxide experiment, it was found that corresponding 60-100 subsurface layers took part in the diffusion process.

Using silica-supported bismuth molybdate catalyst, Ueda *et al.* [1999] concluded that the activity, and to a smaller extent the selectivity, of the catalyst is proportional to its coverage at low coverage (1/3 of ideal monolayer coverage). They suggested that bismuth-molybdate catalysts will be ineffective for selective catalytic olefin oxidation when found either in an ultra-fine particle state or in a very thin layer and/or film due to the absence of utilisable lattice oxygen to replenish the used surface lattice oxygen.

### 2.1.9 Re-oxidation of Reduced Catalyst

The catalytic performance (activity and selectivity) drops sharply with time on stream (on-line), thus showing that the catalytic performance is dependent on the framework oxygen available. Terminal oxygen groups, Me=O, and oxygen bridging positions, Me-O-Me, are both in the $O^{2-}$ state. When the oxidation of propene occurs, the catalyst is reduced, leaving lattice vacancies. This lattice oxygen can be replenished by gaseous oxygen.

There are two types of oxygen ions, namely electrophilic and nucleophilic. The latter is responsible for the selective oxidation of propene to acrolein by attacking a propene molecule in the region of its highest electron density to produce the symmetric $\pi$-allylic specie, which is the kinetic limiting step, and oxygen insertion, to produce acrolein. Electrophilic ion species are the super oxide ($O_2^-$), peroxide ($O_2^{2-}$) and oxide ($O^-$) and are responsible for the total combustion products. The incorporation of oxygen into the bulk layer may occur as shown in Figure 9.

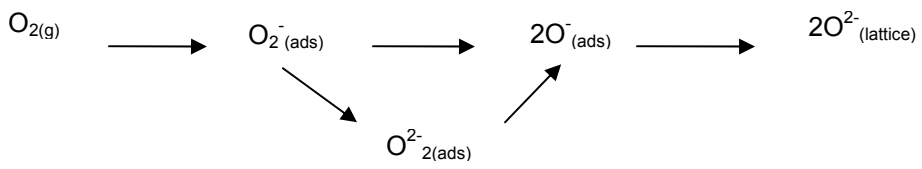


**Figure 9: Transformation of oxygen ions from gaseous oxygen to lattice oxygen.**

Direct transformation of $O^{2-}$ to $O^{-}$ is the more probable and energetically more favourable route. When the temperature is increased, the surface becomes increasingly populated with electrophilic oxygen species, leading to an increase in total combustion products. At low temperature, a high selectivity for partial oxidation is observed, but the conversion is lower. Oxides in which the metal cation is in its highest oxidation state do not readily adsorb oxygen. The probability of forming electrophilic oxygen is low, and thus better selectivity is obtained.

Even in the absence of gaseous oxygen, carbon dioxide and water are produced, which implies that electrophilic species are still produced on the catalytic surface. It has been shown that nucleophilic oxygen is also responsible for carbon dioxide formation by the further oxidation of acrolein. This is in direct contrast with findings that imply a parallel reaction involving centres activating oxygen molecules [Haber *et al.,* 1987[a]].

The re-oxidation of surface lattice oxygen is faster than that of bulk lattice oxygen due to the lower activation energy. The bulk diffusion is also strongly dependent on the crystal structure of the catalyst, as it determines the activation energy. On the basis of re-oxidation kinetics, Grasselli *et al.* [1980] suggested a mechanism showing the rate of re-oxidation being of the first order in oxygen vacancies and of the half order in gaseous oxygen. The overall re-oxidation rates of partially reduced catalysts at 430°C decreased in the order: $Bi_2MoO_6$ > $Bi_2MoO_9$ > $Bi_2Mo_3O_{12}$. Grasselli *et al.* also observed two re-oxidation regimes: One regime is characterised by low activation energy at low degrees of initial reduction and involves the re-oxidation of the surface vacancies. A second regime is observed for deeper degrees of reduction and is characterised by higher activation energy and involves the re-oxidation of anion vacancies in the bulk of the catalyst.

For the mixed oxide ($Bi_2O_3$-$MoO_3$) catalyst systems, maximum selective utilisation of reactive lattice oxygen is obtained for $Bi_2Mo_3O_{12}$ and $Bi_2MoO_9$ after partial reduction. After a loss of a critical number of oxygens ($\pm 0.355 \times 10^{19}/m^2$ [Grasselli *et al.,* 1980[b]] for the α-phase), the molybdenum polyhedra restructures to provide a shear domain in the reduced catalyst, which is consistent with a mechanism requiring co-ordinately unsaturated metal ions for selective oxidation. $Bi_2MoO_6$ shows maximum lattice oxygen

activity at its highest oxidation state. Thus, the unit area rate of lattice oxygen participation at 430°C is: $Bi_2MoO_9$ > $Bi_2Mo_3O_{12}$ > $Bi_2MoO_6$. Figure 11b (p 2-30) shows the restructuring that happens with the reduction of the catalyst surface. Structures 1 (totally oxidised,), 3 (reduced and restructured) and 6 (reduced and restructured) are very selective, while 2 (reduced) and 5 (reduced) have poor selectivity.

The re-oxidation of the catalyst involves adsorption and activation of gaseous oxygen, followed by the incorporation of oxygen into the vacancies. Partial oxidation catalysts must be capable of reduction and subsequent re-oxidation, in which gaseous oxygen is incorporated into the lattice as $O^{2-}$ to replenish the catalyst vacancies. Recent studies on the reduction and re-oxidation of α- and γ-$Bi_2MoO_9$ [Ayame and Uchida, 2002] concluded the following: The surface reduction of propene generates $Mo^{4+}$ and $Mo^{5+}$ simultaneously and almost equivalently, but no reduced species of $Bi^{3+}$ were found, except for the formation of metallic bismuth on γ-$Bi_2MoO_9$ when reduced by hydrogen for a log time at 723K. $Mo^{5+}$ and $Mo^{4+}$ form by drawing of the oxide ion bridging $Bi^{3+}$ and $Mo^{6+}$ ($Bi^{3+}$-O-$Mo^{6+}$) and by the elimination of the oxide ion double bonded to $Mo^{6+}$ ($O=Mo^{6+}$) respectively. The $Mo^{5+}$ is easily reoxidised by gaseous oxygen. $Mo^{4+}$ is converted to $Mo^{6+}$ via $Mo^{5+}$ by oxygen that diffuses from the bulk or by oxide ions that were newly incorporated on the bridge lattice side between $Bi^{3+}$ and $Mo^{5+}$ and transfers through the bulk to the $Mo^{4+}$ site. The activation energy for $Bi^0$ and $Mo^{5+}$ re-oxidation for α-$Bi_2Mo_3O_{12}$ and γ-$Bi_2MoO_9$ determined by heating in UHV and exposure to an $O_2$-jet is shown in Table 6 [Ayame and Uchida, 1996].

**Table 6: Activation energy for the re-oxidation of $Bi^0$ and $Mo^{5+}$ [Ayame and Uchida, 1996].**

| Sample | Activation Energy [kJ/mole] | | | |
|---|---|---|---|---|
| | UHV | | $O_2$-jet | |
| | $Bi^0$ | $Mo^{5+}$ | $Bi^0$ | $Mo^{5+}$ |
| $Bi_2Mo_3O_{12}$ | 38 | 59 | 54 | 74 |
| $Bi_2MoO_6$ | 24 | 30 | 20 | 33 |

The larger activation energy difference between the $O_2$-jet and UHV for the α-BiMoO is attributed to the difficulty of gaseous oxygen dissociation on its surface.

If Grasselli's results are compared to those of Ayame, the activation energy suggested for the re-oxidation of γ-$Bi_2MoO_9$ compares well (30kJ/mol and 30-33 =kJ/mol ($Mo^{5+}$) respectively), but the results for α-$Bi_2Mo_3O_{12}$ differ greatly (102-108kJ/mol and 59-74kJ/mol ($Mo^{5+}$) respectively).

## 2.1.10 Active Sites

With bimetallic catalysts, the oxidation, reduction and re-oxidation of the catalyst surface occur simultaneously. Numerous studies has been conducted in the search for the particular sites responsible for the different steps in the Mars-van-Krevelen mechanism [Haber *et al.,* 1987[a&b] & Haber and Brückman, 1988 ($Bi^{3+}$ for hydrocarbon activation), Carrazán *et al.* 1996 ($Mo^{6+}$ for $O^{2-}$ insertion), Grasselli *et al.* 1984 and Ono *et al.,* 1998]. In mixed metal oxide catalysts this is particularly difficult because of the vast variety of possible active sites. The partial oxidation of propene, for instance, needs not only oxygen insertion sites but also hydrogenation and acid-base sites. Grasselli [1980] compared some mechanisms and suggested active sites shown in Table 7.

**Table 7: Selective oxidation comparisons [Grasselli *et al.,* 1980].**

| Step | Matsuura | Haber | Sleight | Grasselli et al. |
|---|---|---|---|---|
| Olefin chemisorptions | Mo (B site) | Bi | Mo | Mo |
| 1st allylic H abstraction | Mo (B site) | Bi | Mo | Bi |
| 2nd (3rd) H abstraction | Mo (B site) | Mo | Mo | Mo |
| O insertion | Bi (A site) | Mo | Mo | Mo |
| Electron flow | $e^-$→Bi→Mo→$O_2$ | $e^-$→Mo→Bi→$O_2$ | $e^-$→Mo→Bi→$O_2$ | $e^-$→Mo→Bi→$O_2$ |
| Remarks | | | | |
| | Site density (B) = site density (A) A, high DH ads. B, low DH ads. | If no Mo present, $C_6H_{10}$ forms from 2 allyls | Bi6p/Mo4d overlap serves as $e^-$ sink | Bi facilitates 2nd/3rd H abstractions by $e^-$ sink effect |

### *2.1.10.1 Propene Co-ordination*

Considering bismuth molybdate, it has been proposed that individual chemisorptions occur on co-ordinately more unsaturated molybdenum centres (Mo=O) bringing about the rate determining α-hydrogen abstraction [Grasselli *et al*., 1984]. In bismuth

molybdate catalysts, the rate of propene oxidation decreases in the order multicomponent > $Bi_2O_3 \cdot 2MoO_3$ ~ $Bi_2O_3 \cdot 3MoO_3$ > $Bi_2O_3 \cdot MoO_3$ > $MoO_3$ ~ $Bi_2O_3$. Grasselli *et al.* [1997] explain this result as a balance between the number of Mo chemisorption sites and Bi H-abstraction sites. It has also been suggested by Ayame and Uchida [2002] that the propene molecule rapidly attacks the lattice oxygen bridging $Bi^{3+}$ and $Mo^{6+}$ and that the oxygen doubly bonded to $Mo^{6+}$ interacts with the π-bond of the propene π-complex almost at the same time. There is some controversy about the involvement of Bi (also seen in the Table 7), but it is generally accepted that chemisorption occurs on molybdenum centres.

### *2.1.10.2 Propene Activation*

It is generally agreed that $Bi^{3+}$-oxygen polyhedra are responsible for rate-controlling hydrocarbon activation, yielding a symmetric allylic species [Ono *et al.,* 1998]. Haber *et al.* [1987[b]] & Haber and Brückman, [1988] showed that the acrolein yield increased proportionally to the number of supported $Bi^{3+}$ ions for a low bismuth coverage, which indicates that individual $Bi^{3+}$-oxygen polyhedra function as centres activating hydrocarbon molecules. The species formed from the C-H cleavage is found to be a symmetric allyl species with a radical nature. The specific mechanism involved in the H-abstraction is not yet clear due to the numerous possibilities. The oxygen involved in the H-abstraction may be terminal or bridging and, if bridging, may be Bi-O-Bi or Bi-O-Mo. The oxidation state of the two metals both before and after the first H-abstraction is also controversial [Hanna, 2004].

### *2.1.10.3 C-O Bond Formation*

The oxygen insertion takes place at the $MoO_3$ site. This means that an allylic species must migrate from the $Bi^{3+}$ to the $MoO_3$ species [Haber *et al.,* 1987[a], Grasselli, 1980]. The presence of a dynamic σ-allyl/π-allyl intermediate is supported by microwave spectroscopy [Ono, 1998]. Moro-oka *et al.* [1982] as sited by Hanna [2004] demonstrated that the type of lattice oxygen used for dehydrogenation is different from the type used for oxygen incorporation. This means that more than one type of lattice oxygen is involved in propene oxidation. As mentioned previously, $Mo^{5+}$ and $Mo^{4+}$ are

produced on the catalyst surface with the oxidation of propene to acrolein [Ayame Uchida, 2002]. In the initial stage, the generation of $Mo^{5+}$ occurs faster than that of $Mo^{4+}$. $Mo^{5+}$ is produced by oxygen abstraction from $Bi^{3+}$-O-$Mo^{6+}$ and $Mo^{4+}$ is formed from O=$Mo^{6+}$. $Mo^{5+}$ is thus formed by $\alpha$-hydrogen abstraction (activation of propene) and $Mo^{4+}$ from oxygen insertion.

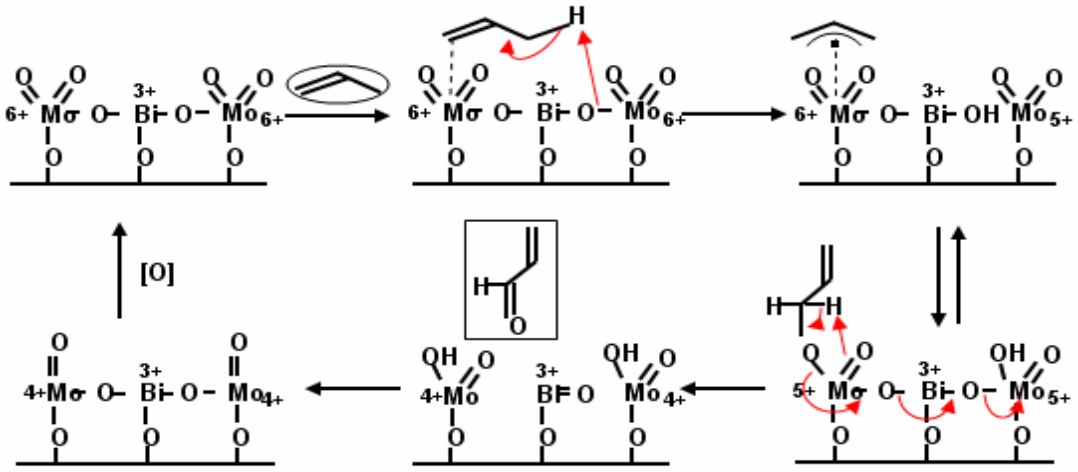


**Figure 10: Bismuth molybdate active sites and reaction mechanism for selective oxidation of propene: dilute conditions [Grasselli et al., 1984].**

Active sites, Figure 10, are also influenced by process conditions. Under low turnover conditions (dilute feed, low temperatures, 320°C), both Mo sites can participate in the catalytic cycle, one as the O-inserting species and the other as a redox element, and the surface accommodation of catalyst reduction is important. At high turnover (high concentrations of feed or high temperatures, > 350°C), selective products result from the reaction of propene at one Mo-dioxo site. Bulk lattice participation is the major mechanism for the accommodation of catalyst reduction.

### *2.1.10.4 Second Hydrogen Abstraction*

The second hydrogen abstraction may occur at either bismuth or a molybdenum site. Microwave spectroscopy studies by Ono *et al.* [1998] suggest that the second hydrogen abstraction is facilitated by the presence of molybdenum-oxygen polyhedra. It is noted that the presence of bismuth enhances the second hydrogen abstraction but the detail of the mechanism is unknown. Kinetic and isotope-labelling experiments indicate that the second H-abstraction must either occur after reversible C-O bond formation or before

irreversible C-O bond formation. Grasselli *et al.* [1980] contends the former. Present suggestions include the involvement of a Bi-O bond and availability of a low-energy sink of overlapping Bi 6p/Mo 4d orbitals for electron transfer after hydrogen abstraction by the Mo oxygen [Haber, 1986].

### *2.1.10.5 Re-oxidation of catalyst (oxygen absorption)*

Various contradictory views exist about the re-oxidation active site. Experimentally and theoretically, no single view is generally accepted. Exclusive molybdenum, bismuth and Mo-O-Bi bridging sites are suggested in various studies, as well as a multiple site theory.

Ono *et al.* [1998] suggested different molybdenum associated oxygen. $^{18}O$ exchange and Laser Raman studies showed that oxygen atoms are mainly inserted at vacancies corresponding to the Mo(1)-O(5) bond in the $\alpha_1$ tetrahedron and the Mo(2)-O(9) bond in the $\alpha_2$ tetrahedron (see Fig. 1 and Fig 11a), The oxygen atoms strongly bonded in each Mo tetrahedron are not related to re-oxidation.

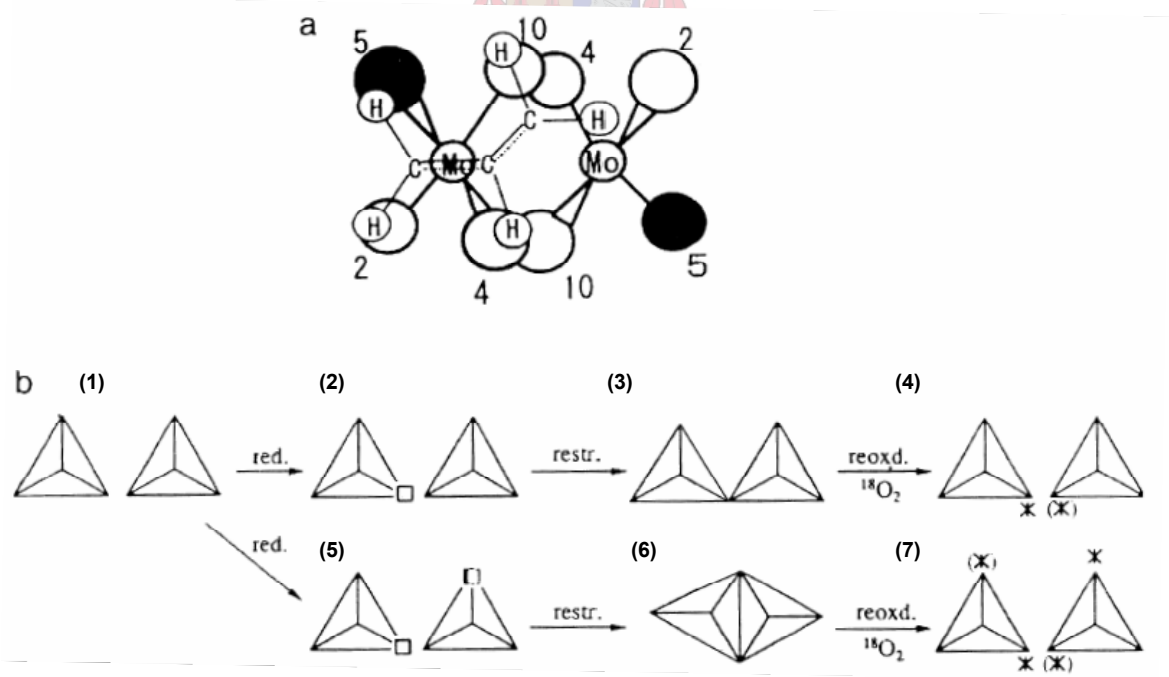


**Figure 11: (a) Possible oxygen species and π- or σ-allyl species on the a1 tetrahedron. The dark shaded circle denotes the well-exchanged positions and the light shaded circles denote the unexchanged positions; (b) Mechanism for vacancy formation, restructuring, and re-oxidation of $\alpha_1\alpha_1$ Mo tetrahedra at the surface.**

The latest view is the dissociative chemisorption of $O_2$ at overlapping Bi orbitals suggested by Grasselli (sited by Hanna [2004]).

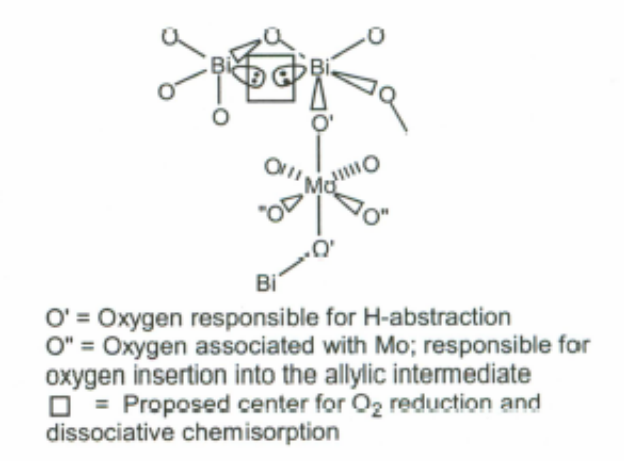


**Figure 12: Grasselli diagram for active** site [Hanna, 2004].

### *2.1.10.6 Total combustion product sites*

Haber and Brückman [1988] suggested that the formation of total oxidation products takes place at active centres different from those responsible for the activation of propene in the first step of its selective oxidation to acrolein and that combustion products are not products of the consecutive oxidation of acrolein, but are rather formed in a parallel reaction due to activation of oxygen at some surface defects of $MoO_3$. Keulks [1980], on the other hand, suggested that the combustion products are produced by the consecutive oxidation of acrolein on the basis of similar amounts of $^{18}O$ incorporated in $CO_2$ and acrolein in isotopic studies and that lattice oxygen and not molecular oxygen are responsible for combustion products. The problem with this argument is that $CO_2$ may still be formed by a parallel reaction mechanism in which lattice oxygen is exclusively utilised, similar to the formation of acrolein resulting in similar $^{18}O$ incorporation.

## *2.2 Catalyst Preparation*

To understand what directs the preparation method it is necessary to study its chemistry and the different possibilities available to obtain the required catalyst for use in further kinetic experiments.

### 2.2.1 Precipitation of $Bi_2Mo_3O_{12}$

Bismuth molybdate catalysts as applied for selective oxidation of olefins are usually prepared via some type of precipitation from solutions of ammonium molybdate and acidified bismuth nitrate. The resulting precipitate is subsequently treated at a temperature in the vicinity of 500°C, during which solid state reactions may and do occur. It is often assumed that the composition of the calcined catalyst is ultimately defined by the Bi/Mo ratio. Experiments by various workers have shown that this assumption is not altogether satisfactory and that the conditions of preparation and thermal treatment also play a significant role in the end product. In order to study the catalytic properties of α-$Bi_2Mo_3O_{12}$, a pure phase is required. It is thus of importance to be familiar with the effects of differing conditions of preparation and thermal treatment.

To shed some light on the subject, Trifiro *et al.* [1972] examined the conditions which allow the precipitation of pure bismuth molybdate with Bi/Mo ratios of 2/3, 1/1 and 2/1, avoiding the solid state reaction. To prepare a particular bismuth molybdate with a higher or lower degree of purity, very specific preparation conditions must be adopted. This study was further extended by Keulks *et al.* [1974].

It is first necessary to examine what is known in the field of chemistry about the bismuth and molybdenum solutions.

#### *2.2.1.1 Bismuth and Molybdate Solutions*

Bismuth can give salts of the following two cations: $Bi^{3+}$ and $(BiO)^{+}$ (Note: Bi has the same co-ordination number in each case). Bismuth precipitates as bismuthyl

compounds, which are very slightly soluble. The pH of the solution must be kept low in order to avoid the precipitation of $Bi(OH)_3$ [Baes and Mesmer]

The chemical behaviour of $Mo^{VI}$ in solution is determined by the degree of polymerisation of the $Mo^{VI}$ anions. The extent of polymerisation can be controlled by adjustment of the pH, the temperature of precipitation, the concentration and the age of molybdenum. High molybdenum concentrations cause a higher degree of polymerisation of $Mo^{VI}$ anions. At low concentrations (<0.0003 M) only normal molybdate, $MoO_4^{2-}$, exists throughout the entire pH range. However, at higher concentrations of molybdate, the normal $MoO_4^{2-}$ anion is only stable above a pH of 6.5. As the acidity of the solution is increased, the normal molybdate anions can condense to form higher polymers (isopoly anions) until the isoelectric point is reached (pH: 0.9) and molybdic acid precipitates. Further acidification causes the precipitate to dissociate and form molybdenyl cations, $MoO_2^{2+}$ [Cruywagen *et al.,* 2002].

The protonation and condensation reactions that can occur upon the acidification of molybdate are represented by the following equation:

$$p[MoO_4]^{2-} + qH^+ \leftrightarrow [(MoO_4^{2-})_p(H^+)_q]^{(q-2p)} \quad \text{....14}$$

For brevity, a species will be described by simply using the stoichiometric coefficients (p, q) given in equation 1, which define its composition, for example (7, 8) for the heptamolybdate polyanion $[Mo_7O_{24}]^{6-}$ and (8, 12) for the octamolybdate $[Mo_8O_{26}]^{4-}$ [Cruywagen *et al.,* 2002]. The reaction above also suggests that the Mo-salt has an exceedingly high buffering capacity.

Figure 13 generated by Cruywagen *et al.* [2000] show the pH and concentration dependence of the polyanion. As the acidity increases, the molybdate is protonated and new species are formed. The types of species as well as the pH at which a species peaks seem to be dependent on the molybdenum concentration, as can be seen from the different species present and in the pH shift respectively in the two graphs. We are particularly interested in the species present at a pH of 1.5-1.2. As can be seen from Figure 13 the predominant species present is the (18, 32), $[Mo_{18}O_{56}(H_2O)_8]^{4-}$. In a review

by Cruywagen *et al.* [2000], the existence of this particular (18, 32) species is still in doubt (or not yet proven to exist), but the presence of its double (36, 62), $[Mo_{36}O_{112}(H_2O)_{16}]^{8-}$, is proven at molybdenum concentrations larger than $10^{-3}$M and in a solution with $NH_4^+$ present. Therefore, considering the precipitation method for catalyst preparation, concentration dependence also means that adding the Bi-salt to the Mo-salt or vice-versa will make a considerable difference.

Throughout this process there are no dimers or trimers of molybdate present in a solution held at room temperature.

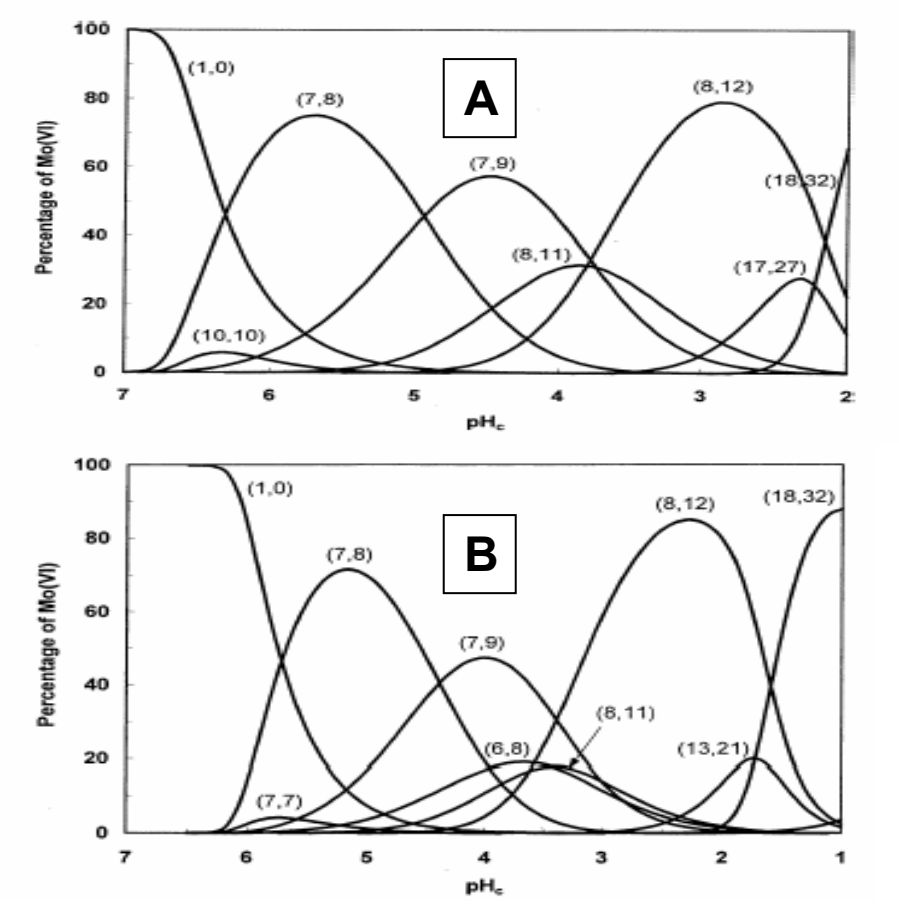


**Figure 13: Distribution of molybdate polyanions in A: 0.4 M $Li_2MoO_4$ and B: 0.10 M $Na_2MoO_4$ solution as a function of pH$_c$ at 25°C [Cruywagen *et al.*, 2002].**

In the preparation studies, the controlling polymerisation characteristics of molybdate seem to govern the preparation technique. The isopolyanion that forms in the acidified molybdate solution must be present throughout the precipitation in order to obtain the

least disturbed precipitation of the α-phase. It is therefore imperative that all the parameters that support the existence of the isopolymolybdate be optimised.

### *2.2.1.2 Precipitation according to Trifiro*

Table 8 summarises Trifiro's findings on the effect of preparation conditions on the precipitation of $\alpha$-$Bi_2Mo_3O_{12}$ compounds. To obtain the pure 2/3 precipitate, his research suggests slowly adding the bismuth solution to a concentrated molybdate precipitate at room temperature and a pH = 1.5.

**Table 8: Summary of Trifiro's preparation condition study; indicates the effect of Mo concentration, temperature and pH by Bi/Mo ratios of the products obtained.**

| Range of Conditions Under Which BiMo Forms | | | | |
|---|---|---|---|---|
| **→ increasing Mo concentration** | | | | |
| **2/1.**<br>**1/1.** | **2/1.**<br>**1/1.**<br>**2/3.** | **2/3.**<br>**1/1.** | **2/3.**<br>**$MoO_3$** | **No Precipitate**<br>**(Bi/Mo ratios of product)** |
| **pH = 2.2**<br>**80°C** | | | | **pH = 1.0**<br>**0°C** |
| **← increasing temperature** | | | | |
| **← increasing pH** | | | | |

Trifiro *et al.* [1972] also investigated solid state reactions between different precipitates. The formation of the α-phase from a pure 2/3 precipitate occurs at relatively low activation temperatures (120-200°C) and is fully proceeded at 300°C. However, formation of the α-phase from the solid state reaction of $(BiO)_2Mo_2O_7$ + $MoO_3$ (Bi/M0 = 2/3) and $Bi_2O_3$ + $MoO_3$ (Bi/M0 = 1) did not occur at 300°C, but rather at 500°C. Bi-molybdate 2/1 ($(BiO)_2MoO_4$) was synthesised from $(BiO)_2Mo_2O_7$ + $Bi_2O_3$ (Bi/M0 = 2) and $Bi_2O_3$ + $MoO_3$ (Bi/M0 = 2) only at 500°C.

### *2.2.1.3 Precipitation according to Keulks*

Keulks *et al.* [1974] also investigated the preparation parameters with the focus on a precipitation technique to prepare pure α-$Bi_2Mo_3O_{12}$. They derived the following:

The equilibration of the isopolymolybdate anions during acidification is slow, and therefore, the addition of acid to paramolybdate solution and the addition of the bismuth nitrate solution to the molybdate solution must also be done slowly. A predominant species in solution appears to be necessary in order to obtain a pure α-phase and bismuthyl ions are probably not involved in the precipitation step with the molybdate species. Pure α-phase precipitate can be obtained at a solution pH value of 1.5 (molybdenum concentration range from 0.3 M to 0.03 M), but impurity phases are obtained if the solution pH is less than 1.0. Back titration of excess acid in the bismuth solution was found to be an effective method of maintaining the solution pH at 1.5 during the precipitation. Back titration was found to be unnecessary if the bismuth concentration was lowered so that the solution pH could be raised to around 1.4. The initial precipitate, and the precipitate after drying at low temperatures, are amorphous and are suspected to be a heteropoly bismuth-molybdenum species. Stepwise calcinations, as opposed to single calcinations at 450°C, yielded a product that had a more clearly defined X-ray diffraction pattern.

The following method was suggested by Keulks *et al.* [1974] for the preparation of pure α-$Bi_2Mo_3O_{12}$.

Acidify 200 ml 0.45 M $(NH_4)_6Mo_7O_{24}\cdot 4H_2O$ slowly to a pH = 1.5 by adding $HNO_3$ and age for 1 hr at a temperature of 25°C. Slowly add 1200 ml (30 ml $HNO_3$ + 1170 ml $H_2O$) of 0.05 M $Bi(NO_3)_3\cdot 5H_2O$ solution to the molybdate while back titrating with 25% $NH_3$ to maintain the pH at 1.5. A Bi/Mo ratio of 2/3 must be used and the precipitate must be left to stand in its mother liquor for 20 hr after full addition. The precipitate must be calcined stepwise (2 hrs at 115°C, 5 hrs at 200°C and 15 hrs at 450°C).
This method can be modified by using more dilute bismuth salts with a higher pH (pH around 1.4) and thus, no back titration in order to keep the pH above 1.3.

### *2.2.1.4 Conclusions on the Precipitation Method*

The findings of both Keulks *et al.* and Trifiro *et al.* assumed that the polyanion needed for the formation of 2/3 BiMo precipitate is the (8, 12) component, but on the basis of recent studies by Cruywagen *et al.* it seems more probable to be the (18, 32) or its double

(36, 64) compound that is responsible for its formation. These new components suggested also contain nonzeolitic water, which corroborates Keulks's reasoning for the necessity of stepwise calcination of the catalyst to obtain a better defined crystal structure. The precipitate formation reaction can be written as follows:

$$12BiO^{+} + Mo_{18}O_{56}(H_2O)_8^{4-} + 8OH^{-} \rightarrow 6(Bi_2Mo_3O_{12}) \cdot (H_2O)_8 + 8H_2O \qquad \text{....15}$$

### 2.2.2 α-$Bi_2Mo_3O_{12}$ Nanorods

Pure α-$Bi_2Mo_3O_{12}$ nanorods were recently synthesised by Ghule *et al.* [2004] via the pyridine intercalative sonochemical route. Using this method, $Bi_2Mo_3O_{12}{\cdot}5H_2O$ was synthesised by the reaction of $Bi_2O_3$ and $Na_2MoO_4{\cdot}2H_2O$ (1:3) in 1 M nitric acid solution at 60°C for 12 hrs. The product was calcined in open air at 450°C to produce pure α-$Bi_2Mo_3O_{12}$ with spherical particle sizes of 100-200 nm. This product was treated with excess pyridine and sonicated at 30-40°C using a fixed power sonicator. The pyridine was vacuum evaporated, followed by an acetone wash and dry at 60°C, after which the nanorods were calcined at 450°C to produce pyridine-free nanorods of α-$Bi_2Mo_3O_{12}$. Well-defined nanorods with a diameter of ~10 nm and a length of a few hundreds of nano-metres to micro-metres were obtained.

The exact mechanism of the formation of α-$Bi_2Mo_3O_{12}$ nanorods is not yet clear, but, on the basis of on their experimental results, Ghule *et al.* [2004] proposed the following diagram.

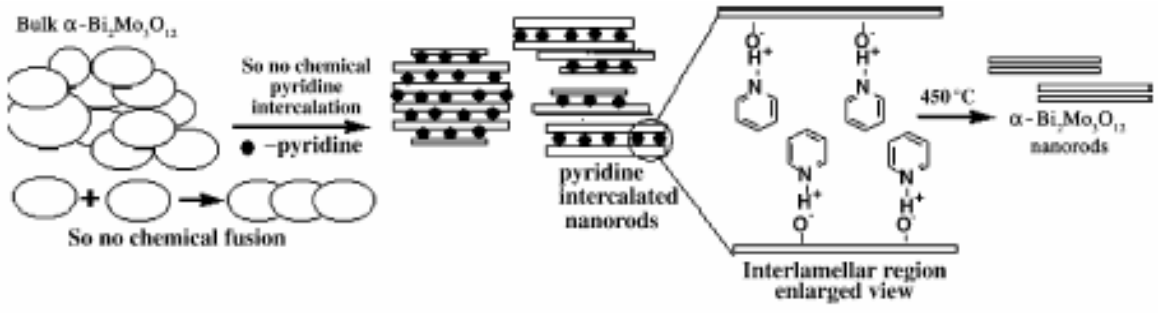


**Figure 14: Schematic diagram for the proposed mechanism of α-$Bi_2Mo_3O_{12}$ nanorod formation** [Ghule *et al.,* 2004].

### 2.2.3 α-$Bi_2Mo_3O_{12}$ Crystals

Single monoclinic α-$Bi_2Mo_3O_{12}$ crystals were grown by Miyazawa *et al.* [1974] and Chen [1973] by pulling crystals from a molten solution with a seed. Stoichiometric ratios of $Bi_2O_3$ and $MoO_3$ were calcined and used as a starting material for the single crystal growing experiments. The equipment used for the 'pulling seed' growth includes an RF generator and a modified Lepel Czochralski puller. The single crystal is pulled from the molten solution (mp 670°C) in a platinum crucible by a rotating platinum seed at temperatures below 650°C. Rod-like crystals with diameters of 10-15 mm and a length of about 30 mm were obtained.

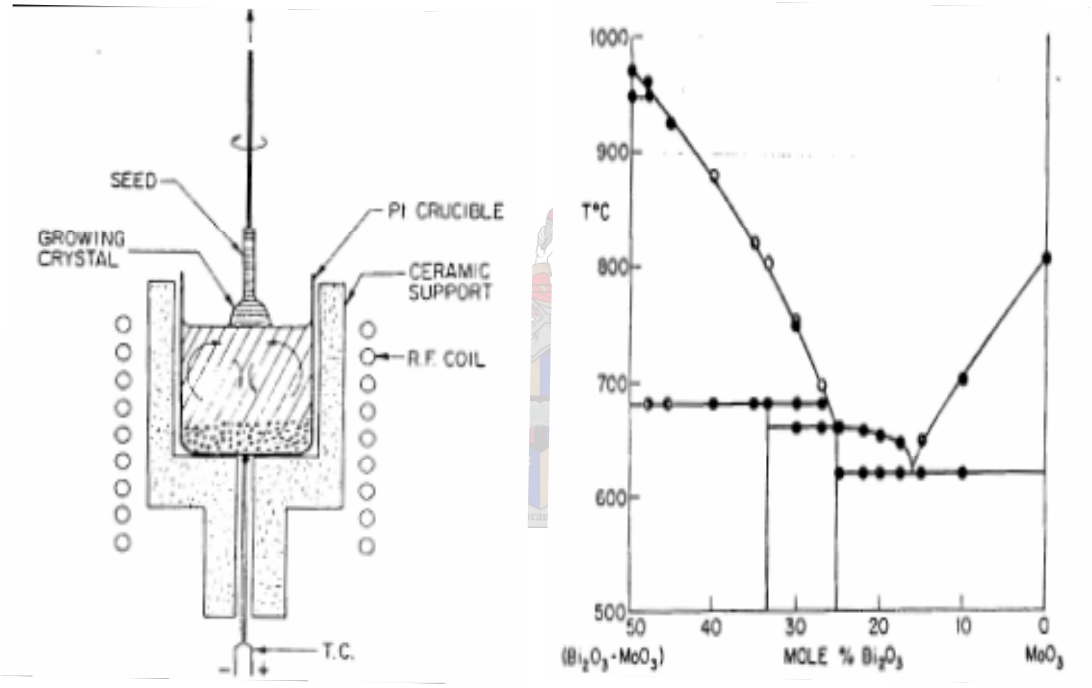


**Figure 15: Lepel Czochralski furnace schematic: Pulling seed growth from molten solution, and phase diagram of $MoO_3$-rich $Bi_2O_3$-$MoO_3$ [Chen, 1973].**

### 2.2.4 Slurry Reaction to Synthesise $Bi_2Mo_3O_{12}$

Batist *et al.* [1972] obtained pure bismuth molybdate 2/3 using a slurry reaction between precipitated oxyhydrates. An acidic solution of $Bi(NO_3)\cdot 5H_2O$ is added to a large excess of concentrated ammonia solution giving a precipitate ($Bi(OH)_3$) that is washed with water until the ammonia has been removed. This is added to water and a large excess of $H_2MoO_4$, after which it is boiled and stirred for 20 hours. The product is filtrated, dried

and calcined, and then treated with warm concentrated ammonia to remove excess MoO3. The white powder is washed with water and calcined again.

Batist et al. [1972] also suggested a precipitation technique that yielded a mixture of 2/3 and 2/1 compound, which is transformed to pure α-phase by the stepwise calcination process at 450°C.

## *2.3 Nano-Emulsion Technology*

This section will describe the reverse micelle technique used to synthesis the required nano-sized particles needed for the kinetic studies. It focuses on the stability requirements and kinetics of reverse micelles, and how reverse micelles may be utilised to synthesise nano-sized particles.

### 2.3.1 Nano-Emulsions

Nano-emulsions (also called nano- and mini-emulsions) are a class of emulsions that can be transparent or translucent (size range 50-200 nm) or 'milky' (up to 500 nm). At macroscopic scale, a macro-emulsion looks like a homogeneous solution, but at molecular scale, it appears to be heterogeneous. Unlike micro-emulsions, which are thermodynamically stable, nano-emulsions are only kinetically stable. However the long term physical stability of nano emulsions (with no apparent flocculation or coalescence) make them unique, and they are sometimes referred to as "approaching thermodynamic stability". The internal structure of the nano-emulsion at a given temperature is determined by the ratio of its constituents. A nano-emulsion consists of uniform and spherical water droplets dispersed in a continuous medium. The structure consists either of nanospherical monosized droplets or a bicontinuous phase called lamellar liquid crystal phase ($L_\alpha$). Oil droplets in both the continuous water phase (micelles, $W_m$) and water droplets in the continuous oil phase (reverse micelles, $O_m$) exist, as can be seen in Figure 16 the latter being of importance to this project.

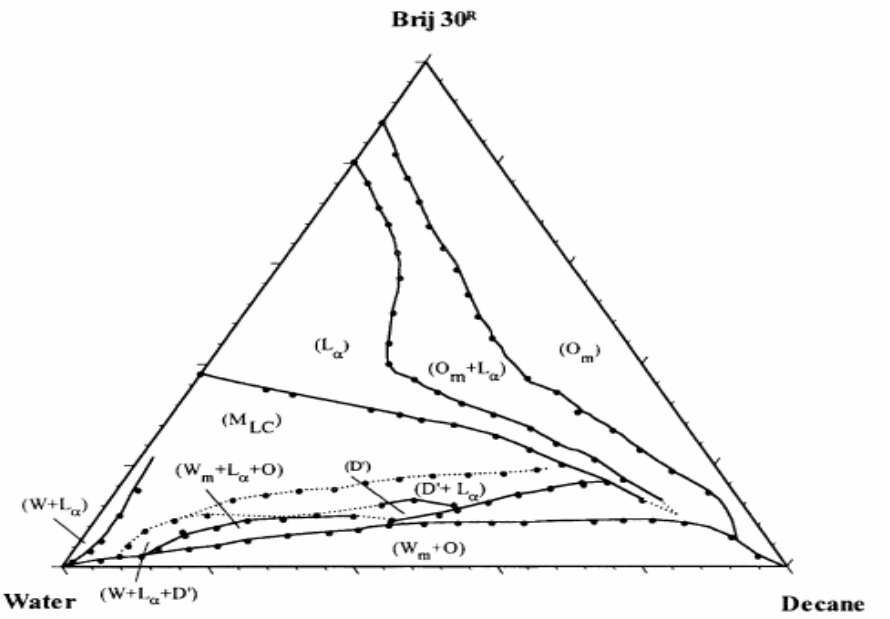


**Figure 16: Phase behaviour of water/Brij 30/decane system at 25°C: $O_m$, isotopic liquid phase; Lα, lamellar liquid crystalline phase; D', shear brefringent liquid phase; Wm, blush liquid phase (O/W microemultion); W, aqueous liquid phase; O, oil liquid phase; $M_{LC}$, multiphase region including lamellar liquid crystals [Forgiarini *et al.,* 2001].**

The droplets can solubilise oil dispersed in water (oil-in-water nano-emulsion or micelle) or solubilise water and be dispersed in oil (water-in-oil nano-emulsion or reverse micelle), the latter being shown in Figure 17.

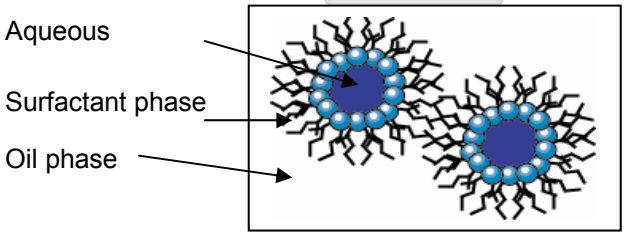


**Figure 17: Water in oil nano-emulsion [Mabaso, 2002].**

### 2.3.2 Preparation of Micro-Emulsions

Micro- or nano-sized droplets are produced in a contagious oil phase by energy-intensive sheering and breaking of larger droplets. The smaller a droplet, the larger is the pressure difference between its inside and outside. The pressure (p) is given as a function of its radius (Ri) and interfacial tension ($\gamma$).

$$p = \frac{2\gamma}{Ri} \qquad \text{....16}$$

To break a droplet into smaller ones, it must be strongly deformed, increasing its internal pressure. The increased pressure makes it possible for the drop to split into smaller, stable droplets. Since stress is generally transmitted by the surrounding liquid via agitation, high stresses need more vigorous agitation, hence more energy is needed to produce smaller droplets.

Surfactants play a major role in the formation of nano-emulsions by lowering the interfacial tension, causing a reduction in internal pressure. The stress needed to break the drop is consequently reduced. In turbulent regimes, the droplet diameter is proportional to $\gamma^{3/2}$ and the amount of surfactant required to produce the smallest droplet will depend on its activity *a* (concentration) in the bulk, which determines the reduction in $\gamma$.

$$-dy = RT\Gamma \ln a \qquad \text{....17}$$

$\gamma$ : Interfacial tension

$R$ : Gas constant

$\Gamma$ : Surface excess (number of moles adsorbed per unit area of interface)

a: Activity

The surface excess is dependent on the surfactant activity and is sometimes influenced synergistically by co-surfactants.

Surfactants also prevent the coalescence of newly-formed drops. When two droplets containing an adsorbed layer approaches a separation distance of less than the combined layer thickness, repulsion occurs due to (i) unfavourable mixing of stabilising chains of the adsorbed layers, referred to as the mixing parameter; and (ii) a reduction in the configurational entropy of the chains on significant overlapping, referred to as elastic interaction. One of the problems with nano-emulsions is the Ostwald ripening effect, which causes droplet growth as a result of the difference in solubility between small and large droplets. Theoretically, the Ostwald ripening effect should lead the to condensation of all droplets into a single drop, but, in practice, the rate of growth decreases with an increase in droplet size. The rate of growth due to the Ostwald ripening effect is a function of the interfacial tension and thus decreases with the introduction of a surfactant [Tadros *et al.,* 2004]. The Ostwald ripening effect can be means of expressed by the Lifshitz-Slezov and Wagner (LSW) theory [Izquierdo *et al.,* 2002]:

$$\omega = dr^3/dt = 8/9\left(\frac{C_\infty \gamma V_m D}{\rho RT}\right) \qquad \text{....18}$$

Where $C_\infty$ is the bulk phase solubility (solubility of an infinitely large droplet), $V_m$ is the molar volume of oil, D is the diffusion in the continuous phase and $\rho$ the density of the oil. The equation predicts a linear relationship between $r^3$ and $t$. The Ostwald ripening effect thus increases with surfactant concentration and decreases with an increase in oil chain length, as also shown in Figure 18 (a & b).

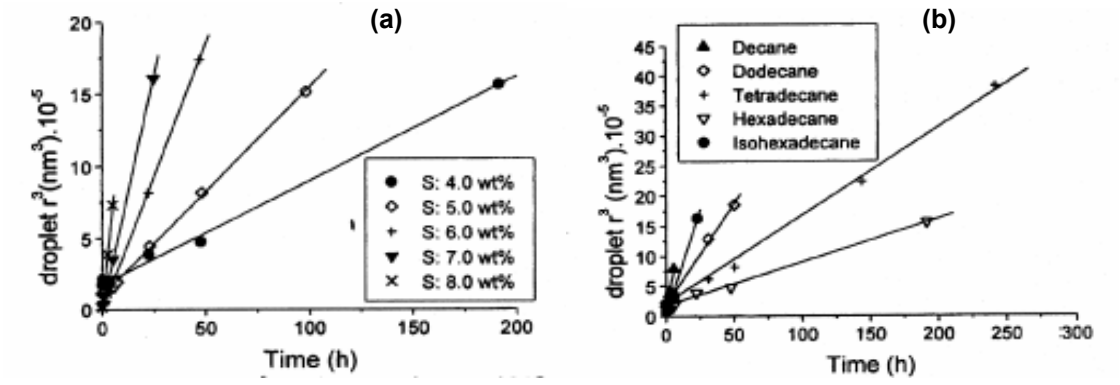


**Figure 18: Droplet size growth due to the Ostwald ripening effect, $r^3$ as a function of time at 25°C. (a) water/$C_{12}E_4$/Hexadecane at different surfactant concentrations and constant oil concentration (20%); (b) water/C12E/aliphatic hydrocarbon for various alkanes at constant oil concentration (20%) and surfactant concentration (4%) [Izquierdo *et al.,* 2002].**

Bouchemal *et al.* [2004] investigated a range of surfactants, oils and water-miscible solvents and mixtures on nano-emulsion size distribution to point out the role of their physico-chemical properties. The oil viscosity (increase in viscosity causes a decrease in micelle size), the surfactant HLB and the solvent miscibility with water represent important parameters in determining the quality of the final nano-emulsion obtained by the spontaneous emulsification process. It should be pointed out that the system is strongly sensitive to temperature, particularly in the case of non-ionic surfactants. Ionic surfactants, on the other hand, are sensitive to a change in the pH level and the presence of reactants in the water phase.

Nano-emulsions can be obtained by various methods, which are summarised in a review by Tadros *et al.* [2004], but for the purpose of this work, only the low-energy methods studied by Forgiarini *et al.* [2001] and the principal of phase inversion temperature (PIT) [Kunieda *et al.,* 1996] will be discussed.

### *2.3.2.1 Low-Energy Method*

Forgiarini *et al.* [2001] studied the phase behaviour of water/oil/surfactant systems to demonstrating that emulsification can be achieved by three different low-energy methods shown in Figure 19: (a) stepwise addition of oil to a water surfactant mixture; (b) stepwise addition of water to surfactant in oil; and (c) mixing all components in the final mixture. From their studies they concluded that only method b, stepwise addition of water to surfactant in oil, formed stable, narrow (50 nm) droplets.

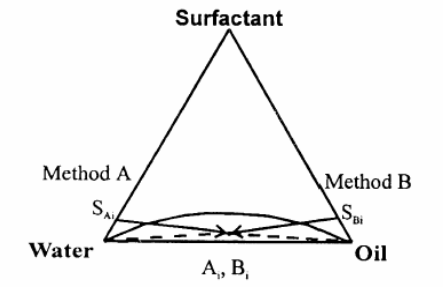


**Figure 19: Method a, b and c; water/decane/brij 30 solution [Forgiarini et al., 2001].**

With the addition of water to an initial oil/surfactant mixture, the conductivity changes due to the formation of different phases. The region in which reverse micelles are stable

has a very low conductivity due to the fact that the aqueous phase is not continuous. A liquid lamellar crystal phase, on the other hand, has more continuity than reverse micelles and thus conducts better. If oil-in-water micelles are formed, the system conducts even better due to the continuous water phase. Figure 20 illustrate this concept.

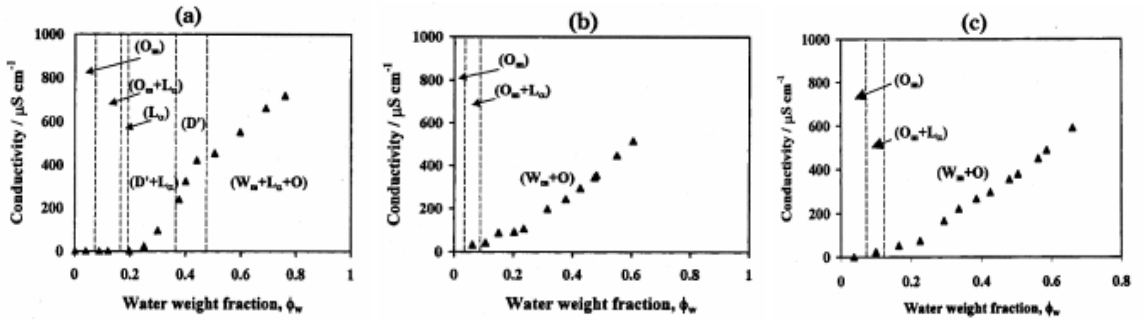


**Figure 20: Conductivity as a function of water weight fraction at 25°C for method B. Initial decane/Brij 30 ratios were: (a) 79.2/20.8 (b) 90.5/9.5 and (c) 91.9/8.1. $O_m$, isotopic liquid phase; Lα, lamellar liquid crystalline phase. This figure is associated with Figure 16 [Forgiarini *et al.,* 2001].**

The downfall of this method is that, although very stable and uniform micelles are formed, only a small amount of aqueous phase can be "dissolved" and high amounts of surfactant are needed to dissolve more (Fig. 16). The next method may be used to obtain highly concentrated water-in-oil emulsions.

### *2.3.2.2 Phase Inversion Temperature (PIT) Method*

Phase inversion in emulsions can be one of two types: (a) Transition inversion induced by changing factors that affect the hydrophilic-lipophilic balance (HLB) of the system, e.g. temperature and/or electrolyte concentration. (b) Catastrophic inversion, which is induced by increasing the volume fraction of the disperse phase. The former type will be discussed.

Highly concentrated water-in-oil emulsions can be formed using a temperature swing technique. The hydrophile-lipophile property of the non-ionic surfactant is largely influenced by temperature due to the conformational change in the hydrophilic polyoxyethylene chain. Hence, the non-ionic surfactants tend to form aqueous micelles at lower temperatures, whereas they form reverse micelles at higher temperatures. At

the transition temperature called the HLB (hydrophilic-lipophilic-balance) temperature the bicontinuous micro-emulsion (or surfactant phase) coexists with the excess water and oil phases. Above the HLB temperature, water-in-oil type, highly concentrated emulsions form because the non-ionic surfactant is lipophilic in a given water/oil system. Kunieda *et al.* [1996] have investigated the phase behaviour of a nonionic surfactant system (water/tetraoxyethylene dodecyl ether/oil) by studying its electroconductivity. They concluded that the highly concentrated emulsions (gel emulsions) are spontaneously formed from oil-swollen micellar solutions with an abrupt increase in temperature. The phase change occurs from water continuous micro-emulsion to water-in-oil gel emulsion via a lamellar liquid crystal and bicontinuous surfactant ($L_3$) phase.

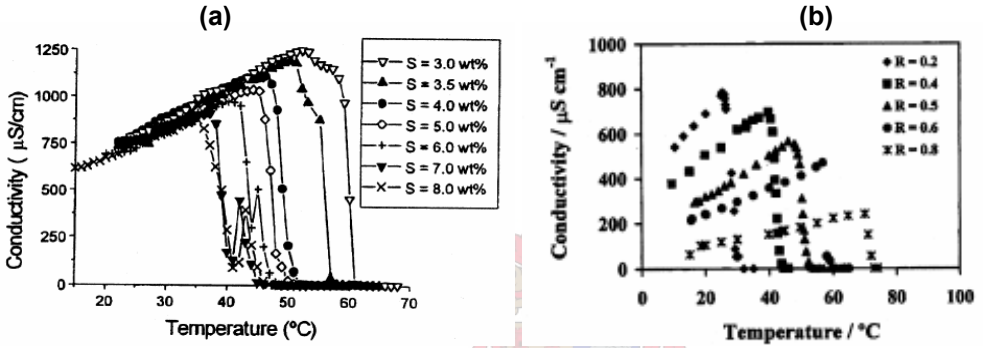


**Figure 21: Conductivity as a function of temperature: (a) aqueous $10^{-2}$ M NaCl/C12E4/hexadecane at different surfactant concentrations and constant oil concentration (20%) [Izquierdo *et al.,* 2002]; and (b) aqueous $10^{-2}$ M NaCl/Brij 30/decane at different oil weight fractions R=O/(O+W) and constant surfactant concentration (5 WT %) [Forgiarini *et al.,* 2001].**

Figure 21 show the change in conductivity as a function of temperature for different surfactant concentrations and different water contents. Oil-in-water micelles are formed at low temperatures, causing high conductivity, and reverse micelles are formed at temperatures above the HLB temperatures, indicated by the low conductive region (an increase in water content for a constant surfactant concentration and an increase in surfactant concentration for constant oil concentrations decrease the HLB temperature). The lack of continuity for systems with high surfactant concentrations (Figure 21(a) above 5 wt %) is caused by the formation of a liquid crystal phase, as can be seen in the graph in Figure 22. The mechanism in Figure 23 shows how the reverse micelles are spontaneously formed from micelles via the vesicle, the lamellar liquid crystal and the surfactant-continuous $L_3$ phase during temperature change. Emulsions in the $L_3$ + W region are extremely unstable and the complete phase separation takes place with in a

short time. When the temperature change is slow, the water droplet size in the resulting highly concentrated emulsion is large because coalescence of the water droplets occurs in the $L_3$ + W region. Consequently, it is very important to change the temperature quickly in order to produce fine emulsions.

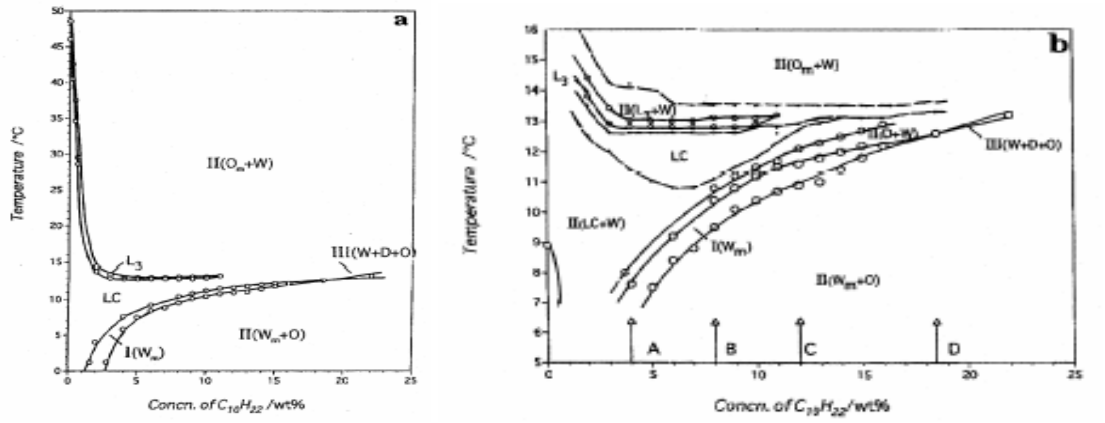


**Figure 22: Phase diagram of 0.1 M aqueous NaCl/C12EO4/decane system as a function of temperature. Decane was added to 3 wt% $C_{12}EO_4$ aqueous solution. (a) Phase diagram over a wide temperature range, and (b) detailed phase diagram: $W_m$, oil-swollen micelles; $O_m$, water-swollen reverse micelles; $L_3$, bicontinuous surfactant phase; LC, lamellar liquid crystal phase; W and O, excess water and oil [Kunieda *et al.,* 1996].**

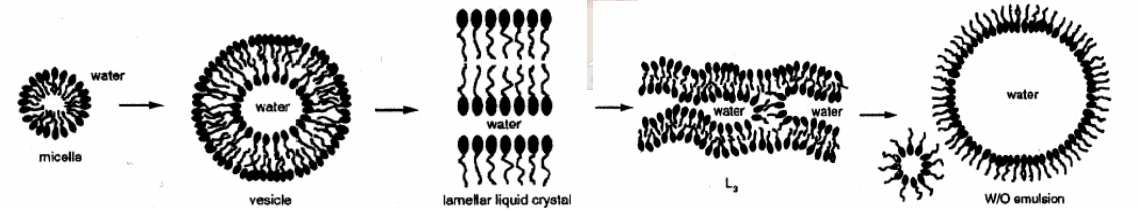


**Figure 23: Proposed mechanism for the spontaneous formation of gel-emulsions [Kunieda *et al.,* 1996].**

### 2.3.3 Preparation of Nanoparticles

Water-in-oil (w/o) micro-emulsions provide particularly favourable reaction conditions for the preparation of mono-dispersed crystallites. In this technique, the synthesis of nano-oxides is based on the principle of confining the precipitation of metal oxide crystallites to tiny water drops of the w/o emulsion. When a soluble metal salt is incorporated into the aqueous phase of the micro emulsion, it will reside in the aqueous micro droplets

surrounded by oil. Precipitation will take place when the droplets containing different salts collide with each other. Each of the droplets will become a nano-size reactor for the formation of nano-sized particles [Mabaso, 2002]. The particle size is influenced by the droplet size, as well as by the rate of particle growth.

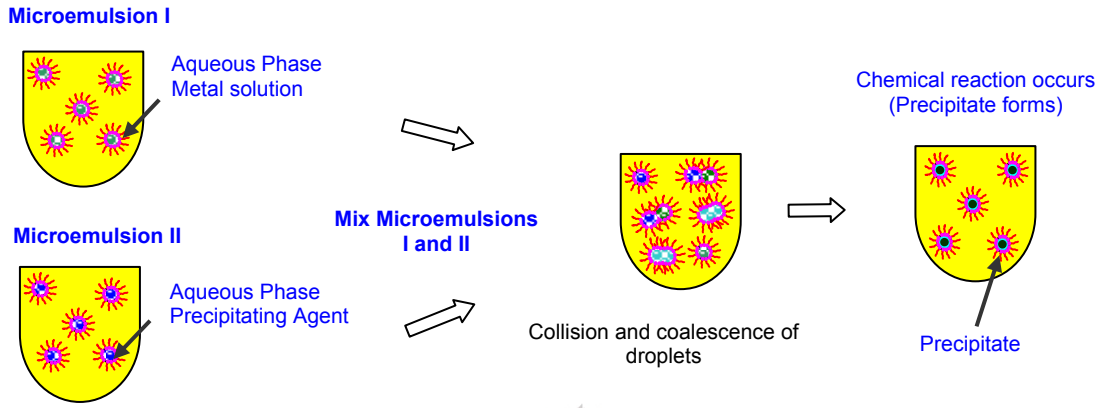


**Figure 24: Catalyst preparation using water-in-oil micro-emulsion [Mabaso, 2002].**

There are two main methods of precipitation to obtain nanoparticles from micro-emulsions:

1. By mixing two micro-emulsions, one is containing the precursor and the other the precipitating agent (see Fig. 24).
2. By adding the precipitating agent directly to the micro-emulsion containing the metal precursor.

### 2.3.4 Particle Size Control

Pileni [1997] noted that an increase in water-to-surfactant ratio increases the domain size of the product. The characteristic size of the micro-emulsion (droplet radius) can be controlled by changing composition parameters, temperature, salinity, etc. By increasing the water-to-surfactant ratio, the average diameter of the droplet increases, with a subsequent increasing effect on the final particle size. When the water-to-oil ratio is kept at a fixed value, an increase in the amount of surfactant will increase the number of droplets. This means that the number of metal ions per droplet will decrease and,

consequently, so was the size of the particles. By changing the salinity, reaction time and using a co-surfactant, Bender and Burlitch [2000] also obtained reproducible size control. A lower salt concentration and short reaction time produce smaller particles, but also smaller yields. By increasing the volumetric fraction of MeOH in the salt solution, the particle sizes are decreased almost linearly by decreasing the solubility of the salt in solution. Co-surfactants can also be used to alter the pacing parameter through sterical effects and by influencing the interfacial film by compacting it, favouring the formation of smaller droplets with a lower water content. It was observed that decreasing the chain length of the co-surfactant alcohol increased the particle size [Curri *et al.,* 2002].

The particle size is not ultimately controlled by the droplet size, although it has a great influence. The particle sizes were found to be larger than the droplet sizes, showing that it is not the final particle that is formed inside the droplet, but rather only the nuclei. Within the micro-emulsion, being a dynamic system of constant collisions, formation of particles proceeds in two steps. The first is the nucleation process inside the droplet, followed by then the aggregation process to form the final product. The rate of particle growth is controlled by the presence of the surfactant, which sterically prevents the nuclei from growing too fast. Consequently, the particles will grow at the same rate, favouring the formation of particles of homogeneous size distribution. Thus, the size of the droplet will influence the size of the nuclei, but the size of the final particle will be controlled by the surrounding surfactant molecules [Eriksson *et al.,* 2004].

### 2.3.5 Supported Catalyst from Micro-Emulsions

To minimise the sintering of the particles at high temperatures they have to be strongly adhered to a support. It is also necessary to maintain a homogeneous distribution when transferring the particles onto the support.

The most common way up until now to carry out this process has been to add a solvent like tetrahydrofuran (THF) to the micro-emulsion, which will destabilise the solution and bring about the sedimentation of the particles. THF will compete with the surfactant molecules that are strongly adsorbed onto the particle and displace them, resulting in an unstable suspension. If the support powder is added at the same time as the solvent, the

particles will stick onto the support. The proper mixing of the solution with the powder will increase the possibility of obtaining a homogeneous distribution of particles on the support. This is a difficult task and its success is greatly dependent on the properties of the support [Eriksson *et al.,* 2004].

## *2.4 Previous Studies performed at the University of Stellenbosch*

A study done by Swart [2002] has shown that it is possible to produce pure α-$Bi_2Mo_3O_{12}$ after calcination by using the precipitation method of Batist *et al.* [1972]. Pure α-phase was also obtained after calcination using the reverse micelle technique, based on the precipitation method suggested by Batist, yielding a mixed precipitate of 2/3 and 2/1 compounds. The resulting precipitate thus had to be calcined at a temperature of 450$^{o}$C to obtain the pure α-phase. Further studies by Agenbag [2003] showed that it was possible to produce particles with a size of ±17 nm with a narrow size distribution by using the reverse micelle technique. However, the precipitated particles conglomerated when they were calcined stepwise at 450$^{o}$C, which was necessary to obtain the α-phase. Thus, a method should be found to keep the particles liberated during calcination or the method must be altered to obtain the required catalyst.

# 3. Hypothesis and Project Design

## *3.1 Hypothesis*

**The depth of oxygen utilisation on bismuth molybdate during the partial oxidation of propene to acrolein may be determined by measuring the rate of acrolein formation and lattice oxygen usage over a range of particle sizes that are synthesised using reverse micelle technology.**

Assuming that the reaction only occurs on the surface and that there is no lattice oxygen gradient through the catalyst's penetration depth (Fig. 25), the following results would be observed: As one plots the fraction of lattice oxygen that can be utilised in the oxidation of propene against particle size (Fig 26), at some stage the curves will flatten out as the particle size decreases. This means that lattice oxygen is utilised throughout the catalyst and that the penetration depth is equal to the radius of the particle.

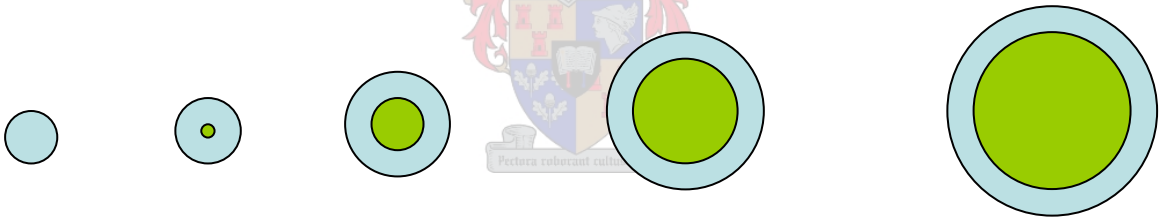

**Figure 25: The effect of particle size on the percentage catalyst utilised.**

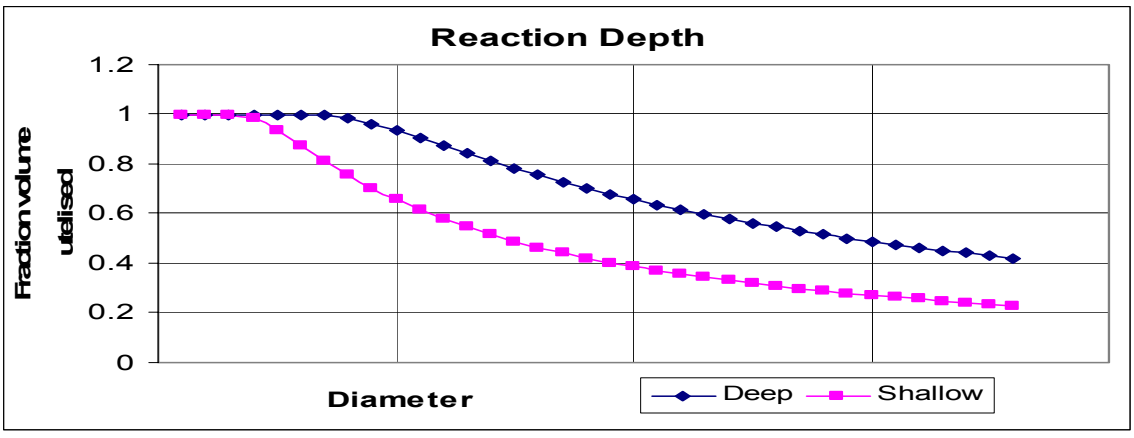


**Figure 26: Oxygen utilised with decreasing particle diameter; deep and shallow penetration depth.**

This is an extremely simplistic model, but it illustrates the concept. Multi-layer models will be used for data fitting and lattice oxygen gradients should also be taken into account.

By sampling throughout the reduction run of the catalyst, the differences in activity and selectivity can be studied. Knowing the point of total oxygen utilisation, the catalytic performance can be correlated as a function of oxygen diffusion (mobility) and grade of reduction.

## *3.2 Scope of This Project*

Although previous attempts to synthesise the catalyst particles were successful, not much has been done to find the operating conditions and parameters under which this is possible. Neither has there been attempts to produce pure precipitate or to support the catalyst particles for stabilisation in the calcination step so that they may be used in kinetic experiments. In order to obtain reproducible size control of pure precipitated particles in such a complex system, it is imperative that the conditions and parameters in which this is attainable are known. Thus, a systematic approach was taken to attain knowledge of the system and so define the operating window in which size control, precipitate purity and/or particle support can be obtained. The following aspects were investigated:



- The reverse micelle technique with which particles were successfully synthesised.
- Low temperature calcination options.
- A simple precipitation method to attain pure 2/3 (Bi/Mo) precipitate.
- Formation and stability of reverse micelles.
- Reaction kinetic studies using $\alpha$-BiMoO prepared according to Keulks's method.
- Reaction kinetic studies using catalyst prepared by the reverse micelle technique.

### 3.2.1 The Reverse Micelle Technique Used Previously

Different aspects and steps of the reverse micelle technique that was used previously to successfully obtain catalyst particles in the nano-meter range were investigated to see whether they could be altered slightly to achieve size control. Theoretically it is possible to attain particle size control by varying the salt concentration, aqueous salt/surfactant/oil ratios, temperature, co-surfactant, stirrer speed, aging, etc. The micelle stability region in the ternary diagram (aqueous-salt or water/surfactant/oil) is also of importance in the process of defining an operating window. Other aspects such as the aggregation of particles, may be solved by investigating the effects of the wash and drying steps of the technique.

### 3.2.2 Low Temperature Calcination

Using lower calcination temperatures may help prevent the sintering of catalyst particles. Trifiro *et al.* [1972] suggested that the phase transition is complete at temperatures as low as 300°C. The catalyst calcination step was thus investigated using temperature range calcination of pure 2/3 precipitate prepared using the method suggested by Keulks and inspecting the degree of solid state phase transition using XRD analysis. Thermal gravitational analysis (TGA) was also done to determine the percentage weight loss as a function of temperature. TGA can be done in an oxygen (air) or nitrogen atmosphere, thus further oxidation may be measured exclusively by comparing the oxygen and nitrogen atmosphere results. This may also explain solid state reactions as well as precipitation reactions.

### 3.2.3 A Simple Precipitation Method to Attain Pure 2/3 (Bi/Mo) Precipitate

The precipitation method of Batist *et al.* [1972], although simple, did not produce pure precipitate. Keulks *et al.* [1974], on the other hand, investigated the parameters leading to the formation of pure precipitate and came up with a more complex co-precipitation with the back titration method. They also suggested a simpler co-precipitation method without back titration. If the precipitation method is to be integrated into the reverse micelle technique to produce pure precipitate particles, it should be a simple precipitation

reaction (the addition of two stable salt solutions causing a precipitation reaction resulting in the formation of pure 2/3 precipitate without back titration or co-precipitation). The principles governing the co-precipitation method of Keulks should thus be used to derive a simple precipitation method that can be used in the reverse micelle technique to obtain pure 2/3 precipitate particles.

### 3.2.4 Formation and Stability of Reverse Micelles

To ensure reproducible results, it was necessary to investigate other controlling factors, such as reverse micelle growth, stability and whether the chosen system may successfully be used to attain size control. There was some doubt about the use of hexane as the oil, because of its low viscosity and short chain length. Photon Correlation Spectroscopy (PCS) is a direct way to measure the size, size change and stability of the reverse micelles. The pH and salinity effects of the aqueous phase, as well as temperature effects on the system, can then be investigated.

### 3.2.5 Reaction Kinetic Studies Using Keulks's $\alpha$-$Bi_2Mo_3O_{12}$

Kinetic studies were done on $\alpha$-$Bi_2Mo_3O_{12}$ prepared using the method of Keulks *et al.* [1974]. This was done to validate the working of the experimental apparatus by comparing the results to previously published results, and to develop an accurate measuring and analysing technique.

### 3.2.6 Reaction Kinetic Studies Using Catalyst Prepared by the RMT

The hypothesis states that the reaction depth (depth of oxygen utilisation) and lattice oxygen mobility can be studied by doing kinetic experiments over a range of discrete particle sizes.

## *3.3 Key Questions*

The first key question is if the required catalyst, pure calcined $\alpha$-$Bi_2Mo_3O_{12}$ particles with narrow size distribution in the nano-meter range, can be synthesised using the reverse micelle technique.

Another equally important question is whether reproducible size control of the nano-size crystal particles can be attained using the reverse micelle technique or any other combined method.

There is some uncertainty as to whether the catalyst performance changes drastically with a reduction in size. Bismuth molybdate catalysts are known to have a layered structure. It could be that structural deformation, due to the decrease in particle size and high surface-to-volume ratio, influences the catalyst performance (selectivity and activity). Ueda *et al.* [1999] attempted to attain silica-supported $Bi_2Mo_3O_{12}$ catalysts using impregnation and co-precipitation methods. The catalyst was intrinsically active, but poorly selective to acrolein. This result demonstrates that, for activity and selectivity, the bismuth molybdate catalyst needs to be of a certain particle size that can provide sufficient lattice oxygen ions during the catalyst redox cycle.

# 4. Experimental

This section will describe and evaluate the experimental setup used for the kinetic experiments, as well as the analytical apparatus used to analyse kinetic samples and to characterise the catalyst.

## *4.1 Chemicals used*

**Table 9: List of chemicals used.**

| Chemicals | Purity | Obtained from |
|---|---|---|
| | | |
| Acetone | 98.00% | Merck |
| Ammonium Molybdate Tetrahydrate | ≥99.9% | Fluka |
| Bismuth(III)Nitrate Pentahydrate | ≥98.0% | Fluka |
| Berol 050 | | UCT |
| Fumed Silica | 99.80% | Aldrich |
| HNO3,>55% con. | analytical grade | |
| NH3, 25% con. | analytical grade | |
| Silicon Carbide, 200-450 mesh | | Aldrich |

## *4.2 Setup for Kinetic Experiments*

### 4.2.1 Reactor Rig

The diagram in Figure 27 shows the layout of the reactor rig used for the kinetic experiments. Bottled helium, oxygen, propene and ethane gases were used in the experiments. Oxygen and propene are the reactants and helium is used to dilute the reaction mixture to prohibit high energy release from the exothermic reaction. Nitrogen or argon could also be used and are the cheaper option. Helium is needed for the analysis that is performed by a thermal conductivity detector. Ethane is the internal standard added to the reaction mixture after the reactor in order to calculate the carbon balance of the experiments. The flows are directed by stainless steel three- and four-way valves and controlled by calibrated mass-flow controllers and needle valves. The micro-reactors are suspended in a temperature-controlled oven and the outlets are heated with heating wire to prevent the condensation of products in the tubing. All the tubing

upstream of the oven is 1/8' stainless steel tubing to prevent a drop in pressure drop and those downstream are 1/16' stainless steel ensuring turbulent flow, good mixing and low hold-up.

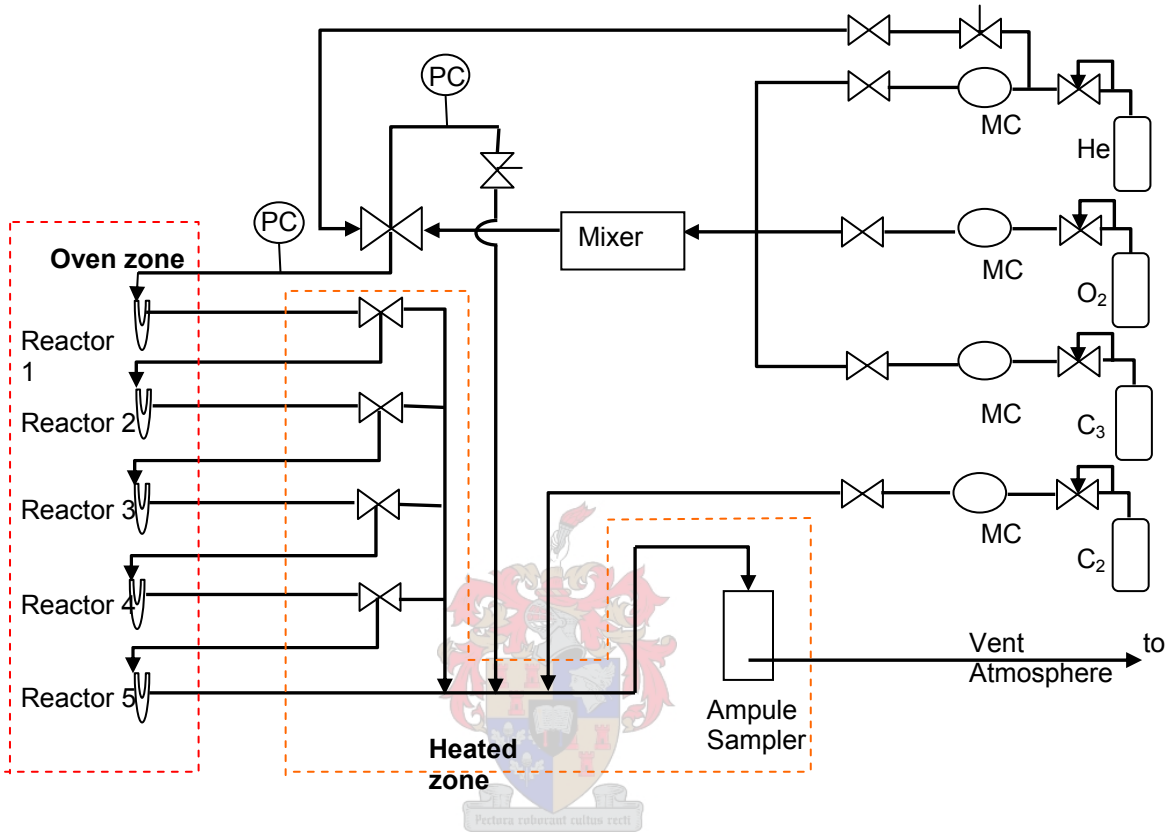


**Figure 27: Flow diagram of the reaction rig used for the kinetic experiments.**

A reaction mixture containing propene, helium and oxygen is obtained by the mass-flow controllers and mixed in the mixer. At first, reaction gas is vented to the atmosphere while the reactors are purged with helium. The temperatures, flow rates, composition and pressure are checked before switching the four-way valve. This allows the reaction mixture to flow to the oven-heated micro-reactors. Depending on the position of the three-way valves, one to five micro-reactors can be used in series. The internal temperatures of the reactors are measured by a thermo couple in a thermal well at the centre of the reactor. Care should be taken to keep the reactors at isothermal conditions, and for this oven temperature control as well as the heat generated by the highly exothermic partial oxidation reaction should be monitored. The reaction product leaving the oven flows through a heated zone, where the internal standard is added to the

heated sampler. The gaseous samples are taken using an evacuated glass ampoule and sealed for later analysis. The excess product gas is carefully vented to the atmosphere to prevent releasing toxic acrolein and combustible gases into the laboratory. The pressure drop over the venting system should be as low as possible to prevent a high pressure in the sampler. This helps to seal the glass ampoules.

The temperature range at which the experiments are done is 350-410$^{o}$C and the pressure is 1.1-2 bar, depending on the pressure drop and the number of reactors in series. The reaction must be done under isothermal conditions and thus low concentrations of reactants obtained by dilution with helium. Care must be taken not to exceed the temperature specifications of the equipment e.g. the valves.

### 4.2.2 Kinetic Reactors

Two types of reactors were evaluated, namely glass and metal reactors. The glass reactors were chosen for their transparency and formability. Graphite ferrules were used in the swage lock fitting to connect these class reactors to the stainless steel tubing at high temperatures. A thin layer of diluted catalyst particles were uniformly distributed on a fine sinter (no 5) to ensure an even reaction rate and a low pressure drop throughout the catalyst bed. The reactor was equipped with a temperature well and had a reverse funnel inlet to avoid the reaction gasses concentrating at the centre of the reactor. The metal reactor was made from stainless 316. It consisted of a screw cap sealed with a graphite seal to a cylindrical reactor tube fitted with a thermocouple well at its centre. The inlet and outlet were fitted with short ¼’ stainless steal tubing. The length of the cylindrical hull of the reactor was fitted with screw-thread, which acted as fins and reduced the minimum diameter to 0.3 mm. This helps considerably to transfer the excess exothermic heat generated by the reaction, ensuring isothermal conditions. The thermo well fitted at the centre was made using 1/8’ tubing which wall thickness at its tip were reduces to 0.2 mm for better and faster temperature response. The reactor was packed with a layer of glass wool, followed by a layer of silicon carbide particles to ensure a stable catalyst bed on which the silicon carbide dilute catalyst bed was placed, followed by a glass wool plug.

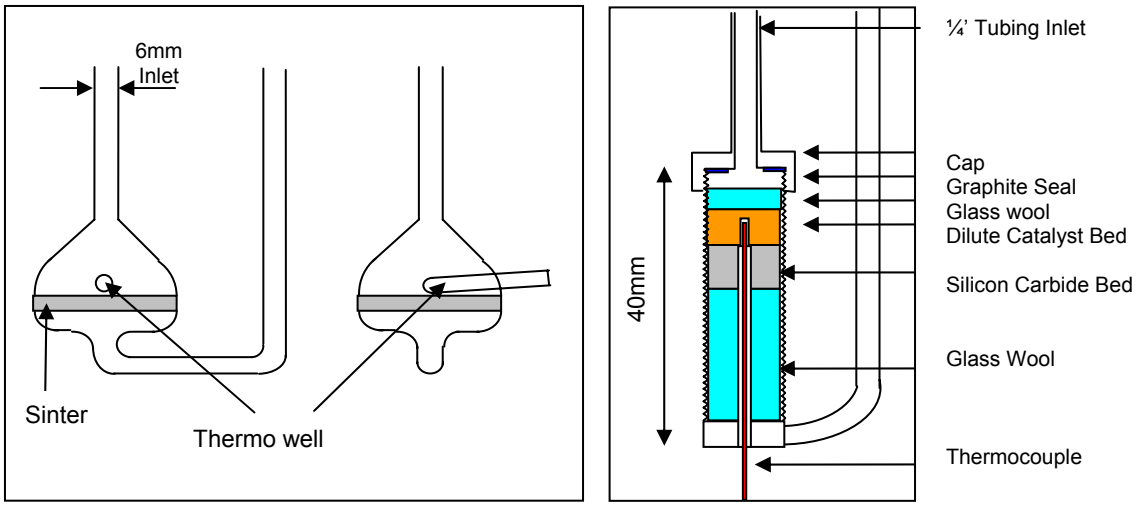


**Figure 28: Front and side view of the Pyrex glass and stainless steel reactor used in the kinetic studies.**

### *4.2.2.1 Reactor Flow Characterisation*

Characterisation of the glass reactor and for the system as a whole was done by means of a pulse input tracer study. A tracer was suddenly injected into the feed stream in one shot, entering the reactor in as short a time as possible. The outlet concentration was then measured as a function of time, C(t), using a TCD detector. The exit age, E(t), and the cumulative F(t) residence-time distribution (RDT) function, as well as the mean residence time, $t_m$, and exact reactor volume, V, can then be determined using the following equations:

$$E(t) = \frac{C(t)}{\int_0^\infty C(t)dt} \qquad ....19$$

$$F(t) = \int_0^t E(t)dt \qquad ....20$$

$$t_m = \int_0^\infty t.E(t)dt \qquad ....21$$

$$V = v.t_m \qquad ....22$$

The RTDs are compared using three of their moments. The first is their mean residence time, and the second their variance, which is defined by

$$\sigma^2 = \int_0^\infty (t - t_m)^2 E(t) dt \qquad \text{....23}$$

The magnitude of this moment is an indication of the distribution of the sample ($\sigma$ = 68%, $2\sigma$ = 95% & $3\sigma$ = 99.8%, thus after a period of time equal to $\sigma$, 68% of the sample introduced to the reactor has exited). The third moment is that of skewness and is defined by:

$$s^3 = \frac{1}{\sigma^{3/2}} \int_0^\infty (t - t_m)^3 E(t) dt \qquad \text{....24}$$

The magnitude of this moment measures the extent of a distribution is skewed in one direction or another with reference to the mean [Fogler, 1999].

The reactor itself was first evaluated using different flow rates at ambient temperatures. The reactor was then placed in the reaction rig and the rig was evaluated as a whole at different flow rates and at typical reaction temperatures. The results are summarised in Figures 29 to 31 and Table 10.

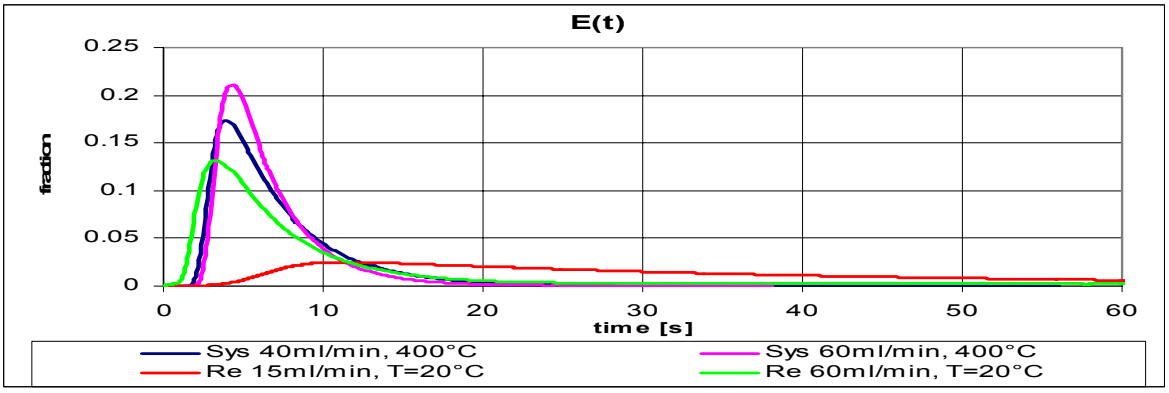


**Figure 29: The exit-age distribution function, E(t), for the reactor and reactor system at different flow rates and temperatures. Re, reactor only; Sys, whole system (reactor including tubing and valves at typical reaction temperatures)**

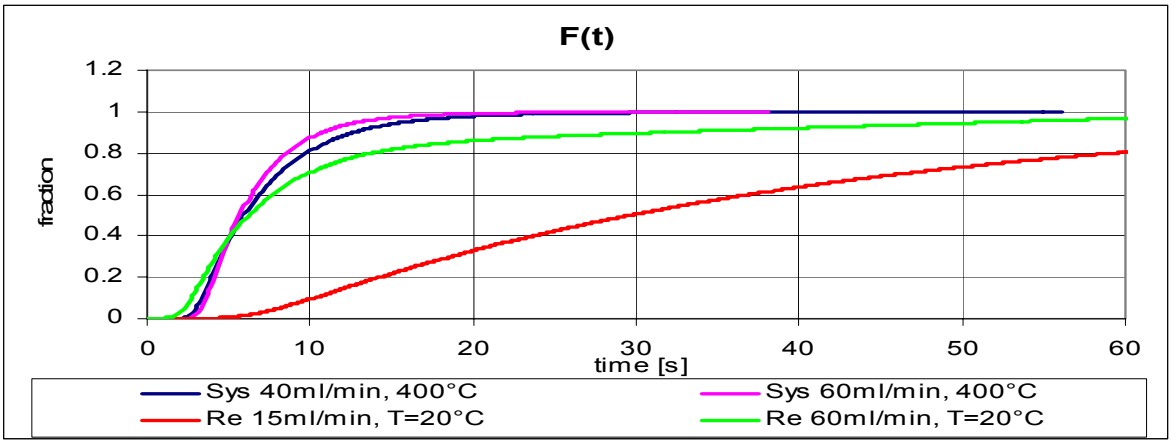


**Figure 30: Cumulative distribution function F(t) for the reactor and reactor system at different flow rates and temperatures. Re, reactor only; Sys, whole system (reactor including tubing and valves at typical reaction temperatures)**

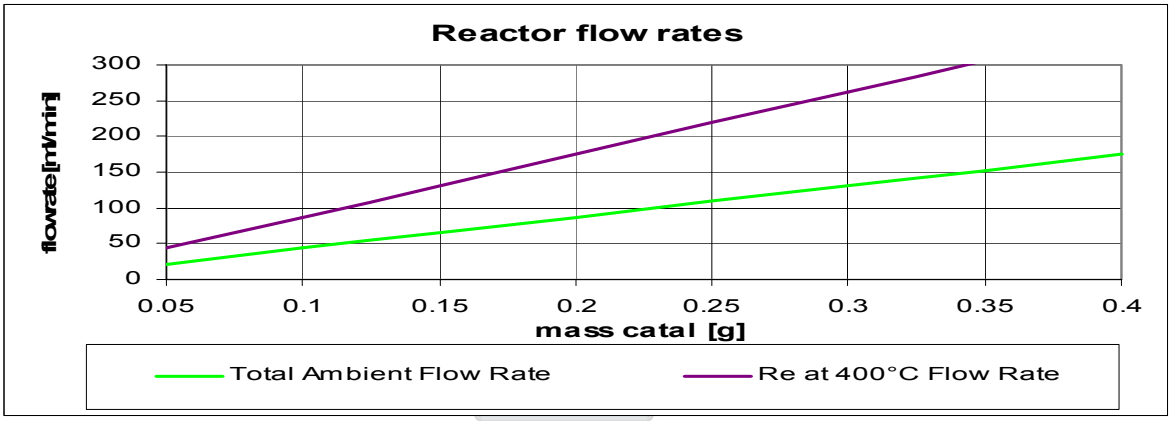


**Figure 31: Reactor rig flow rates at ambient and reactor temperatures at 4.5 g propene per gram catalyst per hour (1:2:7 for Propene:Oxygen:Helium); Re ,Reactor**

**Table 10: Summary of evaluation moments of the reactor and reactor system.**

| Re: Reactor | **V** | **σ** | **s** | **$t_m$** |
|---|---|---|---|---|
| Sys: Reactor System | ml | | | |
| Re 15ml/min; T=20°C | 9.37 | 13.97 | 1.55 | 38.8 |
| Re 60ml/min; T=20°C | 11.91 | 8.65 | 1.65 | 11.9 |
| Sys: 40ml/min;T=400°C | 4.87 | 7.49 | 1.40 | 7.3 |
| Sys: 60ml/min;T=400°C | 6.64 | 6.18 | 0.76 | 6.6 |

It can be seen from both the E(t) and the F(t) functions that the reactor performs much better at higher flow rates and even better at reaction conditions (T=400°C). The increase in effective volume, V, with an increase in flow rate for the reactor as well as the system as a whole (Table 10) indicates an increase in reactor back mixing with

increasing flow rates due to the post catalytic bed free volume. Inserting the reactor into the rig causes a small delay of ±2.0 seconds at a flow rate of 60 ml/min, but due to the higher flow rate through the reactor caused by the expanding heated gas (seen Fig. 31), the mean residence time decreases drastically. As can be seen from Table 10, the reactor variance and skewness decrease with increasing flow rates and reactor temperatures.

At a weight hour space velocity (WHSV) of $4.5 g_{propene}/(g_{catalyst}.hr)$, using a composition ratio of 1:2:7 for propene : oxygen : helium, the ideal catalyst weight was around 0.15-0.25 g, resulting in a reactor ambient flow rate of ±100 ml/min. This was even higher than the flow rates examined and should give even better results.

The metal reactor had a much smaller total volume (1/2 of that of the glass reactor), which was totally packed (no free volume). Thus, much less back mixing was expected, resulting in much better plug-flow characteristics.

#### *4.2.2.2 Reactor Temperature Distribution*

Isothermal and isobaric conditions are required in kinetic studies. The ideal reactor would then be a reactor with a minimum diameter so that the radial temperature difference would be minimised and the bed depth would be as small as possible to prevent a pressure drop over the reactor. The glass reactor had a relatively wide diameter (30 mm) to decrease the pressure drop. It was thus important to determine and minimise the temperature distribution and to find the operating conditions under which this was possible.

The catalyst bed gets rid of its excess heat (exothermic reaction heat) by radial conduction of heat and by transferring heat to the constant flow of gasses. Assuming the amount of heat removed by the gas flow was the same throughout the reactor bed, the temperature distribution can be attained by only looking at the radial conduction. The temperature distribution for a cylindrical geometry in which heat is generated can be obtained using the following equation [Incropera and De Witt, 1996]:

$$T(r) = \frac{\dot{q} r_o^{\,2}}{4k}\left(1 - \frac{r^2}{r_o^{\,2}}\right) + T_{s1} \qquad \text{....25}$$

T(r): Reactor radial temperature

The rate at which heat was generated ( $\dot{q}$ ) and the thermal conductivity (k) of the catalytic bed were unknown because the amount of heat removed by the passing reaction gas was unknown, thus we had to obtain the equation for the non-dimensional temperature distribution as a function of the temperature at the centre of the reactor ($T_o$), the temperature at the inner wall ($T_{s,1}$) and the ratio of radial distance (r) over total radial ($r_0$) distance:

$$\frac{T(r) - T_{s,1}}{T_o - T_{s,1}} = 1 - \left(\frac{r}{r_o}\right)^2 \qquad \text{....26}$$

Similarly, an equation for the temperature distribution through the cylindrical glass reactor wall can be obtained if the inner wall ($T_{s,1}$), and outer wall ($T_{s,2}$) temperature are known ($r_1$ and $r_2$ are the inner and outer wall radii, respectively) [Incropera and De Witt, 1996]:

$$T(r) = \frac{T_{s,1} - T_{s,2}}{\ln\left(r_1 / r_2\right)} \ln\left(\frac{r}{r_2}\right) + T_{s,2} \qquad \text{....27}$$

A temperature distribution model (eq. 27) is derived by combining equations 25 and 26. Only the central reactor temperature, the oven temperature and one catalyst bed temperature at a known radial distance are needed to find the total radial temperature distribution. The graph in Figure 32 shows the relative radial temperature distributions with different inner wall temperatures. The inner wall temperature is a function of the degree of heat removal by the reactant gas flow, the WHSV and the amount of catalyst in the catalyst bed (the catalyst was diluted with silica particles to make up 1 g). By diluting the reactant gas with He, the temperature difference through the catalyst bed will decrease due to an increase in the degree of heat removal by the reactant gas. The

exothermic heat generated is proportional to the catalyst weight and increases with an increase in WHSV. If the WHSV is kept constant, the degree of He dilution and the catalyst weight control the degree of temperature difference through the catalyst bed.

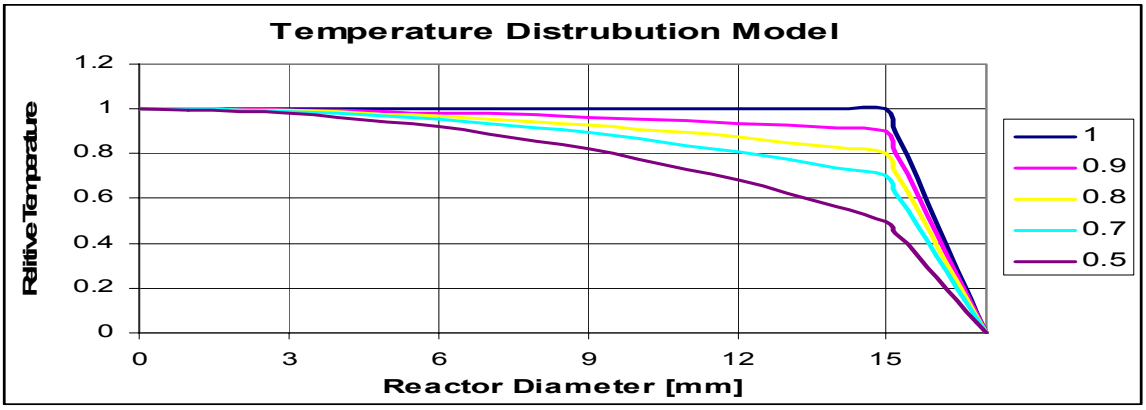


**Figure 32: Relative radial temperature distribution through the reactor bed and wall for different inner wall temperatures.**

The temperature rise was 9°C at the centre of the reactor when the reaction gasses were fed to the reactor using 0.45 g of catalyst at a WHSV of 4.5 $g_{C3}/(g_{Cat.}h)$ and a $C_3^=:O_2$:He ratio of 1:2:7 at an oven temperature of 450°C. By decreasing the catalyst weight to 0.18 g with the same WHSV and a $C_3^=:O_2$:He ratio of 1:2:9 at 450°C, the central temperature rise was reduced to 4°C. The temperature distribution for the 0.18 g catalyst and flow ratio of 1:2:9 at 450°C was determined by measuring the temperature at a distance of 12 mm from the centre and was found to rise 1°C less than that of the centre. The relative radial temperature distribution was thus represented by the 0.7 line in Figure 32. The maximum temperate difference (temperature difference between the centre of the reactor and the inner wall) is 2°C.

The maximum internal temperature change for the metal reactor using similar conditions (0.18 g catal., WHSV 4.5, $C_3^=:O_2$:He ratio of 1:2:9 at 450°C) was 2°C.

### 4.2.3 Oven Temperature Control

It was found that the oven temperature control was insufficient, causing a temperature oscillation with a significant effect on the kinetic reaction results. A typical oscillation is shown in Figure 33:

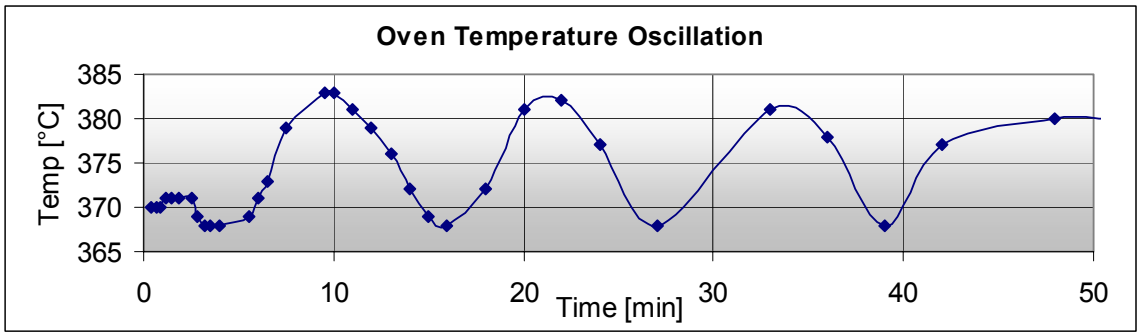


**Figure 33: Reactor oven temperature oscillation.**

The oven temperature oscillated at an amplitude of ±15°C. The slow response thermocouple was substituted with a fast response one, decreasing the temperature amplitude to ±5°C. This was still a significant temperature change and it was decided to control the oven manually by specifying the percentage at which it is powered (normally 35-40%). The oven was thus initially controlled automatically and switched to manual control when the desired temperature was reached. Using manual control, the oven temperature can be controlled to within 1°C.

### 4.2.4 Ampoule Preparation

The product gas coming from the catalytic plug flow reactor was sampled using evaluated ampoules made from glass basture pipettes. The outlet of the ampoule sampler was bubbled through water before it was vented to an extractor fan so that the suction caused by opening the ampoule could be observed to check if it worked properly. In the preliminary experiments it was found that a considerable number of the ampoules did not work because of cracks in them or insufficient vacuum. The preparation method was altered as follows:

A 20 cm long capillary nose was pulled and sealed at its tip replacing the thicker and shorter nose of the pipette. Secondly, a thin tube was pulled in at the back side of the pipette. The pipette was attached to the vacuum system (see Figure 34) using a soft rubber tube and a vacuum was pulled by opening a valve. The pipette was then heated well before sealing it off at the thin tube, which helped to ensure a strong vacuum. The ampoule, still hot, must be placed on an insolating type of material to prevent it from cracking from thermal shock.

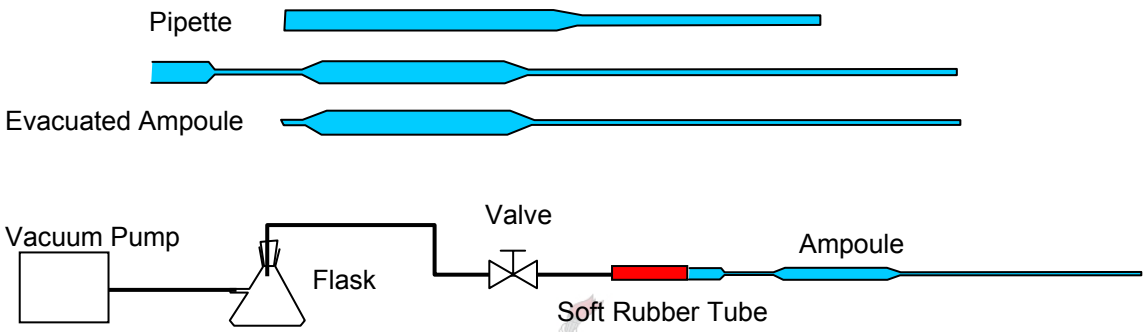


**Figure 34: Making the evacuated ampoules.**

### 4.2.5 Thermocouple Calibration

Long and thin type K thermocouples were used in the kinetic experiments. It was found that the temperature indicators did not show the correct temperatures and had to be calibrated using another thermocouple. Figure 35 shows the thermocouple calibration function.

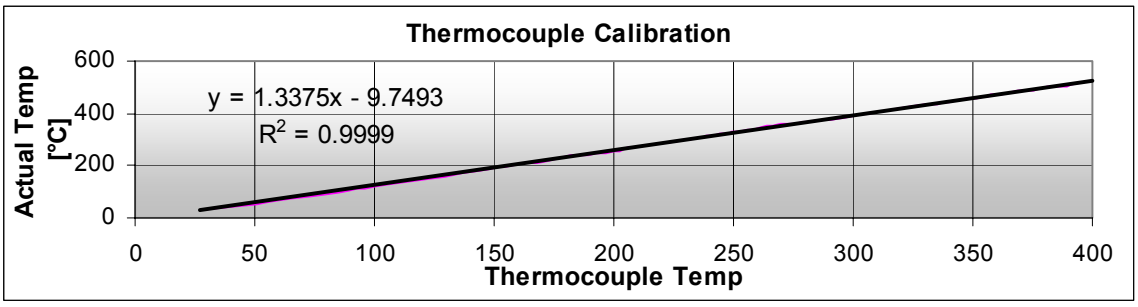


**Figure 35: Thermocouple calibration function for reaction rig.**

## *4.3 Methods of Analysis & Catalyst Characterisation*

### 4.3.1 Analysing Kinetic Samples

The samples that need to be analysed could include the following compounds: the reactant gasses, propene and oxygen; the products, acrolein, carbon monoxide and carbon dioxide; ethane, the internal standard; and small amounts of nitrogen coming from the trace air left after the ampoule is evacuated.

Thus, to do an accurate analysis of the samples it is necessary to separate all of the above components. The components are light and heavier permanent gasses, as well as acrolein, which is a highly polar liquid with a boiling point of 58°C. The following GC rig was set up to be used in the analysis of the gaseous samples.

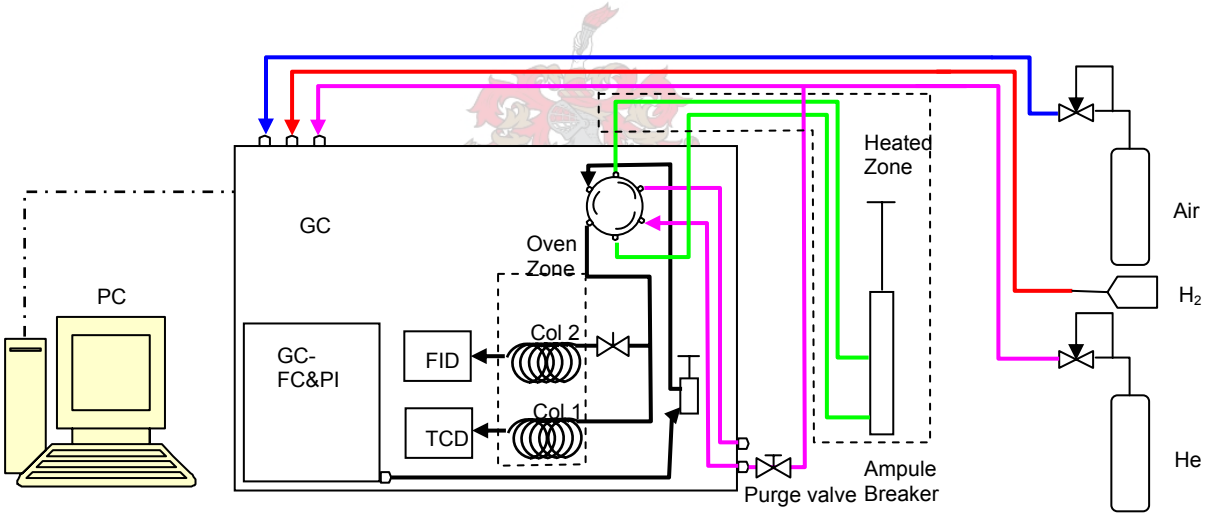


**Figure 36: GC analyser setup.**

Helium is used as a carrier and reference gas for the TCD, while the air and hydrogen are needed for the FID detector. An ampoule breaker is fitted in the GC sample loop in which the gas sample is liberated and injected into the column stream. The GC six-port-two-way valve enables the user to purge and insert the ampoule breaker in the column stream. Two columns are used in parallel and analysed individually by TCD and FID detectors. The data is captured by a PC and analysed using a data system.

The glass ampoule containing the sample is put in a heated ampoule breaker, which is sealed and purged with helium to remove all air. The first column separates the light gasses and its product is analysed by a TCD detector. The second column is unable to separate the light gasses, but separates the acrolein, ethane and propane. The product of column 2 is analysed by an FID detector, meaning that the unseparated light permanent gasses ($N_2$, $O_2$, CO and $CO_2$) will not be detected. Figure 37 shows typical results obtained using a glass reactor that will be discussed in a later section.

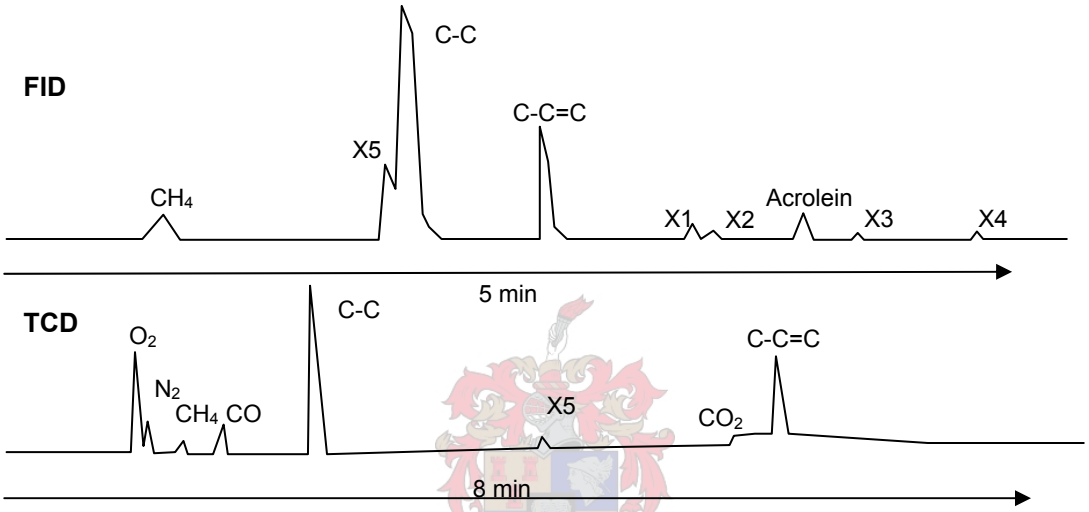


**Figure 37: Typical GC results using a glass reactor at 450°C.**

### *4.3.1.1 Response Factors and Quantitative Analysis*

A known amount of ethane was added to the sample stream of the reaction rig as an internal standard in order to quantify its constituent components. When a sample was analysed in the GC analysing rig the components were detected as respective peaks by a TCD and a FID detector. The areas of these peaks were not directly representative of their molar quantities because of the different detecting sensitivities of the components. They have to be quantitatively scaled relative to the internal standard, using a response factor. The easiest way of obtaining these response factors was to make up a binary sample of a known amount of both the internal standard and a component expected in the reaction sample and to analyse it. From the peak areas, the scaling factor (response factor) was derived and this could be used to calculate the true molar weights. The

response factors for the FID detector may also be calculated using group contribution functions and relative component sensitisations published by the detector manufacturers. These were used when it was difficult to make up a known composition binary sample when the component is al liquid for instance (it is almost impossible to make up an accurate gas liquid sample) or when the component was not available. Table 11 shows the FID and TCD response factors used in quantitative sample evaluations.

**Table 11: TCD and FID response factors**

| Component | TCD Response | FID Response | Method |
|---|---|---|---|
| | Area/ True Area | Area/ True Area | |
| | | | |
| $O_2$ | 0.703 | | Binary gas sample |
| CO | 0.74 | | Binary gas sample |
| $CO_2$ | 0.782 | | Binary gas sample |
| Methane | | 1 | Published |
| Ethane | 1 | 1 | Internal standard |
| Ethene | 1 | | Similar as ethane |
| Propene | 1.185 | 1.538 | Binary gas sample |
| Acrolein | | 0.45 | Similar to acetone |
| Acetaldeheid | | 0.5 | Methyl group |
| 1,3 Butadiene | | 1.2 | Similar to 1-butene |

A molecular sieve column was used to separate the light gasses, which were then detected using the TCD detector. Unfortunately, the $CO_2$ did not exit the column as a well-defined, spiked peak, but as a wave-like peak (flat and broad), on which tail the propene peaked. To add more complexity to the system, the $CO_2$ peak was observed at a time where there was a maximum in TCD baseline drift. All these factors made it impossible to obtain accurate $CO_2$ measurements. It was therefore, decided to obtain the amount of $CO_2$ using a carbon balance. An oxygen balance may also be done, but the amount of water formed, which is not detected by either TCD or FID, makes if difficult to do it accurately without making assumptions, especially if there is a product range with unknown products. As there were two detectors, two carbon balances could be done by using either the TCD or the FID feed as reference. The carbon balances were calculated as follows:

$$C-Balance^{(TCD/FID)} = \frac{\sum_i \left( \frac{A_i \cdot C_{noi} / RF_i}{A_{st}} \right)^{(TCD)} + \sum_j \left( \frac{A_j \cdot C_{noj} / RF_j}{A_{st}} \right)^{(FID)}}{\left( \frac{A_{C_3^=} \cdot Cno_{C_3^=} / RF_{C_3^=}}{A_{st}} \right)_{Feed}^{(TCD/FID)}} \quad ....28$$

With i = CO, $CO_2$ and ethene and j = ethane, propene, acrolein, acetaldehyde, 1,3 butadiene and other carbon-containing compounds.

$A_i$ : Peak area of component i

$C_{noi}$ : Carbon number of component i

$RF_i$ : Response factor of component i

$A_{st}$ : Peak area of the internal standard

The amount of $CO_2$ was calculated by calculating the $CO_2$ peak area that was needed to set the carbon balance equal to one. This calculation was done using the TCD and FID C-balance and the result should be similar. The accuracy of the analysis can be evaluated by comparing the $CO_2$ calculated from the two balances. Seeing that the FID detector is more accurate in quantitative measurements, the carbon balance using the FID-feed was used to determine the amount of $CO_2$ in the sample.

The selectivity was calculated as a carbon percentage of the product gas, and conversion as the fraction of propene that was converted to products. The FID areas were used in these calculations as the feed quantities.

$$C\% - Selectivety_i = \frac{\left( \frac{A_i \cdot Cno_i / RF_i}{A_{st}} \right) \cdot 100}{\left( \frac{A_{C_3^=} \cdot Cno_{C_3^=} / RF_{C_3^=}}{A_{st}} \right)_{Feed^{FID}}} \quad \text{....29}$$

Where i is any carbon containing compound.

$$Conversion = \frac{\left( \frac{A_{C_3^=} / RF_{C_3^=}}{A_{st}} \right)_{Feed} - \left( \frac{A_{C_3^=} / RF_{C_3^=}}{A_{st}} \right)}{\left( \frac{A_{C_3^=} / RF_{C_3^=}}{A_{st}} \right)_{Feed^{FID}}} \quad \text{....30}$$

The specific rate of acrolein formation was calculated as follows:

$$r_{sp\,i} = \frac{C_{Feed} \times C_i\%}{C_{no.i} \times 100} = \frac{WHSV \times C_i\%}{3600 \times C_{no.\,propeen} \times Mr_{propeen} \times A_{sp} \times C_{no.i} \times 100} \quad \text{....31}$$

$r_{sp\,i}$ : Specific rate of formation of product i [mol.m$^{-2}$.s$^{-1}$]

WHSV : Weight hourly space velocity [$g_{propene}$.$g_{catal}^{-1}$.hr$^{-1}$]

Mr : Molecular weight [g.mole$^{-1}$]

$A_{sp}$ : Specific area of catalyst [m$^2$.g$^{-1}$]

$C_{no.}$ : Carbon number [C/molecule]

$C_i\%$ : Carbon percentage of component i.

### 4.3.2 TEM

A TEM works much like a slide projector. A projector shines a beam of light through the slide and, as the light passes through it, it is affected by the structure and objects on the slide. The result is that only certain parts of the light beam are transmitted through a certain part of the slide. The transmitted beam is then projected onto a viewer screen for the viewer to see. The TEM works in the same way, except that it shines a beam of electrons through the specimen (sample). Whatever part is transmitted is projected onto a phosphor screen for the user to see [http://www.matter.org.uk/diffraction/x-ray].

### 4.3.3 XRD

The use of X-rays to measure the distances between atomic planes and the position of various atoms within a crystal makes this one of the most important techniques for analysing crystals. X-ray wavelengths can range from 0.02-100 Å; conventional XRD is, however, largely confined to the region of approximately 0.1Å to 25Å. Cu-$K_\alpha$, with a wavelength of $\lambda$ = 0.1542 nm, is frequently used as radiation source. The high energy wave penetrates the crystal, thus giving a bulk volume analysis. The interaction of electromagnetic radiation between the electric vector of X-radiation and the electrons of the matter through which it passes, results in scattering. When X-rays are scattered by the ordered environment in crystals, interference (both constructive and destructive) takes place among the scattered rays because the distances between the scattered centres are of the same order of magnitude as the wavelength of the radiation. The result is diffraction. The intensity of the reflected waves at different incidence angles is measured and recorded and compared to other samples or ASTM (American Society for Testing Materials) cards. The XRD spectrum then serves as a fingerprint of the specific crystal or the combination of crystal phases.

### 4.3.4 SEM

The Scanning Electron Microscope (SEM) is a tool to see into micro-space (100 nm–100 μm). Conventional light microscopes use a series of glass lenses to bend light

waves and create a magnified image. The SEM creates a magnified black and white image by using electrons instead of light waves, resulting in a highly detailed three-dimensional image at a much higher magnification than possible with light microscopes.

The sample is prepared by gold sputter coating it. It is placed in the microscope's vacuum column and scanned row by row by a high energy electron beam. When the electron beam hits a spot, secondary electrons are knocked loose from the surface and detected by a Backscatter or Cathodoluminesence detector, which feeds the signal to an amplifier. The final image is built up from the number of electrons emitted from each spot on the sample.

### 4.3.5 Malvern Zetasizer 1000HS

Photon Correlation Spectroscopy (PCS) is a means of measuring particles, typically in the submicron region, by relating Brownian motion (random movement of particles due to the bombardment by the solvent that surrounds them) to the size of a particle.

The hydrodynamic diameter (d(H), a number that refers to how a particle moves within a liquid) is determined as a function of the Boltzmann constant (*k*), Temperature (T), viscosity ($\eta$) and translational diffusion coefficient (D, Brownian velocity parameter: larger particles move more slowly).

$$d(H) = \frac{kT}{3\pi\eta D} \qquad \text{....32}$$

When light interacts with the particles, it causes light scattering. Particles with diameters less than 60 nm cause isotropic (equal in all directions) scattering. The intensity of the scattered light is proportional to the particle diameter to the power of six. It should be noted that large particles in the sample might overshadow the smaller ones, making it difficult for PCS to analyse samples with large particle size distributions.

The translational diffusion is determined by comparing the measured scattering with a lag time-added scattering. In essence, the change in scattering is measured for different

lag times ($\tau$). At small lag times, the scattering induced by the particles does not change much, thus the correlation between the measured and lag-time-added-measured reading is good. Due to the fact that smaller particles move faster and more easily than large particles, the correlation for a sample containing small particles decreases rapidly with an increase in delay time in comparison to a sample containing larger particles. This is shown in Figure 38. The translational diffusion coefficient is obtained using the following equation [Malvern PCS system training manual]:

$$g_1(\tau) = \sum_i^n c_i \exp\left(-D_i.q^2.\tau\right) \qquad \text{....33}$$

$g_1$ : Correlation function
$c_i$ : Intensity weight of particles
$\tau$ : Correlation time delay
D : Translation diffusion coefficient
Q : $(4\pi m_1/\lambda_o)\ \sin\theta/2$
$m_1$ :R index
$\lambda_o$ : Wavelength of laser
$\theta$ : Scattering angle

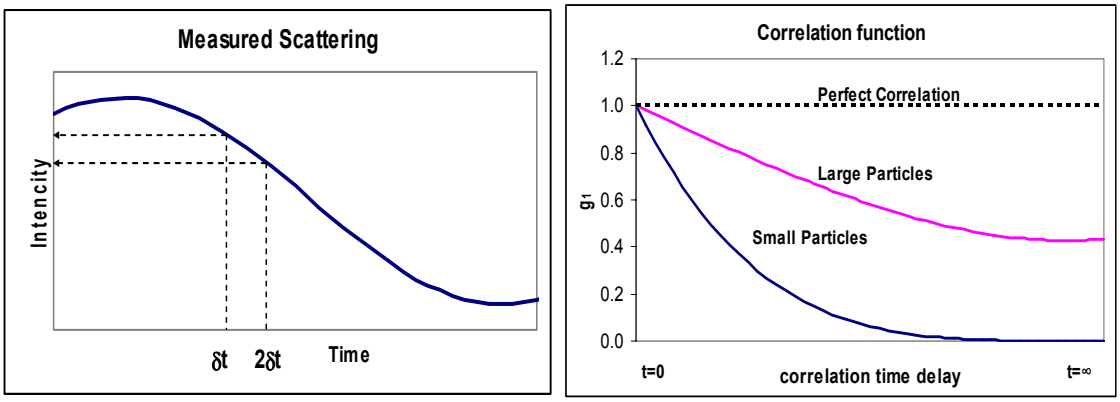


**Figure 38: (a) Graph illustrating the concept of correlation by adding a time delay; (b) typical correlation functions for large and small particles as a function of delay time ($\tau$).**

# 5. Results and Discussion

## *5.1 Catalyst Synthesis*

It was necessary to synthesise the required catalyst before kinetic studies could be done. This was not a trivial exercise as the procedure had not been done with all the required aspects. The nature of the experiments is of such that they contain a lot of detail and cover a wide range of aspects. For the sake of brevity, the detailed preliminary experiments (experimental procedures, results, detailed discussions and conclusions of individual experiments) are listed in Appendix A and the results will only be summarised in the following sections. For detailed information the reader is referred to the appropriate appendices.

The first section will summarise the attempts to prepare catalyst using the preliminary reverse micelle technique (RMT) previously used in our laboratory. This was done with the aim to accumulate knowledge about the RMT to ultimately put forward a method to synthesize the required catalyst. The complete procedure is given in Appendix A. In the subsequent section the attempts to synthesize pure 2/3 (Bi/Mo) precipitate using a simple precipitation method and calcination experiments using pure 2/3 precipitate is discussed. This was investigated with the aim to integrate the results with the RMT. The relevant experiments are detailed in Appendix B. The investigation of the stability and formation of reverse micelles using Photon Correlation Spectroscopy (PCS) are lastly discussed. The relevant experiments are listed in Appendix C.

Experimental results reveal new findings and problems which open up new options and directed the methods for catalyst preparation to ultimately obtain the catalyst needed for the kinetic studies.

## *5.2 Preliminary Reverse Micelle Technique (RMT)*

A variety of experiments were done to investigate the RMT. In order to convey the results structurally the technique will be broken down and discussed in its constituent steps and problems encountered namely:

- **Aqueous Salt Solutions and Reverse Micelle Stability**
- **Mixing Bismuth and Molybdate Emulsions and Stirring**
- **Aging and Heating of Emulsion Mixtures**
- **Washing, Supporting and Calcination**

Figure 39 shows a schematic of the RMT and its constituent steps. The complex inorganic chemistry and numerous sequential steps add to the difficulty of identifying causality and controlling parameters.

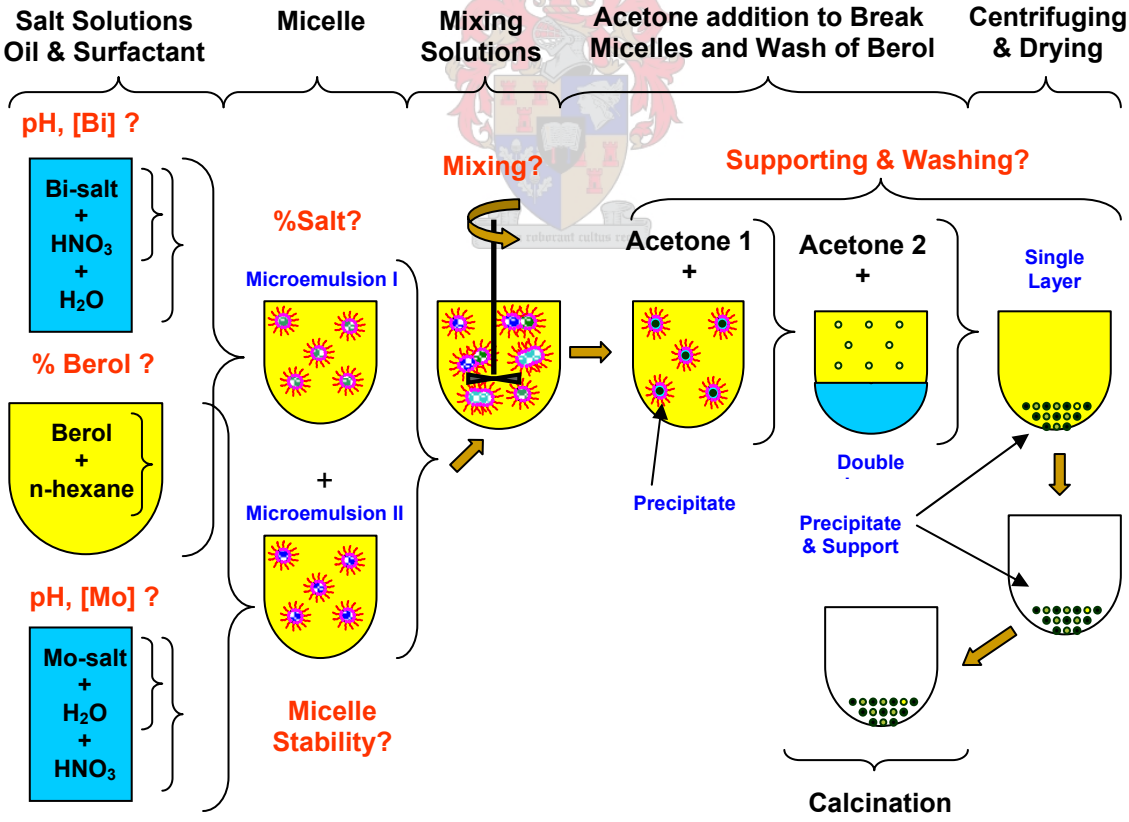


**Figure 39: The preliminary reveres micelle technique (RMT) used to obtain catalyst particles for use in kinetic studies.**

### 5.2.1 Summary of the RMT

**Salt Solutions**

Two salts namely $Bi(NO_3)_3 \cdot 5H_2O$ and $H_{24}Mo_7N_6O_{24} \cdot 4H_2O$ were used to make up stable aqueous solutions (salt solutions should be transparent and free from precipitate). The bismuth salt was dissolved by adding a predetermined amount of $HNO_3$ and slowly adding distilled or demineralised water while stirring vigorously. If the salinity was too high and/or the pH too low, salt crystals were formed. Molybdenum salt was firstly dissolved in water and $HNO_3$ may be added slowly to modify the pH while stirring vigorously. The reaction to form molybdate polyanion species is slow and a function of the pH and salinity [Cruywagen *et al.,* 2002]. A specific polyanion species namely $Mo_{18}O_{56}(H2O)_8^{4-}$ or its double, $Mo_{36}O_{112}(H_2O)_{16}^{8-}$ is responsible for the formation of 2/3 precipitate.

**Oil & Surfactant**

n-Hexane and Berol were weighed and mixed to the predetermined composition (usually 10-25 wt % berol). A white bushy precipitate formed which sank to the bottom of the container and only the clear top liquid was used in further experiments.

**Emulsion Formation (Micelle Mixture)**

A small amount (2-15 wt %) of bismuth and molybdenum solutions were added respectively to an oil-surfactant mixture. The resulting mixture needed to contain stable reverse micelles and a double layer (aqueous and oil-surfactant) had to be avoided. The micelle mixture could be stirred or placed in an ultrasonic bath to stabilise and form reverse micelles. The age and temperature of the mixtures could be varied.

**Mixing of Micelle Mixtures**

The bismuth containing emulsion was usually slowly added to the molybdenum emulsion. The resulting emulsion mixture changed from clear to light-yellow (when molybdenum was in excess) and sequentially to white (when bismuth was in excess). This was a result of particle formation within the reverse micelles due to salt exchange. If the catalyst loading ($mol_{catal.}$/ volume liquid) was high a green-yellowish precipitate formed immediately. The addition rate and sequence (Bi in Mo or *vice versa*), temperature, stirrer speed, duration of stirring and Bi/Mo ratio could be varied in this step.

**Washing and Supporting**

After stirring the emulsion mixtures acetone was added to the mixture. This caused the breaking of the reverse micelles resulting in the liberation of the particles. With a small addition of acetone the emulsion mixture was stable. With further addition a double layer was formed. The top layer (oil and acetone) contains all the catalyst particles (which were hydrophobic due to adsorbed surfactant) while the bottom layer contains water (±50%), berol and some acetone. With further addition of acetone the bottom layer steadily re-dissolved (one phase system) and the character of the suspended catalyst particles changed from a finely dispersed (slow settling) precipitate to a agglomerated fast settling catalyst balls which later broke up to form a fine powdery precipitate. The precipitate may be centrifuged at any of the above acetone addition stages and the liquid removed. The precipitate was usually washed for a second time using acetone.

The particles may be supported onto larger inert particles to prevent sintering of the small particles in the calcination step. The supporting particles may be added to the emulsion mixture at any stage of the acetone addition, after the wash or after drying the catalyst particles.

**Calcination**

The resulting catalyst particles or supported particles are calcined stepwise to obtain the required crystal structure. The following is the calcination program previously used.

- 25$^{o}$C – 120$^{o}$C in 3 hrs
- 120$^{o}$C – 200$^{o}$C in 2 hrs
- 200$^{o}$C – 450$^{o}$C in 4 hrs
- 450$^{o}$C for 12 hrs

## 5.2.2 Aqueous Salt Solutions and Reverse Micelle Stability

### *5.2.2.1 Pure Salt Crystallisation*

Both bismuth and molybdate salt solutions should be stable when they are introduced into the oil and surfactant mixture to avoid the crystallisation of bismuth or molybdate crystals within the micelles. The crystallisation of pure salts has happened in Experiment A1 for bismuth and in Experiment A3 for molybdenum. Bismuth forms uniform well defined sharp egged crystals while molybdenum crystallisation causes thin plate like crystals or shavings to form. The bismuth crystals (Fig. 78B) were formed as a result of a high salinity ([Bi] = 1.03 M & 12% $HNO_3$) and the molybdenum crystals (Fig. 89A&C) as result of a low Bi/Mo ratios (<0.3) causing an excess of molybdenum which crystallized out when the catalyst was dried.

The salt solution stability will be discussed in more detail in a later section when a simple precipitation method is discussed.

### *5.2.2.2 Emulsion Stability*

It was evident from the Experiment A1 that it was necessary to find the region in which the reverse micelles are stable. A ternary diagram was therefore generated by adding distilled water stepwise to a range of oil-surfactant mixtures. The detail of the procedure used to generate the ternary diagram is described in Experiment A2 and the effects of salinity and aging was investigated in Experiment A3. It was necessary to shake the mixture formed by adding water, in order to obtain stable micelles. At a later stage (Exp. A3) it was found that vigorously stirring using a magnetic stirrer or using a sonic bath decreased the time to attain stable micelle mixtures dramatically. Due to the manual shaking technique (not very effective and tedious technique) the ternary diagram may be slightly inaccurate but it was sufficient at this stage of the project.

**Surfactant-Oil Mixing**

When the surfactant and the oil were mixed (Exp. A3) a critical amount of surfactant was needed (16 mass%) to prevent a white bushy precipitate from forming. Below 16% and

above 9.1% the precipitate formation was slow (10 min until completion) and below 9.1% it was much faster resulting in an immediately milky mixture. This bushy precipitate sunk to the bottom (within an hour) resulting in a clear solution above it. The solution could be filtrated to get rid of the precipitate but due to the high vaporisation of n-hexane it was preferred to carefully remove the top clear liquid without mixing the precipitate. Attempts were made to isolate the precipitate but it broke down and dissolved when it came in contact with small amounts of water. When a few drops (±3 drops) of water was added to 50 ml oil-surfactant solution in which the precipitate was present, the bushy precipitate broke down forming a small amount of white powder that settled to the bottom which was to little to filter or analyse. The origin of the precipitate was probably impurities in the surfactant.

**Water-Oil-Surfactant Mixing**

Figure 40 summarises the observations as the water was added to the range of oil-surfactant mixtures. The mixture (initial wt % above 5%) starts clear (oil-surfactant mixture) and turns hazy after a small amount (±0.2 wt %) of water was added. This first hazy region shifts to slightly higher water concentrations with the increase in surfactant concentration. The haziness disappeared with further addition of water and again the point at which this happened shifted to higher water concentrations with increase in surfactant concentrations. The mixture was then crystal clear until a second cloudy region was reached. With further addition of water the mixture then turned white quickly. At initial surfactant concentrations below 5 wt % the mixtures stayed white or become a gel like emulsion with a higher viscosity. The point at which the mixture becomes a gel was indicated by the PL point in Figure 40.

The reason for the first hazy region and how the reverse micelles were influenced was unclear. The region was also present for bismuth solutions but not for molybdenum. In Experiments A1 and A3 the particle yield obtained from micro emulsions containing small amounts of aqueous phase (within the first hazy region in the ternary diagram) included larger quantities crystals and nanorods.

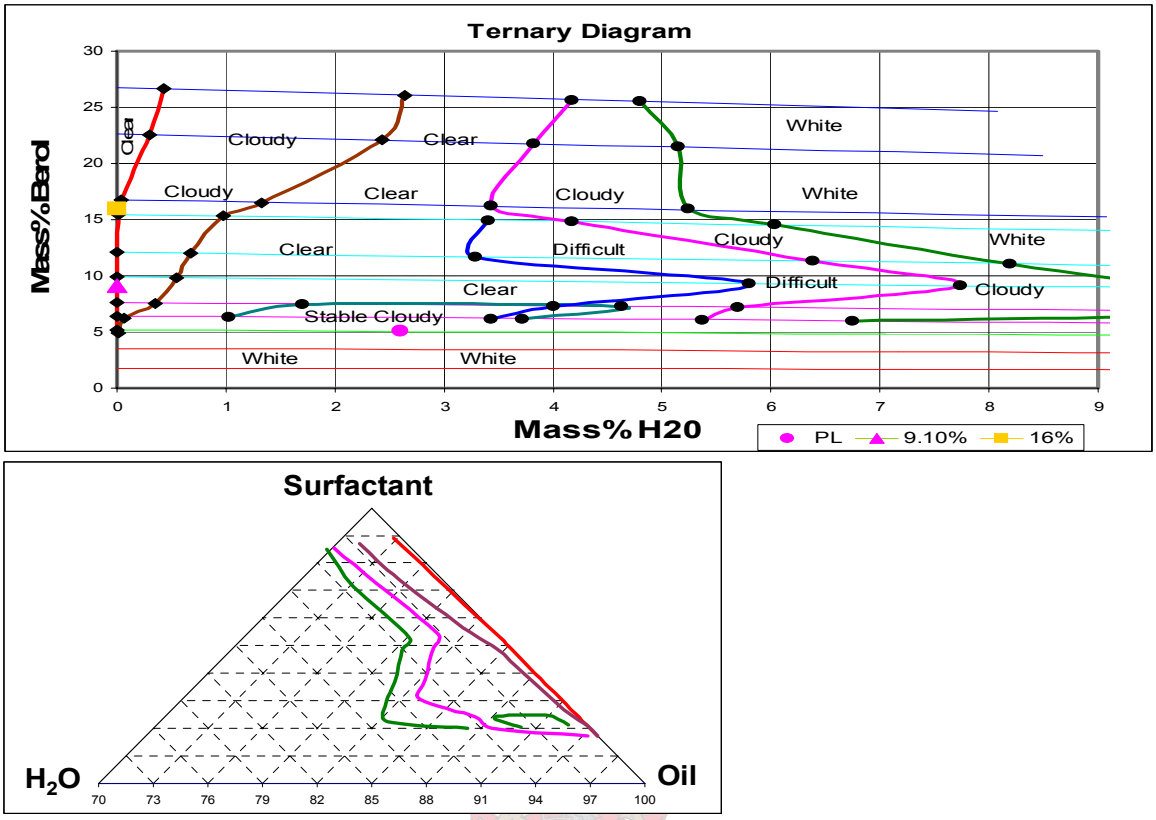


**Figure 40: The different regions observed in the water-oil-surfactant ternary diagram. Clear, Solution is clear; Cloudy, Solution is cloudy; Difficult, not easily dissolved; Stable Cloudy, The slight cloudiness does not change with addition of water; PL, point at which solutions are gel like, 9.1% berol-hexane critical point, 16% berol-hexane critical point.**

### Salt Solution-Oil-Surfactant Mixing

The effects of reverse micelle mixtures were investigated in Experiment A2 and A4 by changing salts (bismuth and molybdate), their salinity and pH as well as aging the oil-surfactant mixture. It was found that bismuth salt solutions increased the stability of the reverse micelles. The amount of aqueous bismuth solution that may be added increases with an increase in salinity. Molybdenum on the other hand destabilises the reverse micelles and less of its aqueous salt is “dissolved” in the oil-surfactant mixture before the mixture became cloudy and unstable. Both salts solutions approach the result obtained for water with decreas in salinity which is expected.

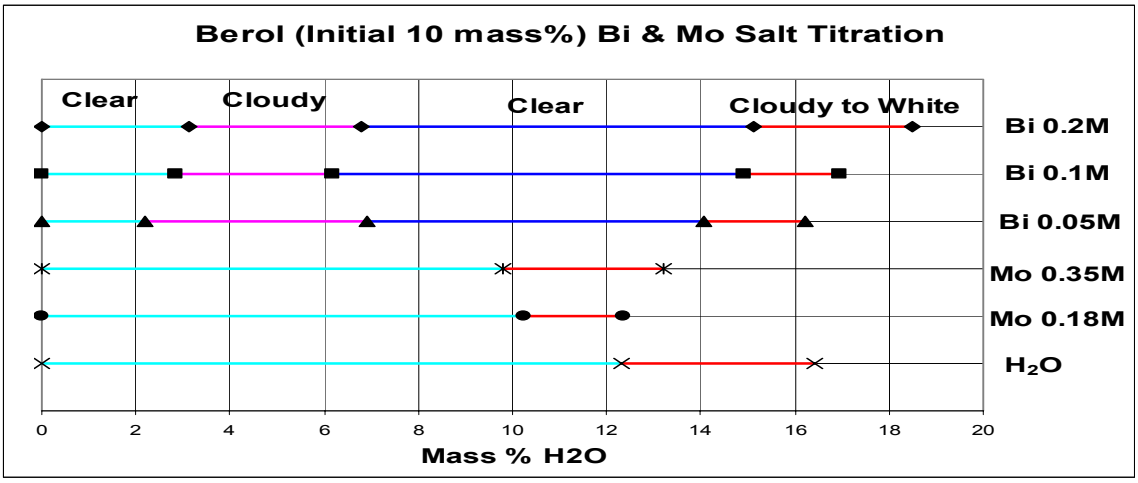


**Figure 41: Bi salt solution (pH = 1.5), Mo salt solution (pH = 4.0) and water titrations in 10% berol mixture.**

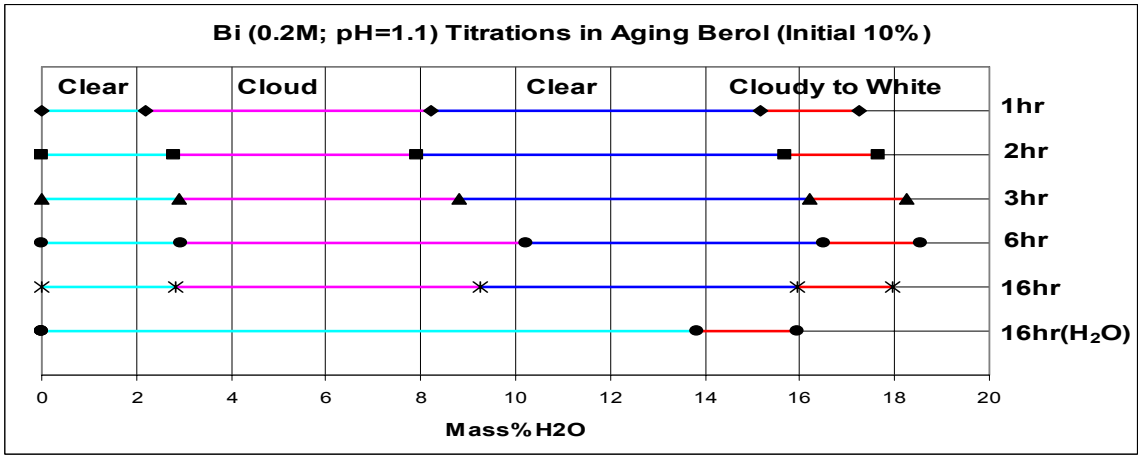


**Figure 42: The effect of aging on a 10% berol-hexane mixture. Titrations were done with 0.2 M bismuth salt solution (pH of 1.1). A water titration is included at 16 hrs.**

Figure 42 shows the effect of aging of the oil-surfactant mixture on the reverse micelle stability. No significant differences were observed. The small changes were due to changes in temperature of the mixture and light intensity which influence the observations.

In Experiment A4 acetone was added to the bismuth and molybdenum solutions to see whether it influenced the resulting particle sizes in the RMT by changing the solubility of the salts in the aqueous phase. It was found that more aqueous-acetone mixture is “dissolved” in the oil-surfactant mixture compared to normal salt solutions, which is

explained by the acetone diffusion from the aqueous phase to the oil. This acetone addition to the system caused the instability and breakdown of the reverse micelles. Similarly methanol and ethanol also destabilised the reverse micelles. The effect of the addition of other solutions thus may destabilise the reverse micelle formation.

### 5.2.3 Mixing Bismuth and Molybdenum Emulsion and Stirring

The effect of emulsion mixing parameters and stirring in the RMT was investigated by studying the TEM pictures taken of the catalyst particles. Because of the difficulty to identify causality due to the numerous unknown influencing parameter this is not a very effective way to study the system but some important findings were made.

In all the experiments bismuth emulsions were added to molybdenum micelle emulsions. The reason for this stems from the co-precipitation method used by Keulks. The bismuth solution is added to molybdenum solution in order to insure a high molybdenum concentration and sufficient time for the slow formation of the required molybdenum polyanion.

It was noted in Experiments A1, A3 and A4-A7 that the nano sized particles tended to stick to each other. Various possible causes have been investigated in attempts to stop the agglomeration and formation of three dimensional structures. In some experiments (Exp. A3) totally liberated particles were formed but the reason for their formation is to a large extent still unclear (the specific run had a high aqueous content, low surfactant content and was washed with a high fraction of acetone). This section will only discuss the mixing parameters namely Bi/Mo ratios, catalyst loading and micelle collision mechanisms due to stirring.

### *5.2.3.1 Bi/Mo Ratio*

Table 12 sums the liberation status of the catalyst particles obtained by the RMT as a result of varying Bi/Mo ratios. It should be noted that other parameters may directly or indirectly influence the degree of particle agglomeration but they are not known at this stage. It is interesting to note that the degree of liberation increases with deviation from the ideal 2/3 Bi/Mo ratio. This might be due to the difference in core and shell compositions of the particles. The particles form in a nucleation step followed by a particle growth step which implies that the particle shell composition was a result of the aqueous composition at the final mixing stages. The particles with their cores now rich in one component might not stick to each other as well as the uniform 2/3 ratio particles.

**Table 12: Catalyst particle liberation status summary as a result of Bi/Mo ratios.**

| Exp. | Bi/Mo | Liberation |
|---|---|---|
| | | |
| | | |
| A1 | 0.66 | Aggregated Heaps |
| A3 | 0.14 | Well liberated when washed thoroughly with acetone |
| | 0.29 | Well liberated when washed thoroughly with acetone |
| 1.5 | 0.66 | Three dimensional structures |
| | 0.5 | More liberated three dimensional structures |
| 1.6 | 0.25 | Moderate degree of liberation |
| | 1 | Small degree of liberation |
| 1.7 | 0.5 | Moderate degree of liberation |

### *5.2.3.2 Catalyst loading*

The catalyst loadings were varied in Experiment A6 by varying the salinity of both bismuth and molybdenum solutions but keeping a constant ternary composition (constant aqueous/oil/surfactant ratio) and maximum aqueous loading (the maximum aqueous loading for bismuth salt solution was taken as double that of molybdenum solution). No significant changes were observed with respect to the degree of agglomeration of the catalyst particles.

### *5.2.3.3 Collision Mechanism*

In Experiment A6 interesting results were obtained when the theoretical sizes of the micelle droplets for the bismuth emulsion and the molybdenum emulsion were different. One of the salts solutions was added to the surfactant until it has reached its maximum holding capacity (just before it became milky and unstable) while the other only contained half of its maximum capacity. This theoretically meant that the salt at its maximum holding capacity had large swollen micelles and the other salt had smaller micelles. When emulsions containing two salts are added together collisions between salt micelles during stirring caused the exchange of salts resulting a reaction and particle formation within the micelle. In this specific experiment two definite particle sizes were obtained, say large and small. This would only be possible if the interaction (salt exchange) between the two salt micelles were slow. This might be one of the reasons for the catalyst particles sticking. If the salt exchange was extremely slow it could be that the some unreacted salts were present inside the micelles. When the micelles are broken with the addition of acetone the unreacted salts were also liberated and when further mixing occurs these salts react to form catalyst by a mechanism other than that of the RMT. The result was that samples containing distinct, recognisable particles were mixed in a slush of catalyst. Figure 43 show the two distinct particle sizes and the particles mixed with slush respectively.

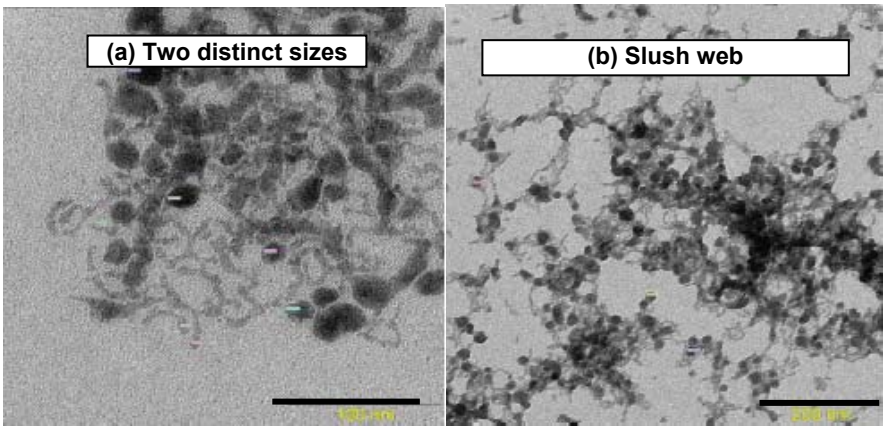


**Figure 43: (a) Two distinct particle sizes and (b) particles mixed with slush**

Figure 44 (a) show the formation of two distinct particle sizes due to interaction between two salt micelles of different sizes and the formation of slush (Fig 44 b) due to the

liberation of unreacted salt solution which causes the formation of catalyst via a mechanism other than the RMT.

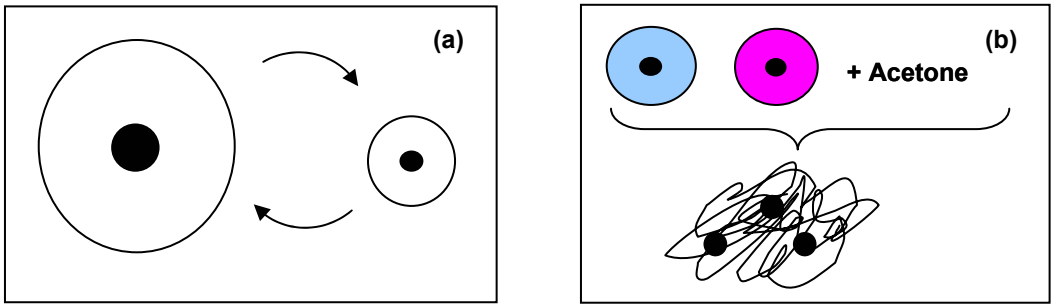


**Figure 44: Schematics for (a) particle size difference and, (b) slime formation.**

On a macroscopic scale it was observed that the catalyst particles take longer to settle after the acetone liberation (acetone wash) for samples which were stirred for a longer period of time (30 min instead of 15 min). This indicates that less unreacted bismuth and molybdenum solution was present at the liberation step which could cause agglomeration. One disadvantage of working with hexane (oil) is that it has a low boiling point (69°C) resulting in a high evaporation rate and thus a substantial loss of oil while stirring for an extended period. This causes a significant change in the ternary composition which will also influence the particle sizes.



### 5.2.4 Aging and heating of Emulsion Mixtures

One of the most interesting results obtained by the RMT was that of nano-rod formation. The nano-rods were not a direct result of the RMT but a secondary mechanism which seem to be initiated by the presence of the surfactant and were promoted by the small sized particles. The parameters and conditions leading the formation of nano-rods are not entirely known but aging and heating in the presence of surfactant plays an important role.

#### *5.2.4.1 Aging Reverse Micelle Mixtures*

In Experiment A5 nano particles were prepared using 10 and 20 wt% berol. The particles were liberate by washing with acetone and studied under the TEM. Both the 10 and 20

wt% (berol wt%) samples yielded 6 nm particles which were entangled in a three dimensional structure (see Figure 45). After aging the unwashed (still in its micelle mixture) mixture for three days at ambient temperatures a small amount of white precipitate formed on the bottom of the vile. The top clear liquid as well as the bottom precipitate were sampled and inspected using the TEM photos. Aging the samples resulted in the formation of nano-rods with width between 50-150 nm and length more than 100 times the width. The sample initially containing 20 wt% berol was almost totally reduced to nanorods with only small amounts (less than 5%) of original particles left. Liberated nanorods were found in the top clear liquid mixture and agglomerated nanorod were found when the settled precipitate was examined.

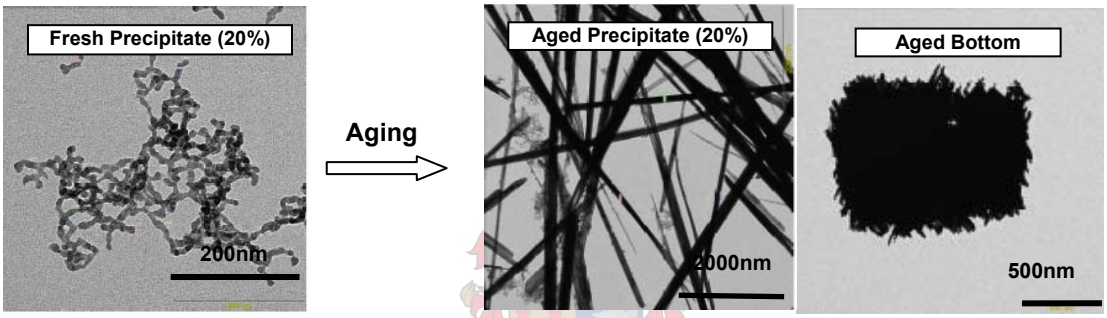


**Figure 45: Aging of reverse micelle mixture resulting in the formation of nanorods.**

### *5.2.4.2 Heating and Drying of Reverse Micelle Mixtures*

In an attempt to prevent the catalyst particles from sintering in the calcination step the surfactant was not removed in some samples in Experiment A3. This was done by not washing it with acetone. The micelle mixture was simply heated to evaporate the oil. The evaporation of the low boiling hexane caused the catalyst to be wetted by high boiling surfactant. At temperatures between 100 and 150°C the catalyst particles were transformed into nano-rods. The asbestos like structures obtained at 120°C correlate well with the mechanism proposed by Ghule *et al.* [2004]. Ghule *et al.* suggested that the polar molecules (in his experiments pyridine and in this case the surfactant used) adsorb to the surface of the nanoparticles and caused inter lamellar sticking of the particles (see Fig. 14, p2-36) which in turn led to the formation of these asbestos like structures resulting in nanorod formation.

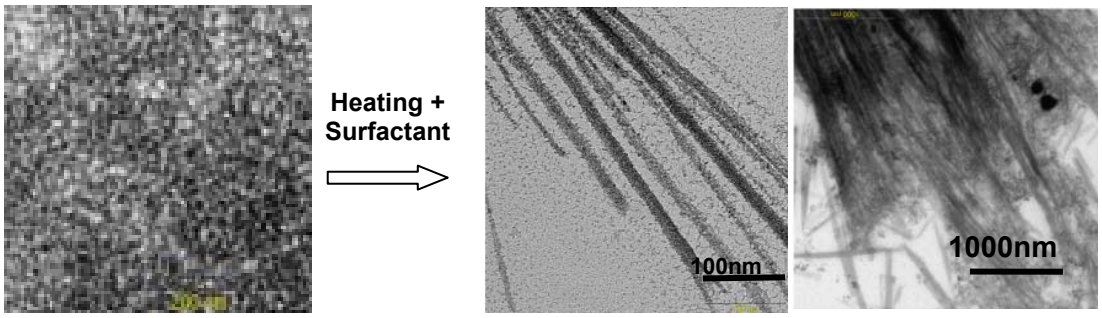


**Figure 46: Nano-rod formation when hexane is evaporated from the micelle mixture**

The lamellar interaction (Velcro effect) between the adsorbed surfactant on the surface of the catalyst particles could also be a reason for particles sticking. Thus, care must be taken to thoroughly remove as much adsorbed surfactant as possible to avoid particles from sticking. The wash step was then investigated.

## 5.2.5 Washing, Supporting and Calcination:

### *5.2.5.1 Washing*

The acetone wash step was investigated in Experiments A3, A5 and A6. In Experiment A3 the catalyst particles were washed using 20 and 60 volume % acetone. In the cases where 60% were used, the particles were well liberated suggesting that the acetone removed adsorbed surfactant which cause sticking by a Velcro like effect. Contradicting results were obtained in Experiment A5 where a range of acetone volume percentage washes were done. This experiment suggested that using less acetone caused better liberation. It could be that other factors like unreacted liberated salts caused the sticking. A temperature range acetone wash was done in Experiment A6 which showed that by using heated acetone (30-40°C) the degree of liberation increased slightly. An interesting result was observed when a high temperature acetone wash was done. This caused the particles to stick to the inside of the glass vile. This and other factors were then investigated to find out whether it is possible to support the catalyst particles.

### *5.2.5.2 Supporting*

Attempts to support the catalyst particles were made in Experiments A1, A3 and A8. In Experiment A1 the catalyst particles were wet (washed particles wetted by acetone) and dry (washed and dried) mixed with tiny silica particles (10 nm) and calcined. Due to the similar size, and interaction with the TEM electron beam, the catalyst and support particles could not be distinguished. This made it difficult to evaluate whether the catalyst particles were successfully supported. In the case of the dry mixed sample, the catalyst particles sintered into larger structures which did not happen in the wet mixed sample. If the TEM beam intensity was increased to a maximum it caused the sintering of uncalcined catalyst particles. Thus, in Experiment A3 the beam intensity was increased to a maximum while looking at a wet mixed uncalcined sample. The catalyst particles were identified as those particles that move as a result of melting and sintering. In the case of the wet mixed samples the particle distribution did not change, suggesting that the catalyst particles were well spaced by the silica particles thus, preventing the particles from sintering into larger structures.

Different methods and approaches were made in the attempt to support the catalyst particles. The support was added at different stages (before and after the acetone wash), at different acetone additions (different volume % acetone added or unwashed) and at different temperatures (the temperatures of the micelle mixture and the acetone were varied) with no success.

Silicon-carbide particles were also used in an attempt to support the catalyst particles (Exp. A3) but it was unsuccessful.

### *5.2.5.3 Calcination*

In the calcination step particles tend to agglomerate due to sintering effects. It was noted in Experiments A3 and 8A that by mechanicly mixing the catalyst particles with silica particles, which were smaller than the catalyst particles, the silica particles space the catalyst particles preventing sintering. By decreasing the amount of small silica particles added to the catalyst particles the degree of sintering is increased in the calcination step

resulting in the formation of larger catalyst sausage like structures. In essence this might be used to obtain size control of the catalyst particles starting from similar sized particles in the calcination step. The disadvantage is that the particles are usually not spherical.

Further calcination experiments were done using pure 2/3 (Bi/Mo) precipitate and will be discussed later.

## *5.3 Low Temperature Calcination*

### 5.3.1 Keulks Co-Precipitation Reaction (Exp. B1)

Pure catalyst was needed for test runs of the reaction rig, temperature range calcination studies and for large crystal preparation. Pure α-$Bi_2Mo_3O_{12}$ was prepared according to the method proposed by Keulks and Daniel [1974] and a similar method with a slightly lower pH.

A pale yellow powder (±30 g) was obtained from the co-precipitations which turned slightly darker after calcination. The precipitate, mother liquor and the calcined product of the second (pH = 1.2) batch was more yellow than that of the first (pH = 1.5) suggesting β-phase (bright yellow) was percent.

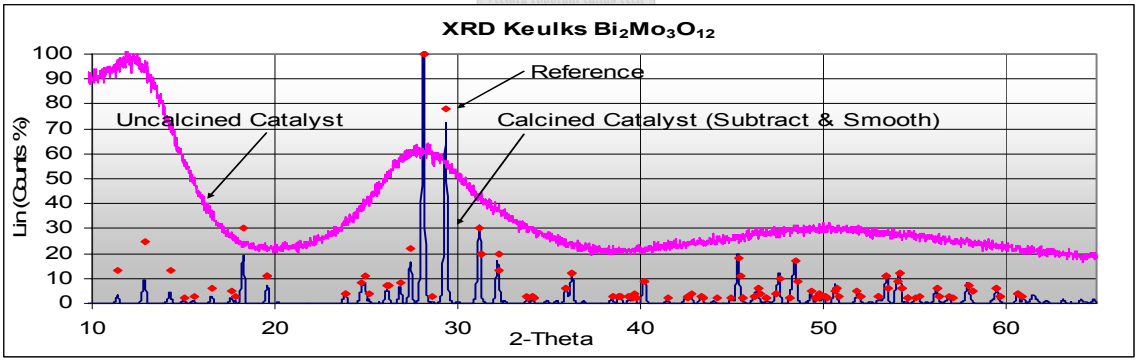


**Figure 47: Calcined (subtracted & smooth) and uncalcined Keulks catalyst (pH = 1.5) compared with a computed reference [Theoblad and Laarif, 1985].**

The XRD analysis for the uncalcined catalyst showed typical amorphous characteristics as expected. No specific peeks were found, only base drift. The calcined catalyst on the other hand showed well defined powder diffraction. The spectrum of the first sample (pH of 1.5) compared extremely well with the reference for α-$Bi_2Mo_3O_{12}$ [Theoblad and Laarif,

1985]. Possible β-$Bi_2Mo_2O_9$ [Chen and Sleight, 1986] impurities were not found, not even in trace amounts. There were no unaccounted peaks in either the sample or reference. Although the specific attenuation in especially the lower range of the XRD diffraction is 10% of, the relative attenuation is fairly accurate. The reference was also shifted to the left by 0.2 units and had to be aligned with the sample. The small difference between the sample and reference is due to non-ideal powder condition and calibration offset. The spectrum obtained for the second sample on the other hand showed some traces of β-$Bi_2Mo_2O_9$.

Figure 48 shows the XRD references for the $MoO_3$, α- and β-phase and indicates the major peaks by which the $MoO_3$ and β-phase can be identified. Figure 49 shows the XRD analysis for the second Keulks precipitation (pH of 1.2) which confirms the presence of β-phase impurities indicated by arrows.

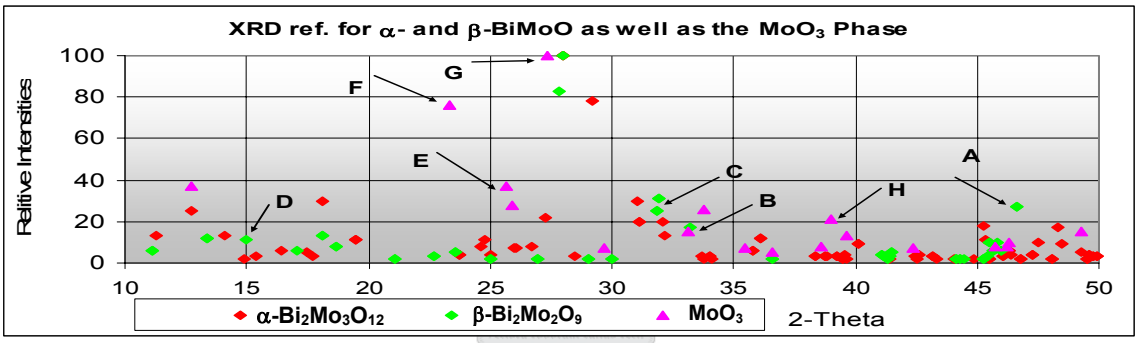


**Figure 48: Calculated XRD reference spectra for α-$Bi_2Mo_3O_{12}$ [Theoblad Laarif, 1985], β-$Bi_2Mo_2O_9$ [Chen and Sleight, 1986] and $MoO_3$ [Kihlborg, 1963]. The arrows show the prominent peaks (A-D)by which β-$Bi_2Mo_2O_9$ and $MoO_3$ (E-H) are distinguished from α-$Bi_2Mo_3O_{12}$.**

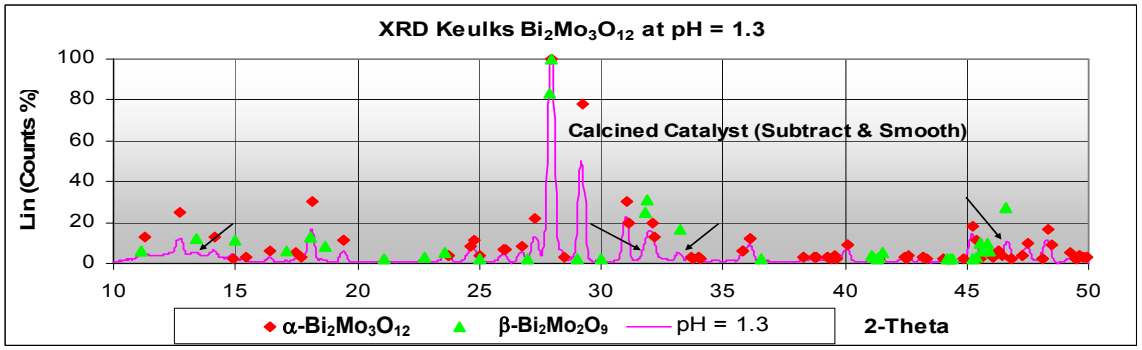


**Figure 49: Calcined (subtracted & smooth) and uncalcined Keulks catalyst (pH =1.2) compared with a computed reference for α-$Bi_2Mo_3O_{12}$ [Theoblad and Laarif, 1985] and β-$Bi_2Mo_2O_9$ [Chen and Sleight, 1986]. The arrows show some traces of β-$Bi_2Mo_2O_9$.**

A well defined sharp peaked XRD diffraction was thus obtained for the calcined sample while an expected total amorphous result was found for the uncalcined samples. The Keulks method proved to be an excellent way to obtain pure α-$Bi_2Mo_3O_{12}$. Small amounts of β-$Bi_2Mo_2O_9$ impurities are observed if the pH decreases to values below 1.2.

### 5.3.2 Temperature Range Calcination (Exp. B2)

Samples of Keulks's α-$Bi_2Mo_3O_{12}$ which were prepared in Experiment B1 were calcined at temperatures between 180°C and 300°C to deterine if a lower temperature calcination is possible. This might be helpful in preventing small catalyst particles from sintering at a later stage. The same sample were also analysed using simultaneous TGA and DC.

The samples which were calcined at high temperatures (250°C, 270°C and 450°C) decreased in volume in the calcination process. The XRD results are summarised in Figure 50.

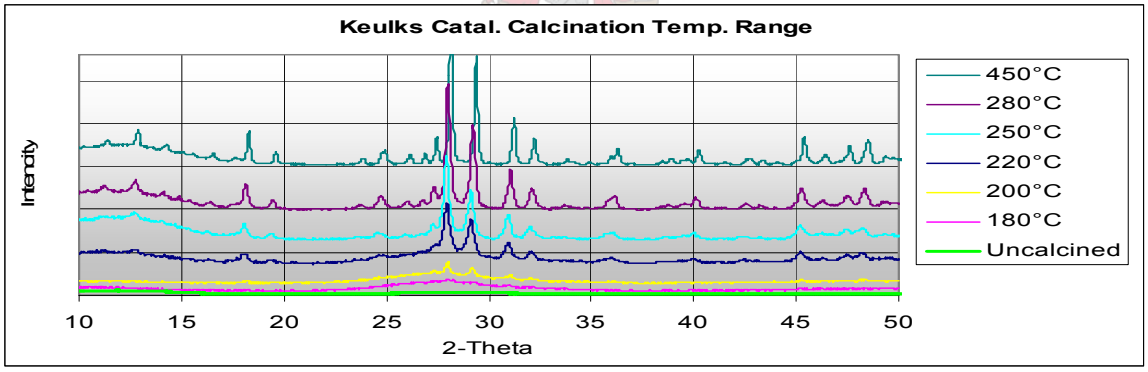


**Figure 50: Temperature range calcination of pure 2/3 (Bi/Mo). Calcination above 250°C result in a well defined XRD diffraction.**

Little or no calcination effects were observed at temperatures below 200°C. The degree of crystalasion increased as 280°C was approached from 200°C. At 280°C the XRD patern was similar to that of a samplel being calcined at 450°C. Thus, a 24 hr calcination period at 300°C to calcined the pure 2/3 catalyst precipitate to α-$Bi_2Mo_3O_{12}$ seems sufficient. These results compare well with the results published by Trifiro *et al.* [1972], but XRD can be misleading for it can only show the presence of the alpha phase and not

total calcination. Therefore the samples (calcined and uncalcined catalyst)) were analysed using TGA and simultaneous TGA and DSC.

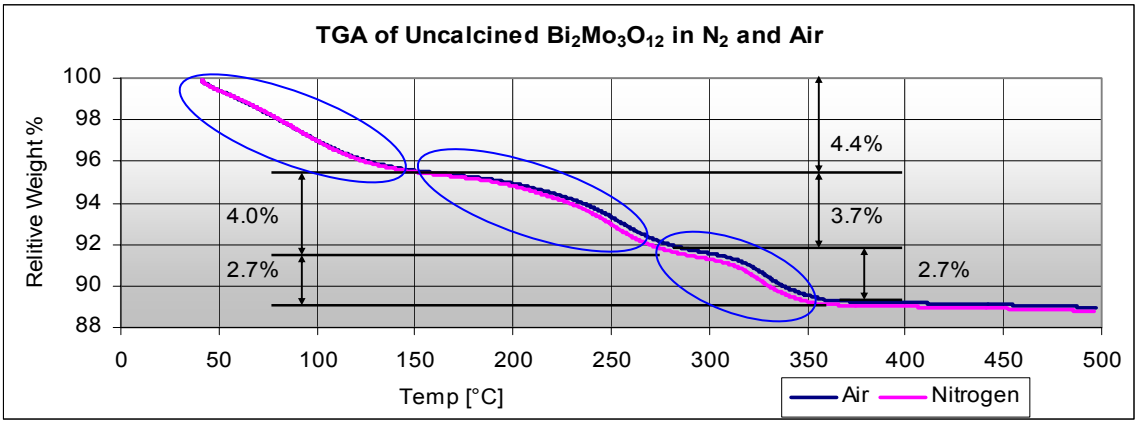


**Figure 51: TGA analysis of calcined 2/3 precipitate in a nitrogen and air atmosphere.**

Figure 51 shows a Perkins Elmer TGA analysis of uncalcined catalyst in nitrogen and air atmospheres. The TGA shows a three step mass decreas in the temperature range of 30-130°C, 150-270°C and 280-370 °C. The weight loss was most probably due to the loss of different bonded waters. The first being surface adsorbed water the second lightly bonded water and the last stronger bonded water. This corresponds well with the proposal of Keulks *et al*. (1974) that a spesific polyanion specie is responcible for the formation of 2/3 precipitate in the co-precipitation reaction. From the work done by Crywagen et al. [2002] discussed in section 2.2.1.1 and 2.2.1.4 It was postulated that the $[Mo_{18}O_{56}(H_2O)_8]^{4-}$ spiecie is responsible for the formation of $Bi_2Mo_3O_{12}$. This spiesie and its double ($[Mo_{36}O_{112}(H_2O)_{16}]^{8-}$), are the only spiesies that contain a extra water, thus resulting in a three step mass decreas (including adsorbed water).

$$12BiO^{+} + Mo_{18}O_{56}(H_2O)_8^{4-} + 8OH^{-} \rightarrow 6(Bi_2Mo_3O_{12}) \cdot (H_2O)_8 + 8H_2O \qquad \text{....15}$$

The precipitate contains two types of water both, contributing 2.54% to the weight of the uncalcined precipitate on a dry basis (no surface adsorbed water, $Mr_{precipitate}$ = 945.86g/mol). On a dry basis the weight loss in the heating process were 4.60%, 4.18% and 2.62%, and 4.60%, 3.97% and 2.62% for the three weight loss steps in a nitrogen and air atmosphere, respectively. The last step corresponded well with the loss in the strongly bonded water. The 1.0% higher weight loss (Fig. 51) of the second step may be

due to a weight loss contribution from the first step which was attributed to desorption of adsorbed surface water. Figure 51 also indicates that the weight loss in the second step was more significant in a nitrogen atmosphere than in the oxygen atmosphere. This might have been due to experimental error. Thus, TGA measurements were done using a second instrument which resulted in the sample, run in a nitrogen atmosphere, having a smaller weight loss than that in air. This was exactly opposite to the results obtained in the previous run. More precise measurements are needed before significant conclusions can be made regarding the atmosphere in which the precipitate is calcined.

In further evaluation of Figure 51, it should be noted that the XRD shows $\alpha$-phase characteristics at temperatures above 200°C. This corresponded well with the loss of the third type of water which was only totally diminished at 340°C, suggesting that the catalyst needs to be calcined at least to a temperature of 340°C.

The DSC analysis in Figure 52 (primary y-axis) of uncalcined precipitate in nitrogen shows the heat flow to the precipitate as it was heated. Three steps are observed which corresponds well with that of the three weight loss steps. A surprising exothermic peak was observed at 350°C at which no weight decrease was observed. This could be due to crystalline product being formed from the amorphous precipitate, maybe $\alpha$-phase formation, or it could be a result of sintering, the former being the most likely because of the single sharp peak. When the DSC was performed in pure oxygen (Fig. 53), a small (2.007 J/$p_{recipitate}$) negative peak (endothermic) was observed at 161-163°C which also corresponds well with the range (160-180°C) at which a small difference in weight loss was observed between the air and nitrogen TGA analyses (Fig. 50). This strongly suggests that the weight change for the sample performed in air (or oxygen) was due to the presence of oxygen. The large peak at 351°C showed a heat generation of 47.15 J/$g_{precipetate}$ (on a dry basis it is 49.11 J/g or 0.0547 J/mol catalyst).

Although the crystal formation peak only appeared at 350°C calcination started at 200°C. This means that the crystallisation reaction starts at 200°C, but is very slow at such a low temperature, and the calcination period should be much longer for total calcination.

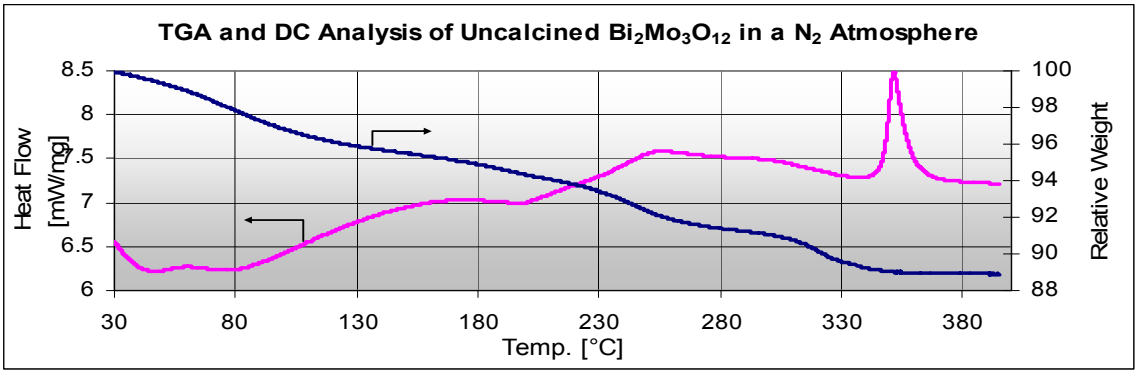


**Figure 52: Simultaneous TGA and DC analysis of uncalcined 2/3 precipitate in a nitrogen atmosphere.**

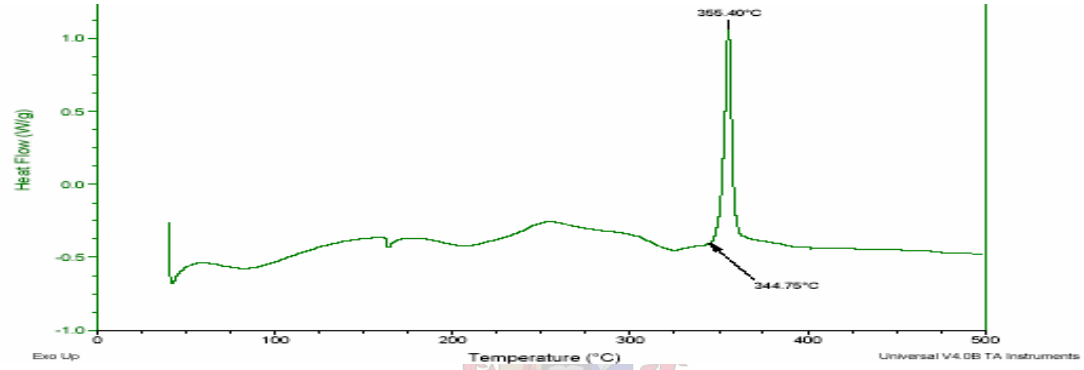


**Figure 53: DSC scan of uncalcined 2/3 precipitate in an oxygen atmosphere.**

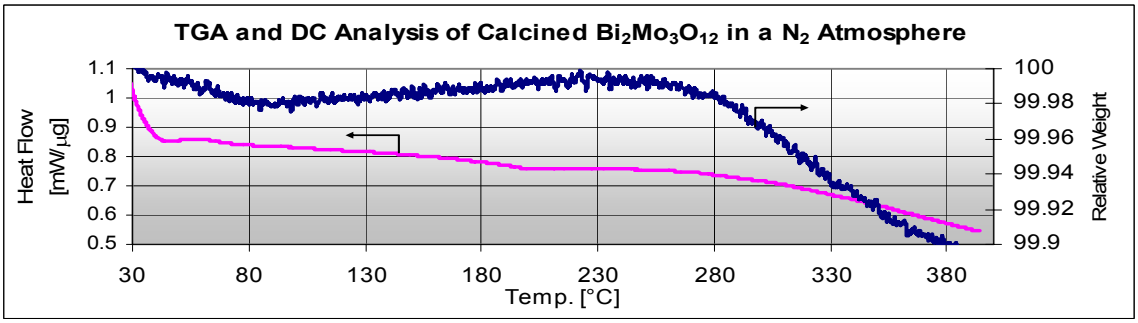


Figure 54: Simultaneous TGA and DC analysis of calcined 2/3 precipitate in a nitrogen atmosphere.

In Figure 54 calcined catalyst were simultaneously analysed using TGA and DC in a nitrogen atmosphere. It shows some weight loss due to the loss of adsorbed surface water from 30-100°C. In the temperature range from 100-230°C a small weight gain was observed due to the adsorption of gaseous nitrogen on the catalyst which was followed

by a weight loss of almost 1 percent, which may be due to desorption of the nitrogen and water. No peak was observed in the heat flow at 350°C confirm that the peak seen in the uncalcined catalyst was due to some irreversible process most probably phase transition to form $\alpha$-$Bi_2Mo_3O_{12}$ crystals. The small negative peak observed in the analysis of the uncalcined sample (at 161°C) in pure oxygen disappeared as well, also indicating an irreversible process.

## *5.4 A Simple Precipitation Method to Attain Pure 2/3 (Bi/Mo) Precipitate.*

A simple precipitation method was required so that it could be integrated into the reverse micelle technique. Keulks and Daniel [1972] did propose a simple precipitation method but the salt solutions he used were too dilute to be used in a reverse micelle technique. The following experiments were, therefore, done in an attempt to attain a simple precipitation method that could be integrated in the reverse micelle technique. This required maximum salinities yet solution stability, and a pure 2/3, Bi/Mo, precipitate.

### 5.4.1 Ammonium Molybdate Titrations (Exp. B4)

In a simple precipitation method a low pH bismuth solution (pH ± 0.9) was added to a high pH molybdenum solution (pH ± 5). The degree of condensation of the molybdate in the ammonium molybdate solution was a function of the acidity of that solution. The identity of the molybdate ion can range from the monomeric molybdate, $MoO_4^{2-}$, to the molybdenyl cation, $MoO_2^{2+}$. Thus, it was important to consider any pH changes of this solution during the precipitation. With full addition of the bismuth solution to the molybdenum the pH should not be less than 1.2 and both salt solutions must be stable through the whole addition period (individual salt should not crystallise out or form a precipitate). To determine at which point (pH) the molybdenum precipitate (polyanion) forms and how much acid can be added to the specific molybdenum concentration before if reaches a pH of 1.2, acid titrations were done with molybdenum solutions over a concentration range while monitoring the pH. This was needed to determine the maximum amount of acid that may be used in the bismuth solutions.

Figure 55 shows the pH curves for the three measured concentrations as well as a 0.3 M curve published by Keulks *et al.* [1974]. In all the curves a break was observed around a pH of 2 which was a result of the condensation step forming an octamer. The lower pH readings obtained for the measured samples relative to that of the published curve was due to a faster acidification rate and the slow reaction. The effect of acidification rate can be seen in Figure 57, showing a lower pH for the faster edition.

If the pH is plotted against the amount of concentrated acid per mole of molybdenum (Fig. 56) very similar plots are observed for all concentrations. This indicates that the amount of acid needed was only dependant on the molar amount and not the concentration of molybdenum. From the graph, 24-27 ml concentrated nitric acid was needed to acidify one mole of molybdenum in solution to a pH of 1.6-1.3.

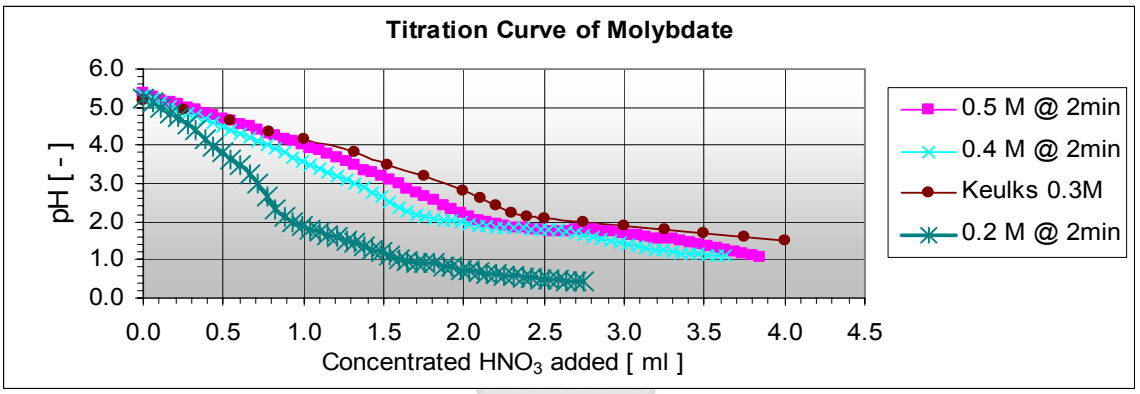


**Figure 55: Titration curves for aqueous ammonium paramolybdate acidified by concentrated nitric acid. pH vs. millilitres conc. $HNO_3$.**

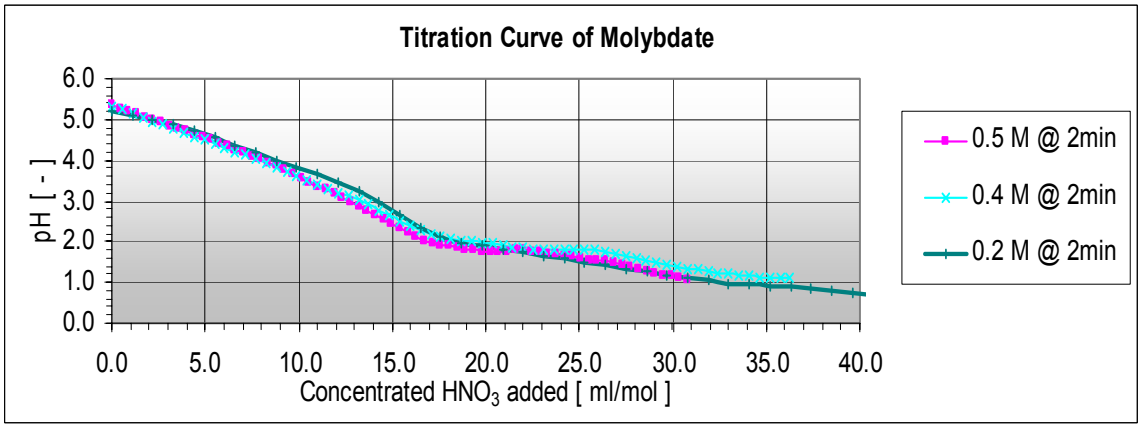


**Figure 56: Titration curves for aqueous ammonium paramolybdate acidified by concentrated nitric acid. pH vs. millilitres conc. $HNO_3$/mole$_{Molybdenum}$.**

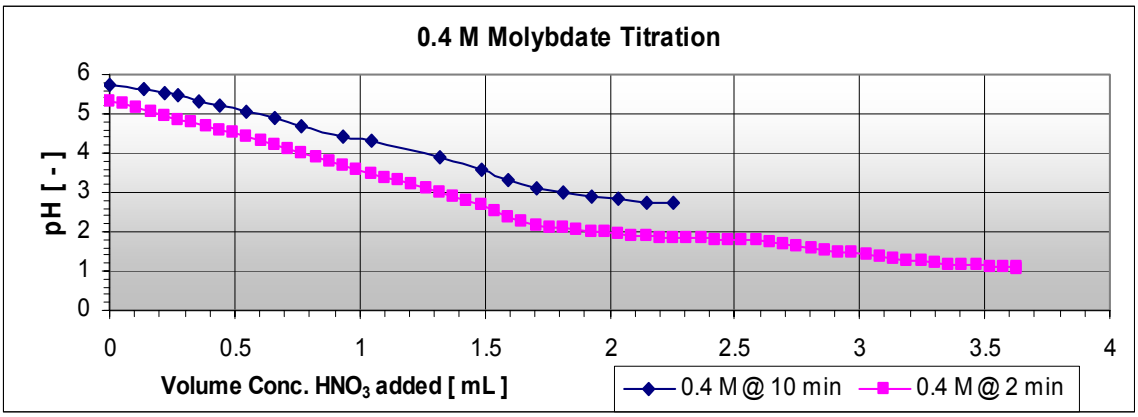


**Figure 57: Titration curves for 0.4M aqueous ammonium paramolybdate acidified by concentrated nitric acid. pH vs. millilitres conc. $HNO_3$ for different addition rates.**

## 5.4.2 Solubility Limits for Bismuth Nitrate Solutions (Exp. B5)

$Bi(NO_3)_3 \cdot 5H_2O$ solutions were acidified with concentrated nitric acid in order to enable dissolution of the salt. The solubility of the salt is very limited in even relatively acidic solutions. In previous experiments (Exp. B4) it was found that 24-27 ml concentrated nitric acid was needed to acidify one mole of ammonium molybdate to a pH of 1.2 (lower limit). This result suggests that 36-41 ml of concentrated nitric acid was needed for the dissolution of one mole of bismuth nitrate for a Bi/Mo ratio of 2/3. It was thus, necessary to find out if this was a sufficient amount of acid to dissolve the bismuth nitrate salt. This was done by checking the solubility with a decrease in acid addition.

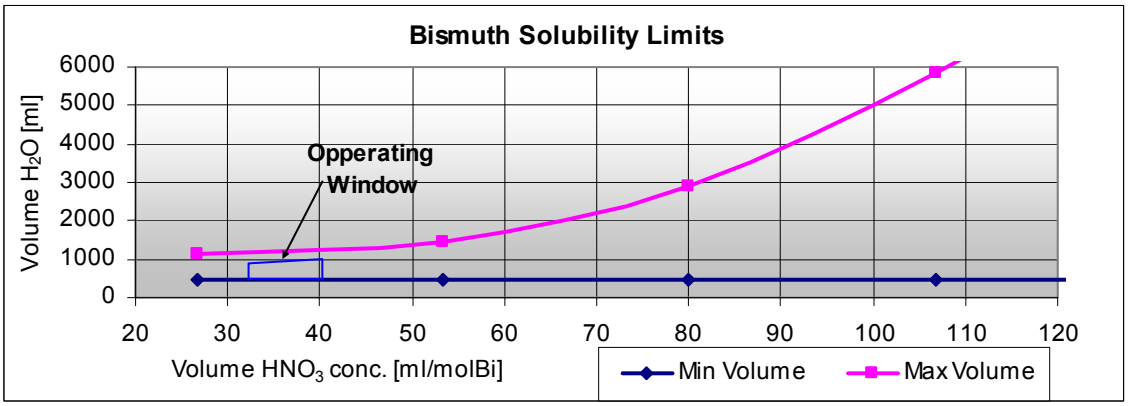


**Figure 58: Bismuth nitrate solubility limits. Volume water that can be added vs. the amount of concentrated $HNO_3$ per mole Bi.**

Figure 58 shows the bismuth nitrate solubility limits per mole bismuth nitrate. The minimum volume curve indicates the minimum amount of water that must be added to the nitric acid and salt mixture to dissolve the salt. The maximum water volume curve indicates the limit for bismuth nitrate solubility beyond which a precipitates form.

If 36-41 ml of concentrated nitric acid was needed for dissolving the bismuth. A small operating window is defined which is shown in Figure 58 resulting in a bismuth concentration of 0.8-1.0 M depending on the amount of water added. It would be sensible to use the lowest concentration permitted to avoid the high acid concentration. The corresponding equal volume molybdenum concentration is thus 1.5-1.2 M, but may be lowered to 0.7-0.8 M.

Theoretically the bismuth nitrate could be dissolved in the maximum acid available but there was uncertainty about its stability in the addition step. The operating window was so small that a small addition of water caused the bismuth salt to form small crystals. This could pose a problem when the bismuth solution is added to the molybdenum solution as the bismuth may become unstable resulting in the formation of small bismuth hydroxide crystals within the precipitate.

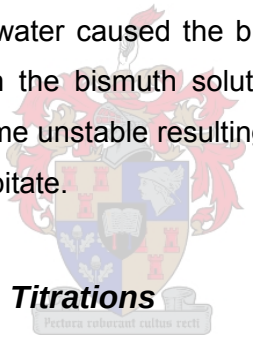


#### *5.4.2.1 Bismuth Molybdenum Titrations*

In all samples the bismuth solutions were slowly added in small steps to the molybdenum solution except sample 11, which was added in one step and evaluated for 3 hours. The curve for sample 11 in Figure 60 is thus a pH vs. time with 100% being 3 hours. In some of the runs the bismuth salt started precipitating out resulting in the bismuth solution becoming slightly milky. The time during which the solution was stable is noted in Tables 13 and 14. Tables 13 and 14 and Figures 59 and 60 summarise the runs and show the pH curves of the mixtures as a function of mole % bismuth solution added to the molybdenum solutions ending at a Bi/Mo ratio of 2/3.

**Table 13: Simple Precipitation Runs 1-6**

| Run | 1 | 2 | 3 | 4 | 5 | 6 |
|---|---|---|---|---|---|---|
| $V_{Mo}$ (ml) | 50 | 50 | 50 | 25 | 20 | 20 |
| [Mo] (mol/l) | 0.045 | 0.045 | 0.045 | 0.0899 | 0.398 | 0.113 |
| $V_{Bi}$ (ml) | 300 | 300 | 50 | 50 | 20 | 50 |
| [Bi] (mol/l) | 0.00497 | 0.00498 | 0.0295 | 0.0295 | 0.0721 | 0.0295 |
| Volume $HNO_3$ (ml) | 1.875 | 1.3 | 0.8 | 0.9 | 0.8 | 0.8 |
| $V_{TOTA}L$ (ml) | 350 | 350 | 100 | 75 | 40 | 70 |
| Addition time (min) | 60 | 75 | 40 | 50 | 50 | 50 |
| Bi Stability time (min) | Stable | 45 | 20 | Stable | Stable | 30 |

**Table 14: Simple Precipitation Runs 7-11**

| Run | 7 | 8 | 9 | 10 | 11 |
|---|---|---|---|---|---|
| $V_{Mo}$ (ml) | 25 | 25 | 50 | 50 | 50 |
| [Mo] (mol/l) | 0.09 | 0.398 | 0.045 | 0.045 | 0.045 |
| $V_{Bi}$ (ml) | 100 | 150 | 50 | 150 | 50 |
| [Bi] (mol/l) | 0.0148 | 0.00993 | 0.0295 | 0.00994 | 0.0297 |
| Volume $HNO_3$ (ml) | 1 | 1 | 0.85 | 0.9 | 0.55 |
| $V_{TOTAL}$ (ml) | 125 | 175 | 100 | 200 | 100 |
| Addition time (min) | 50 | 75 | 50 | 30 | - |
| Bi Stability time (min) | 25 | Stable | Stable | Stable | - |

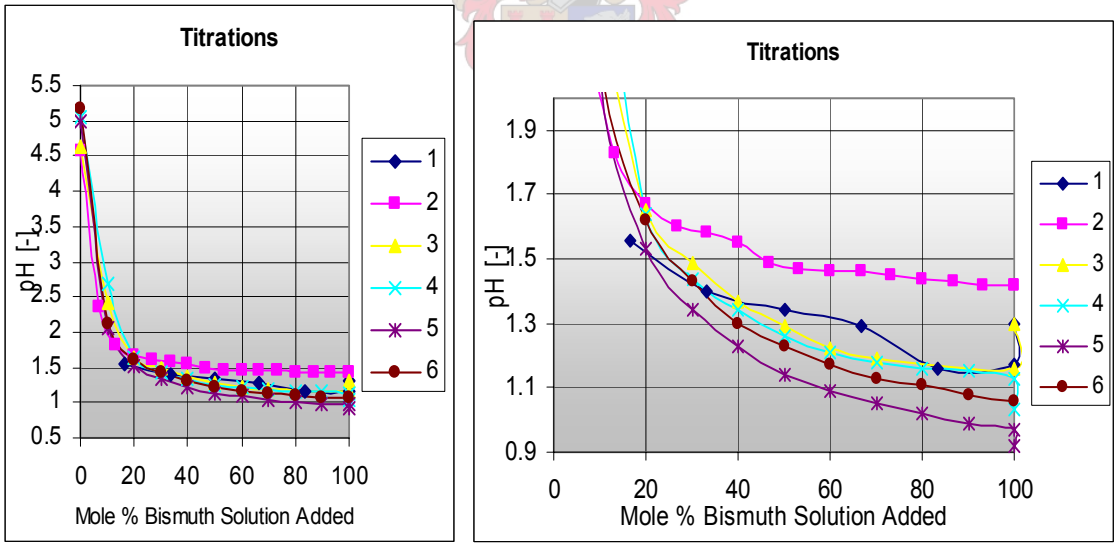


**Figure 59: pH curves for precipitation run 1-6. pH as function of mole % bismuth solution added to the molybdenum solution (Bi/Mo = 2/3).**

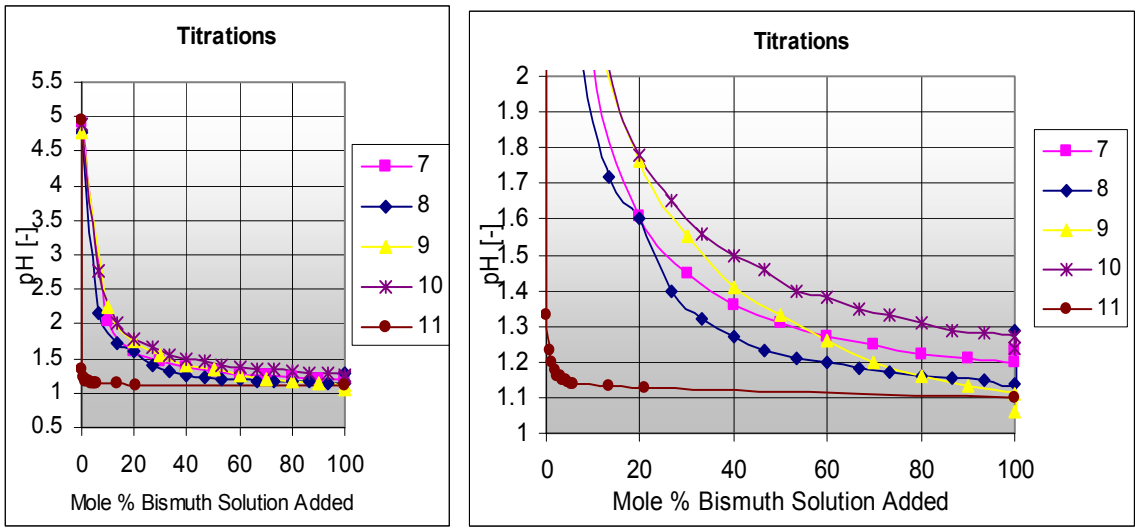


**Figure 60: pH curves for precipitation runs 7-11. pH as function of mole % bismuth solution added to the molybdenum solution (Bi/Mo = 2/3).**

Run 1 was similar to the simple precipitation method proposed by Keulks [1972]. It reached a minimum pH of 0.2 and after aging, the pH was 1.3. Slower addition of the bismuth solution, thus, will increase the pH because of the slow buffering effect of the molybdenum due to the slow reaction. Run 2 had the highest end pH (1.45) but the bismuth solution formed crystals after 45 minutes meaning that less acid was used in the bismuth solution. Runs 7, 8 and 10 also looked promising with a minimum pH of 1.2 and 1.14, respectively. These samples were calcined resulting in a bright yellow product which is characteristic of the β-phase. (The samples could not be analysed using the XRD due to the small quantities formed).

It seemed that the end pH was higher for the samples with higher total volume thus lower salt concentrations. The end pH was also increased using less acid, which was expected, but it reaches a point at which the lowering of the acid content causes the precipitation of the bismuth salt.

### *5.4.2.2 Pre-Addition of Ammonium to the Molybdenum Solution*

Ammonium was added to the molybdenum solutions of the following titrations in an attempt to increase the pH at full addition of the bismuth solution. Both the ammonium

and subsequent bismuth titration curves of the molybdenum solutions are shown in Figures 61 and 62.

**Table 15: Simple Precipitation with $NH_3$, Runs 12-15**

| **Run** | 12 | 13 | 14 | 15 |
|---|---|---|---|---|
| **$V_{Mo}$ (ml)** | 70 | 50 | 50 | 70 |
| **[Mo] (mol/l)** | 0.0321 | 0.045 | 0.045 | 0.0321 |
| **Volume $NH_3$ (ml)** | 1.6 | 2 | 1.5 | 1.6 |
| **$V_{Bi}$ (ml)** | 70 | 50 | 50 | 70 |
| **[Bi] (mol/l)** | 0.02118 | 0.0295 | 0.0295 | 0.0211 |
| **Volume $HNO_3$ (ml)** | 0.81 | 0.83 | 0.81 | 0.81 |
| **$V_{TOTAL}$ (ml)** | 140 | 100 | 100 | 140 |
| **Addition time (min)** | 50 | 40 | 50 | 70 |
| **Bi Stability time (min)** | Stable | Stable | Stable | Stable |

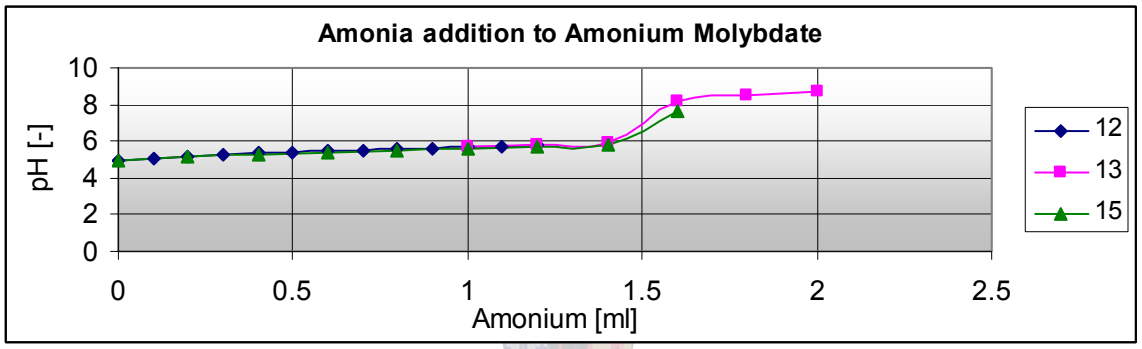


**Figure 61: pH curves for ammonium added to ammonium molybdate solutions.**

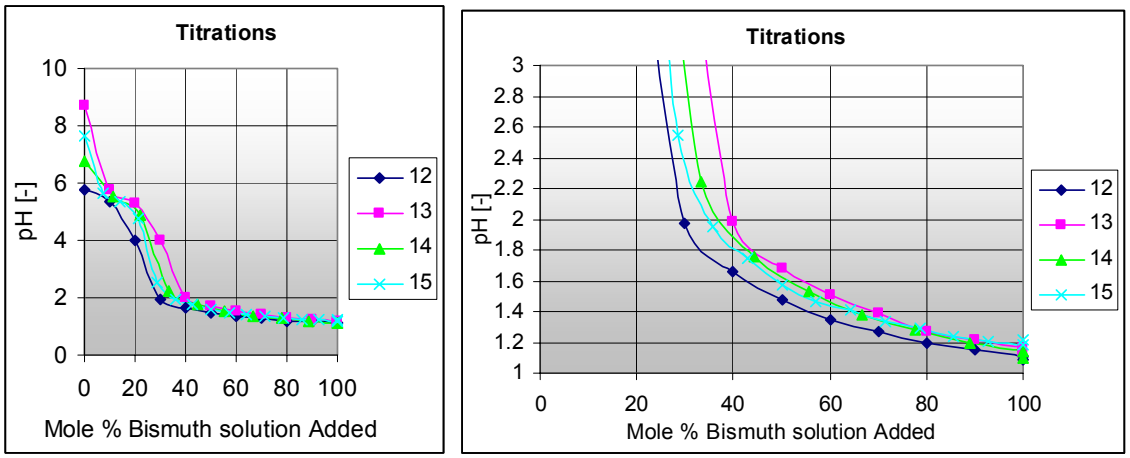


**Figure 62: pH curves for precipitation run 12-15. pH as function of mole % bismuth solution added to the molybdenum solution (Bi/Mo = 2/3)**

The titration curve for the addition of ammonium to the molybdenum solution has a break at a pH of 5.8 which most probably indicates the break up of the heptamolybdate anion

species. When the molybdate solutions were acidified by adding the low pH bismuth solutions, an extra break was observed in the titration curve at the same pH indicating the reformation of the heptamolybdate anion by the following reaction:

$$7MoO_4^{2-} + 8H^+ \leftrightarrow Mo_7O_{24}^{6-} + 4H_2O \qquad \ldots 34$$

The final pH of these ammonia pre-treated samples was similar to the previous samples. The addition of ammonium thus, only brings in an unknown factor which does not seem to have the necessary effect on the end pH of the system.

### *5.4.2.3 Molybdenum Buffered Titrations*

From the previous titrations it can be seen that molybdenum is a good pH buffer. For that reason an excess of molybdenum was used to buffer the precipitate mixture so that the pH does not decrease to a value below 1.4. This also implied that the Bi/Mo ratio decreased and that other impurities might form. Similar titrations to run 5 and 9 (high salt concentrations) were done by slowly adding a bismuth solution to a molybdenum solution. When the pH decreased to a value of 1.4, more molybdenum solution was added to the mixture as a buffer. Usually about double the molybdenum content were used and the resulting precipitate was washed thoroughly with distilled water to rinse it from any excess molybdenum. The precipitates were calcined and the following XRD was obtained (Fig. 63).

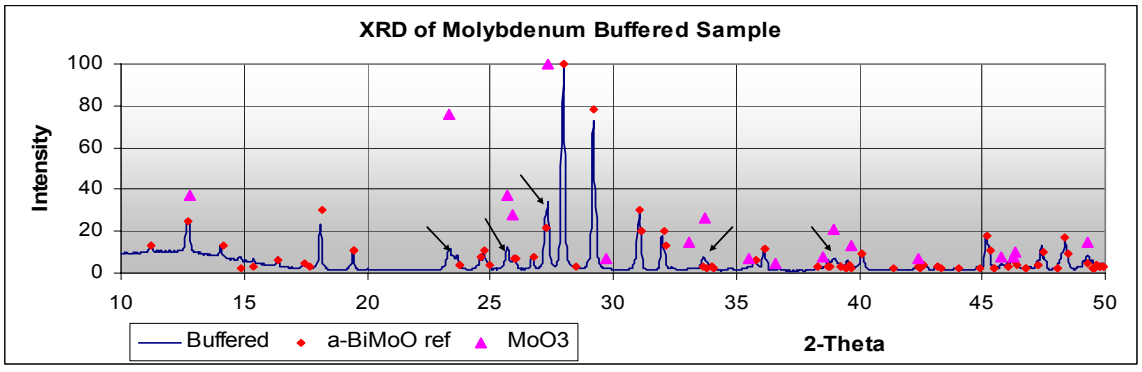


**Figure 63: Calcined buffered precipitate compared with a computed reference for α-$Bi_2Mo_3O_{12}$ [Theoblad and Laarif, 1985] and $MoO_3$ [Kihlborg, 1963]. The arrows show some traces of $MoO_3$.**

The excess molybdenum used caused the formation of a small amount of $MoO_3$ mixed with the $\alpha$-phase but no impurities other than $MoO_3$ were observed. In the slurry reaction proposed by Batist *et al.* [1972] (c.f. section 2.2.2) to prepare $\alpha$-$Bi_2Mo_3O_{12}$ he used a warm concentrated ammonia treatment to successfully remove excess $MoO_3$ from the calcined product after which it was washed with water and recalcined. When the sample, which was analysed above, was washed with warm (100°C) concentrated ammonium, the colour changed from slightly grey to pale yellow (indication of $\alpha$-phase) with the filtrated ammonium being grey. Then the sample was washed with warm water and recalcined. Figure 64 shows the XRD analysis which indicates that all the $MoO_3$ is successfully removed in the wash step and only pure $\alpha$-$Bi_2Mo_3O_{12}$ is left.

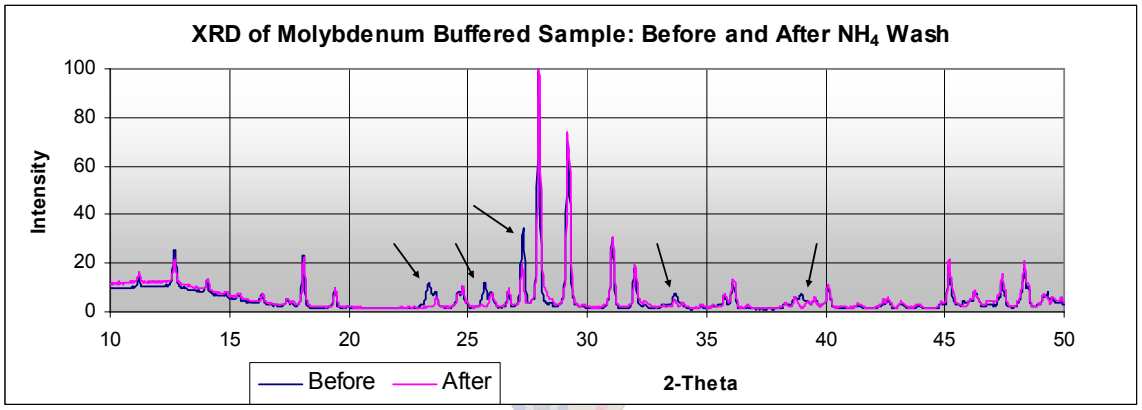


**Figure 64: Calcined molybdenum buffered precipitate before and after the ammonium wash. Arrows indicate the disappearance of the $MoO_3$ peaks.**

A simple precipitation was thus possible if an excess of molybdenum was used to buffer the mixture when the low pH bismuth solution was mixed to avoid the formation of $\beta$-$Bi_2Mo_2O_9$. This excess molybdenum caused the formation of $MoO_3$ impurities which can be removed from the calcined product using a warm concentrated ammonium wash followed by a water wash and recalculation to remove adsorbed ammonia.

## *5.5 Formation and Stability of Reverse Micelles*

### 5.5.1 Malvern Zetasizer Analysis

A Malvern Zetasizer 1000HS was used to measure the sizes of the reverse micelle over a period of time to determine their growth and stability. The equipment, however, was being used to analyse latex particles in an aqueous solution and was not rigged to analyse samples containing large amounts of oil. The oil caused the plastic cuvette to dissolve and thus had to be replaced by glass or quartz cuvette. The samples were analysed at 25°C by detecting the light scattering at a 90° angle. In the following experiments the reverse micelles resulting from the addition of distilled water, a molybdenum solution and a bismuth solution were evaluated. Analytical models were used to evaluate the measured data and attempts were made to calibrate the equipment.

### 5.5.2 Calibration and Model Evaluation ( Exp. C1)

The exact particle sizes are calculated as a function of viscosity of the medium in which it is suspended. The Zetasizer thus, had to be calibrated for specific oil-surfactant mixtures viscosity to determine the exact particle sizes. A standard of latex particles (220±6 nm) suspended in a water medium is usually used to calibrate the sizer but in this case the small amount of water which was added, to the oil-surfactant mixture when the standard latex particles was added posed a problem. It has been found that small amounts of water added to the hexane-berol mixture caused droplets of sizes in the same order of magnitude as the standard latex particles. It was also noted that at certain higher water concentrations the reverse micelles were much smaller than the standard particles. The standard particles were thus added to such a mixture so that the small amount of water (water added due to the addition of the standard) did not cause reverse micelles that could interfere with the measurements. The results were then used to evaluate different analysing models to determine which one results in the smallest fitting error.

A correlation function is generated by comparing the measured signal with itself at different delay times and is fitted with a polynomial function from which the droplet size, polydispercity index and fitting error are calculated. If the correlation function, for the

standard particles, was fitted with a second order polynomial function a narrow size distribution was obtained with a small fitting error (±0.00015, relative units). If a third or higher order polynomial functions were fitted a broader size distributions were obtained with a higher fitting error (0.05-0.0001). Different fitting algorithms were evaluated and the mono-model (usually used for smooth narrow size distributions) and a CONTIN model (high resolution used for smooth distributions) using a second and third order fit gave the best and most realistic results.

The sample was analysed 45 times using the default values for water. This means that the standard 220±6 nm latex particles will have a different measured size (seeing that the viscosity of the oil-surfactant mixture was lower a smaller particle was expected). Seen that the actual size was known, a scale-up factor could be derived. To evaluate the data, the second and third order mono- and CONTIN models were used and resulted in different average values and distributions. The second and third order models resulted in an average size of 166±11 nm and 185±6 nm, respectively. The average sizes were also strongly dependent on the first and last point selection parameters (advance fitting model parameters) resulting in the sizes changing from 150-230 nm. It was thus impossible to obtain a precise measurement for the standard latex particles because these point selection parameters were unknown. The exact sizes could not be obtained, thus scale-up factor was unknown. All reverse micelle measurements were thus relative values. The exact droplet sizes, however, were not as important.

### 5.5.3 Distilled Water in 10% Berol/Hexane Mixture (Exp. C2)

A Malvern Zetasizer 1000HS was used to determine reverse micelle stability, size and growth for distilled water added to a 10% berol-hexane mixture.

The reproducibility of the analysis was evaluated by preparing and analysing a similar sample (0.3 ml water added to 3.0 ml oil-surfactant mixture) three times. It was found that by using a magnetic stirrer, broad and uneven droplet size distributions were obtained. By putting the micelle mixture in a sonic bath resulted in a smooth, narrow and reproducible size distribution. Figure 65 shows very similar results for all three samples analysed. The initial droplet sizes were 43-47 nm and the change in size as a faction of

time was similar. The Malvern Zetasizer and the analyzing technique thus give reproducible results.

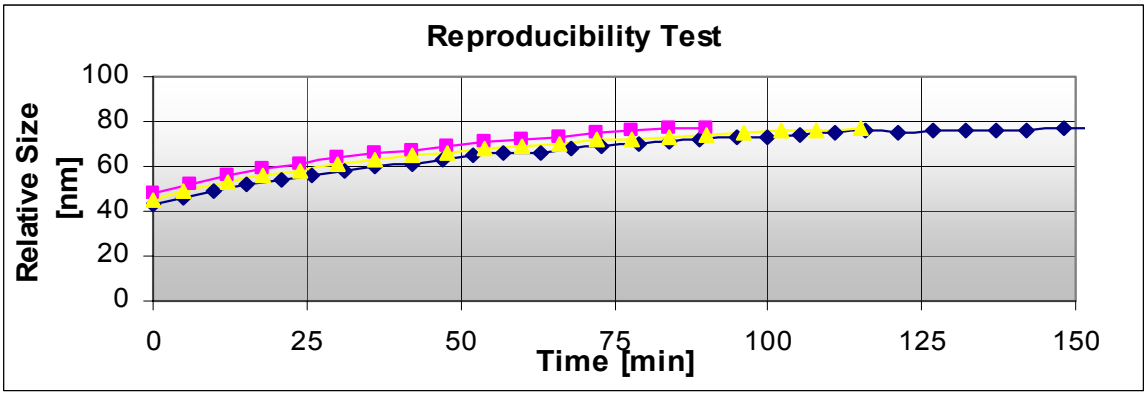


**Figure 65: Reproducibility test. 0.3 ml water added to 3 ml oil-surfactant mixture.**

The effect of surfactant concentration was tested by adding 0.35 ml of water to a 10% and a 20% surfactant mixture. The initial droplet sizes were the same but the droplet sizes for the sample containing more surfactant decreased more rapidly with time (see Figure 66). This shows that the surfactant concentration plays an important role in the dynamics of a reverse micelle system.

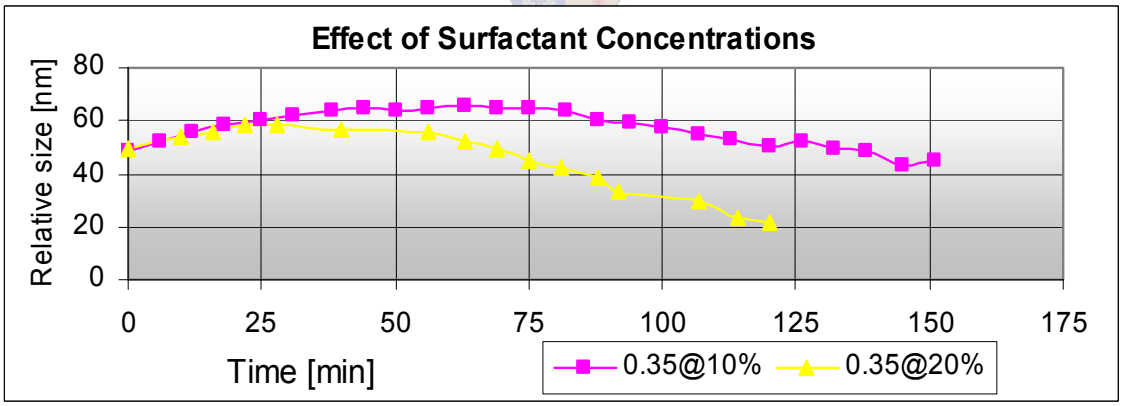


**Figure 66: Effect of 10% and 20% surfactant concentration on droplet sizes. 0.35 ml water added to 3 ml oil-surfactant mixture.**

A range of water volumes were then added to a 10% berol-hexane mixture and evaluated. The result is given in Figure 67 as millilitre water added to 3ml of 10% berol-hexane mixture.

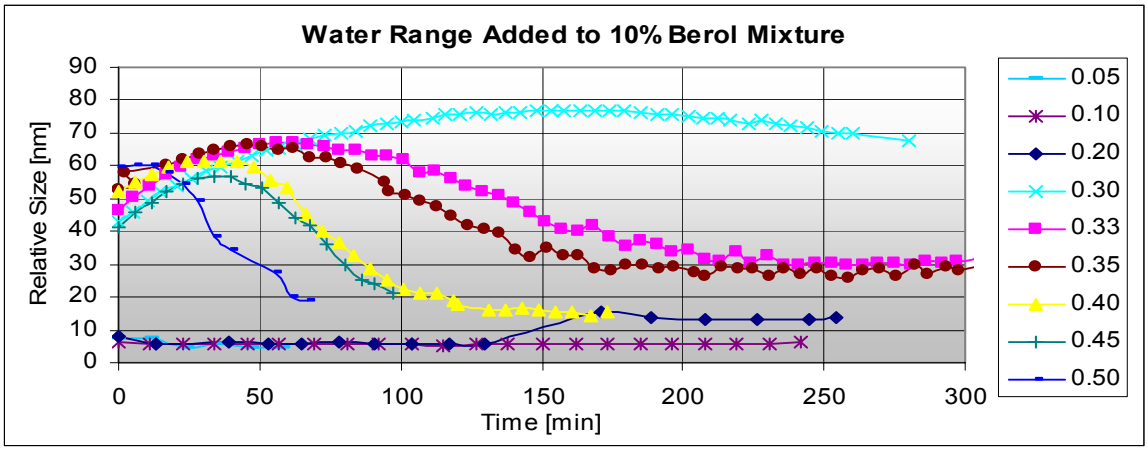


**Figure 67: Water range added to 10% berol-hexane mixture. Given as millilitre water added to 3 ml mixture.**

If small amounts of water (0.05-0.2 ml) were added to the oil-surfactant mixtures the reverse micelles were small (6-8 nm) and constant over time except for the sudden jump for the 0.2 ml sample at 150 min. These samples were totally transparent and the size values obtained were below the minimum analysing range of the sizer (15-20 nm). All other samples (0.2-0.5) had roughly the same initial droplet size and similar initial gradients for the first 40 min. After 40 min the curves started diverting at increasing degrees with an increase in the water content. They then became constant and started increasing linearly with time as can bee seen for the extended 0.33 ml curve in Figure 68.

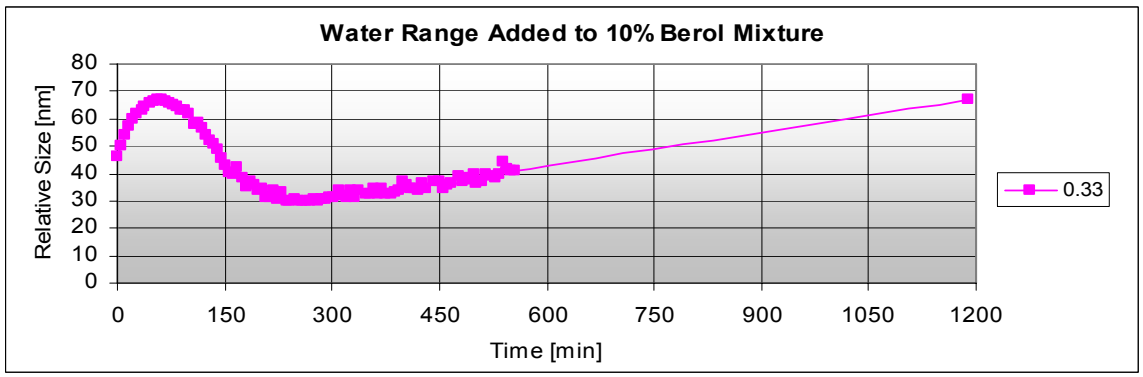


**Figure 68: Time extended 0.33 ml curve. Linear function of time after 300 min.**

The droplet sizes as a function of time show a complex dynamics system with probably more than one mechanism playing a role in the sizes change, hence, the typical third order plot. To explain the dynamics of the reverse micelles it should be noted that the

sizes are given as an average of the size distribution. Investigating the change in size distributions suggested that the increase seen in the initial 50 min were due to the incorporation of smaller droplets into the larger ones of smaller droplets (at this stage the size distribution was reasonably wide). The difference in internal pressure of small and larger droplets drives the consumption of small droplets (high internal pressure) resulting in a narrower size distribution which have an increased average size value. The exact reason for the subsequent decrease in micelle size (50-150 min) is unclear but it could have something to do with the surfactant arranging around the micelles in a more organised structure. From Figure 68 it is clear that the degree of the decrease in size is a function of the concentration of the aqueous phase. It is also unclear to what extent the size measurement is influenced (change in light diffraction or light adsorption). The third change seen is that of a linear region. This corresponds well with the Ostwald ripening effect discussed by Tadros *et al.* [2004].

### 5.5.4 Molybdenum Solution in 10% Berol-Hexane Mixture (Exp C3)

Experiment C2 was repeated substituting the distilled water with ammonium molybdate solutions to see what the effect of the salt is on the stability of the reverse micelles.

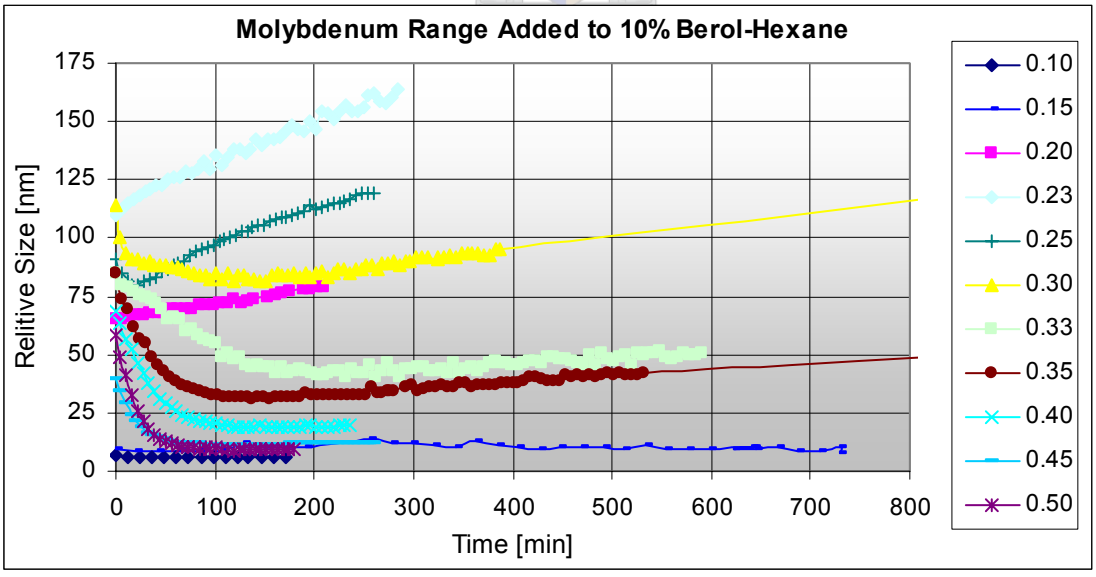


**Figure 69: Ammonium molybdate solution ([Mo] = 0.04M ) range added to 10% berol-hexane mixture. Given in millilitre water added to 3 ml berol-hexane mixture.**

Figure 69 shows the droplet sizes for the 0.04 M molybdate solution added to 10% berol-hexane. When small amounts (0.1-0.5 ml) were added to the standard 3 ml mixture, small (10-15 nm) and stable sizes were observed. The curve for sample 0.2 started higher than the 0.1-0.5 ml samples at 65 nm and increased with a constant gradient. For all other samples (0.23-0.50 ml) a specific pattern was observed. The degree at which the droplet sizes decrease and the subsequent linear increase changed with the additional amount of molybdenum solution. Higher amounts of molybdenum solutions caused a faster initial decrease but a slower subsequent increase. Figure 70 shows the gradients of the subsequent linear regions plotted as a function of aqueous volume %. A definite trend was observed for the 0.23-0.5 ml samples and could be fitted using an exponential function.

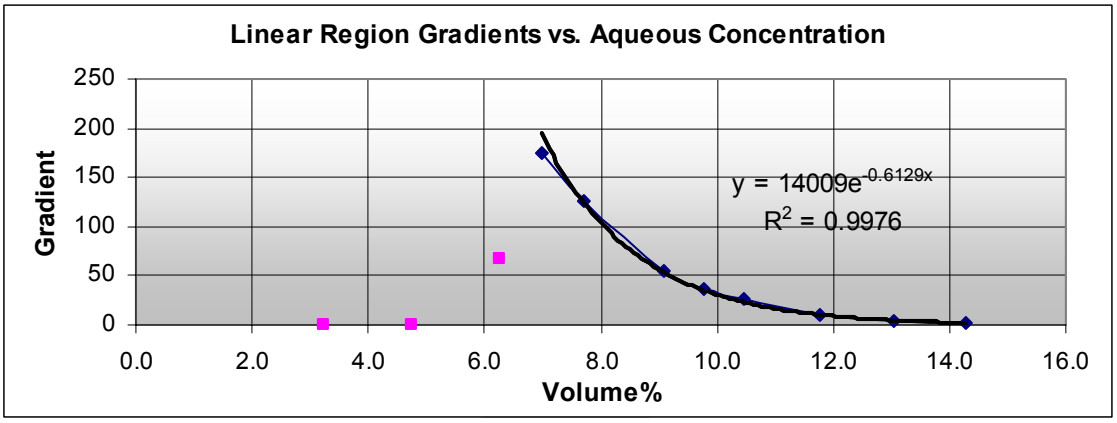


**Figure 70: Gradients (droplet growth per 1000 min) of the linear region as a function of aqeous volume %.**

As previously mentioned, the addition of an aqueous phase to the surfactant-oil mixture may result in the mixture becoming hazy then clear and then cloudy again. In Figure 70 only samples containing an aqueous volume fraction between 3% and 15% were analysed with the range above 6% giving large reverse micelles. However, in cases where a hazy region were observed or when smaller aqueous fractions were used (>0.5% vol.), large droplets in the size range 100-200 nm were observed.

The dynamic changes in the droplet sizes of the molybdenum containing aqueous volume range differs considerably from the results obtained by adding pure water to the oil-surfactant mixture. The disappearance of the initial size increase seen in the water addition (Fig. 67) may be the result of salt stabilisation effect which prevents the

formation of small droplets causing a much narrower initial size distribution (see Figure 69). The micelle sizes for samples 0.20 and 0.23 (Fig. 69) only increased linearly due to the Ostwald ripening effect but did not decrease in size first . Only the next sample (0.25 ml) showed a small decrease. This indicates that the mechanism causing the decrease needs a critical amount of aqueous phase. For all subsequent samples (0.25-0.50) similar results were observed to that of the pure water addition. The good trend fit in Figure 68 is further evidence of the Ostwald ripening being a function of the concentration of the aqueous phase or a secondary effect there of (e.g. increase in reverse micelle surface area with increase in aqueous phase).

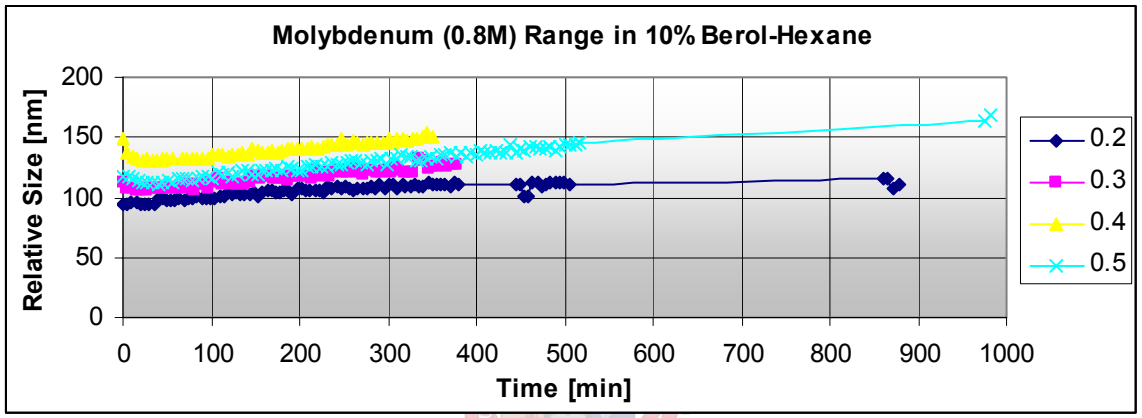


**Figure 71: Ammonium molybdenum solution range added to 10% berol-hexane mixture. Given as millilitre water added to 3 ml mixture. [Tee, 2004]**

In Figure 71, a higher ammonium molybdenum salinity (0.8 M) was used than in Figure 69. It should be noted that the droplet sizes as well as the growth as a function of time for equal volumes aqueous additions, change dramatically. It would appear that the higher salinity stabilised the reverse micelle to a great extent. The droplet sizes were increased to very similar sizes for the whole volume range and were steady over time. Only a small initial size decrease can be observed for samples above 0.2 ml.

### 5.5.5 Bismuth Solution in 10% Berol-Hexane Mixture (Exp C3)

Experiment C2 was repeated but substituting the distilled water with a bismuth nitrate solution, [Bi] = 0.21 M.

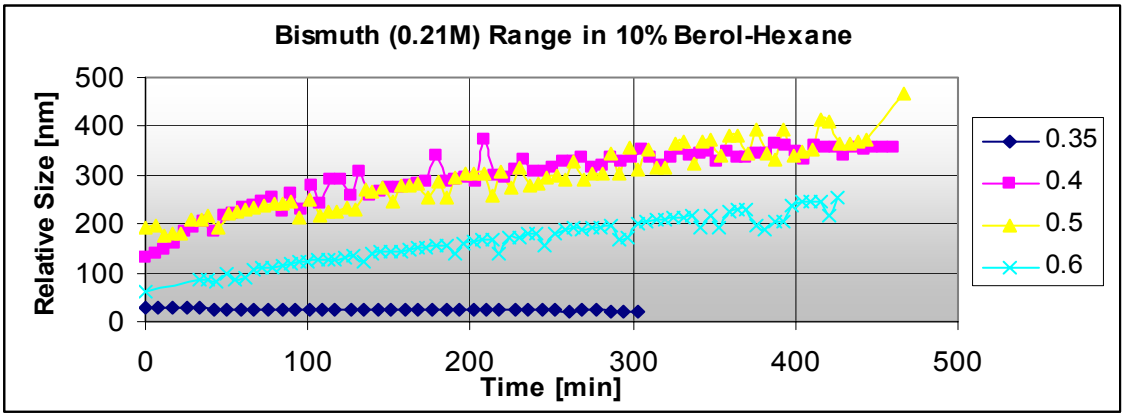


**Figure 72: Bismuth nitride solution (0.21M) range added to 10% berol-hexane mixture. Given as millilitre water added to 3 ml mixture. [Tee, 2004]**

The results for equal volume reverse micelles for bismuth solutions were very different than those of the molybdenum in size as well as the size growth as a function of time. The micelles were much bigger and it steadily increased in size over time. It also seemed like the sizes for the higher volume fractions 'oscillated' between a higher and lower value. It is uncertain why this happens. The bismuth seemed to stabilise reverse micelles more than molybdenum causing larger droplets and no initial decrease in size.

### 5.5.6 Catalyst Particle Analysing using the Zetasizer

Catalyst particles were prepared using the reverse micelle technique, as discussed previously, with the exception of using a sonic bath to mix the micelle mixture instead of the lab mixer. High salinity salts ([Bi] = 0.21 and [Mo] = 0.8) were used and the resulting particles were centrifuged and washed thoroughly using acetone. The particles were suspended in water and analysed using the Zetasizer. Particle sizes of 120 nm were obtained which were much larger than those previously synthesised. Due to time constraints this experiment was the only one of its kind. The preliminary run showed large particles with a narrow size distribution. The fact that the particles were suspended in water made it easy to determine the actual particle sizes using the normal Zetasizer

settings and calibration technique. The results should also be verified by TEM. This may potentially be a low-cost and easy way to determine catalyst particle sizes and size distributions.

### 5.5.7 Questions and Limitations

**Reverse Micelles or Not?**

One of the important and unanswered questions is that of the appearance and disappearance of reverse micelles over the aqueous addition range. This causes uncertainty about the existence of stable micelles at the typical aqueous concentrations used. The Zetasizer did show typical reverse micelle sizes but this could also be due to layers of bicontinuous phases overlapping giving the appearance of droplets. A bicontinuous phase can be distinguished from reverse micelles by measuring the conductivity of the phase using a very sensitive conductivity meter (20 μc). It should also be possible to view the micelles using a powerful microscope.

**Oil (n-hexane) Used to Obtain Reverse Micelles**

In this study only n-hexane was tested as the oil medium. Although cheap, it is merely oil and is not the optimal choice to obtain stable micelles. The oils regularly researched are compounds with carbon numbers of at least 10 or more. Choosing an already well defined oil-surfactant system for further work may help understand the reverse micelle technique better.

### *Reaction Kinetic Studies Prepared $\alpha$-$Bi_2Mo_3O_{12}$Using Keulks Method*

These experiments were done to ensure the effective operation of the reaction rig to ensur accurate and reproducible results. Validation of the system was done by comparing results obtained here to previously published data. This section contains evaluations of different aspects within the kinetic experiments and analysis of the samples. Detailed experimental procedures can be found in Appendix D.

### 5.5.8 Glass and Metal Reactor Evaluation

The residence time and temperature distribution of the two types of reactors were discussed in section 6.2. This section will discuss and compare results from catalytic and blank runs done using glass and metal reactors as well as the results obtained using different catalyst diluents.

**Glass Reactor Blank Run**: Blank runs were done using a Pyrex glass reactor fitted with a Pyrex sinter. At temperatures around 400°C the empty reactor caused a conversion of reaction gasses and formed CO, $CO_2$, methane, acetaldehyde and ethene (trace amounts of 1,3 butadiene and some unidentified compounds were also formed). Several attempts were made to catalytically deactivate the Pyrex but none of the attempts were successful. The results are summed in theTable 16.

**Table 16: Pyrex glass reactor blank run products for different glass pre-treatment.**

| Treatment | Main Product | Trace Products | Conversion @ 450°C |
|---|---|---|---|
| | | | % |
| Untreated | CO, $CH_4$, C=C, C=C=O | 1,3 butadiene, $CO_2$ | 10-20 |
| Propanol saturated with KOH | CO, $CH_4$, C=C, C=C=O | 1,3 butadiene, $CO_2$ | 10-20 |
| 2-10% HCl | $CO_2$ | CO | 20-30 |
| 2-55% HNO3 | $CO_2$ | CO | 40-50 |
| 2-33%NH3 | $CO_2$ | CO | 20-30 |

Definite differences were observed for the different pre-treatments. The untreated and the propanol treated reactor started with a low conversion which increased with time on stream (on-line). The product distribution can be explained by Keulks and Daniel [1972], which suggests a surface initiated homogeneous reaction in which propene and acetaldehyde take part. $CH_4$ formation suggested a surface generated radical causing homogeneous reaction in the gas phase. These surface sites are most probably –OH terminal groups bound to a Si. When treated with acids or ammonium solutions the conversion was much higher. The products were always combustion products by nature and no other product were observed. The surface silanol groups, thus have changed resulting in the total combustion of propene.

The reaction temperatures were too high to use silica based oils as an inert coating thus, it was not tested. The failure of the glass reactor led to the construction of a stainless steel reactor.

**Metal Reactor Blank Run**: The stainless 316 reactor, manufacture by the workshop of Process Engineering, was initially cleaned using a pickling gel to rid it of any ion oxides. It was then placed in the reactor oven as an empty reactor and later filled using packing material and it was run for 10 hours under reaction conditions before it was used for experimental runs. At 450°C and no catalyst, no conversion of propene took place. The metal reactor also had the advantage of being much more robust than the glass reactor and was used in all experiments reported further.

### 5.5.9 Reaction Kinetics: Technique Optimising (Exp. D1)

Kinetic experiments were done to optimise the technique. The time it took for the reactor to stabilise, reactor loading, sampling and analysing techniques were evaluated. Figure 73 shows the reactor temperatures (333°C-514°C) for the range of kinetic experiments done.

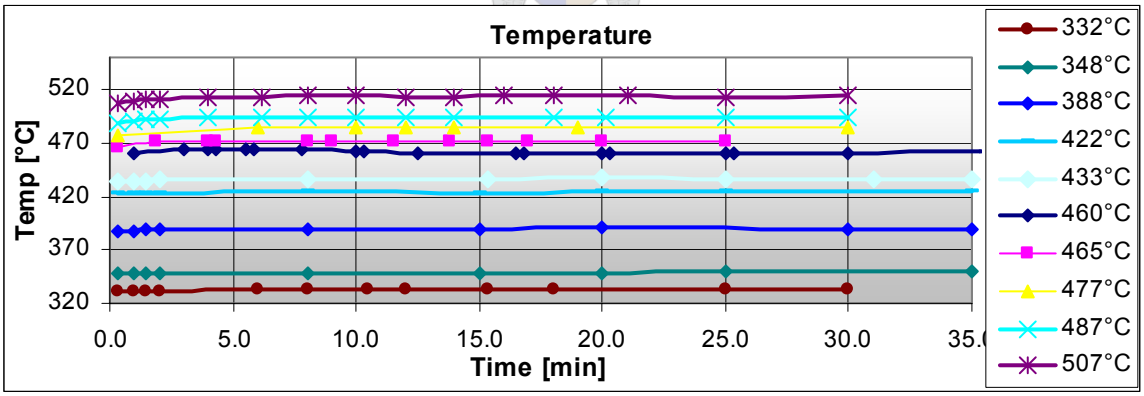


**Figure 73: Reactor temperatures as a function of time. Experiment D1.**

Due to the highly exothermic reaction it was necessary to evaluate the temperature increase of the reactor (metal reactor). A weight hourly space velocity (WHSV) of 3 $g_{propene}/g_{catal}$.hrs was used with a catalyst weight of 0.15 g and a feed stream containing $C^{=}_{3}$:$O_2$:He in a 1:2:7 ratio. For runs below a temperature of 450°C, the temperature only

increased with 1°C and those around 500°C increased by 3°C. Seeing that the typical temperature range is 350°C-450°C the initial temperature increase did not have a great effect on the reaction temperature.

Figure 74 shows the acrolein formation, as a carbon percentage of the product stream. The rate of acrolein formation increased with an increase in temperature until 460°C when it starts decreasing. The acrolein formation runs below 460°C resembled linear functions of time while those above are best described as powers or exponentially decreasing functions which seem to stabilise after 30 min. If runs 460 and 465 are examined it will be noted that the when two samples are taken quickly after one another, the second sample gives a higher acrolein content. This was due to the instability caused when the first sample was taken. This effect was minimised by changing the ampoule quality and by waiting a minimum of 15 sec between samples.

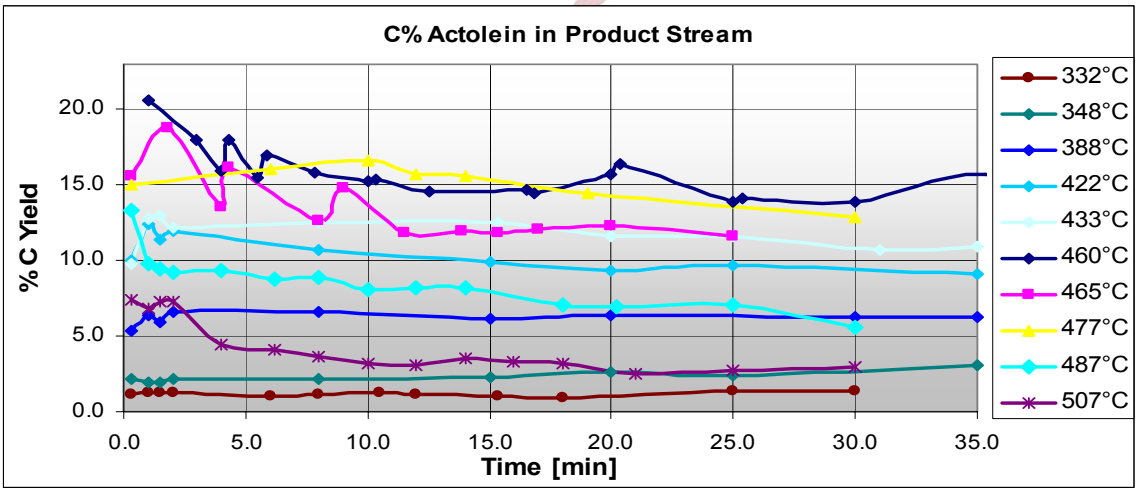


**Figure 74: Acrolein formation in C% as a function of time for a range of reaction temperatures. Exp D1**

Figures 75 and 76 show the CO and $CO_2$ formation for the respective runs. The CO formation increased slightly with increasing temperature from 332°C until 433°C, after which it increased in a sudden jump. When run 460 is examined it can again be seen that quick consecutive sampling also influences the CO, with the second sample being the lower one. The CO makes up a small carbon fraction of the total gas sample and is analysed using the less accurate TCD detector. One should thus expect relatively more experimental error.

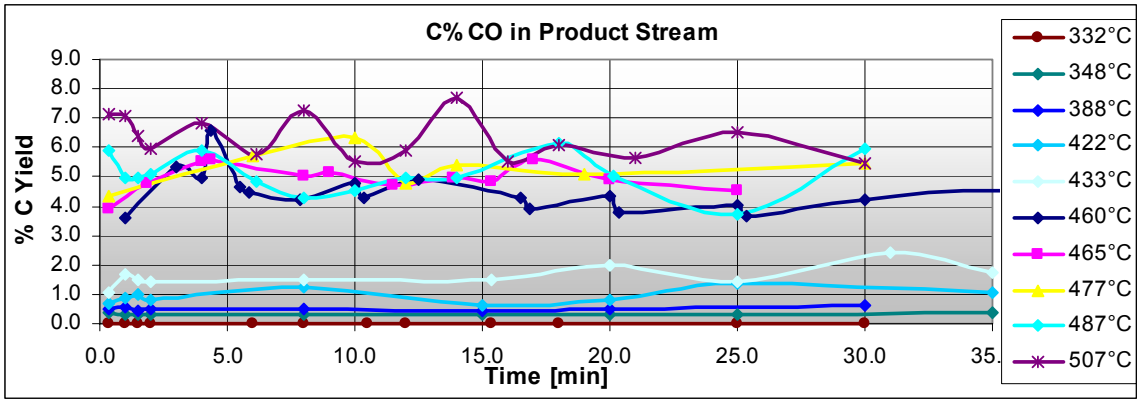


**Figure 75: CO formation in C% as a function of time for a range of reaction temperatures. Exp D1**

Carbon-dioxide was not measured but calculated using a carbon balance. It is done by calculating the amount of carbon dioxide needed to satisfy the carbon balance (carbon in feed stream = carbon in product stream). Any noise in acrolein or CO formation is thus imposed on the $CO_2$ formation. The experimental error and carbon balances can thus be evaluated by looking at the predicted amount of carbon dioxide in the temperature range where there is no carbon dioxide formed. The error in the calculations can be seen by examining run 332°C and 348°C which had very little or no CO formation. The values should thus be steady and close to zero, which is the case (±4%). Run 465°C is an example of inaccurate acrolein measurements, due to a bad sampling technique, leading to an imposed decrease in $CO_2$ formation for the reaction time under 5 min. Unfortunately this technique only allows the evaluation of the carbon balance error under conditions where carbon dioxide is not formed.

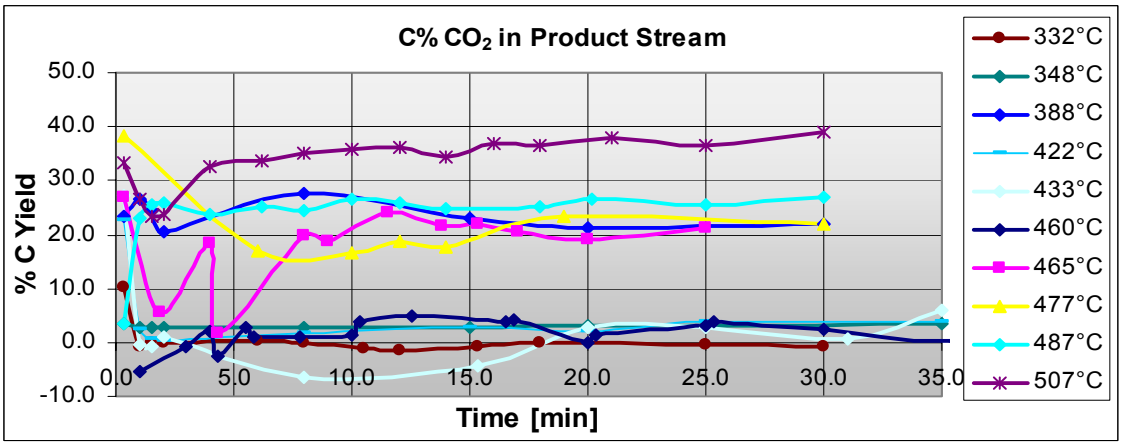


**Figure 76: $CO_2$ formation in C% as a function of time for a range of reaction temperatures. Exp D1**

Initial inaccuracy (time frame) was caused by the switching from the bypass line to the reactor. This could lead to inaccurately high initial conversions being obtained.

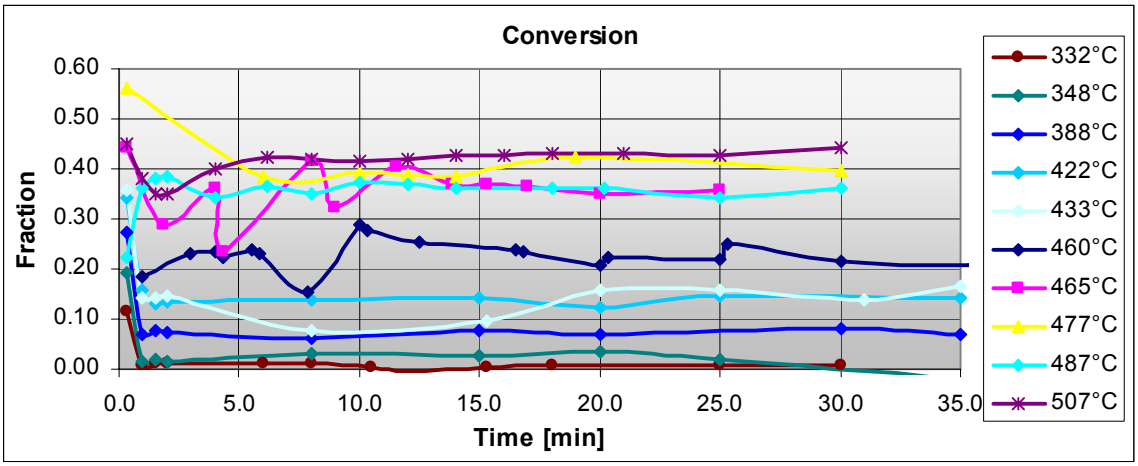


**Figure 77: Conversion as a function of time for a range of reaction temperatures. Exp D1**

The data was used to generate an Arrhenius plot for different times on stream. In order to do this a rate model and reaction orders were needed. The model of Haber and Brückman [1988] (equation 13, page 2-17) was used combined with the reaction orders obtained by Keulks and Krenzke [1980[c]] (Table 3, page 2-15) for $\alpha$-$Bi_2Mo_3O_{12}$. Trends were fitted to Figure 77 and a smoothened acrolein formations in Figure 78 were generated using the model functions.

The specific rate of acrolein formation was calculated using equation 31 (page 4-69) and the reaction constant (k) using the model proposed by Haber and Brückman [1988] and the reaction orders of Keulks and Krenzke [1980[c]] (Table 3, page 2-15). The Arrhenius plot for the formation of acrolein is shown in Figure 79.

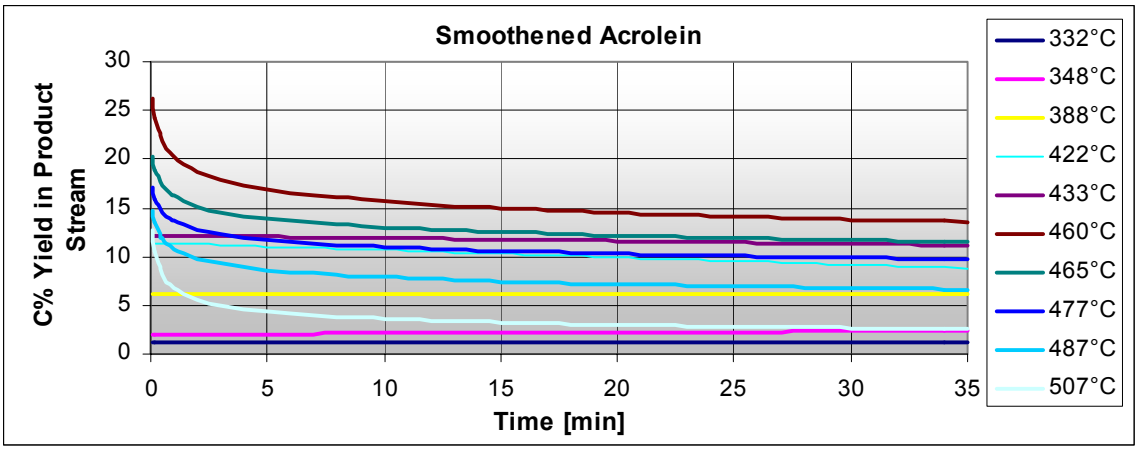


**Figure 78: Smoothened acrolein formation in C% of product stream as a function of time for a range of reaction temperatures. Exp D1**

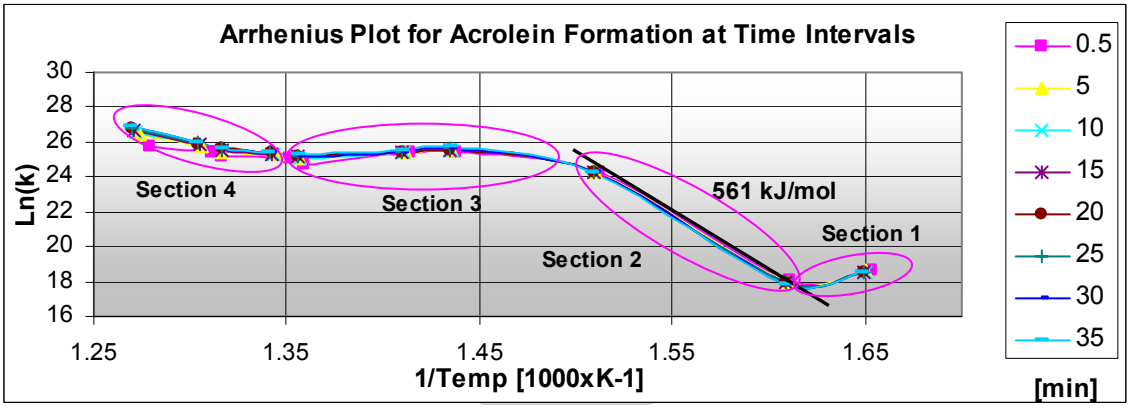


**Figure 79: Arrhenius Plot for Acrolein formation at different time intervals in minutes.**

The Arrhenius plots are shown for different time intervals (scale in minutes). The resulting curve can be divided in four sections corresponding to 330°C-350°C, 350°C-410°C, 420°C-460°C and 460°C-500°C called sections 1, 2, 3 and 4 respectively. Each section indicates a change in limiting step or a change in mechanism. The change from section 1 to section 2 at 350°C corresponds well with the change in mechanism, from the hydro-peroxide to the redox mechanism suggested by Keulks *et al.* [1980[a]]. They showed that acrolein is formed exclusively via the redox mechanism in the temperature range 350°C to 450°C. This means that the change in slope from section 2 to 3 is due to a change in limiting step which corresponds with both the findings of Keulks *et al.* [1980[b]] and Haber *et al.* [1988]. At temperatures higher than 460°C another change is observed, most probably a change in mechanism (a fraction of the acrolein is consumed in a gas

phase reaction). For this study the temperature range of 350-450°C is of particular interest. The activation energy for section 2 is found to be 561 kJ/mole. The slope for section 3 is positive suggesting that the model may not be sufficient to explain the results. If the plots for the different times on stream is evaluated it can be seen that after 10 min on stream (on-line) the samples stabilised. It is also evident from the plot that there are not enough data points to make accurate measurements.

### 5.5.10 Reaction Kinetics (Exp. D2)

The same catalyst was used throughout Experiment D2 and was reoxidized using 20% oxygen-helium mixture and then pure oxygen between every run. Four to five samples were taken 30 seconds apart after 10 minutes on stream for each run and an average product formation for the samples were used. A WHSV of 3 $g_{propene}/g_{catal}$.hr was used with a $C^{=}_{3}$:$O_2$:He ratio of 1:2:7. Figure 80 shows the product formation for acrolein, CO and $CO_2$ (calculated) as a function of temperature.

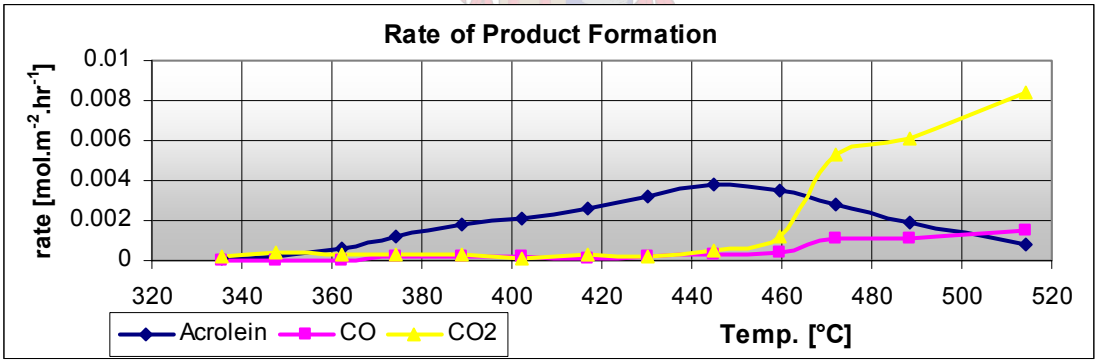


**Figure 80: Rate of product formation (mole/m$^2$.hr) as a function of temperature.**

In the model used by Keulks and Krenzke [1980[c]] (equasion 8, page 2-15) they used a parameter, $\Theta_{ox}$ describing the fraction of active sites which are fully oxidised. This results in the rate of acrolein formation being described by the following function:

$$\frac{d[Acrolein]}{dt} = k_o e^{\frac{-E}{RT}} P_{C_3} P_{O_2} \Theta_{ox} \qquad \text{....35}$$

In Figure 5 (page 2-16)) the fraction of fully oxidised sites is a function of the ratio of rate of re-oxidation to the rate of reduction. At low temperatures the catalyst surface is well reduced due to a slow re-oxidation rate, and at higher temperatures it is in a high oxidative state. To calculate the active site oxidative state, $\Theta_{ox}$ as a function of temperature both the activation energies and pre-exponential factors for both the rate of re-oxidation and reduction are needed (the activation energies are shown in Tables 3 and 4, on page 2-15 and 2-18). To add more complexity to the already complex system it should be noted that the activation energies (and their pre-exponential factors) for both the rate of reduction and rate of re-oxidation are dependant on the temperature regimes and oxidative states. This also brings up the problems of model compatibility for different published data.

Grasselli *et al.* [1980[a]] investigated the kinetics of catalyst re-oxidation and defined the initial reduction state of the catalyst in molar amount of lattice oxygen removed per surface area. To convert this molar amount reduction to the fraction of active sites fully oxidised, $\Theta_{ox}$ , the molar amount of surface and bulk lattice oxygen available for utilisation should be known. The percentages of lattice oxygen that can participate in the reaction are summarised in Table 5 (page 2-21) [Keulks *et al.,* 1979] and are also a function of temperature. This also raises the question of the type of lattice oxygen involved in the hydrocarbon activation and oxidation and surface and bulk diffusion, studied by Ono *et al.* [1998]. Another factor that should be kept in mind is that of the multi active site reaction mechanism. This implies that the rate of re-oxidation for different required sites (Table 6, page 2-24) can influence the abundance of adjacent sites which are needed for the reaction. Grasselli *et al.* [1980[b]] also suggests a crystal restructuring after the loss of a critical number of oxygen ($\pm 0.355 \times 10^{19}/m^2$) which means that the reaction order for the oxidative state parameter, $\Theta_{ox}$ could change as well.

Another problem is that of the pre-exponential constants. If the models and reaction conditions for different published data were different the pre-exponential constants derived from the Arrhenius plots will not be compatible and cannot be used together.

At this stage it is thus impossible to calculate the fraction of fully oxidised active sites as a function of temperature which is needed for the second model. Using chosen values for $\Theta_{ox}$ (Figure 81) an Arrhenius plot (Figure 82) was generated using both the first and second models. The fractions of fully oxidised sites were chosen over a temperature range so as to obtain an Arrhenius plot with a slope that corresponds with the activation energy published by Keulks and Krenzke [1980[a]] for the 410°C to 450°C region. The slope, and thus the activation energy, for the 350°C to 410°C region changed slightly to 590 kJ/mole. This chosen values for $\Theta_{ox}$ formed an s-curve and corresponds with Keulks and Krenzke's [1980[a]] reasoning: At low temperatures the catalyst surface is well reduced due to a slow re-oxidation rate, and at higher temperatures it is in a high oxidative state with propene activation being the limiting-step (see Figure 81).

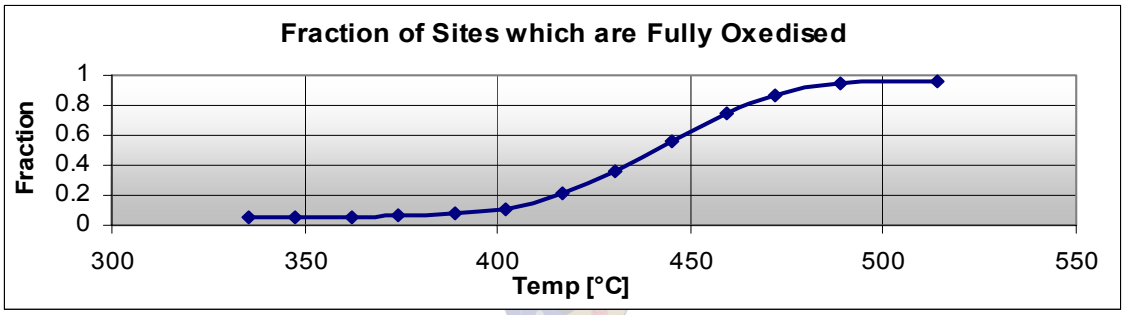


**Figure 81: Fraction of fully oxidised active sites as a function of temperature.**

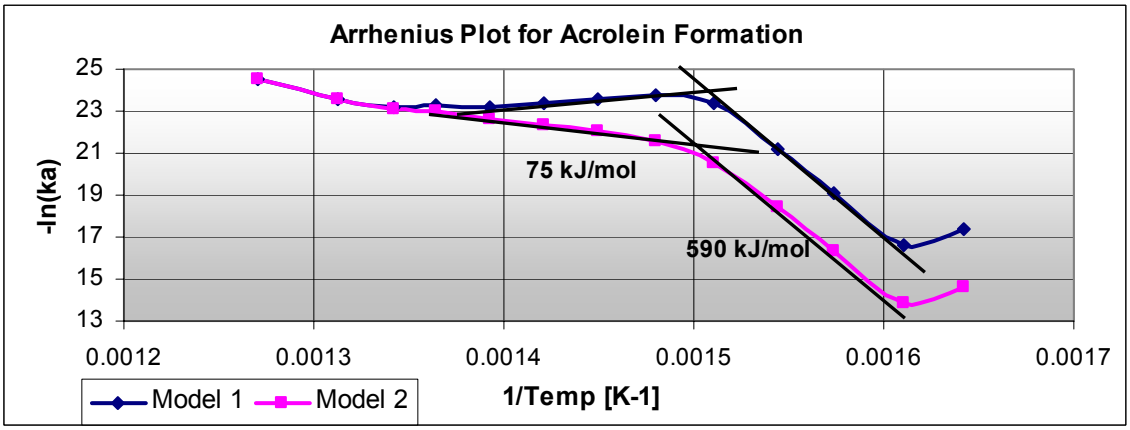


**Figure 82: An Arrhenius plot for Experiment D2 evaluated using models 1 and 2.**

This result suggests that the model of Keulks and Krenzke [1988] (model 2) is the more likely model to describe the kinetic results. Expanded models to describe the surface and subsurface oxidative state separately, may describe the kinetics even better. This reasoning is consistent with the results of Grasselli *et al.* [1980[b]] who suggested a crystal restructuring after the loss of a critical number of oxygen.

By changing the reaction conditions (very low WHSV and high $O_2$ partial pressures) it could be possible to keep the catalyst in a high oxidative state resulting in oxidative state parameter, $\Theta_{ox}$ being closer to one through out the temperature range of 350 to 450°C which will simplify the modelling.
More kinetic experiments, both in catalyst reduction and re-oxidation, need to be done over a wide range of reaction conditions in order to develop a representative kinetic model. This also includes and requires development in model parameters which are theoretically or empirically obtainable and quantifiable.

### 5.5.11 Limitations of Kinetic Experiments

The kinetic experiments were limited to what the reaction rig allowed. Very small WHSV is difficult to attain which is needed to study the catalyst in a high oxidative state. The problem of small WHSV was effectively solved by Grasselli *et al.* [1980] using a pulse micro-reactor method.

The reaction orders for the reactants could not be measured due to the lack of accurate reactor pressure readings or reactor pressure control, published data was thus used.

Much more experimental work is needed to give conclusive results on the modelling of the reaction kinetics.

Although the $CO_2$ formation was calculated using the carbon balance, it is not ideal. The molecular sieve packed column used may be replaced by a column that will effectively separate $CO_2$ or a more expensive CO-$CO_2$ analyser can be used on line.

# 6. Conclusions

## *6.1 Catalyst Preparation*

### 6.1.1 The Reverse Micelle Technique to Synthesise Nano-Sized Particles

When the reverse micelle technique was investigated as a whole, its subsequent steps and their possible operating windows were identified and are summarised in section 5.2. Although discrete nano-sized particles could be produced within the range 3.5-20 nm there was no size control over the outcome and, in most cases, there was some degree of particles sticking to each other. It was also found that nanorod formation occurred when the nano-sized particles were heated or aged in the presence of a surfactant, and the size-controlling parameters were again unknown. In this study attempts to support the catalyst particles on a catalytic inert particle were unsuccessful. It was evident that more in-depth studies has to be done in order to achieve particle size control and the liberation of calcined particles. The following sections will describe the investigations of the different steps and aspects of the reverse micelle technique.

### 6.1.2 Low-Temperature Calcination

- Pure $\alpha$-$Bi_2Mo_3O_{12}$ can be prepared by the method proposed by Keulks *et al.* [1974]. The 2/3 (Bi/Mo ratio) precipitate and the $\alpha$-$Bi_2Mo_3O_{12}$ calcined product are a pale, almost white, powder.
- The pH in the Keulks co-precipitation method should be kept above 1.3 (preferably at 1.5) in order to avoid the formation of $\beta$-$Bi_2Mo_2O_9$ which cause the precipitate to turn yellow.
- XRD studies of a temperature range calcination show that the calcination of the 2/3 (Bi/Mo ratio) precipitate may be achieved at temperatures as low as 200°C and at temperatures of 280°C or higher the calcination goes to completion (calcination period of 24 hrs).

- A three-step mass decrease obtained by a TGA on uncalcined precipitate indicating that $Mo_{18}O_{56}(H_2O)_8^{4-}$ or its double, $[Mo_{36}O_{112}(H_2O)_{16}]^{8-}$, may be responsible for the 2/3 precipitate formation.
- Simultaneous DSC and TGA analysis show that solid-state crystal formation occurs at 350°C, most probably being the formation of □-Bi2Mo3O12 crystalline structures. This temperature is much higher than the temperature indicated by the XRD experiments. This indicates that the calcination temperature may be decreased below 350°C but a much longer calcination period is needed.

### 6.1.3 Simple Precipitation Method

- A maximum of 24-27 ml of concentrated $HNO_3$ is needed to acidify one mole of molybdate in solution to a pH of 1.6-1.3 independent of the concentration ([Mo] = 0.2-0.5).
- Using a Bi/Mo ratio of 2/3 corresponds to 36-41 ml of concentrated $HNO_3$ being available for the dissolution of one mole of bismuth nitrate in order not to decrease the pH of the bismuth-molybdate mixture below 1.3. Only a very small low pH (almost concentrated acid) operating window, in which a merely stable salt solution exists, was found (Fig. 58). This extremely low pH (almost concentrated acid) was foreseen to be a problem when it was to be added to the oil-surfactant mixture to form reverse micelles and addition stability (stability of the bismuth when it was mixed with a higher pH molybdenum solution) was in doubt.
- By adding ammonium to the molybdenum salt before the bismuth salt is added to the molybdenum solution does not increase the final pH above the crucial value of 1.3 with out adding to the complexity of the system. This ammonium addition causes the reversing in subsequent polyanion species formation.
- A simple precipitation (mixing of two stable salt solutions to attain the precise operating condition) is possible if an excess of molybdenum is used to buffer the mixture when the low pH bismuth solution is added. $MoO_3$, however, is formed as an impurity in the precipitate. The $MoO_3$ can be successfully and selectively removed using a warm ammonium wash of the calcined precipitate mixture, followed by a hot water rinse and a recalcination step.

### 6.1.4 Formation and Stability of Reverse Micelles

- The Malvern Zetasizer 1000HS appears to give accurate, easily obtainable and reproducible results in the size analysis of reverse micelles.
- A degree of uncertainty exists about what analysing models to use in the size and size distribution calculations of the reverse micelle. Both second and third order correlation fits, using the mono- and CONTIN models, give good results.
- Calibration of the Zetasizer could not be done accurately due to too many varying parameters. All sizes are thus relative sizes.
- The reverse micelles appear to be a dynamic system that is strongly influenced by surfactant and aqueous concentration, salinity and type of salt solution.
- The use of a sonic bath to mix and break up the aqueous phase into small droplets decreases the initial droplet sizes and results in a much more uniform size distribution compared to using a magnetic stirrer.
- Micelle growth occurs over time due to the Ostwald ripening effect. Another initial size-decreasing mechanism comes into play at low salinities and high aqueous concentrations that are unknown.

## *6.2 Kinetic Studies*

- The metal reactor gave much better results than the glass reactor. It showed much better plug flow characteristics, thermal exchange and was found to be catalytically inactive. Moreover, it was more robust and easier to work with than the glass reactor.
- The reactor rig and analysing apparatus were adequate for these kinetic studies. The reaction experiments were accurate (carbon balance of ±4%) and reproducible, but very time-consuming. The experimental procedures were evaluated and optimised in preliminary experimental runs and is summarised in Appendix D.
- $CO_2$ formation could not be measured and had to be calculated using a carbon balance.

### 6.2.1 Reaction Kinetic Studies Using Keulks's $\alpha$-$Bi_2Mo_3O_{12}$

- The model used by Haber *et al.* [1988] was found to be insufficient to describe the kinetic results obtained.
- The model used by Keulks and Krenzke [1980[a]] was able to describe the kinetic result but the parameter describing the oxidative state of the catalyst surface could not be calculated due to the lack compatibility between published models. Values were awarded to this parameter so to give an Arrhenius plot which corresponded to published data. The parameter describing the oxidative state vs. temperature took on a function that was consistant with the reasoning of Keulks and Krenzke [1980[a]].
- More kinetic experiments, both in catalyst reduction and re-oxidation, need to be done over a range of reaction conditions in order to develop a representative kinetic model. This requires advancement in model parameters which are theoretically or empirically obtainable and quantifiable

### 6.2.2 Reaction Kinetic Studies Using Nano-Sized Catalyst Particles

Unfortunately the catalyst preparation studies have not progressed to the stage where the required particle size range could be synthesized. Comprehensive preliminary kinetic studies are also needed to determine the reaction conditions and models needed to describe the reaction kinetics sufficiently.

# 7. Recommendations

## *7.1 Catalyst Preparation*

Although much was accomplished in this study, more investigations into the constituent steps of the reverse micelle technique are needed to ultimately develop a method to synthetise the range of discrete catalyst particle sizes required for kinetic studies. The most important step to attain size control seems to be that of the formation and mixing of the reverse micelles, which was only touched on in this study. The Malvern Zetasizer was shown to be a helpful tool to obtain insight into the dynamics and stability of reverse micelles. It could also be used to determine particle sizes and size distributions for particles larger than 20 nm if the results are verified by the TEM results. Sensitive conductivity measurements may also give insight into the stability and formation of reverse micelles.

In this study, the oil-surfactant system only allowed the formation of reverse micelles by the addition of a small amount of aqueous phase to the oil-surfactant mixture. Other methods, like the PIT method described in section 2.2.3.2, allow much larger aqueous fractions and micelle size-controlling options. The other methods and particle size-controlling parameters are presided over by oil-surfactant systems. Longer-chained oils, like decane, dodecane and tetradecane, are typical oil systems studied in the literature and might be worthwhile investigating in future studies.

The problem of sintering, supporting and preventing the agglomeration of particles may be solved by using a high-pressure cell in which particles are calcined while being dispersed in water and heated to 350-360°C, resulting in a pressure of 170-190 bar. Sedimentation can be prevented by rotating the sell in the oven. Particle agglomeration due to evaporation on the liquid-phase boundary layer may be prevented using a similar high-pressure technique. Heating the particles suspended in water to a temperature of 180°C will result in a pressure of 10 bar and an enthalpy of the water being 2780 kJ/kg. The enthalpy for the liquid under these conditions is similar to the enthalpy of vapour at 100°C and at atmospheric pressure. Thus, if the vapour was to be released slowly from

the cell the critical liquid will be vaporised. This vaporising is not confined to a boundary layer and will most probably be initiated at irregularities on the particle surfaces, resulting in the particles being liberated after the liquid is evaporated.

## *7.2 Kinetic Experiments*

It is important that the reaction pressures are measured accurately and that theh can be controlled before accurate reaction order experiments can be done. Reactor head pressure was measured upstream from the reactor resulting in the pressure increasing due to pressure losses over the tubing. A separate open line should be used to evaluate the pressure inside the reactor (see Figure 83). The pressure control can be achieved by inserting a needle valve in the reactor outlet line as shown in figure.

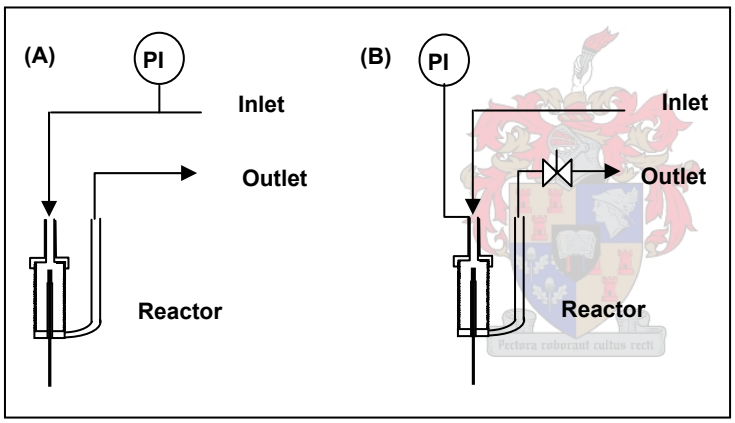


**Figure 83: Pressure measurement and control changes. A, present configuration; B, proposed configuration.**

The mass flow controller which controls the internal standard flow rate only works effectively when the head pressure to the controller is below 0.5 bar. If the pressure is increased the controller cannot control at low flow rates. This will cause problems when low flow rates are required. The controller thus needs to be repaired.

Comprehensive preliminary kinetic studies are needed in order to determine the reaction conditions, explore more advanced kinetic models and investigate model parameters which are theoretically or empirically obtainable and quantifiable.

# 8. References

**Primary references**


Agenbag, J., Final Year Project, Chem Eng, US, (2003), Selective Oxidation of Propene to Acrolein on $Bi_2Mo_3O_{12}$ Catalyst

AsahiKasei Press Release, 2000, http://www.asahikasei.co.jp/asahi/en/news/2000/e001026.html.

Ayame, A. and Uchida, K., Applied Catalysis A: General, 227 (2002) 7-17, X-ray Photoelectron Spectroscopic Study on α- and γ-BiMoO Surfaces Exposed to Hydrogen, Propene and Oxygen.

Ayame, A. and Uchida, K., Surface Science 357-358 (1996) 170-175, Dynamic XPS measurements on bismuth molybdate surfaces.

Aykan, K., J. Catal. 12 (1968) 281-290, Reduction of $Bi_2O_3$-$MoO_3$ Catalyst During the Ammoxidation of Propylene in the Absence of Gaseous Oxygen.

Baes, C.F. and Mesmer, R.E., The Hydrolysis of Cations, Publication John Wiley and Sons, N.Y.

Batist, PH. A.,. Der Kinderen, A.H.W.M, Leeuwenburgh Y. and. Schuit, G. C. A, J. Catal, 12 (1968) 45-60, The Catalytic Oxidation of 1-Butene over Bismuth Molybdate Catalyst.

Batist, PH. A., Bouwens, J. F. H. and Schuit, G. C. A., J. Catal, 25 (1972) 1-11, Bismuth Molybdate Catalyst. Preparation, Characterization and Activity of Different Compounds in the Bi-Mo-O System.

Bender, C. M., Burlitch, J. M., Chem. Mater. 12 (2000) 1969-1976, Synthesis and Fluorescence of Neodymium-Doped Barium Fluoride Nanoparticles

Bettahar, M.M., Costentin, G. and Lavalley, J. C., Appl. Catal. A: General 145 (1996) 1-48, On the Partial Oxidation of Propane and Propylene on Mixed Metal Oxide Catalyst.

Bleijenberg, A. C. A. M., Lippens, B. C. and Schuit, G. C. A., J. Catal 4 (1965) 581-585, Catalytic Oxidation of i-Butene over Bismuth Molybdate Catalyst.

Bouchemal, K., Briancon, S., Perrier, E. and Fessi, H., International Journal of Pharmaceutics 208 (2004) 241-251, Nano-Emulsion Formation using Spontaneous Emulsification: Solvent, Oil and Surfactant Optimisation

Callanhan, J. L., Formane, R. W. and Veatch, F. US Patent 3,044,966, 1962

Carrazán, S.R.G, Martín, C., Rivers, V. and Vidal, R., Spectrochimica Acta Part A 52 (1996) 1107-1118, An FT-IR Spectroscopic Study of the Adsorption and Oxidation of Propene on Multiphase Bi, Mo and Co Catalyst.

Chen, T., Journal of Crystal Growth 20 (1973) 29-37, Crystal Growth of $BaMoO_4$, $Bi_2O_3$-$3MoO_3$ and from Molten Salt Solution by "pulling seed" Method.

Chen, H.-Y.and Sleight, A.W., J. Solid State Chem. Volume 63, (1986) 70

Cruywagen, J.J., Advances in Inorganic Chemistry, Vol. 49 (2000) 127-182, Protonation, Oligomerization, and Condensation Reactions of Vanadate(V), Molybdate(IV) and Tungstate(VI)

Cruywagen, J.J., Draaijer, A.G., Heyns, J.B.B.and Rohwer, E.A., Inorganica Chimica Acta 331 (2002) 322-329, Molybdenum(IV) Equilibria in Different Ionic Media. Formation Constants and Thermodynamic Quantities.

Curri, M.L., Agostiano, A., Mavelli, F.and Della Monica, M., Materials Science and Engineering C 22 (2002) 423-426, Reverse Micellar Systems: Self Orgenised Assemgly as Effective Route for the Synthesis of Colloidal Semiconductor Nanoparticles

Devillers, M., Tirions, O., Cadus, L., Ruiz, P. and Delmon, B., Journal of Solid Sate Chemistry 126 (1996) 152-160, Bismuth Carboxylates as Precursors for the Incorporation of Bismuth in Oxide-Based Materials.

Eriksson, S., Nylén, U., Rojas, S. and Boutonnet, M., Applied Catalysis A: General, In Press, Preparation of Catalysts from Micro Emulsions and their Applications in Heterogeneous Catalysts

Fogler, H.S., Elements of Chemical Reaction Engineering, 3de Edition, Prentice Hall International Series in the Physical and Chemical Engineering Sciences, 1999

Forgiarini, A., Esquena, J., Gonzalez, C. and Solans, C., Langmuir 17 (2001) 2076-2083, Formation of Nano-Emulsification Methods at Constant Temperature.

Ghule, A.V., Ghule, K.A. and Tzing, S., Chemical Physics Letters 383 (2004) 208-213, Pyridine Intercalative Sonochemical Synthesis and Characterization of a-$Bi_2Mo_3O_{12}$ Phase Nanorods.

Godard, E., Gaigneaux E.M. and Ruiz, P., Catal. Today. 61 (2000) 279-285, New Insights in the Understanding of the Behaviour and Performance of Bismuth Molybdate Catalysts in Oxygen-assisted Dehydration of 2-butanol

Gazzoli, D., Anichini, S., De Rossi, S., Inversi, M. and Lo Jacono, M., J. Catal. 119 (1989) 277-287 and J. Catal 100 (1986) 95-102, Structural, Surface and Catalytically Properties of Bismuth Molybdovanadates Containing Foreign Atoms

Grasselli, R. K., Catal Today 49 (1999) 141-153, Advances and Future Trends in Selective Oxidation and Ammoxidation Catalysts

Grasselli, R.K., Burrington J.D. and Kartisek, C.T, J. Catal 87 (1984) 363-380, Surface Intermediates in Selective Propylene Oxidation and Ammoxidation over Heterogeneous Molybdate and Antimonate Catalyst

Grasselli, R.K., Burrington J. D., and Brazdil, J.F., Discuss. Faraday Soc., 72 (1981) 203, Mechanistic Features of Selective Oxidation and Ammoxidation Catalyst

Grasselli, R.K. and Burrington J.D., Advances in Catalysis, Volume 30 (1981) 133-161, Selective Oxidation and Ammoxidation of Propylene over Heterogeneous Catalyst

Grasselli, R.K. and Brazdil, J.F. and Suresh, D.D., J. Catal 66 (1980[a]) 347-367, Redox Kinetics of Bismuth Molybdate Ammoxidation Catalysts

Grasselli, R.K., Burrington J.D. and Kartisek, C.T., J. Catal 63 (1980[b]) 235, Aspects of Selective Oxidation and Ammoxidation Mechanisms over Bismuth Molybdate Catalysts

Greek, B.F., Chem. Eng. News, May 29 (1998) 29

Hanna, T. A., Coordination Chemistry Reviews (2004) In Press, The Role of Bismuth in the SOHIO Process.

Haber, J. and Brückman, K., J. Catal. 114 (1988) 196-199, Kinetics of the Oxidation of Propene on $MoO_3$ Based Model Catalysts.

Haber, J., Brückman, K., Wiltowski, J. and Grabowski, R., J. Catal., 104 (1987[a]) 71-79, The role of Different $MoO_3$ Crystal Faces in Elementary Steps of Propene Oxidation.

Haber, J., Brückman, K. and Wiltowski, J., J. Catal., 106 (1987[b]) 188-201, Active Sites for Reactions of Olefin Molecules at Surfaces of Molybdate Catalysts.

Idol, J. D., US Patent 2,904,580, 1959

Incropera F.P., and De Witt, D.P., Fundimentals of Heat and Mass Transfer, 4th edition, John Wiley and Sons, New York, 1996

Izquierdo, p., Esquena, J., Tadros, Th. F., Dederen, C., Garcia, M.J., Azemar, N. and Solans, C., Langmuir 18 (2002) 26-30, Formation and Stability of Nano-Emulsions Prepared Using the Phase Inversion Temperature Method

Keulks, G.W. and Daniel, C., J. Catal. 24 (1972) 529-535, The Catalytic Oxidation of Propylene.

Keulks, G.W., Hoefs, E.F. and Monnier, J.R., J. Catal 57 (1979) 331-337, The Investigation of the Type of Active Oxygen for the Oxidation of Propylene over Bismuth Molybdate Catalyst Using Infrared and Raman Spectroscopy

Keulks, G.W. and Krenzke, L.D., J. Catal. 61 (1980)[a] 316-325, The Catalytic Oxidation of Propylene

Keulks, G.W. and Krenzke, L.D., J. Catal. 62 (1980)[b] 295-302, The Catalytic Oxidation of propylene

Keulks, G.W. and Krenzke, L.D., J. Catal. 64 (1980)[c] 295, The Catalytic Oxidation of Propene.

Keulks, G.W., Hall, J. L. and Daniel, C., J. Catal, 34, (1974) 79-97, Catalytic Oxidation of Propylene: Preparation and Characterization of $\alpha$-Bismuth Molybdate

Keulks, G.W., J. Catal 19 (1970) 232, The Mechanism of Oxygen Atom Incorporation into the Products of Propylene Oxidation over Bismuth Molybdate

Kihlborg, L., Ark. Kemi, Volume 21 (1963) 357

Kunieda, H., Fukui, Y., Uchiyama, H. and Solans, C., Langmuir 12 (1996) 2136-2140, Spontaneous Formation of Highly Concentrated Water-in-Oil Emulsions (Gel-Emulsions)

Mabaso, E.T., Catal. Research, Dep. Chem. Eng, University of Cape Town, Synthesis of Nano-Oxides using Water-in-oil Microemultion System

Magagula, Z., MSc (Chem.Eng), University of Cape Town, (1999), Initial Activety and Selectivity in the (amm)oxidation of Propene and Propane Over Iron Antimony Oxide

Malvern Training Manual, issue 1.3, www.helpdesk@malven.co.uk

Marinova, V. and Veleva, M., Optical Materials 19 (2002) 329-333, Reflective Index Measurements and Transmission Spectra of $Bi_2(MoO_4)_3$ Single Crystals

Miura, H., Arai, Y., Sugiyama, K. and Matsuda, T., J. Catal. 68 (1981) 264-269, Mechanism of 1-Butene Oxidation in Connection with the Layered Structure of $Bi_2MoO_6$ Catalyst.

Miyazawa, S., Kawana, A. and Koizumi, H., Mat. Res. Bull. Vol. 9 (1974) 41-52, Single Crystals in the $Bi_2O_3$-$MoO_3$ Binary System: Growth and Optical Properties.

Ono, T., Ogata, N. and R.L. Kuczkowski, J. Catal 175 (1998) 185-193, Tracer Studies of Olefin Oxidation over an $\alpha$-$Bi_2Mo_3O_{12}$ Catalyst Using laser Raman and Microwave Spectroscopy.

Perry, R.H. and Green, D.W., Perry's Chemical Engineer's Handbook, 7$^{th}$ edition (1998) McGraw-Hill International Editions

Swart, J. C. W., Final Year Project, Chem Eng, US, (2002), Selective Oxidation of Propene to Acrolein on $Bi_2Mo_3O_{12}$ Catalyst

Tadros, T., Izquierdo, p., Esquena, J. and Solans, C., Advances in Colloid and Interface Science 108-109 (2004) 303-318, Formation and Stability of Nano-Emalsions

Tee, J., Final Year Project, Chem Eng, US, (2004), Selective Oxidation of Propene to Acrolein on $Bi_2Mo_3O_{12}$ Catalyst

Theoblad, F. and Laarif, A., Mater. Res. Bull., volume 20 (1985) 653

Trifiro, F., Hoser, H. and Scarle, R. D., J. Catal 25 (1972) 12-24, Relationship between Structure and activity of Mixed Oxides as Oxidation Catalysts

Ueda, W., Han, Y. and Yoshihiko, M., Applied Catalysis A: General 176 (1999) 11-16, Lattice Oxide Ion Transfer Effect Demonstrated in the Selective Oxidation of Propene over Silica-Supported Bismuth Molybdate Catalyst.

Ueda, W. and Moro-oka, Y., Advances in Catalysis, Volume 40, (1994) 233-273, Multicomponent Catalyst: A Highly Functionalized Catalyst System for the Selective Oxidation of Olifins

Ueda, W. and Moro-oka, Y., J. Catal. 101, (1986) 360-368, Catalytic Properties of Tricomponent Metal Oxides Having the Sheelite Structure

Ueda, W. and Moro-oka, Y., J. Catal. 88, (1984) 214-221, Study of Tellurium Oxide Catalysts by $^{18}O_2$ Tracer in the Oxidation of Propylene to Acrolein

Ueda, W. and Moro-oka, Y., J. Catal. 70, (1981) 409-417, Study of Ternary-Component Bismuth Molybdate Catalyst by $^{18}O_2$ Tracer in the Oxidation of Propylene to Acrolein

Weng, Lu-Tao., Applied Catalysis A: General, 81 (1992) 141-213, Phase Coordination and Remote Control Effects in Selective Oxidation Catalyst.

Wragg, R.D., Ashmore, P.G., and Hockey, J.A., J. Catal. 22 (1973) 49, Selective Oxidation of Propene Over Bismuth Molybdate Catalysts: The Oxidation of Propene Using $^{18}O$ Labeled Oxygen and Catalyst

Yanina, S.V. and Smit, R.L., J. Catal. 213 (2003) 151-162, The morphological Evolution of the $Bi_2Mo_3O_{12}$(101) Surface in Air-$H_2O$ Atmosphere.

## Secondary References

Ayame, A., Uchida, K., Iwataya, M. and Miyamoto, M., Applied Catalysis A: General 227 (2002) 7-17, X-ray Photoelectron Spectroscopic Study on $\alpha$- and $\gamma$-Bismuth Molybdate Surfaces Exposed to Hydrogen, Propene and Oxygen.

Tsunoda, T., Hayakawa, T., Imai, Y., Kameyama, T., Takehira, K. and Fukuda, K., Catalysis Today 25 (1995) 371-376, Propene Oxidation Over $MoO_3$ film Deposited on a Au/YSZ/Ag System.

Gaigneaux, E.M., Ruiz, P. and Delmon, B., Catalysis Today (1996) 37-46, Further on the Mechanism of the Synergy between $MoO_3$ and $\alpha$-$Sb_2O_4$ in the Selective Oxidation of Isobutene to Methacrolein: Reconstruction of MoO3 via Spillover Oxygen.

Williams, S., Puri, M., Jacobson, A.J. and Mims, C.A., Catalysis Today 37 (1997) 43-49, Propene Oxidation on Substituted 2:1 Bismuth Molybdates and Vanadates

Botella, P., Lopez Nieto, J.M. and Solsona, B., Journal of Molecular Catalysis A: Chemical 184 (2002) 335-347, Selective oxidation of Propene to Acrolein on Mo-Te Mixed Oxide Catalysts Prepared from Ammonium Telluromolybates

Godard, E., Gaigneaux, E.M., Ruiz, P. and Delmon, B., Catalysis Today 61 (2000) 279-285, New Insight in the Understanding of the Behaviour and Performance of Bismuth Molybdate Catalysts in the Oxygen-Assisted Dehydration of 2-Butanol.

Keulks, G.W. and Monnier, J.R., J. Catal. 68 (1981) 51-66, Catalytic Oxidation of Propylene. IX. The Kinetics and Mechanism over $\beta$-$Bi_2Mo_2O_9$

Grasselli, R.K., Catalysis Today 49 (1999) 141-153, Advances in Future Trends in Selective Oxidation and Ammoxidation Catalysis

# Appendix

## Appendix A
## Preliminary Catalyst Preparation Experiments: (RMT)

## *Experiment A1: Catalyst Synthesis by RMT (Preliminary)*

### Experimental Procedure of Experiment A1

The oil-surfactant mixture was made up by adding 50 g of berol to 400 g of hexane (11.1% berol solution). After the solution was well shaken, a precipitate formed. The solution was aged for a day and divided into eight 50 g samples. Bismuth and molybdate salt solutions were obtained by dissolving $Bi(NO_3)_3 \cdot 5H_2O$ and $H_{24}Mo_7N_6O_{24} \cdot 4H_2O$ salts in distilled water. In the case of $Bi(NO_3)_3 \cdot 5H_2O$, concentrated $HNO_3$ was used to dissolve the salt before the distilled water was added. Table 17 shows the salts used in the individual experimental runs.

**Table 17: Bismuth and molybdate salt concentrations before mixing, Bi/Mo ratios and salt volumes added to 50g oil-surfactant solution for the individual runs.**

| Run | [Mo] | [Bi] | | Bi/Mo | Volume of Each Salt Solution |
|---|---|---|---|---|---|
| | M | M | volume% $HNO_3$ | | ml |
| A | 1.55 | 1.03 | 12.5 | 0.667 | 2 |
| B | 0.77 | 0.52 | 12.5 | 0.667 | 2 |
| C | 0.39 | 0.26 | 6.2 | 0.667 | 2 |
| D | 0.39 | 0.26 | 6.2 | 0.667 | 1 |

In samples A, B and C, 2ml of both the bismuth and molybdate solutions were added to a 50 g clear oil-surfactant solution. In the case of sample D, only 1 ml of each salt was added to the 50 g solution. The micelle mixtures were left to age for 30 min before adding the bismuth micelle mixture slowly (addition time 5 min) to the molybdenum micelle mixture while stirring vigorously for 15 min. A greenish yellow precipitate formed. The product was centrifuged and the clear liquid poured off. Acetone was then added to the precipitate, which was thoroughly washed, after which it was centrifuged and the acetone removed. Wet mixtures of silica particles and catalyst particles were made by using either a fraction of unwashed sample B (catalyst particles still in the water-oil-surfactant mixture, thus berol was still adsorbed on the catalyst particles), or a fraction of the washed sample B (in the presence of acetone). All samples were therefore further dried at 80$^{o}$C for 8hr. The unwashed catalyst and silica mixture did not dry adequately and were dried at 180$^{o}$C for 300 min. A fraction of the dried sample B was weighed to

make up a 10% dry mixture with the silica. The silica mixtures were calcined step wise as follows:

- 25$^{o}$C – 120$^{o}$C in 3hrs
- 120$^{o}$C – 200$^{o}$C in 2 hrs
- 200$^{o}$C – 450$^{o}$C in 4hrs
- 450$^{o}$C for 12 hrs

To determine the size, size distribution and form of the particles, all the samples were investigated under the SEM and TEM. Due to the small size of the particles the SEM results could not be used because individual particles could not be seen.

## Results of Experiment A1

**Sample A**: Both the bismuth and molybdenum micelle solutions were cloudy before the solutions were mixed. As the two micelle solutions were mixed (bismuth into molybdenum) while stirring, a precipitate formed. After letting the mixture stand for about 5 min a double layer was observed. The denser (bottom) layer was white and the less dense (top) layer was greenish. This mixture was centrifuged and the clear liquor pored off. After centrifuging two precipitates were observed in the settled cake, white on bottom and green on top as were seen in the liquid layers. The sample was washed with acetone, dried and yielded a pale yellow powder.

**Samples B, C**: Both the bismuth and molybdenum micelle solutions were somewhat cloudy before they were mixed (bismuth into molybdenum) to form a greenish precipitate. The precipitate settled after 5 min, leaving a clear top liquid. The samples were centrifuged, washed, dried and yielded a pale yellow powder.

**Sample D**: Both the bismuth and molybdenum micelle solutions were initially clear but the bismuth turned cloudy after 10 min of aging before mixing. A greenish precipitate forms with mixing but the centrifuge product also showed two layers, a greenish bottom one and a thin white top layer.

**Sample B + Silica Mix (Unwashed)**: Silica was mixed with the unwashed precipitate (the water-oil-surfactant liquid was not removed) and was left to dry at 80$^{o}$C. In the drying process the silica tends to settle faster than the catalyst precipitate which still hangs in the liquid above the settled silica. As the hexane (oil) is vaporized a catalyst layer is formed on top of the settled silica which causes a non-uniform silica-catalyst distribution. When a slurry was formed (no excess liquid) it was well mixed and dried yielding a pale yellow powder. This powder turned slightly grey after a few days.

**Sample B Silica Mix (Washed)**: A non-uniform silica-catalyst distribution was also observed because of the difference in settling speeds of the catalyst precipitate and the silica particles. The slurry was well mixed and dried to yield a pale yellow (almost white) powder.

**TEM Results:**

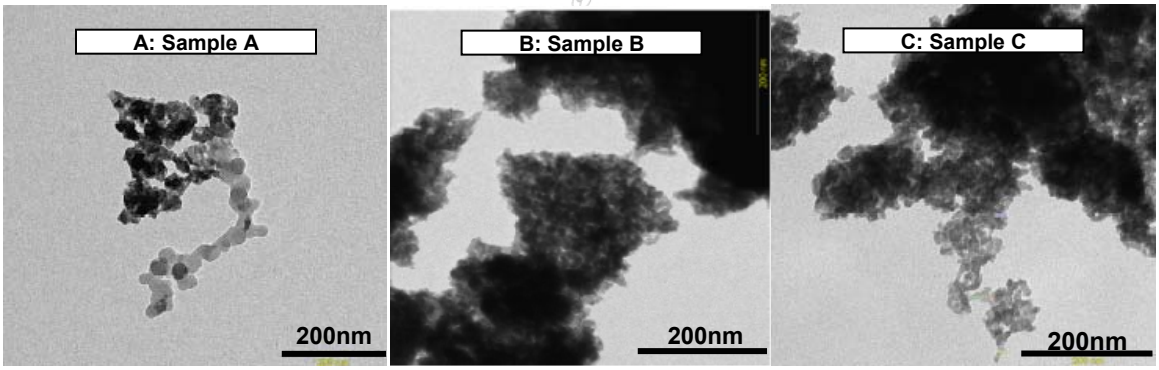


**Figure 84 (A-C): Crystal morphologies observed for samples A, B and C.**

In sample A the catalyst particles observed could be roughly divided into two groups, small spherical particles (6-20nm) and thick chain-like structures (25-30nm) made up of agglomerated large particles. Samples B and C had uniform size distributions but the particles (11-14nm and 8-10nm respectively) tended to conglomerate, making it difficult to determine their sizes.

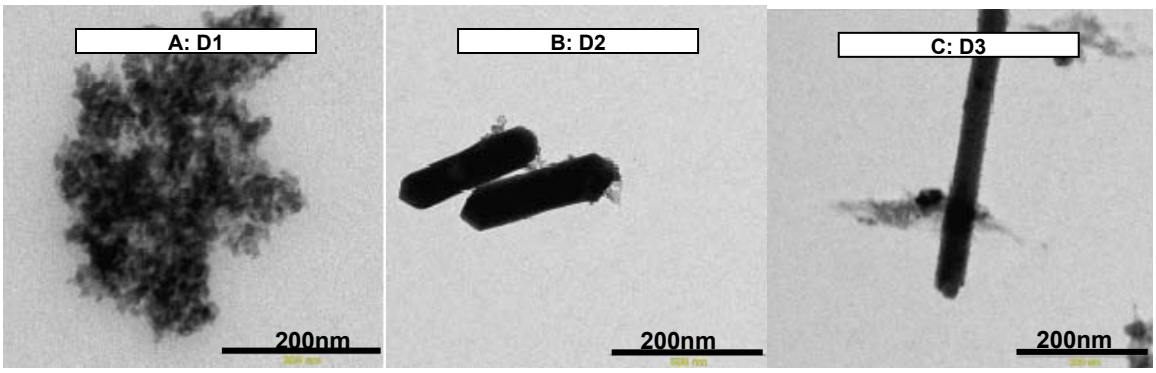


**Figure 85 (A-C): D1: A mixture of particles (8-13nm); D2: Crystals (length 400nm, width 100nm) and D3: nanorods (length 100-1000 nm, width 40 nm).**

Sample D in contrast to sample A, B and C produced a mixture of conglomerated particles (8-13nm), large crystals (length 400nm, width 100nm) and nanorods (length 100-1000 nm, width 40 nm).

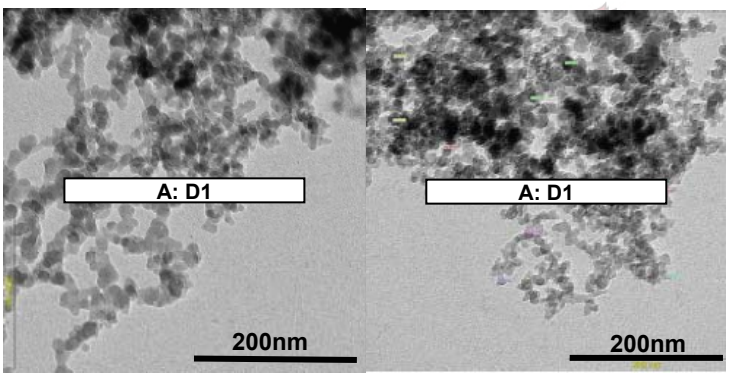


**Figure 86 (A&B): Silica particles: Uniform particles (10-14nm)**

The pure silica samples show a uniform product with a homogeneous size distribution (10-14nm). The silica forms heaps or chain like structures.

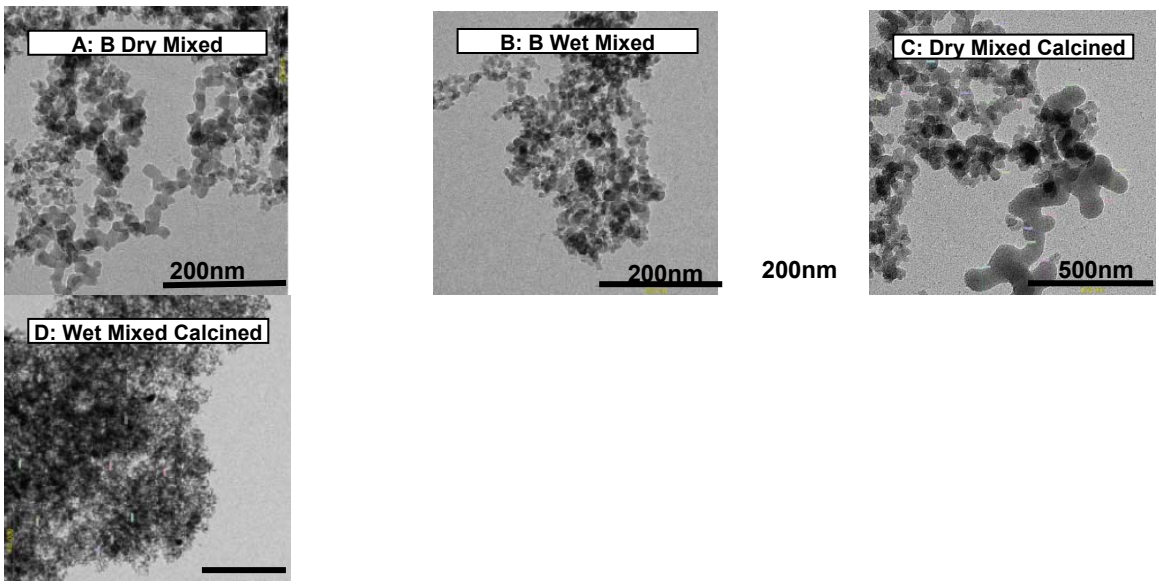


**Figure 87 (A-D): Sample B dry mixed: Large catalyst string and small silica particles. Sample B wet mixed: Uniform particle sizes in both calcined and uncalcined samples.**

A non-uniform catalyst distribution was obtained for the dry-mixed samples both before and after calcination. A more segregated catalyst distribution was obtained for the wet-mixed samples. Even calcination of the wet-mixed samples did not appear to cause agglomeration of catalyst particles. Unfortunately the catalyst and silica particles have roughly the same sizes and thus can not be distinguished from each other. A uniform mixture was observed thus assuming that both the catalyst and silica were evenly distributed.

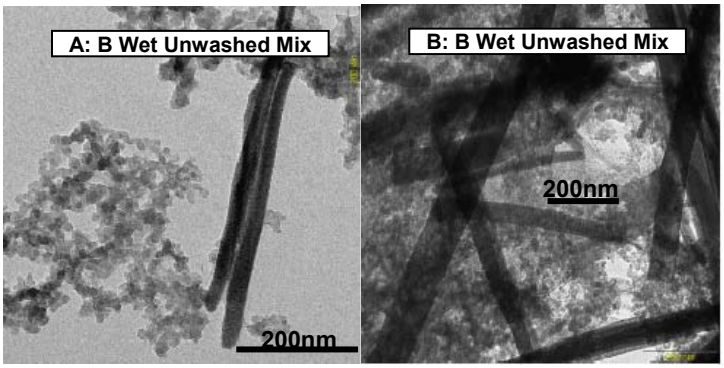


**Figure 88 (A&B): Unwashed catalyst and silica mixture: Mixture of silica particles, catalyst particles and nanorods (length 1000+nm, width 40-150nm).**

The unwashed silica supported sample B, yielded large crystals and nanorods mixed with small particles. These particles, according to their size, are presumably the silica particles that were mixed with the catalyst.

## Discussion of Experiment A1

When the berol and hexane were mixed, an unidentified bushy white precipitate formed, which might be because of impurities in the berol. How it influences the berol-hexane solution and the particle formation was unknown.

The micelle solutions for both bismuth and molybdenum were in most cases cloudy. This might indicates that the micelles were not stable or that the solutions within the micelle were unstable and started crystallizing. The latter could cause the precipitation of pure salts crystals before mixing of the micelle solutions had taken place, and the former would allow the interaction of the species, while not constraint to the micelle dimensions. The latter was observed in sample D where a thin white layer (probably bismuth salt) was found on top of the greenish centrifuged precipitate. The former was observed in sample A where two types of precipitate were formed, these precipitates are also seen in the TEM results.

The most satisfactory results were obtained for samples B and C which yielded particle sizes of 11-14 nm and 8-10 nm respectively. Only agglomerated clusters of particles were observed. This agglomeration of particles could be the effect of static Van Der Waal's forces or a Velcro like sticking effect due to adsorbed surfactant.

Sample D yielded a mixture of particles, crystals and nanorods. The particles being the same sizes as that of sample C (8-10 nm), in which the same salt salinities were used. The dimensions of the nanorods and crystals were much larger, with a width of ±30nm and length from 100 to 1000nm. (The origin of the crystals (Figure 85) might be from the white layer that was observed on the centrifuged product thus could be bismuth related crystals. The white top layer was thin and represented maybe 5% or less of the total solid volume. In the TEM analysis of sample D these similar dimensional crystals were found in quantities representing that of the white layer.)

The silica particles have sizes similar to that of the catalyst particles obtained. It had a homogeneous size distribution and was spherical. When mixed with the catalyst it was very difficult to distinguish between catalyst and silica particles. In the case where silica

was wet mixed with washed catalyst it seemed to give a homogeneous mixture. When it was dry-mixed, the catalyst particles seem to stick to one another. As was expected, the calcined wet mixed sample product was also more homogeneous, Figure 78.

In the sample where the silica was wet mixed with unwashed catalyst particles, crystals and nano rods were formed. This could be explained by the mechanism proposed by Ghule *et al.* [2004] to form nanorods by pyridine adsorption. The surfactant was strongly adsorbed onto the catalyst surface. This causes the catalyst particles to line up which could promote crystal growth and nanorod formation when the sample was dried at high temperatures (ca.180$^{o}$C).

## *Experiment A2: Generation of a Ternary Diagram stability for use in RMT*

### Experimental Procedure 1 of Experiment A2

Mixtures with different oil-surfactant ratios were made by adding various amounts of surfactant to a constant 50 g of oil. Distilled water was then slowly added to ±15 g of the initially clear oil-surfactant mixture using a millilitre syringe. When the micelles were stable, the mixture remained clear, could be distinguished from the cloudy micro emulsion region surrounding it. A few drops of water (±0.1 ml) were added at a time to the mixture which was then shaken well and visually checked for changes.

### Results 1 of Experiment A2

**Surfactant-Oil:** When the surfactant and the oil were mixed a critical amount of surfactant was needed (9.1 mass%) to obtain a clear mixture. Below this critical amount a cloudy solution was immediately formed. A white bushy precipitate formed in the mixtures under a critical berol amount of 16 mass%. The rate at which precipitate formed increased with the decrease in surfactant until it reached the 9.1% (mass) surfactant, at which the solution immediately turned cloudy. This bushy precipitate sunk to the bottom resulting in a clear solution above it. The solution could be filtrated to get rid of the precipitate but due to the high vaporisation of n-hexane it was preferred to carefully remove the top clear liquid with out-mixing the precipitate. When a few drops (±3 drops) of water was added to the oil-surfactant solution (50 ml) in which the precipitate was present, the bushy precipitate broke down forming a small amount of white powder that settled to the bottom.

**Water-Oil-Surfactant:** As water was added to the clear oil-surfactant solution the mass percentages of the individual components change. The following graph shows the different oil-surfactant mixtures which were used and how the components mass percentages change as water was added. If two of the three composition parameters in a ternary diagram are plotted the last one is known.

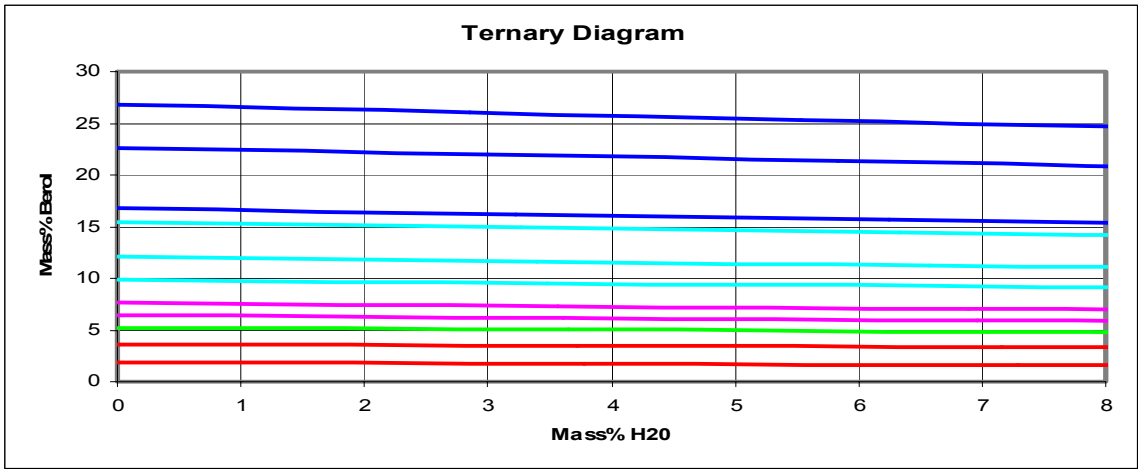


**Figure 89: Water-oil-surfactant ternary diagram. Declining surfactant-oil mass% as water is added.**

- The first two solutions (1.8, 3.5 mass% berol) turned cloudy with the first drop of water and stayed that way for all further addition, thus indicating there are no micelle stability regions at low surfactant percentages.
- The following solution (5.2 mass%) went cloudy with the first drop but cleared up to a clear solution with addition of water till it went slightly cloudy followed by a sudden thickening (increased viscosity), to a gel-like phase, as more water was added.
- The following two (6.4, 7.6 mass%) Went cloudy and then cleared. With the addition of more distilled water it went slight cloudy but the degree of cloudiness did not vary until much more water was added. It also went through a region where it was difficult to dissolve the added water before it went permanently cloudy and later white.
- The next few solutions (9.9, 12.1, 15.5 mass%) went suddenly cloudy and cleared up with the addition of water just like the previous solutions. Then they went through a relatively extended region where the micelles were stable and a clear liquid was observed. When more water was added it became more difficult to dissolve the water and the mixture had to be shaken vigorously for a longer period of time to obtain a clear liquid. Later, the water could not be dissolved and became cloudier with the addition of water till it was white when shaken. If the mixtures were left to stand for a while at this stage a two phase system is observed. The excess water forms a white layer on the bottom of the container.

- All the following solutions (16.8, 22.6 and 26.8 mass %) gave the same results. They went cloudy, followed by a clear stable region. The further addition caused them to become slightly and eventually form an opaque, white mixture.

The following graph summarises the results:

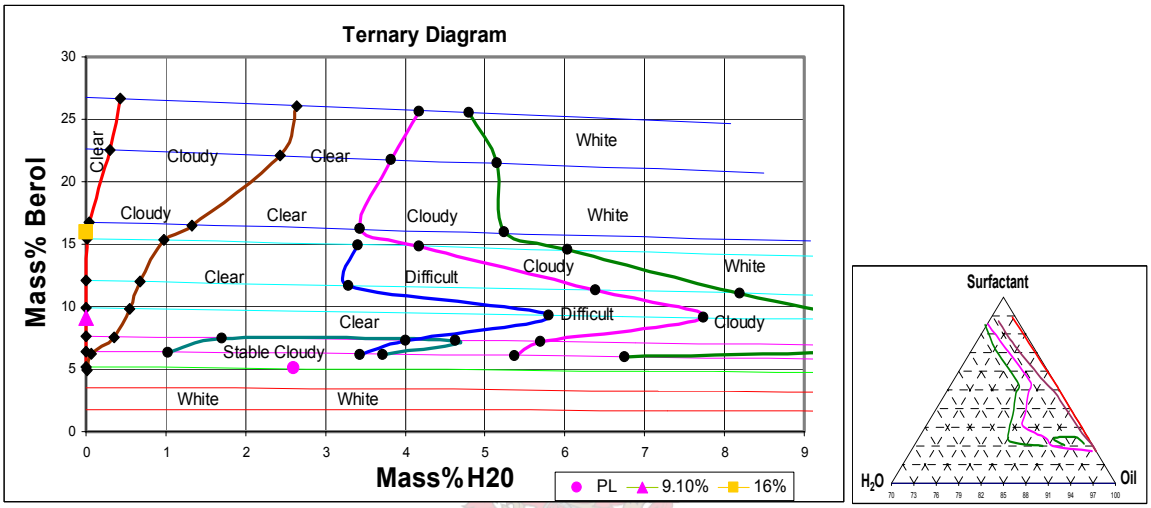


**Figure 90: The different regions observed in the water-oil-surfactant ternary diagram. Clear: Solution is clear; Cloudy: Solution is cloudy; Difficult: not easily dissolved; Stable Cloudy: The slight cloudiness does not change with addition of water; PL: point at which solution are gel like, 9.1% berol-hexane critical point, 16% berol-hexane critical point.**

## Experimental Procedure 2 of Experiment A2

Similar experiments were done by adding distilled water, acidified distilled water (pH=1.5), a molybdenum solution and a bismuth solution to different oil-surfactant ratios to see if there is a significant change in the ternary diagram. The berol-hexane solution was also aged for a week to see if its properties changed. The experiments were as follows:

Distilled water (pH = 6.5) and acidified distilled water (pH = 1.5; $HNO_3$) were tested to see if the pH difference causes a significant change. The bismuth solution (0.05 M) was made by dissolving 0.3396g $Bi(NO_3)_3 \cdot 5H_2O$ in $HNO_3$ and adding 15 ml of distilled water (pH of final solution was 0.85). The molybdate salt (0.07 M, ([Mo] = 0.5)) was prepared by adding 1.2997g $H_{24}Mo_7N_6O_{24} \cdot 4H_2O$ to 15 ml of distilled water, acidifying to a pH of 2.5 with concentrated $HNO_3$. Both 10 and 25 mass% berol-hexane solutions were made up. The berol-hexane solutions were also aged for one week to see if their performance

changed. In each titration, ±15 g of the berol-hexane mixtures were used to add the aqeous phase and visually observed.

## Results of Experiment A2

Consistent with the previous experiments, the 10% berol-hexane solution formed the bushy white precipitate within 10 min and no precipitate was formed in the 25% berol-hexane solution. The stability results for the 10% berol could not be produced accurately using the current experimental setup, thus only the 25% solution will be discussed.

All the starting solutions of berol-hexane were clear liquids and similar results were obtained for all aqueous solutions added. When a specific amount of the aqueous phase was added to the clear solution it suddenly turns cloudy (first cloudy region) and slowly turns clear as more aqueous phase was added. It goes through a stable clear region before turning cloudy again. This subsequent cloudiness increased gradually with further addition of the aqueous phase till the mixture turned white. The compositions of the cloudy and clear regions were found to differ for the various aqueous solutions added to the oil-surfactant solutions and are summarized in Figure 91. The light blue line represents the initial clear solution, the pink the first cloudy region, dark blue the micelle stability region and red the second cloudy region that ends in a white solution.

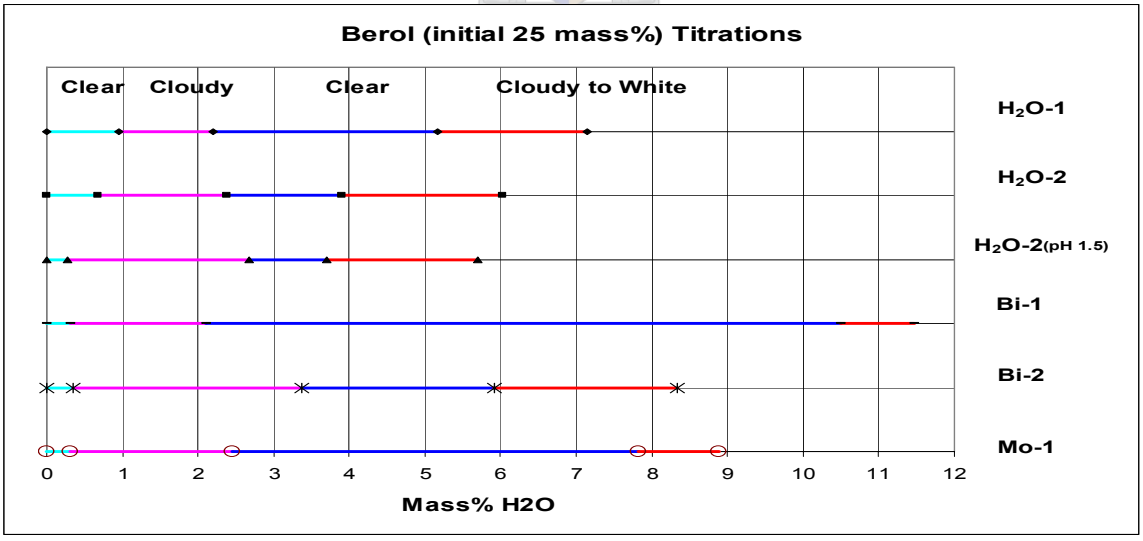


**Figure 91: Various titrations of a 25 mass% berol-hexane mixture showing the clear and cloudy regions. $H_2O$-1: fresh mixtures + distilled water; $H_2O$-2: aged mixture + distilled water; $H_2O$-2-pH1.5: aged mixture + acidified distilled water (pH=1.5); Bi-1: fresh mixture + Bi salt solution; Bi-2: aged mixture + Bi salt solution; Mo-1: fresh mixture + Mo salt solution.**

## Discussion of Experiment A2

It is unclear what forms the bushy precipitate in the region below 16% when berol and hexane are mixed. The solubility curves (Figure 90) also seem to have a turning point on the 16% mark which can not be explained. The reverse micelle stability region for distilled water was shown to be at berol concentrations above 5 mass%, below which no clear solution was observed. The stability region goes through a maximum at 10% berol and decrease as the 16% point was approached. The reason for the first cloudy region is unknown. There appear to be a linear relationship between the berol and water content for this cloudy region.

The stability region (dark blue lines in Figure 91) for the distilled water decreased as the berol-hexane solution was aged ($H_2O$-1: fresh solution; $H_2O$-2: aged solution). The same was observed for the bismuth salt solution (Bi-1: fresh solution; B1-2: aged solution). The solution was aged in a sealed bottle, so no atmospheric water could have condensed in it. The decrease in pH does not seem to have such a big influence on the stable region. It can be observed that the first clear region (light blue line in Figure 90) in all the solutions that had a low pH (Bi, Mo and acidified water) were smaller than that of the distilled water. Although the reason for the first cloudy region was unknown it can be seen that pH does have a small influence on it. The solubility of the Mo salt solution and even more noticeably the Bi salt were much higher than that of distilled water, as can be seen from the result of the Bi and Mo salt solution added to a fresh mixture. The salinity of the salt solutions, therefore, had a stabilizing effect on the reverse micelles. It is possible that the sizes of the micelles were changed in the process.

The experimental setup was not very effective and user friendly. The solutions were shook manually which were not very effective.

## *Experiment A3: Catalyst Synthesis by RMT (Synthesis and Supporting)*

### Experimental Procedure of Experiment A3

Two mixtures of 10% and 25% berol-hexane were made up by adding 22,2 g and 66,7 g of berol to 200 g of hexane respectively. The mixtures were each divided into eight 50 g parts, i.e. four 10% berol-hexane mixtures and four 25% mixtures. A bismuth salt solution was made by dissolving 0.9702g of $Bi(NO_3)_3 \cdot 5H_2O$ in $HNO_3$ and then adding 10 ml of distilled water (solution pH = 0.85). A molybdenum salt solution was made up by dissolving 1.8535 g $H_{24}Mo_7N_6O_{24} \cdot 4H_2O$ in 15 ml of distilled water and then acidifying to a pH of 4.5 with concentrated $HNO_3$. Two runs for both the 10% and 25% berol-hexane mixtures were done. Run 1 and 2 used the 25% mixture and run 3 and 4 used the 10% mixtures. The salts solution volumes used for the individual micelle mixtures and the stability observed is summed in the Table 18.

**Table 18: Catalyst Synthesis 2, Microemultion Technique. Summary of experiment. Bismuth and molybdenum mixtures.**

| Run | Volume Mo-Solution/50g | Volume Bi-Solution/50g | Bi/Mo | Mo Micelles | Bi Micelles | Micelle Mix |
|---|---|---|---|---|---|---|
| | ml of [Mo] = 0.7M | ml of [Bi] = 0.2 | | | | |
| 1 | 8 | 4 | 0.14 | light cloudy | clear | clear yellow |
| 2 | 1 | 1 | 0.29 | misty | clear | clear light yellow |
| 3 | 4 | 2 | 0.14 | clear | misty | clear yellow |
| 4 | 0.5 | 0.5 | 0.29 | misty | clear | clear light yellow |

The bismuth micelle solutions were slowly added to the molybdenum while stirring vigorously.

When acetone was added to the micelle mixture, the micelles were broken and a precipitate started forming. The mixtures to which acetone were added were centrifuged and the clear liquid poured of. The precipitates were washed with acetone and centrifuged to remove the acetone. The washed precipitates were kept in acetone until it was viewed under the TEM.

It was noted that the nature of the precipitate changed when more acetone was added to the micelle mixture. A large excess of acetone was also added to the micelle mixture of sample 1 and 3. The samples were centrifuged, washed and kept in acetone.

Attempts to support the catalyst particles were made by adding silica particles mixed in acetone and silicon-carbide particles mixed in acetone to the micelle mixtures. The role of the acetone was to break the micelles in which the catalyst particles were encapsulated and to wash off the surfactant, so that the catalyst could stick to the support. The samples were also centrifuged and washed after which they were put in acetone for viewing by the TEM.

## Results of Experiment A3

**Berol-hexane solution**: The same results as previously mentioned were obtained for the 10% and 25% berol-hexane mixtures namely that the 10% berol solution formed a white bushy precipitate while the 25% did not.

**Micelle mixtures**: The colour changed from a colourless clear or misty solution (see Table 18) to a clear light yellow solution (no precipitate formation during mixing) for all the samples. Samples 1 and 3 were a brighter yellow than samples 2 and 4.

**Acetone addition to micelle mixture**: Different stages were observed when acetone was added to the micelle mixture and were as follows: initially, no change was observed when a small amount (less than 10 volume % for samples 1 and 3) of acetone was added to the micelle mixture. When the acetone percentage was increased to ±10 volume% (for samples 1 and 3), the micelle mixture became misty resulting in the formation of a double layer. The bottom layer was a clear liquid, presumably a denser aqueous mixture, and the top layer was an oil mixture in which the precipitate was suspended. As the acetone percentage was increased further, the precipitate started conglomerating changing from a fine dispersed misty looking precipitate (only present in the top oil layer) to a spongy chunky precipitate that settled faster. As the acetone was increased, the bottom layer started decreasing (re-dissolved). This kept on till the bottom water phase was completely re-dissolved in the oil at an acetone fraction of ±40 volume%. At this point, the precipitate which was a slow-settling cloudy precipitate changed to a fast dropping conglomerate. With further increase in acetone fraction (±60 volume %) the fast dropping conglomerate broke up in a fast settling powder precipitate.

Both samples 1 and 3 were treated with ±20% and ±60% acetone. When treated till a 20% acetone fraction sample 3 formed a yellow bottom layer and a colourless top layer while both layers were yellow in the case of sample 1. The products were centrifuged and yielded a pale yellow precipitate cake that floats on top of the bottom layer (between layers). The precipitate were washed with and kept in acetone. When treated till a 60% acetone fraction both sample 1 and 3 forms a fast settling powder precipitate which has a pale yellow colour. The product was centrifuged, washed with and kept in acetone.
Both samples 2 and 4 were treated with a 20% acetone fraction. In these cases, the double layer stage was not observed.

A micelle mixture was made up by adding distilled water to an oil-surfactant mixture. A sufficient amount of acetone was added to the mixture to forms a two-layer system. The top and bottom layers were individually tested using Karl-Fisher and a GC to determine their constitutions. The top layer was made up of hexane (±90%), acetone (±10%) and small amounts of water (<1%) as expected. The bottom layer was made up of water (50%) and small amounts of oil and acetone leaving the rest of the volume for the berol (±45%) to balance.

**Support**: The supports (silica and silicon-carbide) were mixed with micelle mixture 1 and 20 volume% fraction acetone. When the silica was used, both the catalyst precipitate and silica never crossed the phase boundary and were only found in the oil phase (top layer). The silicon-carbide was first well washed with acetone before adding it to the micelle mixture and did cross to the bottom phase. Both were washed with and kept in acetone.

**Unwashed Micelle mixtures**: The micelle mixtures (1, 2, 3 and 4) were dried at 60$^{o}$C for a day, but were still wet and were bright yellow. This product was then dried at 120$^{o}$C for 200 min to form a dark yellow-grey precipitate suspended in a small amount of viscous liquid that did not vaporize in the drying. The samples were centrifuged, washed with and kept in acetone.

**TEM Results:**

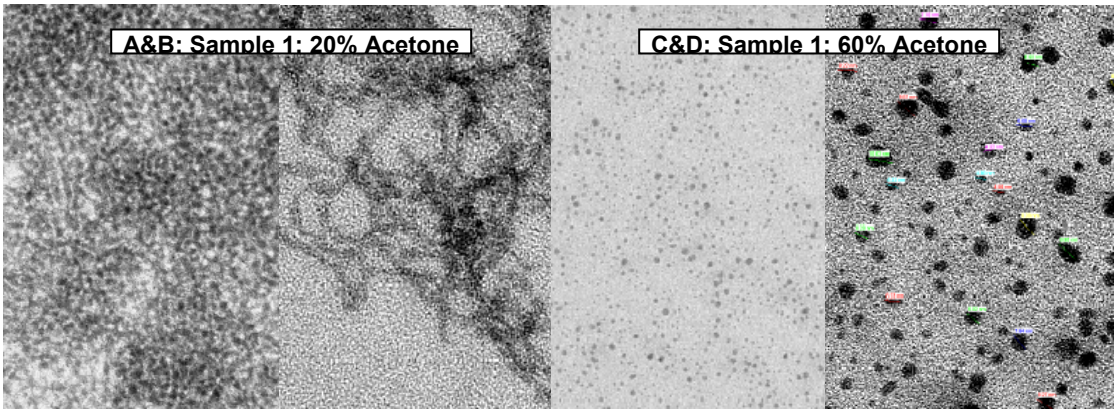


**Figure 92 (A-D): Sample 1, 20% acetone fraction; Sample 1, 60% acetone fraction.**

Figure 92 show micelle mixture 1 treated with 20% and 60% fraction of acetone. In the case of the 20% acetone fraction, the catalyst particles were seen to form either agglomerated heaps or strings of particles. The particle sizes were difficult to see, and range from 3.5-5.5 nm. In the case of the 60% acetone fraction the particles were totally liberated with particle sizes 3.5-9 nm. Only a very small percentage of the particles were found in clusters.

Similar results were obtained in the 20% and 60% acetone fraction for sample 3 which formed larger particles, 12-16 nm.

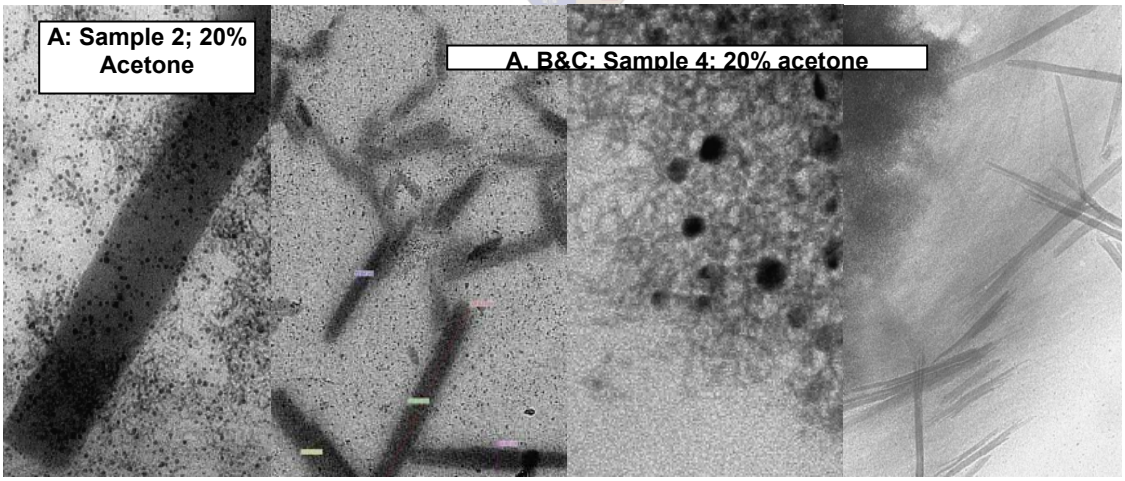


**Figure 93 (A-D): Sample 2, 20% acetone fraction.**

Samples 2 and 4, (20% acetone fraction) were a mixture of particle clusters, liberated particles and crystals.

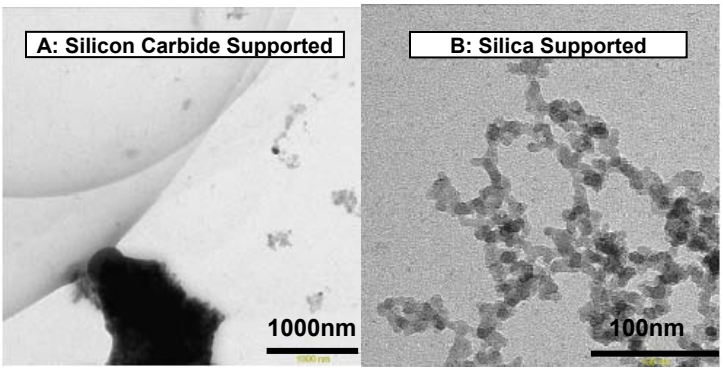


**Figure 94 (A&B): Sample 1 supported on silicon carbide and particles silica in 20% acetone fraction.**

The silica particles were of similar size and density to the catalyst particles making it difficult to distinguish between silica and catalyst on the TEM picture. It was thus impossible to comment on the effectiveness of the support. The silicon-carbide particles, which are much larger than the catalyst particles are almost invisible to the TEM, but do not appear to support the catalyst under the tested conditions.

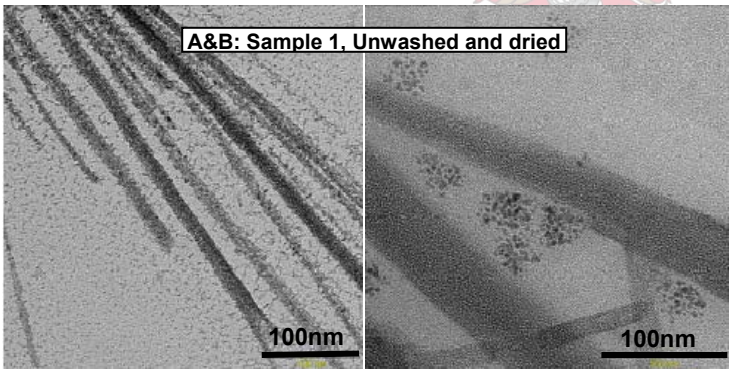


**Figure 95 (A&B): Sample 1: Unwashed and dried. Particles, crystals and nanorods.**

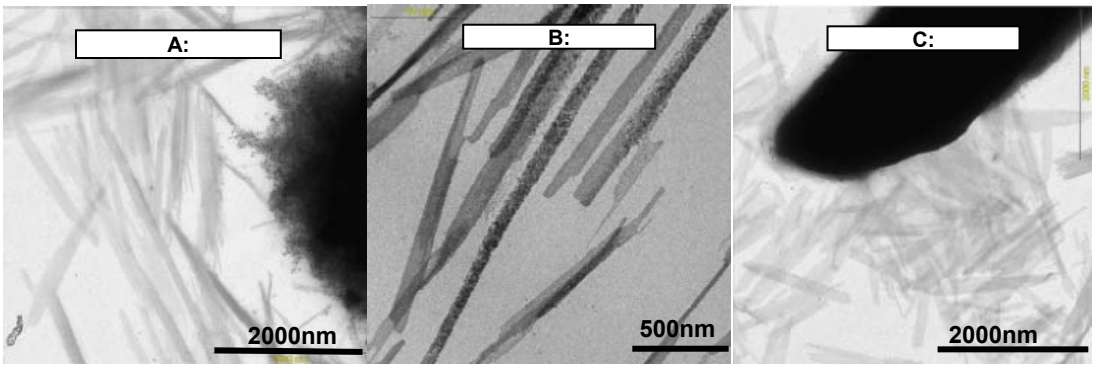


**Figure 96 (A-C): Sample 2: Unwashed and dried. Particles, crystals and nanorods.**

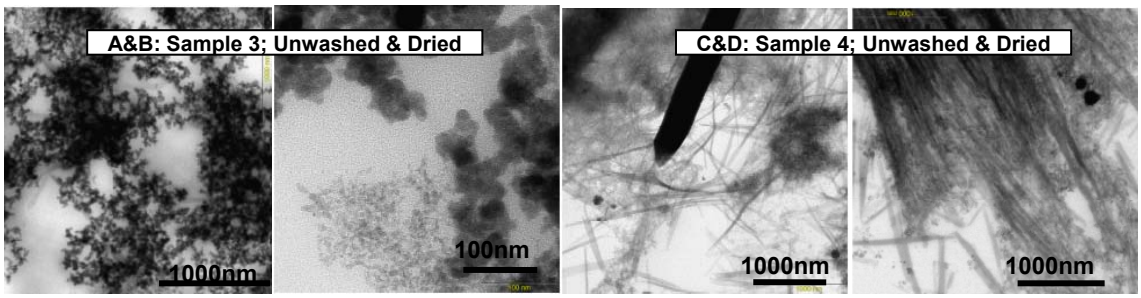


**Figure 97 (A-D): Sample 3 & 4: Unwashed and dried. Particles, crystals and nanorods.**

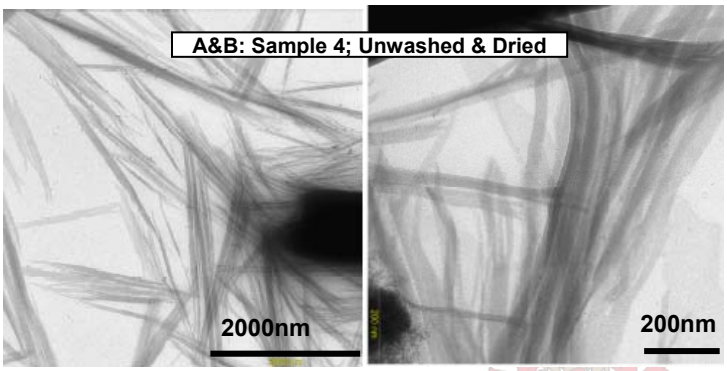


**Figure 98 (A&B): Unwashed and dried samples 4. Mixture of particles, crystals and nanorods.**

The unwashed samples yielded a mixture of small particles, nanorods, crystals and large sintered particles. Samples 1 and 3 showed more small particle-like structures and less large crystals. In the case of samples 2 and 4, the crystal splinters and nanorods made up a large part of the catalyst. Particle sizes, for sample 1, ranging from diameters of 4 nm to 200 nm mixed with crystals and nanorods (width 13-15 nm). For sample 2, crystal shavings (width 80-300 nm; length 1-2 μm) with nanorods (width 96-99 nm) and small particles (4-8 nm) were mostly found. Two sizes particles were observed in sample 3; 4-8 nm particles corresponding with the micelle particle and large (+100 nm) sintered particles. Sample 4 was a mixture of crystals, nanorods and particles. Asbestos like structures were also observed (Figure 97).

## Discussion of Experiment A3

**Micelle Mixtures**: The micelle mixtures were all clear yellow coloured liquids with no visual precipitate, suggesting that the catalyst particles were encapsulated in the stable micelles. Only when acetone was added to the micelle mixture did it cause a

precipitation. The particles formed by the reverse micelle method are thought to be formed in two steps: a nucleation step during which the nuclei are formed and a growth step which are the subsequent growth of the nuclei. In the growth step, particles can grow larger than the micelle droplet and are expected to form a small amount of precipitate when this happens. In this case it did not happen, suggesting that the particles were still smaller than the micelle droplets. The clear liquid could also indicate that there was no interaction between particles after nucleation also verifying the existence of very stable micelles.

**Acetone addition to micelle mixture**: The different steps observed as the fraction of acetone was increased in the micelle mixture can be interpreted as follows:

0-10% Acetone (c.f. acetone addition to sample 1 and 3):
The precipitate only formed when the acetone fraction was large enough to destabilise the reverse micelles. When this happened a double layer formed with the precipitate only being present in the oil phase, suggesting that the surfactant were adsorbed on the surface of the particles, causing them to become hydrophobic.

10-40% Acetone (c.f. acetone addition to samples 1 and 3):
With further addition of acetone, the bottom layer (water and berol mixture) began re-dissolving in the oil until the entire bottom layer was totally dissolved at 40 volume% acetone. The reason for the redissolving, as well as the phases present (micelle or total mixed solution) was unknown. With the addition of acetone (10-40%) the precipitate, which was suspended in the oil phase, changed growing from a fine dispersed, slow-settling precipitate to chunky, rapid-settling precipitate.

40-60% Acetone (c.f. acetone addition to samples 1 and 3):
At 40% the last bottom liquid was re-dissolved and the precipitate forms dense liquid like balls of precipitate that fall to the bottom. If the bottom liquid layer was removed at 20% acetone fraction and acetone was added to the oil-precipitate mix the precipitate only grows to the fast-settling bushy precipitate but does not change to the fast dropping balls. Only when distilled water was reintroduced were the fast dropping balls of catalyst, similar to the previous samples formed. If enough water was introduced it can be observed that the catalyst balls gets a droplet like character and form a viscous bottom

layer. The catalyst particles thus become hydrophilic preferring the water phase. This indicates that the surfactant was removed to a high degree from the catalyst surface, which concurs with the TEM results, (Figures 92C and 92D) that indicate liberated particles for the 60 volume% acetone mixtures. It should be noted that even though the catalyst samples precipitated at 20% acetone were washed and kept in acetone the surfactant was not removed and the particles still stuck to each other forming big clusters of particles (Figures 92A and 92B). The presence of the oil and water thus contributes to the removal of the surfactant by dissolving the surfactant in the oil and pulling the catalyst into the water phase.

When 20 volume% acetone was added to samples 2 and 4 the same result was obtained as for the 60% acetone added to samples 1 and 3. This was because there were much less water in the samples, thus a smaller acetone percentage was needed to dissolve it. The TEM results for the 20% acetone treated samples 2 and 4 showed liberated particles. This agrees with the proposed reasoning.

It can also be noted that samples 2 and 4 (sample with a low water fraction) have a considerable amount of large crystals, crystal shavings and nanorods. The formation of nanorods were consistent with the results found in the previous experiment where nanorods were found in the sample where small water fractions were used corresponding to the first cloudy region in the ternary diagram.

**Support:** When the silica was added (addition of 20% acetone fraction for sample 1), both the silica and precipitate were only present in the oil phase indicating that both are hydrophobic. It could also be that the catalyst particles started adhering to the silica particles and because of the hydrophobic nature of the catalyst particles at this stage (20% acetone), this will keep the silica captured in the oil phase. According to this approach, the catalyst particles were supported by the silica. The TEM results could not, however differentiate between catalyst and silica particles, Figure 94B.

When the silicon-carbide (black powder) was used to support the catalyst particles, the support settled right through the phase boundary to the bottom layer and thus did not have the hydrophobic nature of the silica particles or was to large/heavy to adhere to the tiny catalyst particles, as in the case of the silica. The TEM results (Figure 94A) reveal

large silicon-carbide particles on which the catalyst particles were not adsorbed under the specific conditions.

**Unwashed micelle mixtures:** Crystal and nanorod formation appears to be promoted in samples with a high surfactant-to-water (s/w) ratio. This effect can best be seen when sample 2 (s/w = 12.5) and 3 (s/w = 1.6) are compared in the drying process. The oil (hexane) was vaporised easily leaving a water and surfactant mixture that did not vaporise easily. The catalyst particles were thus suspended in water diluted surfactant. The lower the s/w ratio, the more diluted the surfactant gets. Keeping in mind the suggested mechanism of Ghule *et al.* [2004], the surfactant was responsible for the nanorod or crystal formation

The asbestos like structures seen in Figure 97D were the effect of agglomeration cased by surfactant adsorption, resulting in nanorod formation when the temperature was increased.

## *Experiment A4: Salt and Micelle Stability for use in the RMT*

### Experimental Procedure of Experiment A4

A 10 mass% berol-hexane mixture was made up by adding 11 g berol to 100 g n-hexane and mixing well. Three concentrations of bismuth and molybdenum salts solutions were made up as follows: 3.8806 g of $Bi(NO_3)_3 \cdot 5H_2O$ was dissolved in 1.5 ml concentrated $HNO_3$ and 10 ml of distilled water, after which distilled water was added to obtain a 40 ml solution. The pH was controlled at 1.5 by adding a small amount of concentrated $HNO_3$. 20 ml of the solution ([Bi] = 0.2 M) was removed for use and replaced with 20 ml of distilled water, pH steadied to 1.5 while stirring. A second 20ml solution ([Bi] = 0.1 M; pH = 1.5) was removed for use and replaced with 20 ml of distilled water and a few drops of concentrated $HNO_3$ while stirring. The remaining solution ([Bi] = 0.05 M; pH = 1.5) was bottled for use. The same was done to prepare the 0.7 M, 0.35 M and 0.18 M ([Mo]) molybdenum solutions, starting from 4.9434 g of $H_{24}Mo_7N_6O_{24} \cdot 4H_2O$ diluted in 40 ml distilled water and acidified to a pH of 4.0 with concentrated $HNO_3$.

Acetone was added to all three bismuth and molybdenum salts solutions to determine the maximum acetone fraction at which the salts were still stable. Acetone containing salt solutions were then prepared by adding 80% of the maximum acetone fraction to the salts.

All the salts were tested for micelle stability by adding it to ±10 ml of oil-surfactant solution. The experimental setup was altered by using a small glass bottle with a plastic lid through which a syringe needle was passed. The liquid mixture was magnetically stirred.

Results of Experiment A4

All the salt solutions appeared to be stable, except the 0.7 M and 0.35 M molybdenum solutions that started crystallizing after 4 hours. The experiments were typically completed well within this time limit.

When the acetone was added to various salt solutions, the volume was increased for the same salt content, thus decreasing the salinity. The following graph shows the maximum acetone fractions for the corresponding bismuth and molybdenum salinities.

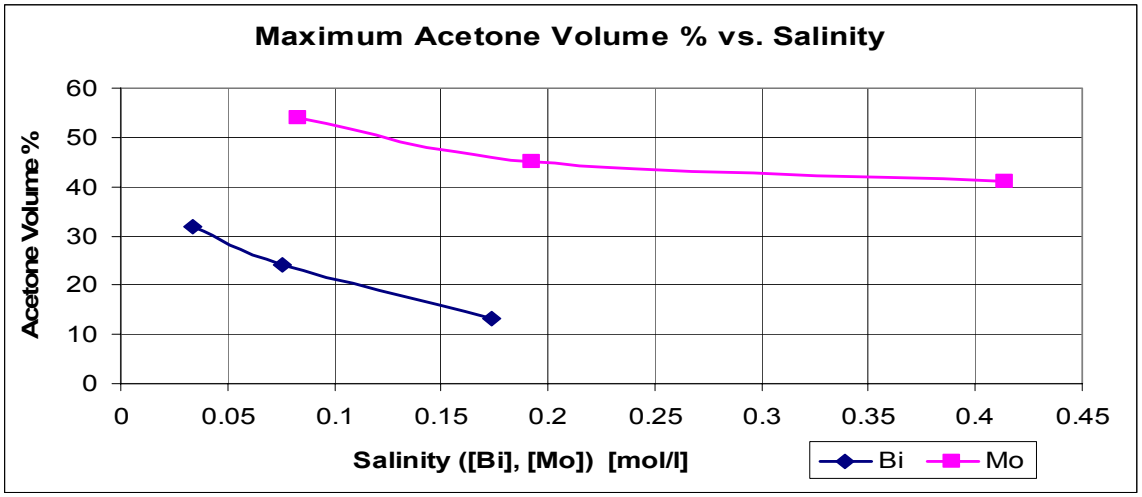


**Figure 99 : Maximum acetone fraction for corresponding Bi and Mo salinities.**

Acetone containing bismuth and molybdenum solutions were then made up by adding 80% of the maximum acetone to the solutions. The following graphs show the stable micelle regions for various titrations.

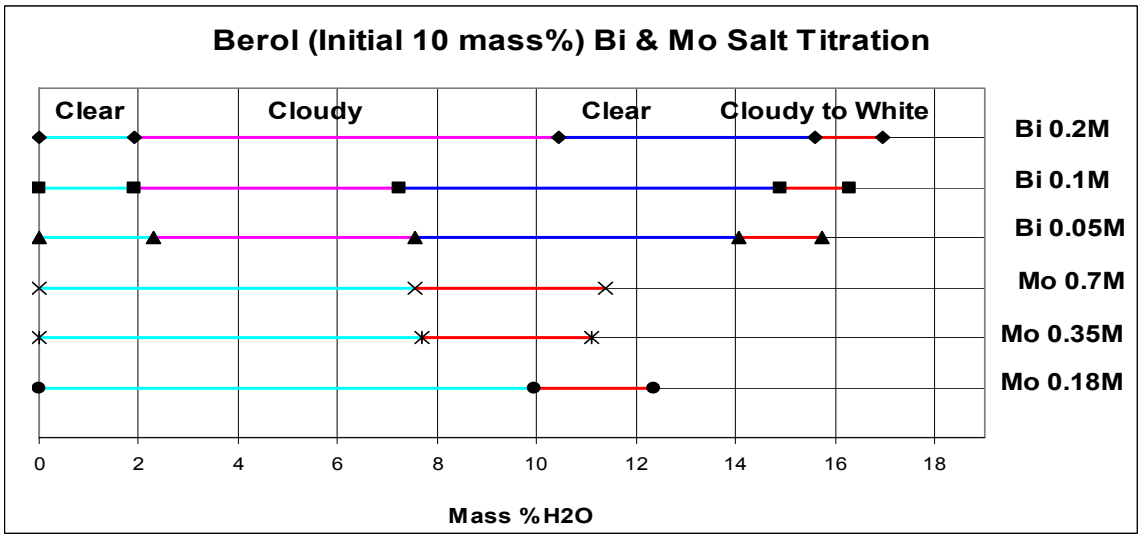


**Figure 100: Bi (pH=1.5) & Mo (pH=4.0) salt titrations in 10% berol solutions.**

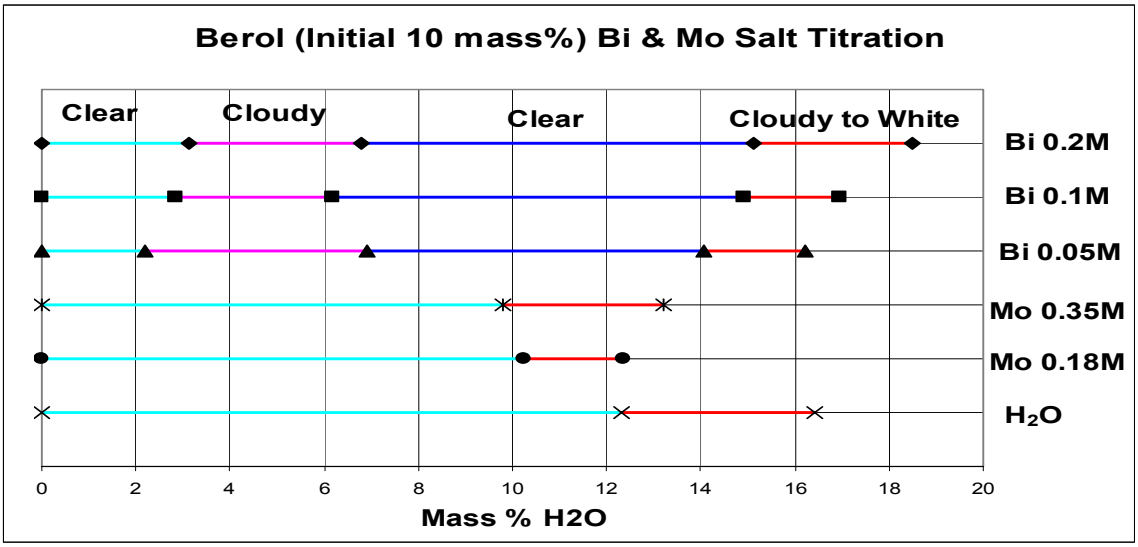


**Figure 101: Bi salt (pH = 1.5), Mo salt (pH = 4.0) and water titrations in 10% berol solutions.**

Figures 100 and 101 were the same experiments done on two separate occasions. The similar results obtained in two separate occasions illustrated the reproducibility of the results obtained with the new experimental setup. The major differences being the tail of the first cloudy region where bismuth solutions were used. In this region the cloudiness was subtle and decreases with solution addition, making it a very subjective differentiation between the two graphs.

In Figures 100 and 101 the first cloudy regions were much more prominent for the bismuth solutions than for the molybdenum solutions or water. Both the molybdenum solutions and water turned cloudy (first cloudy region) when a few (3-4) drops were added and cleared up when two more drops were added. In these cases, the region was very small and is not shown on the graphs. The maximum solution holding capacity (end of dark blue line) for bismuth solutions decreased slightly with decreasing salinity. The molybdenum solutions in contrast, showed an increase in the maximum solution holding capacity with decreasing salinity. All the solutions ended in a cloudy region that turns white and formed a double layer when it were left to settle (red region).

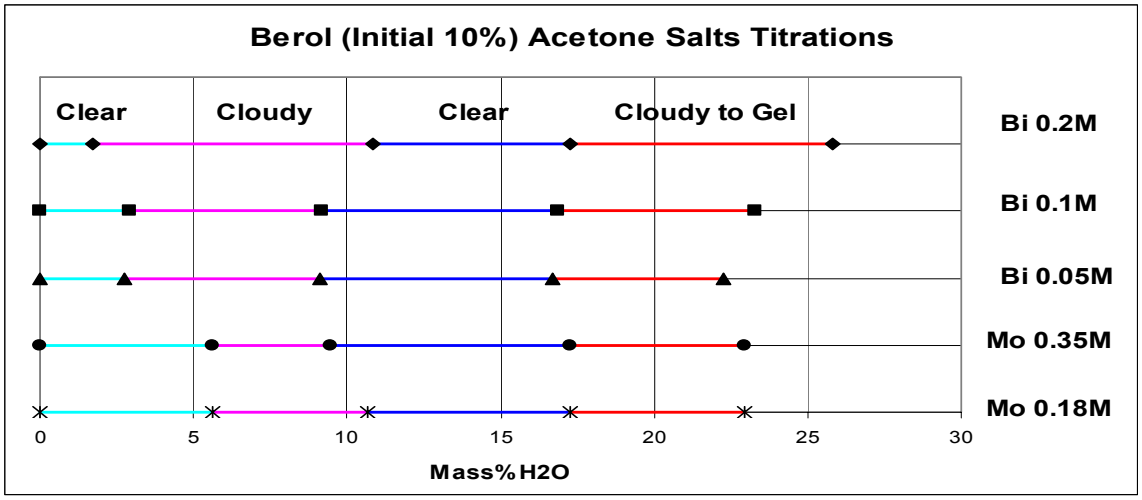


**Figure 102: Acetone salt titration in 10% berol solution. Markers correspond to the original Bi or Mo salt in which acetone is added.**

Figure 102 shows the titration for the acetone containing solutions. It should be noted that the first cloudy regions, although smaller for the molybdenum solution, were prominently present for both the bismuth and molybdenum solution. The maximum salt solution holding capacities (end of dark blue lines) were greater by 2-6% for the acetone containing solutions than that of regular salt solutions. Where over-capacitating with the regular salts caused a white solution resulting in a double layer when left for a period of time, the acetone containing solutions formed a viscose white gel.

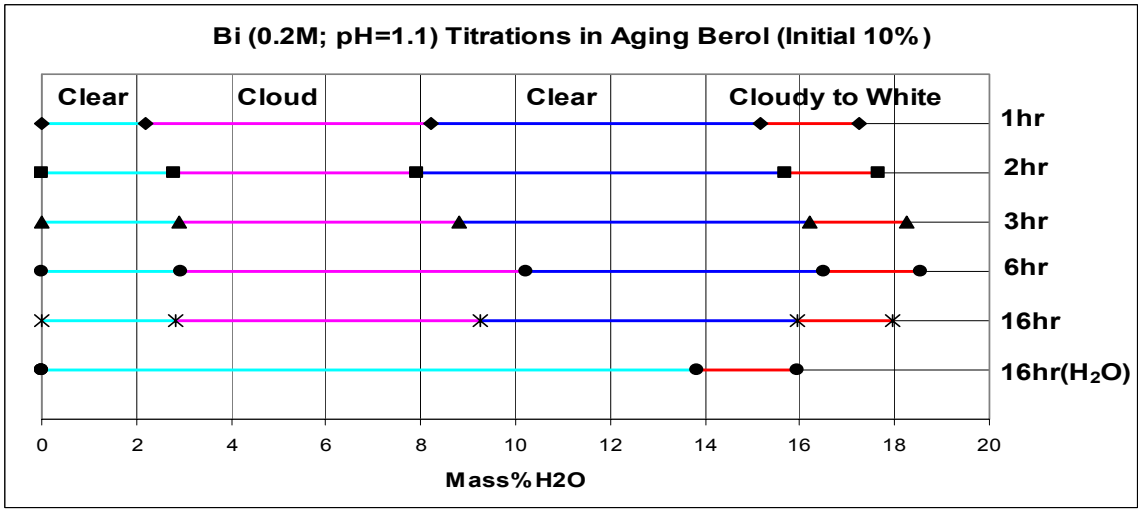


**Figure 103: The effect of aging on a 10% berol-hexane solution. Titrations were done with 0.2 M bismuth salt (pH of 1.1). A water titration is included at 16 hrs.**

The new experimental setup was used to determine the effects of aging of the berol-hexane solutions. The results in Figure 103 show that aging of 24 hrs does not have a great effect on the holding capacity of the berol-hexane solution.

## Discussion of Experiment A4

The new experimental setup gave more accurate and reproducible results. Moreover, the experiments were quick, chemical saving and user friendly.

The maximum allowable acetone fraction increases with the decrease in salinity for both bismuth and molybdenum solution. This meant that the solubility was decreased with the increase of acetone fraction. Bender and Burlitch [2000] decreased particle sizes from 70 nm to 8 nm by increasing the MeOH percentage from 0-100%. In this case, bismuth was limiting the acetone fraction that can be used in a reverse micelle technique to 10-20% acetone. The acetone fraction in the molybdenum can not be higher than the fraction permitted by the stability of the bismuth solution. This restriction limits the operational region that may be used, but may permit a degree of size control.

The decreasing and increasing in maximum holding capacity of bismuth and molybdenum solutions respectively with a decreased in salinity was easily explained. Both the bismuth and molybdenum salt solutions were approaching the maximum holding capacity of water, which was around 12% as their salinities were decreased. The maximum holding capacities for the solutions were greater when acetone was present. The acetone was thus stabilising the micelles in some way; it may be by increasing the sizes or amount of micelles. It is also possible that the acetone dissolved in the oil-surfactant mixture and does not stay in the micelles. Thus, more acetone containing solution was used. The reason for the gel formation in the case of the acetone containing solutions beyond its maximum holding capacity is not understood at this stage.

### *Experiment A5: Catalyst Synthesis RMT: (Synthesis and Supporting)*

Using all the knowledge gained in the previous experiments the following experiments were designed to verify the conditions needed to obtain size control and produce samples of homogeneous size. The particles should be liberated so that it can be effectively spaced or supported. So far it was impossible to distinguish between the catalyst and supporting silica particles because of their similar size, thus causing uncertainty around the supporting status of the catalyst particles on silica. Larger silica particles (200-400 mesh) were used in an attempt to support the catalyst and shed some light on the supportability of the catalyst particles on silica.

### Experimental Procedure of Experiment A5

Two Berol-hexane mixtures were made up by adding 6 g and 13 g of berol to 50 g of hexane respectively, resulting in 10% and 20% solutions. The mixtures were divided in to two 25 g solutions each. Two salt solutions of both molybdenum and bismuth were prepared: 3.4462 g of $(NH_4)_6Mo_7O_{24}{\cdot}4H_2O$ was dissolved in 40 ml distilled water and 0.5 ml $HNO_3$ was added. 20 ml of the solution was removed (0.488 M [Mo]) as the first salt solution and 20 ml of distilled water was added to the remaining solution to obtain a solution of half the salinity (0.244 M [Mo]). 3.8806g of $Bi(NO_3)_3{\cdot}5H_2O$ was dissolved by adding 2 ml $HNO_3$ and slowly adding 40 ml distilled water. Of this solution 20 ml was removed as the first salt solution (0.2 M [Bi]) and 20 ml of distilled water and 1 ml of $HNO_3$ was added to the remaining solution to obtain a bismuth salt of half the salinity of the first salt. The high salinity bismuth and molybdenum solutions were added to the 10% mixture and low salinity salt solutions to the 20% mixture. The runs are summarised in the Tabel 19.

**Table 19: Catalyst Synthesis 4, Microemultion Technique. Summary of experiment: Bismuth and molybdenum mixtures.**

| Run | [Mo] | Volume Mo | [Bi] | Volume Bi | Bi/Mo |
|---|---|---|---|---|---|
| | mol/l | $ml_{salt}/25g_{mixture}$ | mol/l | $ml_{salt}/25g_{mixture}$ | $2/3_{\ ideal}$ |
| Sample A (10% Berol) | 0.49 | 2.2 | 0.2 | 3.6 | 0.67 |
| Sample B (20% Berol) | 0.24 | 2 | 0.1 | 3.25 | 0.66 |

The maximum volumes of bismuth and molybdenum solutions were added to the berol-hexane solution respectively to optimize the yield and prevent the formation of crystals. The bismuth micelle mixtures were slowly added to the molybdate micelle mixtures for both run A and B while stirring vigorously for 15 min.

Acetone was added in large excess (15 ml) to 10 ml of the resulting micelle mixtures to liberate the particles for TEM analyzing. The precipitate was centrifuged out removing the oil and berol where after it was washed and kept in acetone. Large (200-400 mesh) silica particles were added to acetone and the acetone mixture was added to the micelle mixtures in an attempt to support the catalyst on the silica.

## Results of Experiment A5

As expected, the 10% berol-hexane mixture formed the bushy white precipitate while the 20% solution did not. The solutions prepared were stable and did not crystallise or precipitate even after a 24 hr period. When bismuth and molybdenum solutions were mixed with berol-hexane mixtures, they all yielded slight hazy to clear mixtures which indicate that they were saturated with the aqueous phase. When the bismuth mixtures were slowly added to the molybdenum mixtures, while stirring vigorously, the mixtures turn yellow and later pale green. In run A, a settling precipitate formed immediately after mixing the micelle mixtures and in the case of run B a green-yellow coloured but clear mixture was observed. After 3 days sample B also formed a precipitate which settled to the bottom and both samples formed precipitate sheet on the glass edges of their containers. Fresh and aged samples were taken to be viewed under the TEM.

Similar results were obtained with acetone addition as in the previous microemultion synthesis. When 2 ml of acetone was added to 10 ml of micelle mixture a double layer formed for both run A and B. The precipitate was still only present in the top layer. With further addition of acetone the bottom layer re-dissolved and the nature of the catalyst changes from a slow settling spongy precipitate to an agglomerated fast dropping precipitate. With 15 ml acetone added to the mixture the precipitate changed to a slow settling powderish precipitate. These precipitates for both run A and B were prepared.

When 2 ml of acetone-silica (fine silica particles) mixture was added to 10 ml of micelle mixture B a double layer formed with both silica and the catalyst only present in the top layer. 2 ml of pure acetone was then added to another 10 ml of micelle mixture B, causing a double layer. In the second sample B, the bottom layer was removed with a syringe and silica particles added to it. When it was remixed with the top layer all the catalyst precipitate went into the bottom layer in which the silica was, resulting in a viscous greenish bottom layer. When a further 1 ml of acetone was added to this mixture it formed a double layer but both the silica and the catalyst was again only found in the top layer.

When 2 ml of acetone-silica (large silica particles) mixture was added to 10 ml of micelle mixture B, as expected, a double layer formed with both silica and the catalyst only present in the top layer. If the quantity of silica particles were raised the silica particles start to drop out in the bottom layer.

**TEM Results:**

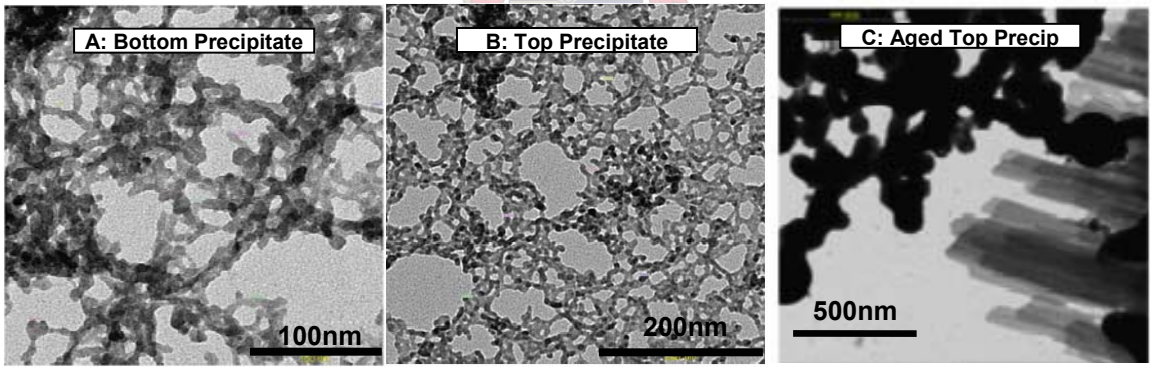


**Figure 104 (A-C): Sample A: A: Bottom precipitate, B: Top liquid precipitate and C: Aged top liquid precipitate.**

The bottom (settled) precipitate, Figure 104A, and the precipitate which was still encapsulated in the micelles in the clear liquid, Figure 104B, were only found in web like strings of particles. The particle sizes were around 6 nm and homogeneous, but no liberated particles were found. The aged top liquid, Figure 104C, presented strings of large particles (100-180 nm) and occasional crystal sheets.

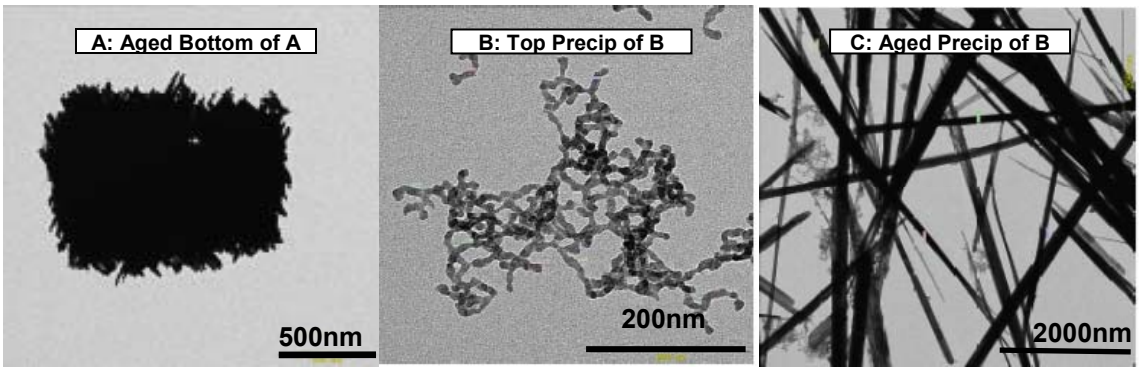


**Figure 105 (A-C): A, Aged bottom precipitate of sample A; B, Top liquid precipitate of sample B; C, Aged precipitate of sample B.**

The aged bottoms precipitate formed agglomerated crystal balls made up of 30 nm width crystal rods. No or trace amounts of original 6 nm particles were found. The fresh sample B, Figure 105B, shows strings of 10 nm particles. Sample B was more liberates than the fresh sample A, but were only found only in string form. The aged sample B, Figure 105C, shows long crystal rods with 50-150 nm width. Only a small amount of original 6 nm particles were found between the nanorods.

Only the sample that was supported on the large silica particles were analysed under the TEM, but the silica particles were to large resulting in only the catalyst particles being seen.

## Discussion of Experiment A5

The experimental observations for the berol and hexane mixing and acetone wash were similar to previous experiments as expected.

It was unclear why the catalyst precipitate was dragged into the bottom layer of the acetone separated sample when a threshold amount of fine silica particles was added to the bottom layer. The acetone concentration seems to play a role, seen that a further addition of 1 ml (total of 3 ml) acetone caused both the catalyst and silica particles to move from only being in the bottom layer to only being in the top layer.

The string like character of both samples A and B were not expected for the fresh samples, neither was the particle sizes obtained. Sample A (low berol% and high salt

solution concentration) was supposed to be large (+10 nm) and liberated particles (6 nm was obtained), while sample B was supposed to be small (±3 nm) liberated particles (10 nm was obtained). This means that size control and liberation of particles were controlled by other parameters than those investigated in this experiment (berol%, salinity and acetone wash). In this experiment the Bi/Mo ratio was also changed to its ideal 2/3 ratio where in previous experiments molybdenum was in excess. The salt solution ratios were thus changed because the salinities stayed similar, this could have a great effect on the micelle sizes. The catalyst loading per volume oil-surfactant mixture was changed as well. In experiment 2 the catalyst loading for the 25% berol mixture was 4mmol/100g (3.5 nm particles were obtained) and that of the 10% berol mixture was 2mmol/100g (15 nm particles were obtained). Keeping in mind the two step mechanism (nucleation and growth) for particle formation in a micro-emulsion system, a larger loading will give rise to further growth and thus larger particles. In experiment 2 the effect of the 25% berol seemed to override the effect of the loading and still produced small particles. It was thought that by lowering the loading in this experiment the particles would be even smaller. This was not the case.

The acetone wash, even in excess of acetone, did not liberate the particles. Another parameter thus also plays a role in the liberation of the particles. It could be that using a Bi/Mo ratio of 2/3 could cause the sticking of the particles. If can be hypothesized that using an excess of molybdenum causes the particle to be covered by a molybdenum rich layer which prevent sticking. This needs to be investigated.

### *Experiment A6: Catalyst Synthesis by RMT (Catalyst loading)*

Size control, by changing the solution salinity and surfactant percentage, could not be achieved and verified in micro-emulsion synthesis A5. There are thus parameters, other than those investigated, that plays a significant role in the particle formation and sizes attained. It was decided to investigate the two step particle formation (nucleation and growth) in the micro-emulsion technique by using different catalyst loadings and Bi/Mo ratios. The presence of acetone in the oil-surfactant mixtures was also investigated to see whether it produces particles and if it influences the particle size.

## Experimental of Experiment A6

Two Berol-hexane mixtures were made up by adding 33 g and 83.3 g of berol to 300 g and 250 g of hexane respectively, resulting in 10% and 20% mixtures. The mixtures were divided into sixteen 20 g mixtures each. 1 ml of acetone was added to four of each the 10% and 25% mixtures. Salt solutions of both molybdenum and bismuth were prepared: 4.5197 g of $(NH_4)_6Mo_7O_{24}\cdot 4H_2O$ was dissolved in 40 ml demineralised water. 20 ml of the salt solution was removed (0.640 M [Mo]) as the first salt solution and replaced by 20 ml water to obtain a second salt solution of half the salinity of the first (0.320 M [Mo]). Again 20 ml of this salt solution was removed and replaced by water to obtain the third solution, which had half the salinity of the second one. This method was used a second time only starting with 6.253 g of $(NH_4)_6Mo_7O_{24}\cdot 4H_2O$ to produce another three molybdenum salt solutions (0.8532 M, 0.4266 M and 0.2133 M [Mo]). 4.1386g of $Bi(NO_3)_3\cdot 5H_2O$ was dissolved in 2 ml $HNO_3$ and slowly adding 40 ml distilled water. The same method was used to obtain three bismuth solutions (0.2133 M, 0.10665 M and 0.0533 M [Bi]) as for the molybdenum, with the exception that the water that replaced the removed salt contained 1 ml of $HNO_3$ per 20 ml of water. The salt solutions were added in such a way to the oil-surfactant and oil-surfactant-acetone mixtures were saturated with the aqueous phase and have a Bi/Mo ratio of 2/3 or 1/2. One of the runs (0.10665 M [Bi] and 0.4266 M [Mo] solutions) was further investigated by taking small stepwise samples during the addition of the bismuth mixture to the molybdenum mixture. This run was also used to take step-wise samples during the addition of acetone to the catalyst mixture in order to investigate the agglomerating nature of the catalyst particles and how it was influenced by acetone addition in the washing step. The experimental runs are summarised in Tabel 20.

**Table 20: Catalyst Synthesis 5, Microemultion Technique. Summary of experiment. Bismuth and molybdenum mixtures.**

| Run | [Bi] | Bi Solution Volume | [Mo] | Mo Solution Volume | Bi/Mo | %Berol | %Acetone |
|---|---|---|---|---|---|---|---|
| | mol/l | $ml/20ml_{mixture}$ | mol/l | $ml/20ml_{mixture}$ | | | |
| | | | | | | | |
| 1A | 0.2133 | 3.0 | 0.6400 | 1.5 | 0.67 | 25 | 0 |
| 1B | 0.1067 | 3.0 | 0.3200 | 1.5 | 0.67 | 25 | 0 |
| 1C | 0.0533 | 3.0 | 0.1600 | 1.5 | 0.67 | 25 | 0 |
| 1X | 0.2133 | 3.0 | 0.8532 | 1.5 | 0.50 | 25 | 0 |
| 1Y | 0.1067 | 3.0 | 0.4266 | 1.5 | 0.50 | 25 | 0 |
| 1Z | 0.0533 | 3.0 | 0.2133 | 1.5 | 0.50 | 25 | 0 |
| A1X | 0.2133 | 3.0 | 0.6400 | 1.5 | 0.67 | 25 | 5 |
| A1Z | 0.0533 | 3.0 | 0.1600 | 1.5 | 0.67 | 25 | 5 |
| 2A | 0.2133 | 3.0 | 0.6400 | 1.5 | 0.67 | 10 | 0 |
| 2B | 0.1067 | 3.0 | 0.3200 | 1.5 | 0.67 | 10 | 0 |
| 2C | 0.0533 | 3.0 | 0.1600 | 1.5 | 0.67 | 10 | 0 |
| 2X | 0.2133 | 3.0 | 0.8532 | 1.5 | 0.50 | 10 | 0 |
| 2Y | 0.1067 | 3.0 | 0.4266 | 1.5 | 0.50 | 10 | 0 |
| 2Z | 0.0533 | 3.0 | 0.2133 | 1.5 | 0.50 | 10 | 0 |
| A2X | 0.2133 | 3.0 | 0.6400 | 1.5 | 0.67 | 10 | 5 |
| A2Z | 0.0533 | 3.0 | 0.1600 | 1.5 | 0.67 | 10 | 5 |

The catalyst was separated from their micelles by adding 10-13 ml of acetone to 10 ml of mixture. The catalyst precipitate mixtures were centrifuged and the clear liquid removed. The catalyst cakes were again washed with 4 ml of acetone, centrifuged to get rid of the dirty acetone and then kept in 4 ml of clean acetone to be viewed under the TEM.

## Results of Experiment A6

The oil-surfactant mixtures (10% and 25% berol) both formed a small amount of white bushy precipitate that settled to the bottom. The mixtures in which 5% acetone was added looked similar to those with out acetone.

When the salt solutions were added the oil-surfactant mixtures they turned white and cleared up with the exception of those from the 25% berol in which high salinity salts were added (1A: Bi & Mo and 1X: Bi & Mo) and the acetone containing mixtures. The 1A and 1X mixtures (Bi & Mo) were centrifuged to obtain a clear liquid with a very small amount of precipitate. The clear liquid mixtures were used in further steps to ensure that

the micelles used were stable. The acetone containing mixtures formed hazy white gels when the salt solutions (Bi & Mo) were added to it.

Bismuth mixtures were slowly added to molybdenum mixtures while stirring vigorously. The stirred mixture went from clear to yellow when 5 ml of the approximant 30 ml bismuth mixture was added. With further addition of the bismuth mixture the stirred mixtures went clear and greenish white for the runs of 1 (25% berol) and 2 (10% berol) respectively. The acetone containing samples were white after mixing. After stirring for 15 min the samples were left to stand for 1hr. All the runs 2 as well as the acetone containing mixtures formed a precipitate while mixing which settled out with in an hour.

Acetone addition to liberate and wash the catalyst particles had the same results as in previous experiments. The catalyst precipitate changed its character dependent on the volume of acetone added to the micelle mixture.

**TEM Results**

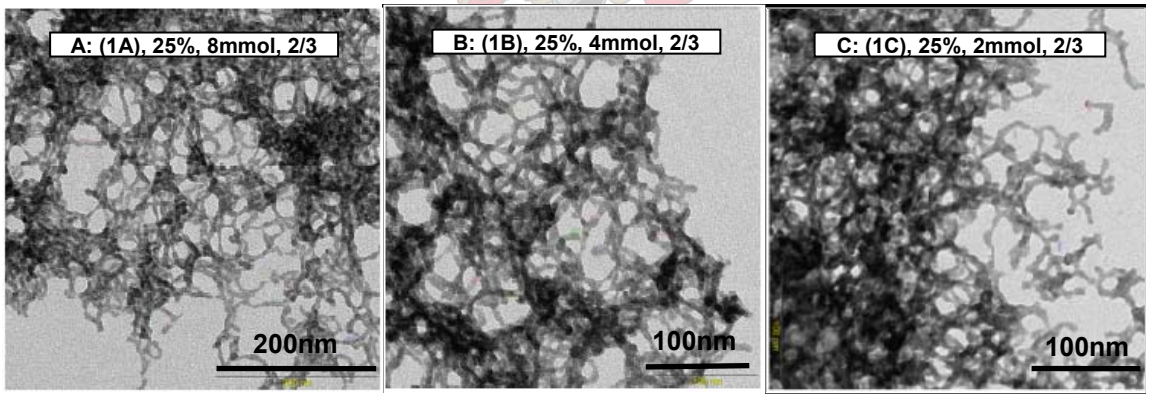


**Figure 106 (A-C): Ran 1 (25% berol) with Bi/Mo ratio of 2/3: Rang of catalyst loadings. A: 8mmol$_{catal}$/100g$_{mixture}$ , B: 4mmol$_{catal}$/100g$_{mixture}$ and C: 2mmol$_{catal}$/100g$_{mixture}$.**

The particle sizes for the range of catalyst loadings of 8, 4 and 2 mmol$_{catal}$/100g$_{mixture}$ were 5.6, 8.5 and 6.0nm respectively for A, B and C. The particles were only found in agglomerated heaps or strings of particles.

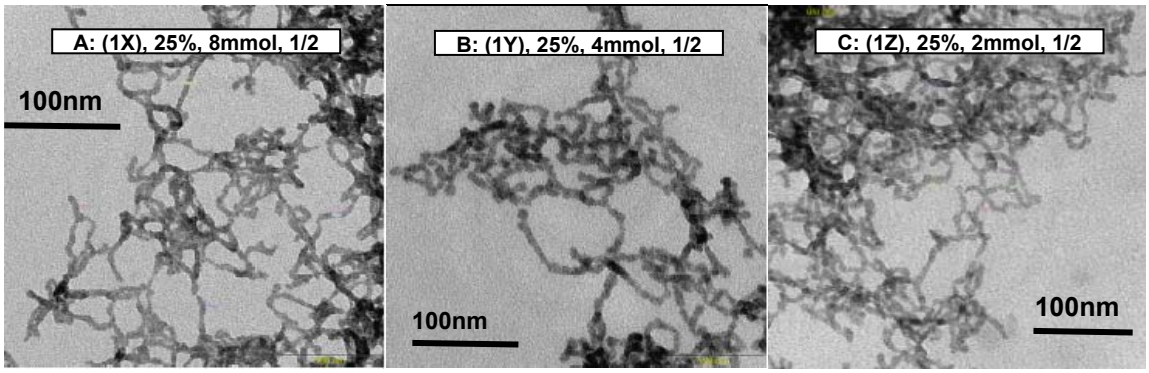


**Figure 107 (A-C): Ran 1 (25% berol) with Bi/Mo ratio of 1/2: Rang of catalyst loadings. A: 8mmol$_{catal}$/100g$_{mixture}$ , B: 4mmol$_{catal}$/100g$_{mixture}$ and C: 2mmol$_{catal}$/100g$_{mixture}$.**

The particle sizes for the range of catalyst loadings of 8, 4 and 2mmol$_{catal}$/100g$_{mixture}$ were 6.5, 8.5 and 6.5 nm respectively for X, Y and Z. The particles were also only found in agglomerated heaps or strings of particles but seem to stick less than samples A, B and C.

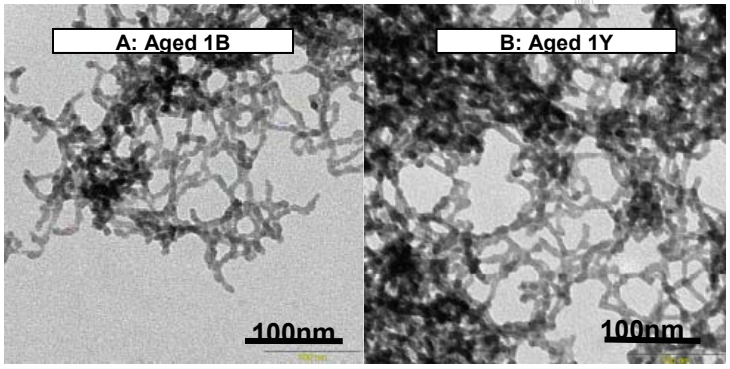


**Figure 108 (A&B): Aged samples 1B and 1Y.**

The aged samples 1B and 1Y were the same as the fresh samples.

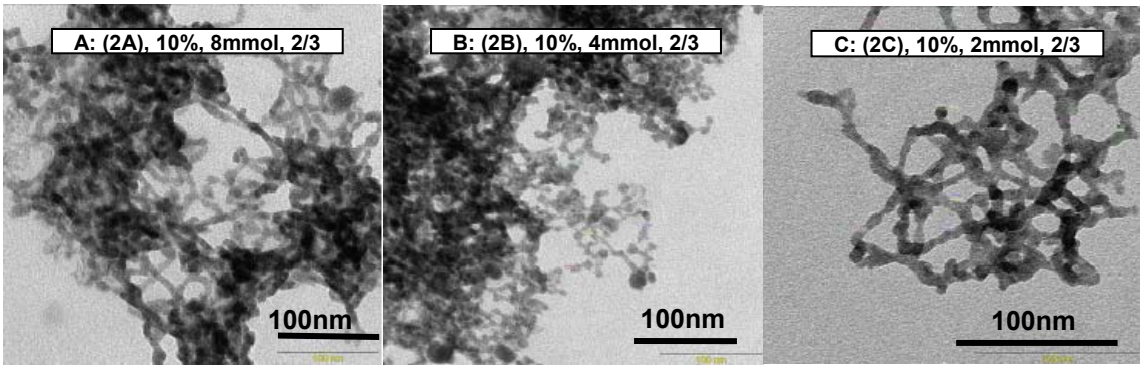


**Figure 109 (A-C): Ran 2 (10% berol) with Bi/Mo ratio of 2/3: Rang of catalyst loadings. A, 8mmol$_{catal}$/100g$_{mixture}$ ; B, 4mmol$_{catal}$/100g$_{mixture}$ and C, 2mmol$_{catal}$/100g$_{mixture}$.**

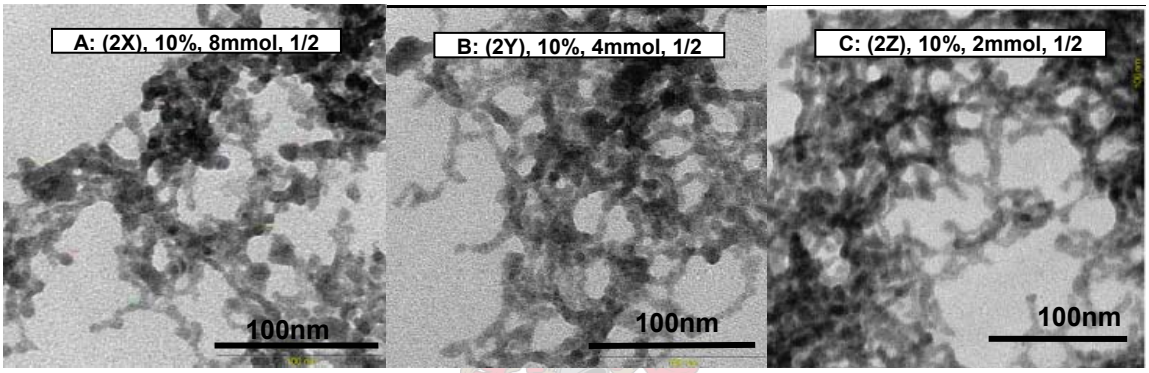


**Figure 110 (A-C): Ran 2 (10% berol) with Bi/Mo ratio of 1/2: Rang of catalyst loadings. X, 8mmol$_{catal}$/100g$_{mixture}$ ; Y, 4mmol$_{catal}$/100g$_{mixture}$ and Z, 2mmol$_{catal}$/100g$_{mixture}$.**

The particle sizes for the range of catalyst loadings of 8, 4 and 2 mmol$_{catal}$/100g$_{mixture}$ were 5.6, 8.5 and 6.0 nm for A, B and C respectively and were similar 7.5 nm sizes for the X, Y and Z of run 2. The particles were only found in agglomerated heaps or strings of particles.

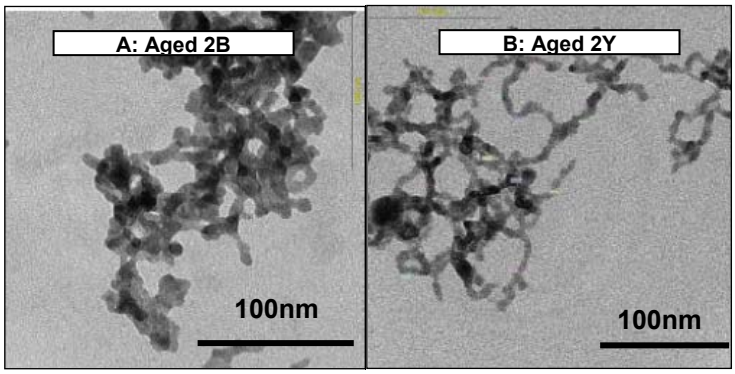


**Figure 111 (A&B): Aged samples 2B and 2Y.**

The aged samples 2B and 2Y also were the same as the fresh samples.

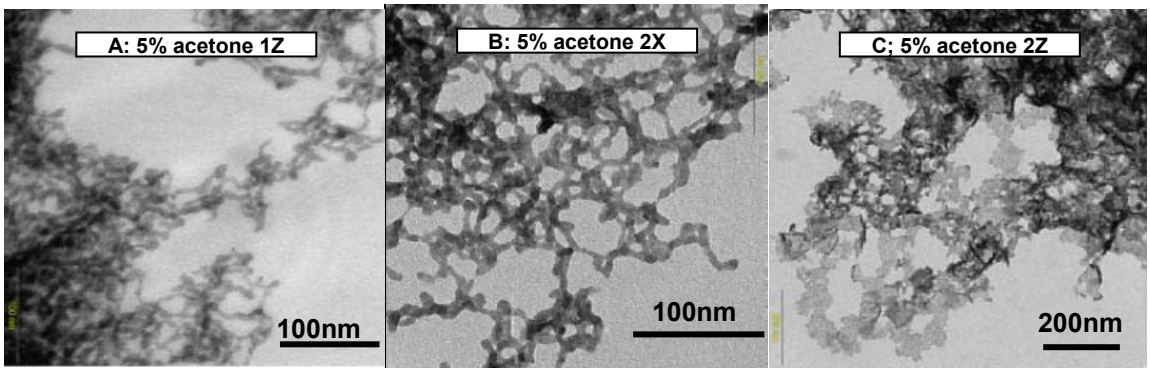


**Figure 112 (A-C): Acetone containing oil-surfactant mixtures of run 1 and 2. X, 8mmol$_{catal}$/100g$_{mixture}$ and Z, 2mmol$_{catal}$/100g$_{mixture}$**

The acetone containing mixtures produced particles of similar sizes (6-9 nm) to those free of acetone. The particles were still found in heaps and strings. In samples A2X and A2Z, a considerable amount of plate like structures were found tangled between the particle strings.

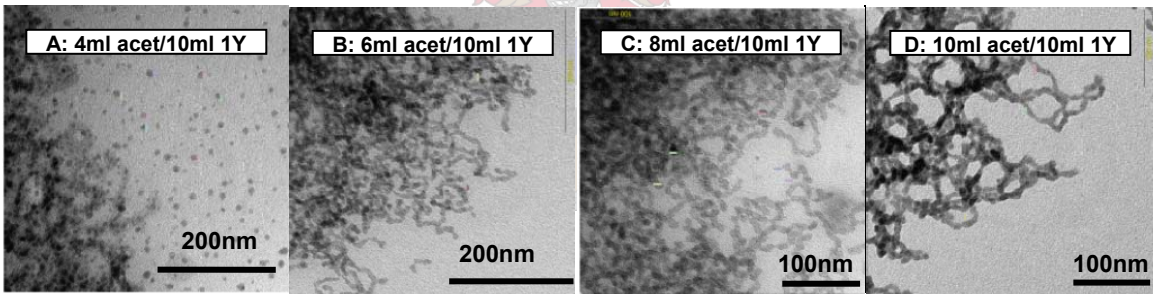


**Figure 113 (A-D): Acetone wash rang: 4, 6, 8 and 10ml of acetone added to 10ml of sample 1Y.**

Contradictory results were found for the acetone liberation and wash. Figure 113 shows more liberated particles when using less acetone (A4). As the acetone volume added to the micelle mixture increased from 4 ml to 10 ml the particles seem to become more tangled.

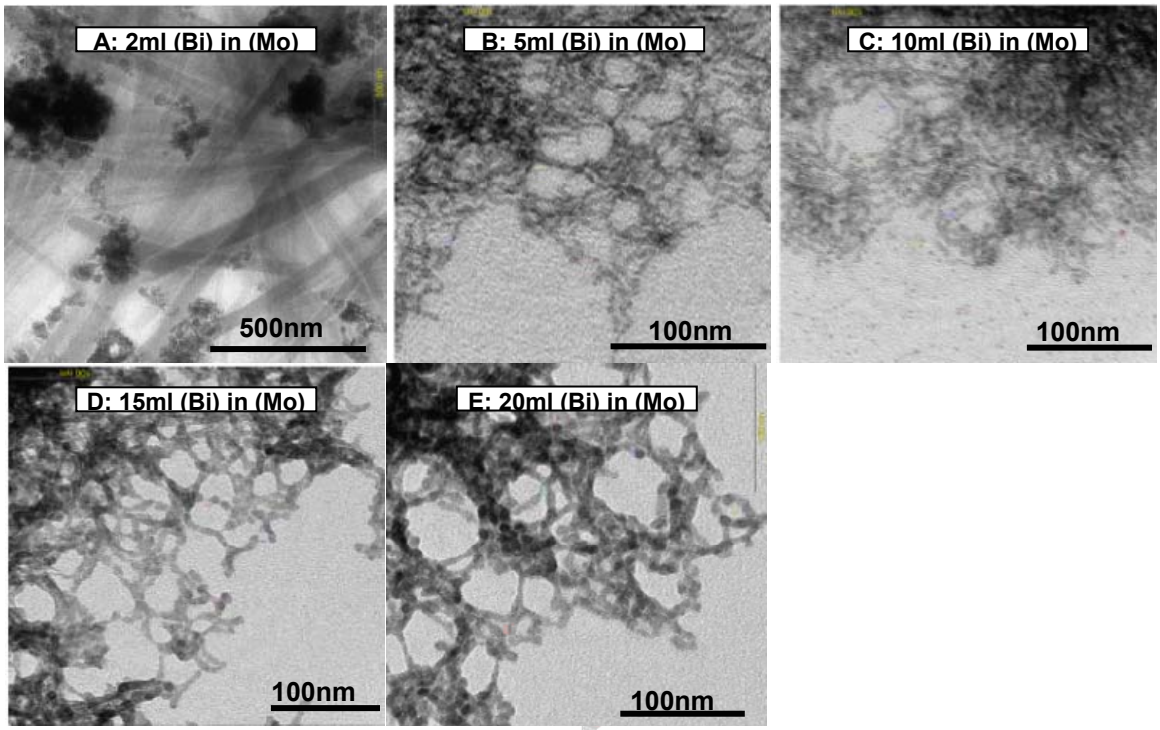


**Figure 114 (A-E): Bismuth mixture addition to molybdenum mixture range: 2, 5, 10 and 20ml of the 30ml (20g) bismuth mixture added to the (20g) molybdenum mixture.**

As the bismuth micelle mixture was added to the molybdenum mixture the particle sizes grew from 2.5 nm to 7.5 nm. The amount and size of crystals found mixed with the particles decreased as the amount of bismuth mixture increased. The particles in all the samples observed were tangled in heaps or strings.

## Discussion of Experiment A6

When this experiment was done the ambient temperature was 13-15$^{o}$C, which was much less than the normal 25$^{o}$C. This might explain some of the results that were obtained such as the formation of a precipitate for the 25% berol mixture and the contradictory results for the acetone liberation and wash.

The catalyst loadings of 2-8 mmol per 100g oil-surfactant mixture for both runs 1 and 2 (25% and 10% berol mixtures) did not have a significant effect on the particle sizes. When the bismuth micelle mixture was added to the molybdenum mixture a degree of growth were observed (2.5 nm growth to 7 nm) in the rang corresponding to a loading of 0.5-1.0 mmol per 100 g oil-surfactant mixture.

It was found that for run 1 (25% berol) the particles in the samples, which had an ideal Bi/Mo ratio of 2/3, were more tangled up than those found in the samples with an excess of molybdenum. This supports the hypothesis that an ideal Bi/Mo ratio contributes the particles sticking to each other. This observation could not be made for run 2 (10% berol) in which both the 2/3 and 1/2 ratios were tangled to the same degree.

The aged samples gave the same results as the fresh samples. This was in a way surprising because the previous experiment formed crystal needles or rods after 2 days. Again the temperature could play a role in the rod formation.

The acetone containing mixtures did not contribute to a change in particle sizes. When the aqeous phase was added to the oil-surfactant-acetone mixture it became a viscous gel. This might have caused the formation of catalyst by a mechanism other than that of the micelle technique causing the plate like structures found tangled in between the particle strings.

The reason behind the increase in degree of entanglement (heap and string formation) with the increase of acetone volume added to the micelle mixture, to liberate the particles from the micelles, was unclear. This contradicts what has been found so far. The temperature effect on this step should be investigated to see whether it plays a significant role.

### *Experiment A7: Catalyst Synthesis By RMT (Liberation of Catalyst Particles)*

The catalyst particles should be totally liberated in order determine their size distribution accurately and to support or space it in the calcination step. In this experiment temperature effects of the acetone wash step are investigated to see whether it could influence the liberation of the particles. Another attempt was maid to investigate the mechanism (nucleation and growth) of the particle formation within the micelles.

## Experimental of Experiment A7

A 10% berol-hexane mixture was made up by adding 8.9 g of berol to 80 g of hexane. The mixture was divided into three 20 g and one 10 g amounts in order to make up two samples and kept in a temperature regulated area at 25°C. Bismuth and molybdenum salt solutions were maid up as follows: 4.1386 g of $Bi(NO_3)_3 \cdot 5H_2O$ was dissolved in 2 ml $HNO_3$ and slowly adding 40 ml distilled water to obtain a bismuth concentration of 0.2133 M. 6.253 g of $(NH_4)_6Mo_7O_{24} \cdot 4H_2O$ was dissolved in 40 ml demineralised water to obtain a molybdate concentration of 0.8532 M. The micelle mixtures were made up as follows and kept at 25°C for 10 min:

**Table 21: Exp. A7: RMT, Summary of experimental mixture compositions.**

| Ran | [Bi] | Bi Solution Volume | Mixture (Bi) | [Mo] | Mo Solution Volume | Mixture (Mo) | Bi/Mo |
|---|---|---|---|---|---|---|---|
| | mol/l | ml | g | mol/l | ml | g | |
| | | | | | | | |
| A | 0.2133 | 1.5 | 20 | 0.8532 | 1.5 | 20 | 0.25 |
| B | 0.2133 | 3.0 | 20 | 0.8532 | 0.75 | 10 | 1.00 |

The bismuth mixture was slowly added to the molybdenum while stirring vigorously for 10 min. In the case of run B, 1 ml samples were taken from the total mixture after the addition of 5, 10, 15, 20 and 30 ml of the bismuth salt. The micelle mixtures were left to sand in the temperature controlled environment for 20-60 min before it were treated to the acetone wash. The micelle mixture of ran A was used to determine the influence of temperature on the wash step. 10 ml of acetone at 10, 20, 30 and 30°C was added to 10 ml of micelle mixture. The washed samples were centrifuged, washes a second time in 4 ml acetone centrifuged and kept in acetone until viewed under the TEM. One 15 ml sample of run A was used to take 1ml stepwise samples as 2, 4, 8, 11 and 20 ml of acetone (30°C) was added in the wash step.

## Results of Experiment A7

Consistent with previous experiment the 10% berol-hexane mixture formed a white bushy precipitate that settled to the bottom. All the micelle mixtures (of both bismuth and molybdate) were clear before they were mixed, suggesting stable micelles.

When the bismuth were added to the molybdate a precipitate immediately formed for both ran A and B. When adding the bismuth to the molybdenum the mixture turns yellow when molybdenum was in excess and gradually pale green as bismuth was added until it was in excess. When the mixtures were left to stand it formed the precipitate settled to the bottom.

When the 10 ml of acetone at different temperatures were added to 10 ml of ran A an interesting phenomenon were observed. The total mixture temperature increased with an increase of acetone temperature, causing a change in precipitate character form a fluffy precipitate at low temperatures (10-20$^{o}$C) to a more viscous liquid character (20-30$^{o}$C) and ultimately to a liquid like form that stick to the glass tube at high temperatures (30-40$^{o}$C).

**TEM Results:**

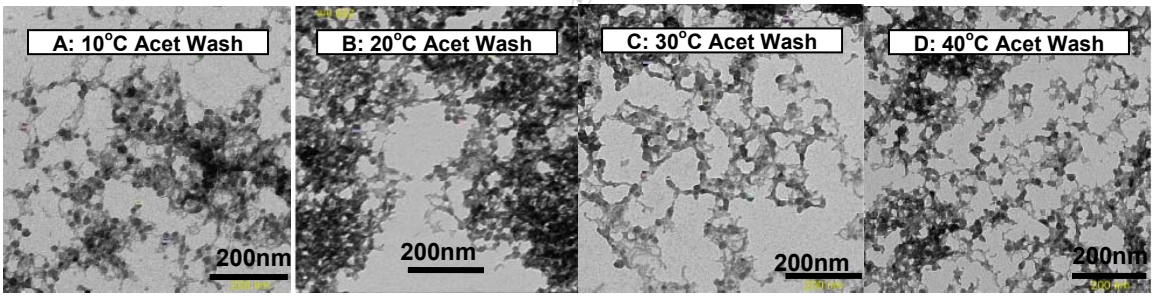


**Figure 115 (A-D): Acetone wash rang: 10, 20, 30 and 40°C acetone wash of ran A.**

Well formed semi-liberated large (17-23 nm) particles were found in ran A. The particles were still bound to each other by slime like catalyst web. No significant changes were observed in the temperature range acetone wash.

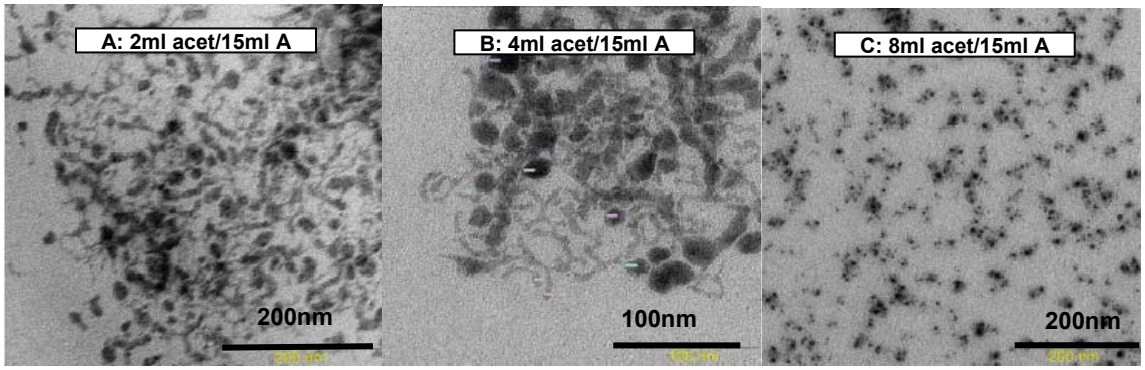

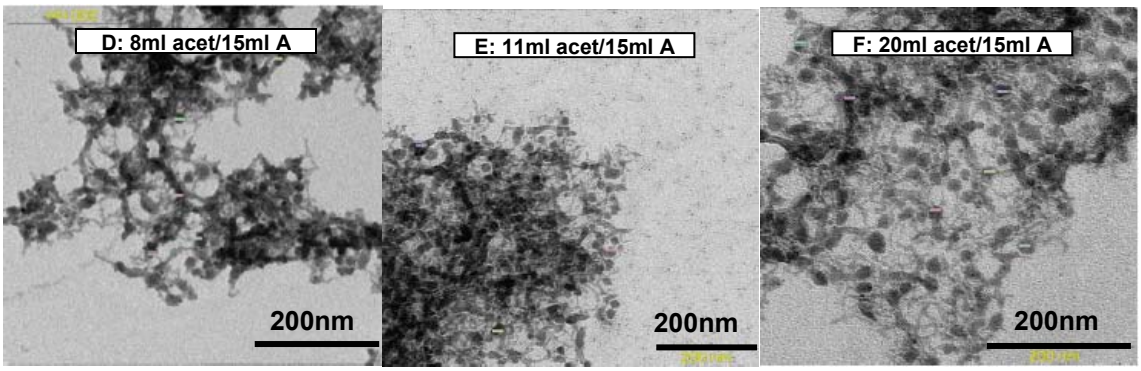


**Figure 116 (A-F): Acetone wash rang: 2, 4, 8, 11 and 20ml of acetone added to 15ml of ran A.**

Using different amounts of acetone in the wash did seem to influence the particle liberation to a small degree. The best results were obtained when 8 and 11 ml of acetone were added to 15 ml of sample mixture. It is noticeable that there were two particle sizes present in run A. The smaller of the two (4-5 nm) is present in a string form as well as totally liberated particles. The larger is mostly tangled between the strings of the smaller.

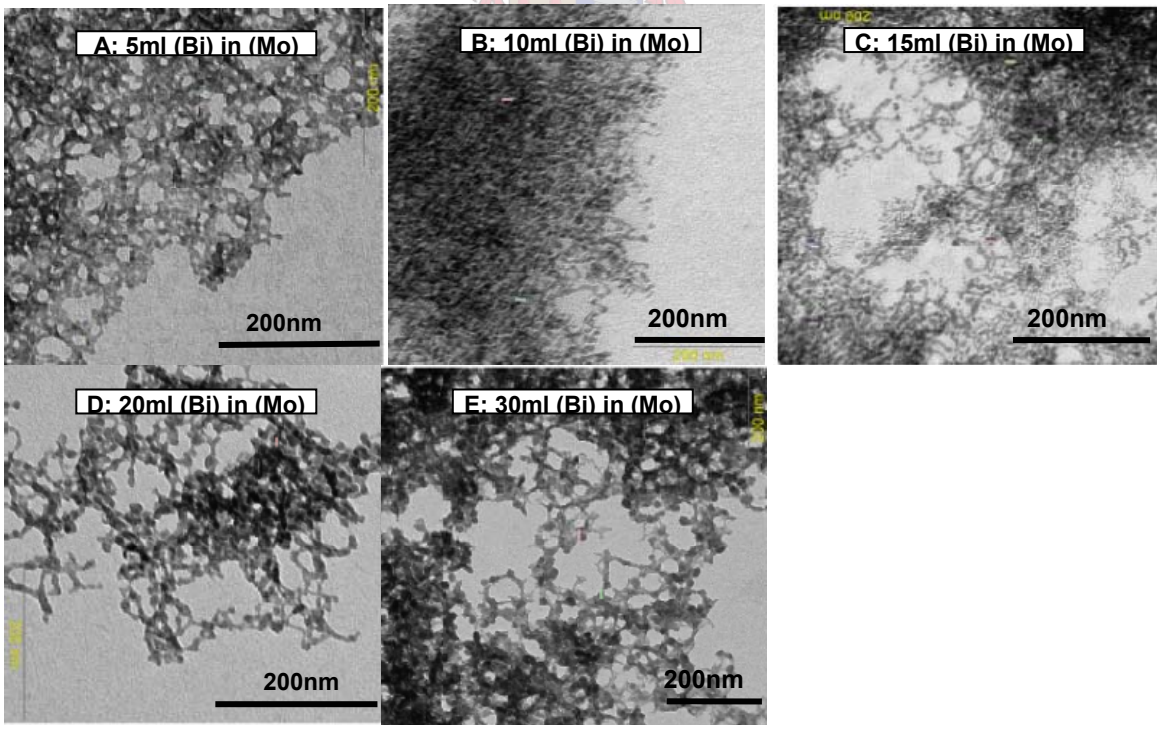


**Figure 117 (A-E): Run B, Bismuth mixture addition to molybdenum mixture range: 5, 10, 15, 20 and 30ml (20 g) bismuth mixture added to the (20 g) molybdenum mixture.**

The particle sizes in the bismuth addition range were similar (7-10 nm) except for the 5 ml one which was a bit smaller (5-7 nm). In the 10, 15 and 20 ml addition sample two particle sizes were observed, as was seen in run A, causing a wide size distribution. As more bismuth mixture was added to the molybdenum the particles tend to stick more to each other.

## Discussion of Experiment A7

The results obtained in this experiment were generally better than of the previous one in which the particles were not liberated at all. Neither the temperature range for the acetone wash nor the acetone addition range had significant liberation influence.

It was observed that both runs A and B had two particle sizes present. This could have originated from the bismuth and molybdenum micelle mixtures that were used. In run A the bismuth salt solution loading was only half of its maximum loading were the molybdate solution was at full loading capacity. In run B the opposite was done. Using less aqueous phase than its maximum loading capacity does theoretically decrease the size of the micelles. If the two salt mixtures have micelles of different sizes it could form particles of different sizes due to small-to-large or large-to-small micelle interaction. Finding these two particle sizes also suggests that the interaction was a slow process that needs outside forces like vigorous stirring the mixture. It also brings up the question of how long and vigorous should the micelle mixtures be stirred? The particles obtained in this experiment were more liberated and better defined than that of the latest experiments. Seen that the acetone wash does not play such a significant role as previously thought in the liberation of the particles, the only other parameter was the degree of completion of the precipitate reactions between micelles. In most of the experiments done the particles were not liberated due to a slush-like web that tangled the particles together and more so when the micelle precipitation was done at lower temperatures (15$^{o}$C). The lower temperature caused the interaction between micelles to be slower. Due to the charged and thus repelling nature of the micelles, the micelles will not mix spontaneously without external force like vigorously stirring. If the salt solutions within the micelles did not exchange, while forced interaction due to stirring, it will be liberated with the precipitated particle in the acetone wash. This causes mixing of salt solutions outside micelles resulting in the formation of catalyst by a mechanism other

than that of micelle interaction. It is highly probable that the slush that causes the particles to stick originate from braking of micelles which still contained salt solutions. This sticking might be minimised by increasing the temperature of the micelle mixtures and stirring more vigorously for a longer duration.

### *Experiment A8: Catalyst Synthesis by RMT (Temp. Mixing and Washing)*

The aim of the following experiment was to determine if temperature and stirring parameters influence particle formation and degree of liberation of particles in the RMT. It was postulated in previous experiment (Exp. A7) that an increase in temperature increases the interaction rate (rate at which salts were exchanged) between micelles, thus using up the salts within the micelles which otherwise can cause particle sticking when the micelles were broken in the acetone wash step. Reproducibility and particle supporting was investigated as well.

### Experimental of Experiment A8

A 10% berol-hexane mixture is made up by adding 8.9 g of berol to 80.0 g of n-hexane. The mixture was split into four 20 g amounts. Bismuth ([Bi] 0.2133 M) and molybdate ([Mo] 0.8532 M) salt solutions are prepared as was done in Exp A7.

**Table 22: Exp. A8: RMT, Summary of experimental mixtures compositions.**

| Ran | Bi Solution Volume | Mo Solution Volume | Bi/Mo | Temp | Stir Time |
|---|---|---|---|---|---|
| | ml/20ml$_{mixture}$ | ml/20ml$_{mixture}$ | | $^{\circ}$C | min |
| | | | | | |
| A1 | 3.0 | 1.5 | 0.50 | 35 | 25 |
| A2 | 3.0 | 1.5 | 0.50 | 35 | 25 |
| B1 | 1.5 | 0.75 | 0.50 | 35 | 25 |
| B2 | 1.5 | 0.75 | 0.50 | 35 | 25 |
| C | 3 | 1.5 | 0.50 | 25 | 25 |
| D | 1.5 | 0.75 | 0.50 | 25 | 25 |

Both the bismuth and molybdenum emulsion mixture were kept at its individual run temperature for about 40 min. The bismuth emultion mixture was slowly added to the molybdenum while stirring vigorously for 25 min. The individual mixture temperatures were kept at a fix using a water bath.

The catalyst was separated from their micelles by adding 10-13 ml of acetone to 10 ml mixture. The catalyst precipitate mixture was centrifuged and the clear liquid removed. The catalyst cake was again washed with 4 ml of acetone, centrifuged to get rid of the dirty acetone and then kept in 4 ml of clean acetone to be viewed under the TEM.

Attempts were made to support or space the catalyst particles of sample A2 by adding fine supporting silica particles during the first acetone addition in the wash step.

## Results and Discussion of Experiment A8

When the bismuth was added to the molybdate a precipitate immediately formed for all runs. When the bismuth emulsion was adding to the molybdenum emulsions the mixture turns yellow when molybdenum was in excess and gradually paler until all the bismuth was added. The resulting mixtures were vigorously stirred for 25 min during which a large fraction of the hexane evaporated especially the samples with the higher temperatures (A and B). The evaporated hexane was partly replaced during the stirring by new hexane in an attempt to keep the ternary composition fairly constant. The resulting mixtures contained a finely dispersed precipitate which took much longer to settle compared to those attained by stirring for a shorter duration.

Even in the acetone wash step the precipitate particles were more finely dispersed compared to those attained by stirring for a shorter duration. This indicated that the particle agglomeration was less with acetone addition meaning that much less unreacted salts solutions were liberated in the wash step. It was also kept in mind that the loss of hexane as a result of vaporisation caused an increase in emulsion mixture viscosity due to the high berol content (berol has a higher viscosity than hexane). This also contributes to the particles settling slower than usually.

## TEM Results

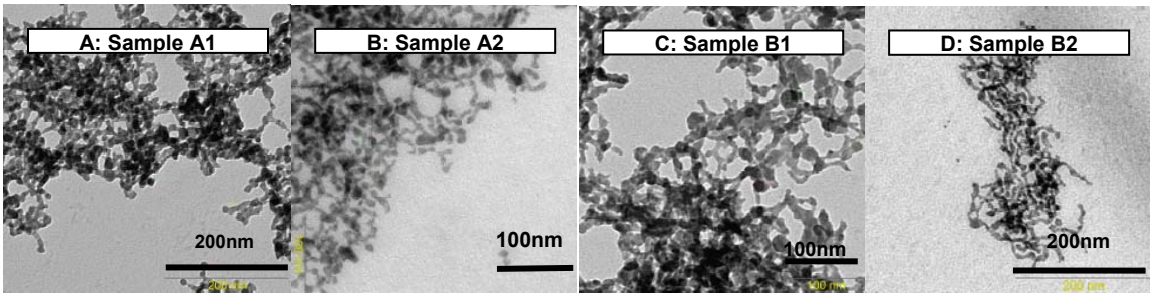


**Figure 118 (A-D): Samples prepared at 35°C. Similar samples A1&A2 and B1&B2 prepared a week apart.**

Figure 118 shows similar samples prepared a week apart. The second of the two (A2 and B2) seems more liberated than the first (A1 and B1). There were no significant difference between samples A(1&2) and B(1&2) respectively.

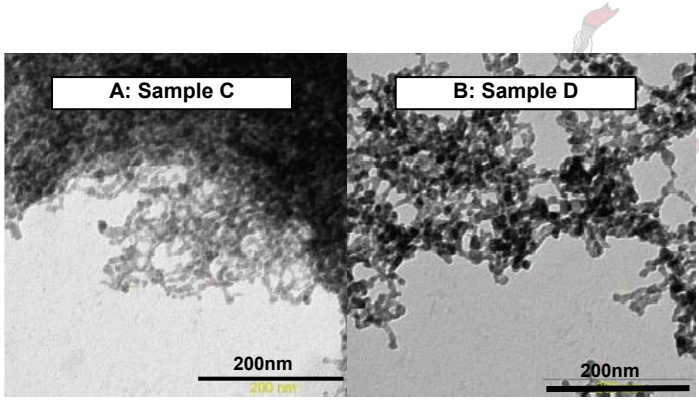


**Figure 119 (A & B): Samples prepared at 25°C. Sample C (A) has double the aqueous content used in sample D (B).**

Figure 119 photos (samples with difference in aqueous contents) prepared at 25°C do not show significant difference in particle size or degree of particle liberation. If the samples prepared at 35°C is compared to those prepared at 25°C no significant differences either observed.

Figure 120 shows two photos of sample B1 washed with different amounts of acetone. No significant difference is observed between the two.

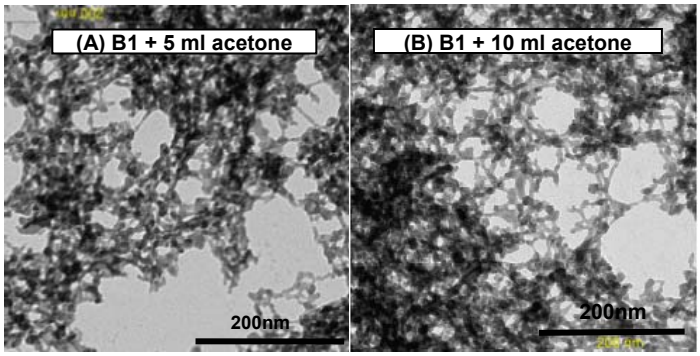


**Figure 120 (A & B): Acetone wash of sample B1, (a) 5 ml acetone per 5ml emultion mixture and, (b) 10 ml acetone pre 5ml emultion mixture.**

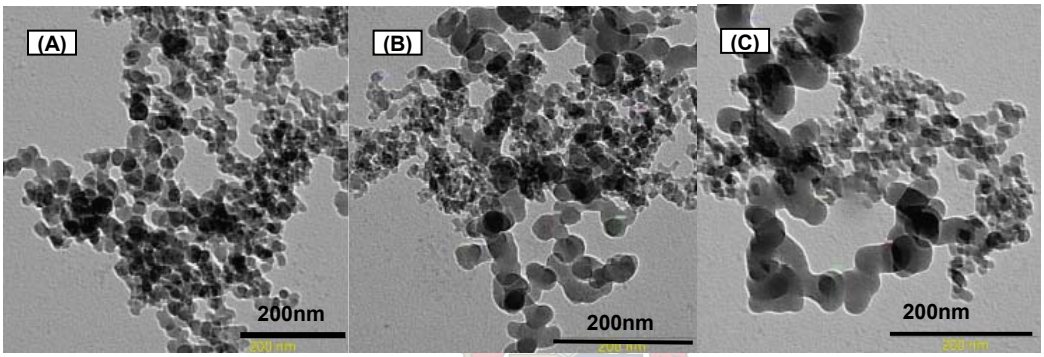


**Figure 121 (A, B & C): Sample A1 mixed with silica particles.**

In Figure 121 catalyst particles can be distinguished from the support as the larger bulky sausage like strictures. The sizes of these structures may vary as a result of the amount of silica particles used to space the catalyst particles.

# Appendix B
# Precipitation and Calcination Experiments

### *Experiment B1: Keulks's Co-Precipitation Method*

A molybdenum solution was made up by dissolving 15.8900 g of $(NH_4)_6Mo_7O_{24}\cdot 4H_2O$ in 200 ml of water. This solution was acidified to a pH of 1.5 by slowly adding an appropriate amount of concentrated nitric acid while vigorously stirring the aqueous molybdenum solution. A white precipitate formed at a pH of ca. 2.5. This solution was allowed to stand for one hour after acidifying. The bismuth solution was made up by dissolving 29.1062 g $Bi(NO_3)_3\cdot 5H_2O$ in 30 ml of concentrated nitric acid. After the dissolution of the salt, the acid solution was further diluted with 1170 ml of distilled water. The bismuth nitrate solution was added slowly (8 ml/min) to the aged, acidified molybdenum solution, while the latter solution was constantly stirred. The temperature of the solution was kept at 25°C. The pH of the mixture was maintained constant at pH 1.5 by back titrating with concentrated ammonium hydroxide. After the addition was complete, the precipitate and the mother liquor were allowed to stand for 4 hrs, after which the solution was filtered. The filtrate was used to clean the glassware and was then passed over the collected precipitate. The precipitate was dried at 60°C for 48 hrs and placed in a crucible for calcination. The calcination program was set as follows:

- 25°C – 120°C for 3 hrs
- 120°C – 200°C for 2 hrs
- 200°C – 450°C for 4 hrs
- 450°C for 12 hrs

A second batch was prepared similarly, except that the pH was kept at 1.2. The calcined and uncalcined powder samples were analysed using XRD. The resulting spectrums were compared to spectra calculated for $\alpha$- and $\beta$-BiMoO samples.

### *Experiment B2: Temperature Range Calcination*

BiMo precipitate (Bi/Mo = 2/3) was prepared using the precipitation technique suggested by Keulks *et al.* [1974] (Exp. B1). 2 g dried precipitates were calcined for 24 hrs at 180°C, 200°C, 220°C, 250°C and 270°C respectively and their XRD compared to that of

samples that were uncalcined and calcined stepwise (25°C–120°C in 3 hrs, 120°C–200°C in 2 hrs, 200°C– 450°C in 4 hrs and 450°C for 12 hrs).
The TGA and DC analyses were done in a nitrogen and air atmosphere at a temperature ramp of 10°C/min.

### *Experiment B3: Molybdate Acid Titrations*

Molybdenum solutions were made up by dissolving 22.0716 g, 17.6615 g and 8.8294 g of $H_{24}Mo_7N_6O_{24}{\cdot}4H_2O$ in 250 ml of distilled water to make up 0.5 M, 0.4 M and 0.2 M molybdenum solutions. To these solutions, 27% concentrated $HNO_3$ was added at a rate of 0.2 ml every 2 min and the pH was monitored using a glass electrode. The experiments were done at 25°C.

### *Experiment B4: Bismuth Solution Stability*

Bismuth solutions were prepared by adding 0.17, 0.2, 0.3, 0.4, 0.5, 0.6, 0.7 and 0.8 ml of 55% concentrated nitric acid respectively to 1 g of $Bi(NO_3)_3{\cdot}5H_2O$. Distilled water was added slowly while stirring vigorously. The volume of water needed to dissolve the salt and the point at which small crystals started to precipitate were noted. The experiments were done at 25°C.

### *Experiment B5: Bismuth-Molybdate Titrations*

Molybdenum solutions were prepared by dissolving $H_{24}Mo_7N_6O_{24}{\cdot}4H_2O$ in distilled water at the required salinity and, in some cases, ammonium was added to increase the pH. Bismuth solutions were made by first adding the concentrated $HNO_3$ to the $Bi(NO_3)_3{\cdot}5H_2O$ salt and stirring vigorously while slowly adding the distilled water. The bismuth solutions were then slowly added to the molybdenum solutions in small steps until it reached a 2/3 Bi/Mo ratio. The experiments were done at 25°C and the pH was measured using a glass electrode.

# Appendix C
# Formation and Stability of Reverse Micelles

### *Experiment C1: Calibration with Latex Particles*

A 10% berol-surfactant mixture was made up. The white precipitate that formed directly after the mixing was left to settle and only the clear liquid was removed and double filtered using a 0.4 μm filter. Care was taken to keep the mixture dust-free at all times and at the same composition by avoiding vaporisation and always keeping it sealed tightly. The cuvette was rinsed with filtrated oil-surfactant mixture to remove all possible dust particles and impurities. It was then filled with 3 ml of the mixture and 0.1 ml of filtered distilled water. The filled and sealed cuvette was then placed in a sonic bath for 3 min after which a small amount (1/2 drop) of standard latex particles was added to the mixture (the mixture turned slightly milky). The mixture was placed in the sonic bath for c3 min for the second time, after which it was cleanly dried and placed in the analyser. Note that the cuvette needs to be sealed to prevent the evaporation of oil over the long analysing periods. The viscosity and the refractive index were taken as 0.89 and 1.332 respectively (default value for water at 25°C).

### *Experiment C2: Micelle Stability of Distilled Water*

A 10% berol-surfactant mixture was made up. The white precipitate that formed directly after the mixing was left to settle and only the clear liquid was removed and double filtered using a 0.4 μm filter. Care was taken to keep the mixture dust-free and at the same composition at all times by avoiding vaporisation and always keeping it sealed tightly. The cuvette was rinsed with filtrated mixture to remove all possible dust particles and impurities. It was then filled with 3 ml of oil-surfactant mixture and a small amount (0.05-0.5 ml) of filtered distilled water was added. The filled and sealed cuvette was then placed in a sonic bath for 3 min, after which it was cleanly dried and placed in the analyser. Note that the cuvette needs to be sealed to prevent evaporation of the oil over the long analysing periods. The viscosity and refractive index were taken as 0.89 and 1.332 respectively (for water at 25°C).

# Appendix D
# Kinetic Experimental Procedures

## *Reactor Rig Experimental Procedures*

### Pre-experiment Preparations

- Check gas bottles for contents: reactor gas bottle pressure must be checked.
- Check gas bottles and connecting tubing for leaks using soapy water.
- Prepare evacuated glass ampoules: ±20 ampoules are used per run of 60 min.

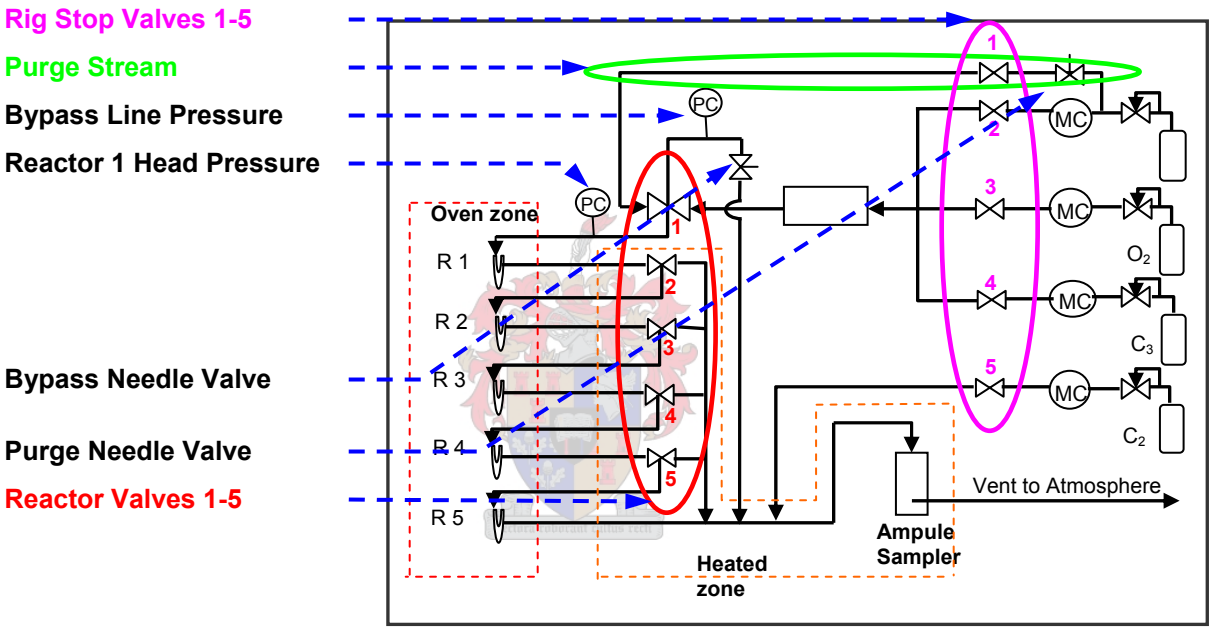


### Setup of Kinetic Rig

- Close all rig stop-valves.
- Close the purge needle-valve and open the bypass needle-valve.
- Open helium, propene, $O_2$ and ethane cylinders and stop-valves at cylinders and verify line pressures at the pressure regulators.
- Switch reactor-valve 1 on purge and check that reactor-valves 2 to 5 are switched correctly, dependent on the number of reactors used in series. Reactor-valves of unused reactors (if a reactor is fitted or not) should be set in a series

configuration so that the reactor product of the used reactors does not leak from the sample collector line back into the oven.

- Pack the reactor with the required amount of catalyst (usually 0.1-0.2 g) diluted with silicon carbide as described in Fig. 28. Secure the reactor into the reaction oven and test for leaks by purging it with helium. (Purge by opening the purge stop-valve and purge needle-valve until the reactor head pressure is 1.5 bar).
- Switch the reactor oven on at a set point of 120°C and increase the temperature in 50°C steps to the desired temperature to ensure uniform expansion of the oven and reactor.
- Switch on the ampoule sampler heating at a set point of 40°C and increase the temperature in 20°C steps to 120°C. (The controller can also be switched on manual and should be switched on at 8-9%).
- The flow rates of the reaction gasses as well as the internal standard can be tuned individually by opening their rig stop-valve and changing its set point value to the desired value, using a calibration curve.
- Glass ampoules must be prepared (marked, numbered or named and put in easy reach of the person taking the samples).

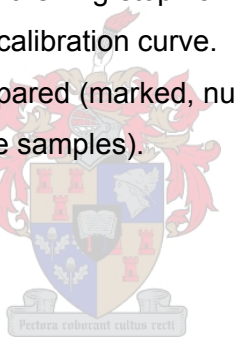


## Experimental Procedure

- Set up the experimental rig as described above.
- When the reactor oven and ampoule sampler reach the required temperature the oven temperature, controller is switched from automatic to manual. The temperature is then controlled by a percentage of its maximum power input (usually between 20 and 35%). The input is adjusted manually until the temperature stabilises at the required value (The temperature control is much more stable using manual control).
- With reactor-valve 1 still on purge, open the helium purge stream to a similar flow rate as the total reaction gas flow rate by opening its rig stop-valve and tuning the needle-valve.
- Open the reaction gasses and internal-standard stop-valve with their mass flow controllers at predetermined set points and leave for 5 min to stabilise.

- Increase the bypass line pressure to a slightly higher pressure than the reactor head pressure by tuning the bypass needle-valve. The reaction mixture now bypasses the reactor at similar pressures to what it will encounter while flowing over the reactor system. This helps to prevent high pressure pushing back from the reactor when the reaction gasses are switched to the reactor and to stabilise mass flow through the controllers.
- If the temperatures, flow rates and pressures are stable and at their desired values, the experimental run is ready to begin! Switch reactor valve 1 to reactor and close the purge rig stop-valve simultaneously. Make sure all flow rates remain constant.
- The product gas mixture is sampled at specific times using an evacuated glass ampoule. The ampoule is loaded into the sampler though a rubber septum and is flame sealed after the sample has been taken. A time of 10-15 sec should pass after the ampoule is loaded before the sample is taken.
- Note the head pressure as well as the reactor bed temperature of every sample.

.

### *Analyzing Rig Start-up and Experimental Procedure*

The detector, injector and flow rate settings need to be set for start-up. In most cases, a stabilisation period is needed for the equipment to warm up and the signals to settle to a steady state. The following two sections will run through the start-up and the experimental procedure.

### Start-up Procedure

1. Supply a 220 V 50 Hz electrical source to the GC, analysing computer and heat controller.
2. Set the gas pressures as follows: He (5 bar), Air (5 bar) and $H_2$ (4 bar)
3. Set the TCD and FID settings. TCD: range 0.5, oven temperature 320$^{o}$C and switch the detector-oven on. Do not switch electronics on. FID: range 9, oven temperature 300$^{o}$C and switch the detector-oven on. Do not switch the electronics on. It will take about 90 min for the detectors to warm up.

4. If the detector temperatures are at their set values, the carrier gas flow-rate must be set to 740 (37 ml/min) and the TCD reference flow rate to 300 (30 ml/min). The needle-valve controlling the carrier gas flow rate through column 2 is opened two revolutions from finger-tight-closed, ensuring a flow rate of 28 ml/min. The pressure gauge should indicate a pressure of around 25 psi.
5. Open the $H_2$ and air valves on the GC fully. The flow rates are prefixed to their required values.
6. Switch on the electronics of both detectors and confirm their signal on the analysing PC.
7. Program the column oven-settings: 35°C for 1 min, temperature ramp of 55°C/min till 280°C and hold for 10 min.
8. Switch on the ampoule-breaker heat-controller and let the temperature rise from ambient to 110°C in 20°C steps to preventing sudden overheating.

## Experimental Procedure

1. Start-up the analysing rig: the start-up procedure is described above.
2. Isolate the ampoule breaker: the ampoule breaker is isolated from the column stream by turning the six-way valve clockwise.
3. Clean the ampoule breaker: the breaker is opened at its large nut and cleaned using a vacuum-cleaner. The glass pieces from the broken ampoules are mostly too big to be sucked up through the thin vacuum tube and need to be crushed thoroughly using a stainless steel rod. A loose brass pellet, a stainless steel pellet with holes and a concave stainless steel cylinder are found in that order (top downwards) at the bottom inside of the breaker to preventing small glass particles entering and blocking the tubes. These may be sucked up by the vacuum cleaner, and should be replaced in the correct order after cleaning. Care must be taken to insure that both pellets lie flat when they are replaced.
4. Prepare the ampoule breaker: a small piece of glass-wool is placed at the bottom, acting as a filter to prevent small glass particles from blocking the tubes.
5. Load the sample: the sample-containing ampoule is carefully placed in the breaker and it is sealed of by replacing the piston section. Make sure the piston is pulled back so that it does not break the ampoule when it is replaced.

6. Purge the ampoule breaker: the breaker is purged with helium by opening the purging valve, causing the helium to flow from the bottom to the top of the breaker. To quickly remove all the air around the sleeve of the piston, the small nut that seals the piston and sleeve can be untied resulting in the leakage of the purging helium. This will flush the trapped air out of the dead volume in the sleeve. The ampoule is purged for about 1 minute and the sleeve nut finger tightened.
7. Reintroduce the ampoule breaker into the column stream: the pressure inside the ampoule breaker should not differ too much from the column pressure when the breaker is reintroduced into the column stream to avoid an upset of the detectors due to a sudden change in flow rate change. A rubber tube at the atmospheric vent is used to ensure the sum degree of pressurisation of the ampoule breaker after the purging valve is closed by bending the connected rubber tube closed and releasing the unwanted high pressure. By turning the six-way vale anticlockwise, the breaker is reintroduced and the pressure should stabilise to its previous value with in a few seconds. It pressure is lost, the ampoule breaker is leaking and should be tightened further.
8. Set up the data capture system: both TCD and FID signals must be captured.
9. Start the run: the run is started at the GC by pushing the start button. The data capture system is automatically started. Ten counts (GC counts, 6 seconds) after the GC program has been initiated, the ampoule is broken by swiftly and uniformly pushing down the piston. The sample gas is liberated and split into individual constitution gasses and detected by the detectors.

# Appendix E
# Savety Aspects and Summery of the Altered RMT

## Safety Aspects

The experimental and analytical work involved the handling of various flammable and toxic chemicals, as well as small inhalable particles, high temperatures and highly explosive gasses. Tabel 23 gives a risk assessment of the experimental work.

**Table 23: Experimental risk assessment**

| Chemicals and Equipment | Hazard | Safety Tips |
|---|---|---|
| | | |
| Acetone | Flammable and evaporates | Keep away from open flames |
| Ammonium molybdate tetrahydrate | - | |
| Bismuth(III)Nitrate pentahydrate | - | |
| Berol 050 | Skin and eyes | Work with gloves |
| Fumed Silica | Inhale | Work in fume cupboard |
| HNO3,>55% and NH3, 25% con. | Skin, eyes and clothes | Use a lab coat |
| Silicon Carbide, 200-450 mesh | - | |
| Hexane | Flammable and evaporates | Keep away from open flames |
| Propene, ethene and $H_2$ | Highly explosive | Check for leaks regularly and extraction fans |
| Gas cylinders | High pressure gas cylinders | Secure firmly to prevent falling |
| CO, $CO_2$, acrolein | Toxic or suffocating | Extraction fans in lab |
| Catalyst particles/nanorods | Inhale | Work in fume cupboard with dry powdery substances |
| Reaction Rig | High temperatures | Use a lab coat and/or gloves |
| | High voltage | Keep dry |
| | Toxic or suffocating gasses | Extraction and ventilation |
| Analytical apparatus | High temperatures | Use gloves |
| | Explosive gases | Check for leaks regularly and extraction fans |
| | High voltage | Keep dry |

## Summary of Altered Reverse Micelle Technique

The bismuth solution is prepared by adding 90-100 ml $HNO_{3\ (CON.)}$/$mole_{Bismuth}$ to the $Bi(NO_3)_3 \cdot 5H_2O$ salt and slowly adding distilled water to make up a stable 0.25-0.3 M solution (see Figure 58) while stirring vigorously.

The molybdenum solution is prepared by dissolving $(NH_4)_6Mo_7O_{24} \cdot 4H_2O$ salt in degassed distilled water. The resulting solution should have a molybdenum concentration [Mo] of 0.8-0.2 M (Figure 56). The high salinity stabilises the reverse micelles

The oil-surfactant mixture is made by adding 10-20% wt Berol to the n-hexane. A white precipitate will form, which is left to settle, and the top clear liquid is used.

The bismuth and molybdenum containing reverse micelles are prepared by adding the salt solutions in separate oil-surfactant mixtures in volumes ranging from 5-14% aqueous solution. The Bi/Mo ratio should be ¼. The reverse micelle mixtures are placed in sealed containers in a sonic bath at 25°C to avoid evaporation of the volatile hexane. After sonification, the mixtures are left to age, resulting in micelle growth.

The bismuth-containing mixture should be added to the molybdenum mixture slowly, while stirring vigorously. The resulting mixture should be sonificated in a closed container after full addition of the bismuth mixture to ensure a well-mixed system in order to use up all the salts in the micelles. Aging or heating of the mixture at this stage may and most probably will lead to the formation of nanorods.

The particles are liberated from the micelles by adding acetone to the mixture. To prevent the formation of nanorods, the particles should be thoroughly washed with hexane and acetone to be free of surfactant.

Particles supporting has thus far been unsuccessful, but using small airogel silica particles the catalyst particles can be spaced if sintering occurs in the calcination step.

The catalyst should be calcined stepwise to ensure well-defined crystallinity of the particles. The minimum calcination temperature is 350°C. The suggested calcination program is: 150°C for 1hr, 250°C for 2hrs and 360°C for 5hrs.

$MoO_3$ impurities are removed from the catalyst particles using a warm ammonium wash, follower by a water rinse and a second calcination to remove adsorbed ammoniac.